The University Of Sheffield.

Title:

Synthesis and Characterisation of Methylammonium Lead Iodide.

By:

Wadir Kargar

Thesis Supervisor:

Prof: Derek C. Sinclair and Prof: Ian M. Reaney

A thesis submitted in partial fulfilment of the requirement for the degree of

Doctor of Philosophy

The University of Sheffield

Faculty of Engineering

Department of Materials science and Engineering

December 2021

Table of Contents

Abstract

Perovskite solar cells based on methylammonium lead Iodide (MALI) have achieved efficiencies as high as 26%. This value is higher than the previous form of dye-sensitised solar cells, or cadmium telluride cells, and similar to silicon-based cells. In the last decade a large amount of research has been conducted into these materials. Mostly due to their ease of preparation not only of the photovoltaic material but the solar cell itself. The economic incentives to commercialise these devices are therefore high. This thesis investigated different compositions of materials (variable methylammonium iodide/lead iodide (MAI/PbI_2) ratios), synthesis procedures and the influence of environmental factors such as moisture, temperature and oxygen on the electrical properties. Herein three different synthesis routes were investigated. (i) A solvent free solid state route using mortar and pestle; (ii) a mechanosynthesis synthesis route using ethanol, and, (iii) using organic solvents like dimethylformamide (DMF) and dimethylsulfoxide (DMSO). A combination of different starting stoichiometry's and the different synthesis methods is used to elucidate which samples might be of high quality for fabrication and which synthesis route might be best for large scale applications. The quality of the samples was assessed by a combination of X-ray diffraction (XRD), low voltage scanning electron microscope (SEM), permittivity and dielectric loss (LCR) measurements, and impedance spectroscopy (IS).

This work was sponsored by Dyesol Ltd, a company that was based in Manchester. The plan was for solar cell construction and testing to be conducted at the company laboratories and for more fundamental, scientific based work, which involved working with bulk powders and characterising their structural and electrical properties in the Materials department at Sheffield University. This would allow insights into factors which affect the materials stability and behaviour to emerge, which would be of benefit in the fabrication of MALI-based cells.

The results showed MALI could be synthesised via the three different routes. The solid state method showed MALI to have a low formation energy and that it could be synthesised by mixing the precursors in a mortar and pestle at room temperature. Three different phase assemblage diagrams were constructed for each synthesis method, by varying the precursor amounts of PbI_2 and MAI and the temperature. The solid state method shows incomplete reaction at room temperature and samples need to be annealed at 120 ˚C to drive reactions to completion/equilibrium. Heating above 140 ˚C initiates decomposition of the methylammonium organic cation, especially for samples annealed for prolonged periods (24hrs). Due to a combination of low annealing temperature and the ease of loss of powders

during mortar and pestle grinding, samples of nominally stoichiometric MALI (x = 0.00) via solid state were not phase pure, and contained PbI_2. However, going off-stoichiometry and increasing the MAI content by 5 or 10 mol% (x = 0.05, and 0.10) produced phase pure powders when annealed at 120 ̊C based on XRD results.

Due to the low sensitivity of XRD, low voltage SEM was conducted to verify phase purity. What emerged was regions of grey contrast (associated with MALI perovskite) and dark regions, associated with an organic MAI-rich phase. Therefore, these samples weren't phase pure. Thin film work from literature also indicates that the tetragonal MALI phase which appears grey in the SEM might be a mixture, which contains the stacked perovskite sheets, or α' phase. These can't be distinguished by XRD or SEM but may be responsible for some of the electrical heterogeneity observed by IS.

This trend (clean XRD results but more phases observed via SEM) continued for other samples made by the other two synthesis techniques. Synthesis of ball milled powders was conducted at 80 ̊C. x = 0.00 still had PbI_2 present and so did x = 0.05, suggesting a slight shift of the PbI_2/MAI ratio in these samples compared to the solid state reaction samples. x = 0.10 and 0.20 were clean by XRD. This was attributed to the easy loss of MAI during the reaction method. The organic solvent synthesis using DMF, showed x = 0.00-0.10 to be XRD clean when heated to 120 ̊C. The x = 0.00 sample via this route produced the cleanest SEM surface image, suggesting that it was the best quality sample prepared via the three routes.

The electrical results from both LCR and IS showed samples always had some hysteresis present between the first heating and cooling cycle. This is attributed to the easy intake of water by MALI. IS results always showed higher conductivity on the heating cycle than on the cooling cycle. The cooling cycle results are therefore best used to establish the intrinsic properties of the materials. IS data showed that samples with a small amount of excess MAI (generally x = 0.05 and 0.10) gave higher conductivity, even on the cooling cycle. This was not dependent on any specific synthesis route. These two phenomena were also observed from the LCR data. The permittivity and dielectric losses were higher on the heating cycle than on the cooling cycle with the more conductive samples having higher losses. The presence of moisture allowed the tetragonal to cubic MALI transition temperature to be elucidated at ~60 ̊C. This was because LCR gathered more data points and experiments were conducted in less time. LCR proved to be a quicker and easier method than IS to examine the electrical stability and behaviour of the samples.

Acknowledgments

I would like to first thank my supervisor Professor Derek Sinclair without his help and supervision and support I would not have been able to complete this work. I would also like to thank Professor Ian Reaney for giving me the opportunity to take up this work, with collaboration with Dyesol later renamed Greatcell solar. I would also like to thank all the members of the functional materials group who offered me help whenever I sought it. Especially Dr Whitney Schmidt, who helped me a lot in the beginning.

1. Introduction

The modern world today requires more energy, not only due to an increased population but as larger parts of the world are becoming more developed. However, due to environmental reasons a cheaper and cleaner energy source is vital if this rate of progress is to be maintained. One area that has garnered a lot of interest in recent years are organic-inorganic halide perovskite (ABX_3) solar cells. These are cleaner and the renewable energy can cater for growing energy [1], [2]. Organic-inorganic perovskite solar cells (PSC) have increased their efficiencies rapidly in the last decade, to the extent they are now comparable to the more established inorganic variants [3]. The power conversion efficiencies of the cells have reached values of 25.5% in the most efficient single junction solar cells [4]. The first use of these hybrid organic-inorganic halide perovskites was in 2009. This was when methylammonium lead trihalides were implemented in a dye-sensitised solar cell, giving an efficiency of 3.8% [5]. It wasn't until 2012 when the first solid state PSC was manufactured with an efficiency of 9.7% and 500 hours [4].

Research into these type of solar cell materials can be split into three main directions, one path was to engineer the right compositions or synthesis methods to give the maximum efficiency. This involves changing the A, B and X species from a variety of different reagents, along with changes in the material synthesis and solar cell structure. Another was to look into scaling up these PSCs to be able to commercialise them. This area also made a great deal of progress. They were first scaled to an area of $1cm^2$ [4] and this standard was to remain for lab testing of cells. When the device area of the cells increases the efficiency tends to decrease, this however is normal. The other major solar cells being investigated include silicon, cadmium telluride and copper indium gallium selenide [4]. The third area of research was a more fundamental scientific approach rather than an engineering one into the materials themselves. This involved both experimental and computational work, which could then be fed back into making more stable and efficient cells.

The efficiency of a solar cell is dictated not only by the photovoltaic material but by many different factors due to the complex nature of the cells. These include the size of the cell, and therefore the size of each layer inside the cell. The electron transport layer, the hole transport layer, the electrodes, how the different layers are deposited on each other and their resultant morphologies. Beside these factors it is also important as to how the cell is encapsulated to ensure it is stable for a long time under different working conditions. Aside from finding a suitable material and manufacturing a high efficient cell from such a material, the main issues with these hybrid perovskites tend to be with their stability [4]-[6].

Scientific lab-based research mainly focuses on compositional studies and synthesis techniques and how these relate to performance. In contrast, solar cell engineering focuses on device fabrication, compatibility and interfacial studies of the various layers. Stability needs to be addressed because not only does the material have to be stable during fabrication but also when layered between different materials and then encapsulated. The environmental factors that influence stability are parameters such as moisture, oxygen, temperature and light [6].

In this work the material which has been synthesised via different routes and then characterised is methylammonium lead iodide (MALI). It has been shown to be an excellent absorber material because it has a direct bandgap and its synthesis is rather straightforward [7]. However, it is problematic due to the ease with which it can degrade. One of the main aspects of degradation is due to moisture. This is not only during the synthesis, which is why in most research labs fabrication is made in a glove box but also once synthesised and encapsulated into a solar cell. It is known that MALI single crystals show better stability than their polycrystalline counterparts. This is due to the microstructure, i.e. grain size and grain boundaries [8]. The grain boundaries lead to infiltration of moisture and there tends to be more moisture gathered at the grain boundaries than inside the grains. As a consequence, the synthesis route is very important as grain boundary engineering is mostly controlled via the synthesis route. The moisture acts as a catalyst, increasing the likelihood of degradation. When MALI is exposed to moisture a hydrated phase is formed and this is the first step of the degradation process [9].

Temperature is another important parameter in determining the overall efficiency of the material. Firstly, MALI has three polymorphs (orthorhombic, tetragonal and cubic) and therefore undergoes phase changes as a function of temperature. Of particular importance is the tetragonal to cubic polymorphic phase transition as this occurs within the working operating conditions of the cells which can range up to 70-85 ˚C [9]. Secondly, the ease with which the organic part of MALI is susceptible to decomposition at modest temperatures, especially when other important factors such as oxygen and light are present [10]. Furthermore, due the materials being susceptible to change at relatively low temperatures, these can introduce artefacts in the material during characterisation. Care must therefore be taken during the characterisation of these materials.

The stability of any material is also dependent on factors such as crystal structure and stoichiometry because they determine the defect states either at the surface or in the bulk of the material. Defects are caused by a deviation of any atom from the position its intended to

occupy in a given crystal structure. Many polycrystalline materials are synthesised using solutions at lower temperatures and this can give rise to a larger concentration of defects. A change in (or variable) stoichiometry can also influence the type(s) of defects and their concentration which can influence the functional properties. For example, this may influence the ease of ion migration in a crystal structure. Ion migration can occur in MALI which is considered to be mixed ionic-electronic conductor. This is especially true under external factors such as light, temperature or applied bias. Ion migration has been attributed as one of the major problems observed in measuring the performance of cells from such materials [11]. This is when current - voltage hysteresis is observed due to a mismatch between the forward and reverse scans that can lead to a misinterpretation of the actual device performance. Hysteresis has been linked to space charge regions in cell interfaces and also due to the grain size and specifically at grain boundaries. This was attributed to ion migration at grain boundaries which is more prominent in MALI due to the presence of iodine ions [9].

This work focuses on the composition-property relationships of bulk MALI powders to establish their basic electrical properties. PSC thin films based on MALI have been extensively studied but elucidating the intrinsic properties of MALI has proved challenging. This is especially true in this case because of the ease with which the electrical properties of MALI can be influenced by external factors and artefacts. The aim was to investigate the structure-composition-property relationships of the MALI system prepared from different synthesis techniques. Carrying out this work enabled a reduction in the number of factors that play a part in changing the material behaviour, especially all the factors that play a part in the building and manufacturing of thin film solar cells. This would then allow for better control of material characterisation, especially the surface/volume ratio effects which are always problematic in thin films. This project was initially sponsored by Dyesol Australia and then Greatcellsolar UK who were interested in gaining a more fundamental understanding of the behaviour of MALI and how the fabrication method may influence the phase assemblage and electrical properties.

The structure of the thesis is as follows:

- Chapter 2: A literature review with a general introduction to organic-inorganic perovskites followed by more detail on the structural, electronic, defect and stability behaviour of MALI.

- Chapter 3: Details the experimental methods and characterisation techniques used in this work. These include the synthesis methods used, which were solid state using a mortar and pestle, mechanosynthesis using ball milling and a solution method using organic solvents. The characterisation techniques used were x-ray diffraction (XRD), low voltage SEM, impedance spectroscopy (IS) and dielectric measurements (LCR).

- Chapter 4: This is the first results chapter, where MALI was synthesised by grinding the precursors methylammonium iodide (MAI) and lead iodide (PbI_2) in a mortar and pestle in an ambient environment. The powders were then annealed at different temperatures and a phase assemblage diagram was constructed as the MALI stoichiometry was altered between the two precursors. The samples were then characterised using XRD, SEM, IS, and LCR. Equivalent circuit fitting to the impedance data was also applied.

- Chapter 5: The synthesis method was altered, where the precursors were mixed in a bottle with milling media and ethanol as a solvent and milled. The MALI and ethanol mixture was then heated for the solvent to evaporate to obtain resultant powders. After this a similar phase assemblage diagram was constructed and the samples characterised using the same techniques as chapter 4.

- Chapter 6: The synthesis method was changed, now the precursors were dissolved in organic solvents of DMSO or DMF, which are the main solvents used in the synthesis of MALI thin films. Once the solvent was evaporated the resultant powders were once again characterised using similar techniques as stated previously. These samples were also used for a DC bias study.

- Chapter 7: Is an overall discussion where the results from Chapters 4-6 are compared and contrasted to observe the general trends in the MALI system and how the synthesis process affects the phase purity and electrical results.

- Chapter 8: summaries the conclusions from the thesis and makes suggestions for further work.

References

[1] A. Dubey *et al.*, 'A strategic review on processing routes towards highly efficient perovskite solar cells', *J. Mater. Chem. A*, vol. 6, no. 6, pp. 2406–2431, 2018.

[2] J. A. Christians, R. C. M. Fung, and P. V Kamat, 'An Inorganic Hole Conductor for Organo-Lead Halide Perovskite Solar Cells. Improved Hole Conductivity with Copper Iodide', *J. Am. Chem. Soc.*, vol. 136, no. 2, pp. 758–764, Jan. 2014.

[3] C. Ashworth, 'Reproducible, high-performance perovskite solar cells', *Nat. Rev. Mater.*, vol. 6, no. 4, p. 293, 2021.

[4] D. Li *et al.*, 'A Review on Scaling Up Perovskite Solar Cells', *Adv. Funct. Mater.*, vol. 31, no. 12, pp. 1–27, 2021.

[5] A. Kojima, K. Teshima, Y. Shirai, and T. Miyasaka, 'Organometal Halide Perovskites as Visible-Light Sensitizers for Photovoltaic Cells', *J. Am. Chem. Soc.*, vol. 131, no. 17, pp. 6050–6051, May 2009.

[6] A. J. Harding, K. D. Dobson, B. A. Ogunnaike, and W. N. Shafarman, 'Thermal and Structural Characterization of methylammonium- and formamidinium-Halide Salts', *Phys. Status Solidi*, vol. 2100246, pp. 1–6, 2021.

[7] A. K. Jena, A. Kulkarni, and T. Miyasaka, 'Halide Perovskite Photovoltaics: Background, Status, and Future Prospects', *Chem. Rev.*, vol. 119, no. 5, pp. 3036–3103, Mar. 2019.

[8] A.-F. Castro-Méndez, J. Hidalgo, and J.-P. Correa-Baena, 'The Role of Grain Boundaries in Perovskite Solar Cells', *Adv. Energy Mater.*, vol. 9, no. 38, p. 1901489, 2019.

[9] M. K. Rao, D. N. Sangeetha, M. Selvakumar, Y. N. Sudhakar, and M. G. Mahesha, 'Review on persistent challenges of perovskite solar cells' stability', *Sol. Energy*, vol. 218, no. July 2020, pp. 469–491, 2021.

[10] N. Aristidou *et al.*, 'Fast oxygen diffusion and iodide defects mediate oxygen-induced degradation of perovskite solar cells', *Nat. Commun.*, vol. 8, no. May, pp. 1–40, 2017.

[11] T. Zhang, C. Hu, and S. Yang, 'Ion Migration: A "Double-Edged Sword" for Halide-Perovskite-Based Electronic Devices', *Small Methods*, vol. 4, no. 5, p. 1900552, 2020.

2. Literature review

2.1. Perovskites

Perovskites are a class of materials with a general crystal structure related to the mineral calcium titanate ($CaTiO_3$). The name perovskite derives from the Russian mineralogist Lev Perovski, on whom the mineral $CaTiO_3$, was named after [1]. Many perovskites are now known and have the general formula of ABO_3 for oxides or ABX_3 for halides. Perovskites exist in a large variety of crystal structures and occur both naturally and via various synthetic routes. Throughout the last six decades, perovskites have been studied in great depth. This is due to their innate properties, especially in electrical applications because of their dielectric, piezoelectric and ferroelectric properties [1]. The range of properties and applications are expanding and include electronic conductivity, superconductivity, thermal, magnetic and optical properties. Fig: 2.1 shows the ideal cubic perovskite structure which is displayed by $SrTiO_3$ at room temperature.

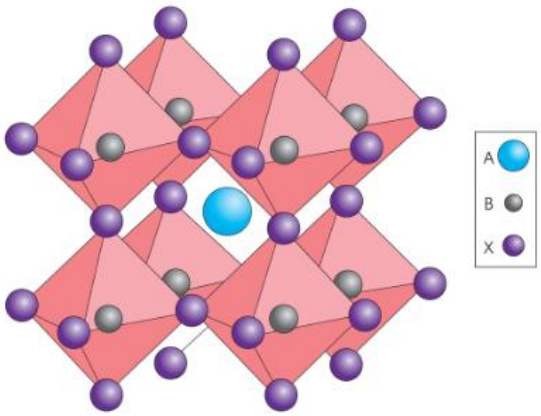

Figure 2.1. The ideal cubic perovskite structure of a material with the formula ABX_3, where A and B are cations and X are the anions. Figure reproduced from [2].

2.2. Organic-inorganic hybrid perovskites

The recent exponential rise in research into organic-inorganic hybrid perovskites is due to their potential to be used in solar cell technology. They were first incorporated into dye-sensitised solar cells (DSSC) [3]. This increased the interest even though it used a liquid electrolyte. Further breakthroughs in cell devices would see these perovskites used in a solid-state system. Incorporating these materials in photovoltaic devices has seen a sharp increase in efficiencies in a relatively short time period. Although it has taken many decades for

silicon-based solar cells to reach high efficiencies, it has taken only a decade for perovskite-based solar cells [4]–[6], as shown in Fig: 2.2. The perovskite cell went from ~10 to ~25% from 2010 to 2020, whereas silicon-based devices went from 12 to 28% over a period of more than 40 years. Although the perovskite structure is very versatile where A, B, and X can be various ions the main material on which most of the photovoltaic research has been concentrated on is organic-inorganic hybrid perovskites. Although perovskites are generally considered to be based on inorganic species, these tend to be a mixture of organic and inorganic ions, like methylammonium lead iodide ($CH_3NH_3PbI_3$), also known as MALI. The A site is an organic cation, and can also be doped with $CH(NH_2)_2^+$ known as the formamidinium ion. The B site ion is generally divalent lead, Pb^{2+}, and the anion, X tends to be a halogen, mainly iodine [7].

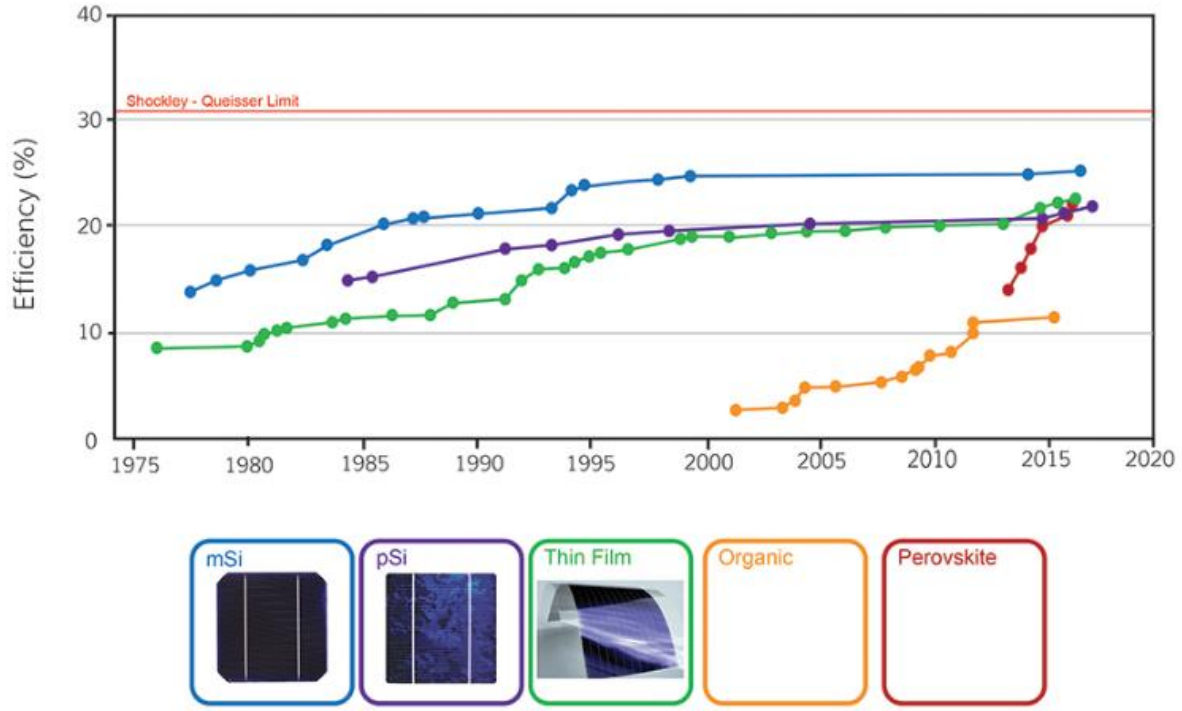

Figure 2.2. Comparing cell efficiency of different solar cell devices over the last 45 years. Figure reproduced from [7]**.**

The stability of a perovskite can be predicted by using the Goldschmidt tolerance factor (t), which is the relationship between the ionic radii of the various perovskite components. The general trend for inorganic perovskites is that if t is lower than 0.81 then structures are formed which are not perovskites, and if t is larger than 1 then hexagonal perovskite structures tend to form [2]. Another factor that is used to predict the stability of the structure is the octahedral factor (μ) which is the ratio between the radii of the B site cation over the anion (r_B/r_x) and measures the stability of the octahedral site [2]. μ values tend to range between 0.44 and 0.9, this means that the probability of a cubic structure is higher [8].

The tolerance factor t can be calculated using the equation below. Depending on the sizes of the cations and anions (where r_A, r_B and r_X are the radii of the A, B and X ions, respectively) in the perovskite, the size and shape of the unit cell can change in a variety of different ways, since the corner-sharing octahedra will change due to their interactions based on their size. Generally, t values close to 1.0 have an ideal cubic structure. t lower than this results in a distorted structure that generally produces tilted BX_6 octahedra.

$$t = \frac{r_A + r_x}{\sqrt{2}\cdot(r_B + r_x)}$$ Equation 2.1

Perovskites have been mostly inorganic, however recently there have been perovskites that are hybrids, i.e. contain both organic and inorganic species in this structure. These hybrid types of organic-inorganic perovskites are generally formed when the A site is an organic species. The perovskite structure is able to incorporate a very large ion on the A site. For example, complex ions such as ammonium $(NH_4)^+$ and variants such as the methylammonium $(CH_3NH_3)^+$ and formamidinium ions $(NH_2{=}CHNH_2)^+$, abbreviated as MA^+ and FA^+, respectively [2]. The compositions gaining the most interest at present tend to be those with the aforementioned A site cations, having a monovalent cation with a charge of +1, whereas the B site cations tend to be from group 14. These generally have a charge of +4 but due to the electron lone pair effect exhibited in lead (Pb) and tin (Sn), they have a charge of +2.The anion or X site generally tends to be a member of the halogen group either chlorine (Cl), bromine (Br), or iodine (I) [1]. Fig: 2.3 shows the cubic phase of MALI, with the methylammonium ion at the A site.

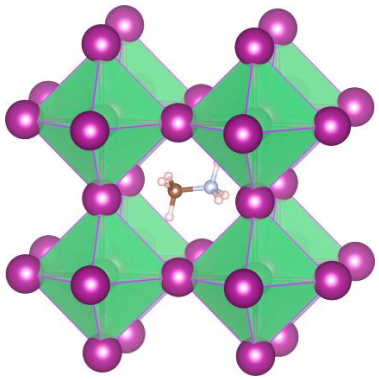

Figure 2.3. Illustration of how a molecular ion such as MA^+ occupies the A site in the perovskite structure. Figure reproduced from [9].

For inorganic-organic halides, since they have an organic molecule on the A-site, they don't exactly match the geometric relationship of the inorganic perovskites which the Goldschmidt

values are based on. When t is lower than 0.8 orthorhombic structures are formed. These and other 2D perovskites, when formed, have applications in light emitting diodes (LED), lasers and capacitors but it is only the 3D structures that have photovoltaic applications [10]–[12]. In the organic-inorganic perovskites for solar cell applications, the organic cations MA^+ or FA^+ have non-spherical geometry, therefore these molecular ions can rotate in the A-site. As a consequence, estimating accurate radius values is difficult, t values therefore tend to be approximations [13]. FA^+ is a larger cation than MA^+, a larger A-site cation generally results in a larger tolerance factor t. The black phase of MALI (α) is desired since it is the photoactive phase with a perovskite structure, whereas the yellow phase (δ) (has a hexagonal structure) gives very poor efficiencies and is not desired for photovoltaic cells [13].

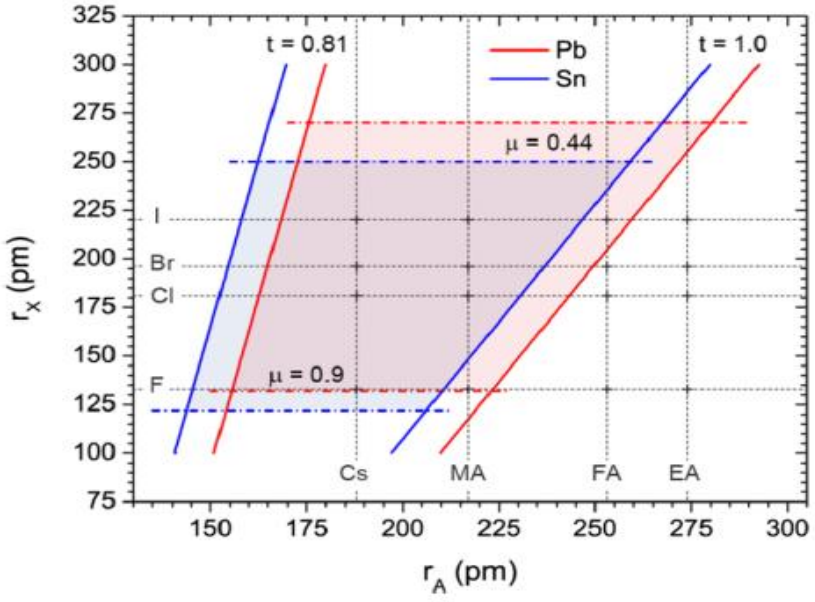

Figure 2.4. A graphical representation of the two factors (Goldschmidt tolerance (t) and the octahedral (μ) factor) that can be used to predict structural stability of organic-inorganic hybrid perovskites, when A, B and X sites are altered. Figure reproduced from [2].

The stability windows for the formation of perovskites based on various A ions (r_A) and halide ions (r_x) for B = Sn or Pb are shown in Figure 2.4. Caesium has the smallest A-site radius and can form a perovskite with all four halides. The MA^+ ion has a larger radius but this is an effective radius since it is a molecular ion rather than a spherical ion like Caesium and can form a perovskite with all four halides if the B site is lead. The larger FA^+ ion can effectively only form a perovskite with iodine when the B site is lead. However, in these type of perovskite materials, these factors have to be slightly altered or at least viewed in a cautionary way. This is because of two reasons. Firstly, the molecular cations are not spherical and also the halides on the X site generally tend to be less electronegative when

compared to oxides [2]. So instead, an effective radius is used. The other modification is addressed by empirical observations of variations from the standard Shannon radii, which uses more electronegative anions. When a more electronegative anion is replaced by a less electronegative halide more covalent behaviour emerges. This decreases the bond length of the metal-halide bond than that which is expected from the theoretical sphere model [2]. Deviation from the Shannon radii is strongly correlated to the difference in electronegativity between the B site and the halide on the X site, so the changes in the bond ionicity are responsible for the discrepancies [2]. The highest symmetry for a MALI perovskite tends to be cubic (space group, P$m\bar{3}m$), and by octahedral rotation, this symmetry can be lowered to tetragonal and orthorhombic. The tetragonal and cubic polymorphs are also known as the black (α) phase (active photovoltaic material) whereas the orthorhombic phase is the yellow (δ) phase which isn't active as a photovoltaic material.

2.2.1. Methylammonium lead iodide (MALI)

The investigation and implementation of hybrid perovskites as thin films in solar cells over the last decade has risen mainly due to their low cost and high efficiency. The main material on which the majority of the research is conducted is MALI. This material produces a high efficiency when incorporated into a solar cell and used in ambient conditions. However, it has stability issues which is why other dopant ions have been researched and have been incorporated into MALI-based systems.

MALI has been characterised to have three polymorphic phases, these are orthorhombic, tetragonal and cubic, however, the contributions of the MA^+ ions in x-ray diffraction data are weak compared to the PbI_2, so from such a technique accurate molecular orientation(s) of MA^+ cannot be obtained [14]. Phase transitions tend to occur on heating in perovskites with distorted structures with the structure altering from one (lower symmetry) thermodynamic state to another equilibrium (higher symmetry) phase state. For these hybrid perovskites they occur when the BX_6 octahedral tilting is coupled with the rotation of the A site cation from in plane to out of plane [15].

Phase transitions influence the electronic band structure which influence the performance of the device, especially if the phase transition temperatures are close to room temperature and/or the operating conditions. Neutron diffraction has been used to show the temperature dependent phase changes in MALI, as shown in Fig: 2.5. The orthorhombic phase occurs at low temperature and MALI retains this structure until around -113 ˚C. The symmetry of the cell has been assigned space group *Pnma*, the PbI_6 octahedra are distorted

with a tilt system of $a^+b^-b^-$. This low entropy state corresponds to an ordered lattice where the molecular cations are static, and being orthorhombic it has four cations per unit cell [14]. As the temperature is increased a tetragonal phase is formed from -113 ˚C until anywhere between ~ 37 to 60 ˚C. This phase change is a first order transition and the tetragonal cell has been assigned space group *I4/mcm*. The MA^+ ions are not static anymore and cause a disordered elongation of the octahedra, which occurs along the c-axis since the ratio of the tetragonal distortion parameter, c/2a is more than 1. The tilt pattern is $a^0a^0c^-$ [14]. The transition to the cubic phase occurs between ~ 37 to 60 ˚C, and the c/2a approaches unity. The molecular disorder increases, therefore it is easier to see the change via neutron diffraction as shown in Fig: 2.5, the space group attributed is $Pm\bar{3}m$[14].

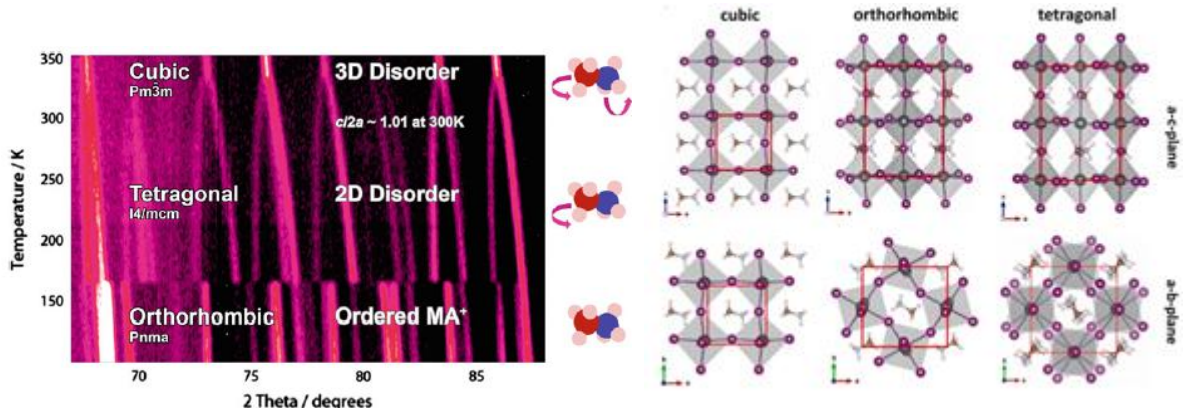

Figure 2.5. Neutron diffraction showing MALI phase changes and the various polymorphic structures. Figures reproduced from [7] & [14] respectively.

In order for solar cells to be built from MALI, they must be able to work at and above the tetragonal to cubic phase transition temperature because this is where the black (α) photovoltaic perovskite phase is present. Solar cells, when encapsulated can reach internal temperatures as high as 70 ˚C. The tetragonal to cubic phase transition is very important since it falls in the operating conditions of the solar cell. Therefore it's important to understand and study it in some detail [16]. Hoque et al conducted an electrical study of thin film MALI where the temperature dependence of the conductivity changes at 45 ˚C, and where the activation energy for conduction changes from 0.7 to 0.5 eV [16]. Studying temperature effects is important since MALI has a low degradation temperature, it can occur at room temperature (i.e. the photovoltaic efficiency drops) if not encapsulated. Across the literature there is not a generally specific consensus on the exact temperature at which the tetragonal to the cubic transition occurs. Hoque *et al* label the transition at ~45 ˚C, whereas generally, it is reported to be somewhere between ~ 37 and 60 ˚C [16]. It is still not clear whether this disparity in the temperature is due to the different ways the material is prepared, the quality

of the samples, the measurement method or other more fundamental reasons. The change in activation energy was determined from an Arrhenius relationship, where data were gathered from IS conducted on solar cells. These cells have many layers and it is challenging to determine if the measured data are due solely to the photoactive material or interactions between the many different materials and interfaces within the solar cell.

Whitefield *et al* [17] conducted studies on powdered MALI to investigate the structures, phase transitions and the tricritical behaviour. Mainly by using neutron diffraction, they observed the coexistence of cubic and tetragonal phases over a range of temperatures. The study also investigated deuterated MALI (where hydrogen is replaced by its isotope deuterium. d6 is when all the hydrogen is replaced, whereas d3 refers to when half of it is replaced). This eliminates incoherent scattering from hydrogen [17]. From their structure refinement of the neutron data for d6 - $CD_3ND_3PbI_3$ at -263 ˚C, it was observed that it had a similar structure to the d3-$CH_3NH_3PbBr_3$ at -264 ˚C and h6-MALI ($CH_3NH_3PbI_3$) at 173 ˚C. The partially deuterated material was investigated (i.e. d3) to see if it (partial deuteration) had any effect on the structure. With the exception of the background noise it did not seem to have any effect on the structure itself [17]. For the tetragonal phase there is general consensus in the literature to assign the *I4/mcm* [17] space group.

The complication in understanding the structures of these hybrid perovskites comes from the organic cations. Even if the structures are similar to other known inorganic perovskites, due to the organic cations, their low symmetry and tilting of the octahedra makes it difficult to pin down the exact temperature(s) at which the phase transition from tetragonal to cubic occurs, since it is dominated by the rotation of the octahedra, as shown in Fig: 2.6.

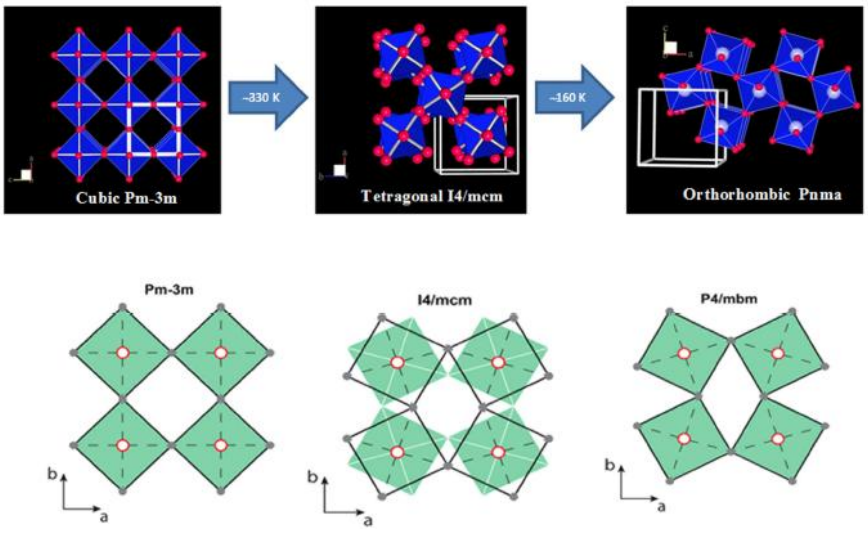

Figure 2.6. MALI structures with changes in their phase transitions. Figure reproduced from [17]**.**

Nandi et al report that at high temperatures the MALI system is cubic but the MA^+ is disordered alongside the iodine in the PbI_6 octahedra. These distortions have led many to believe the material might be ferroelectric [18]. In this study, MALI was prepared by a precipitation method, which can produce single crystals. XRD was performed at -173, -23 and 102 ℃, which confirmed the orthorhombic, tetragonal and cubic phases. The cubic phase present at the highest temperature had a lattice parameter of ~ 6.3391 Å. At lower temperatures, the tetragonal and orthorhombic phases are realised with the ordering of MA^+. The tetragonal phase has lattice parameters of a ~ 8.8755 Å and c ~ 12.7328 Å.

NMR has been used to show that the transformation going from cubic to tetragonal is observed by reorientation of MA^+ ions where the number of disordered states decrease when it transforms from cubic to tetragonal [18]. The orthorhombic phase is obtained at -173 ℃, with lattice parameters a ~ 8.8791 Å, b ~ 12.6574 Å, and c~8.6353 Å [18]. Photoluminescence spectroscopy was carried out between -196 to 117 ℃ and one major difference observed was that unlike the other papers or experiments which show an abrupt phase change at -113 ℃, the PL spectroscopy shows a constant change with the temperature - intensity relationship. Nandi et al also state that discontinuities are present across the phase transition temperatures. This generally occurs due to the morphology of the sample, i.e. how good the thin film quality is or due to the polycrystalline nature of the sample [18]. The band gap is observed to increase with an increase in temperature, where the tetragonal phase has a larger band gap than the orthorhombic phase, which occurs at a lower temperature [18]. In other studies however, especially those based on modelling, the trend seems to be the reverse where the band gap decreases with increasing symmetry from the tetragonal to cubic polymorph.

The main concern about these materials is that they tend to be very unstable especially in humid environments because the organic ammonium group has a hygroscopic nature, therefore it's attracted to water. The lead is also soluble in water [13]. Factors besides the humidity or moisture that can have a major effect on the stability of this material are its thermal decomposition, the phase transitions occurring at different temperatures and the intensity of a light beam or source [13]. These behaviours are intensified when incorporated into thin films. However the properties that have made these materials suitable for photovoltaic applications are its band gap, high absorbance, low exciton binding energy, crystalline film formation, balanced electron-hole transport and excellent charge carrier mobility [2]. One of the main reasons that such materials are used in solar cells is that they have a small band gap and therefore behave as a semiconductor. The concentration of each of

the elements, especially the cation and the halide have a significant effect on the band gap of the material. When light is absorbed by such a material there can be phase segregation because of it. The other major problem is thermal degradation in the region of the operating temperature, therefore it is considered that other cations are explored rather than organic ones, which is why caesium and rubidium have been investigated as A-site cations [19].

2.2.2. Non-stoichiometric MALI

A binary phase assemblage diagram has been constructed between the two end members of MALI, i.e. methylammonium iodide and lead iodide, as shown in Fig: 2.7. This is when MALI is prepared in a thin film form.

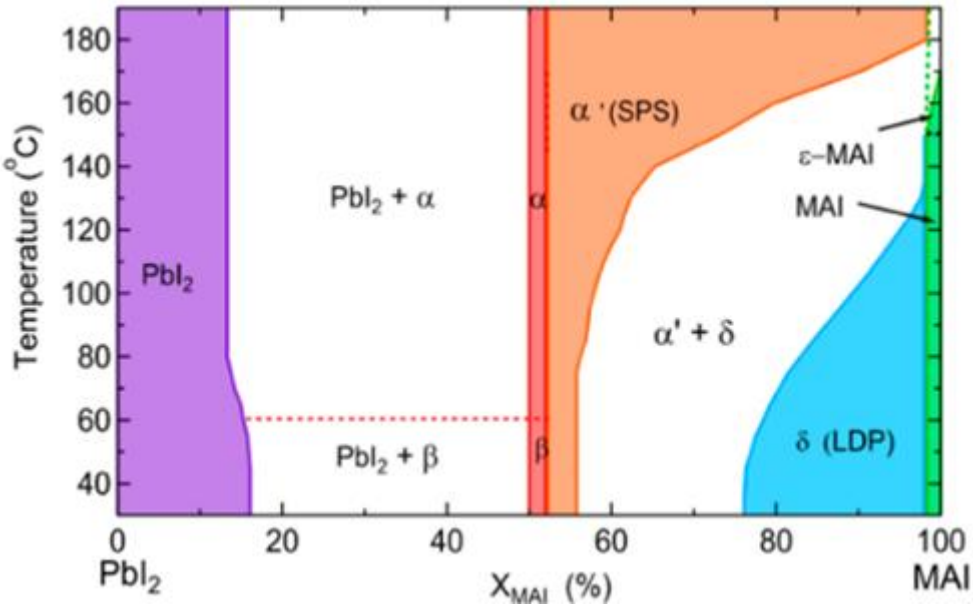

Figure 2.7. Phase diagram between two end members of MALI, PbI_2 and MAI for thin films, constructed under high saturated MAI vapour. Figure reproduced from [20]**.**

Z. Song et al changed the precursor ratios in the MALI system to investigate the width of the MALI phase field. The structural and optical properties were investigated. A high vapour pressure of MAI enabled the high temperature region to be corrected due to volatility of MAI in thin films [20]. They reported that at 50% MAI and at low temperature the β phase (which they classify as the *I4/mcm* tetragonal phase) is present. In this phase the c axis is elongated due to the polar A-cation. Above 60 ̊C the α phase (which they classify as *P4mm* tetragonal phase, which they state is similar to the *Pm-3m* cubic phase) is present and this phase becomes dominant. This and the cubic phase are referred as the α, black photovoltaic phase, as shown in Fig 2.7 [20]. The c axis distortion between the cubic and tetragonal phase is small, they both have similar structures, only the reflection associated with the (211) planes at $2\theta = 23.5°$ can be used to distinguish them. As the temperature increased the dominant XRD peaks become more intense [20]. The decomposition starts at around 150 ̊C, with the

disproportionation complete at 190 ̊C, so only PbI_2 peaks are observed. At low X_{MAI}, which are the lead-rich samples either PbI_2 + α phase is observed, or at very low ratios only PbI_2 is observed.

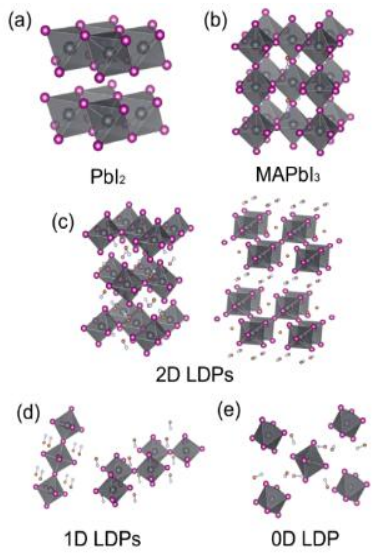

Figure 2.8. Crystal structures of (a) PbI_2, (b) $MAPbI_3$ perovskites, (c) 2D LDPs, (d) 1D LDPs, and (e) 0D LDP. Figure reproduced from [20]**.**

An increase in temperature shows a reduction in the fraction of MALI. Extra peaks are observed for the PbI_2 rich region and at low temperatures they are likely related to the intercalation of MAI ions inbetween I−Pb−I layers, which leads to intermediate structures between PbI_2 polytypes and perovskites. These structures may be similar to the methylammonum iodide - lead iodide - DMSO complexes formed in solutions. For MAI-poor films, it is clear that PbI_2 cannot be completely converted into MALI perovskite, as was expected. The temperature required to form MALI increases with higher MAI content. The off-stoichiometry perovskite phases can be explained as two-dimensional materials. These are stacked perovskite sheets (SPS, the α' phase), so they persist as 3D perovskites but are hard to distinguish since the crystal structure of highly ordered and stacked perovskites are not distinguished, due to the same long-range periodicity of the 3D perovskite framework. Low dimensional perovskites (δ phase) were observed at low angles, at 2θ = 11.3 and 11.7 ̊, the structures of these are shown in Fig: 2.8, they become more dominant at higher MAI content, Fig 2.7.

2.3. Thermal properties

Many issues arise when trying to understand the behaviour of even the basic (stoichiometric) composition of MALI without any doping mechanisms or non-stoichiometry,

due to the different variables that can have an effect on the final product. These include, making it into a thin film, or working with bulk material, a change of solvent, the basic processing conditions such as making it at atmospheric pressure or low pressure/vacuum, the temperature at which it is synthesised or annealed or changing of the X site ions. This is especially true for temperature dependent variables, mainly due to the fact that the organic constituents can easily decompose at lower temperatures than standard inorganic perovskites.

Heating MALI from room temperature to higher temperature has been studied in multiple ways. Aside from doing thermo-gravimetric analysis (TGA) to look at the decomposition of the material, high-temperature XRD has also been implemented to see how the structure of the perovskite changes with increasing temperature. Nenon et al investigated MALI by looking at precursor solutions of methylammonium iodide (MAI) and PbI_2 under high-temperature XRD from room temperature to 400 ˚C. They report an initial precursor phase then a perovskite phase forms until degradation of that perovskite phase, as shown in Fig: 2.9 [21].

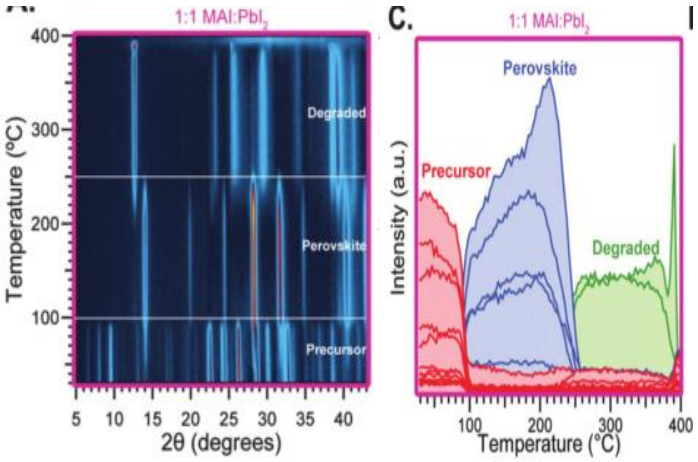

Figure 2.9. High-temperature XRD of the precursor solution being heated until degradation. Figure reproduced from [21]**.**

From Fig: 2.9 and other data Nenon et al report, the formation of MALI films from MAI: PbI_2, contain both MALI and its precursors with growth of the perovskite peaks. When the temperature reaches 80 ˚C there is a decrease in the precursor peaks and this trend continues until the temperature is at 215 ˚C, where hereafter degradation of the perovskite starts to occur until 250 ˚C, after which there does not seem to be any crystalline perovskite material. At the start of the degradation process, the intense peaks associated with the MALI perovskite decrease in intensity whereas the main peaks of PbI_2 emerge [21]. It was also observed by other forms of thermal analysis that once the DMF was evaporated from the thin film solution there occurs a broad temperature range where little else desorbs from the MALI.

This can occur at a higher temperature since DMF can form complexes with MALI. The conclusion they reached was that the degradation temperature of MALI is ~ 224 ˚C with an error of 3 ˚C. This is where the $CH_3NH_2^+$ ions seem to be lost [21].

Stoumpos et al [22] conducted thermal analysis on $CH_3NH_3PbI_3$ and $CH_3NH_3SnI_3$ (shown in Fig: 2.10A and B) under nitrogen flow to avoid oxidation. TGA results showed the material decomposed before melting occurs. Decomposition starts at > 300 ˚C, when the organic material on the A site decomposes then the lead iodide also decomposes and therefore a metallic (Pb) residue remains.

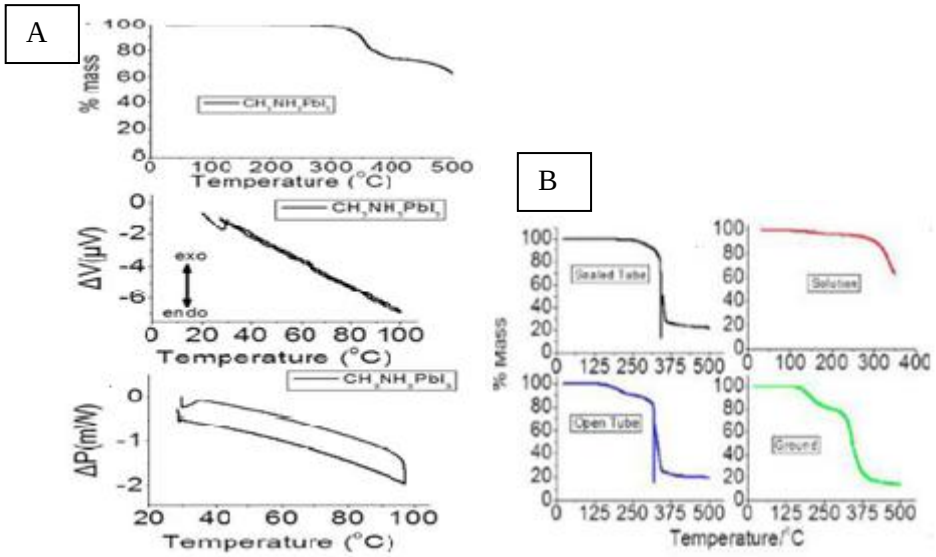

Figure 2.10. TGA and DSC data for MALI, (A) shows results for $CH_3NH_3PbI_3$, showing mass loss along temperature and its derivative (B) shows results of mass loss for $CH_3NH_3SnI_3$ made from solution and grinding method. Figure reproduced from [22]**.**

The method of how the material was made i.e. its synthesis route plays an important role in how the material decomposes [22]. If the material is synthesised in air the decomposition route is different. First the organic cation is decomposed and then the HI group, probably in the form of amine and HI and then by HI molecules. The purity of the material also influences the TGA results, this is seen from experiments on $CH_3NH_3SnI_3$. If the material is made by pestle and mortar then the first mass loss attributed to the organic material is greater than if it is prepared by a solution process [22]. This they attribute to the presence of Sn^{4+}. Also from differential scanning calorimetry (DSC), they could not see a phase change to the cubic polymorph but they attributed it to the sensitivity of the equipment and they also stated the transition to be second order which is contrary to the majority of the literature [22].

Jodlowski et al made both MALI and FALI powders via a ball milled process. TGA/DSC was performed on these powders so as to assess the phase transitions and the stability of the materials. Results show no significant mass loss for either MALI or FALI up to when the temperature reaches 250-350 ̊C. They attribute the degradation of the perovskite to be ~ 250 ̊C. This loss is generally associated with the loss of HI [23]. At temperatures of 55 and 130 ̊C, there is a slight drop in the signal. This also corresponds to the DSC data, which shows endothermic peaks at 60 and 135 ̊C. Both these processes and their respective results are attributed to a phase transition that occurs at the lower temperature. This is associated with the tetragonal to cubic transition for MALI, whereas for FALI it shows the change from the yellow δ phase to the black α phase at 150 ̊C, which when cooled back to room temperature is stable and remains as the black phase [23]. When thermal studies were performed on MALI in other studies similar trends in temperatures at which the material decomposition occurs were reported. TGA analysis shows the mass loss of the different components and showed the organic component undergoes a 100% weight loss in a single step. For example, the temperature at which MAI starts to lose mass is ~ 234 ̊C and is complete by ~ 320 ^{o}C [24].

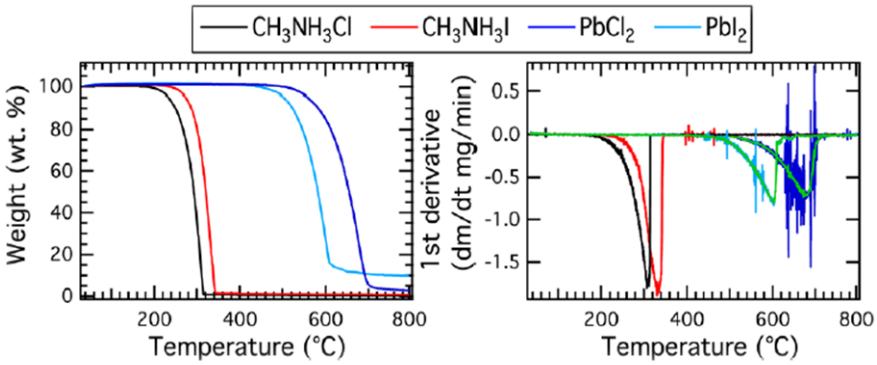

Figure 2.11. TGA data of precursor powders and their first derivatives. Figure reproduced from [24]**.**

Dualeh et al state [24] that MAI starts decomposing at a similar temperature to the one stated previously by Jodlowski [23]. The broad loss profile is seen in the dm/dt curve (Fig: 2.11). It indicates the lead iodide precursor goes through a thermal decomposition process, the phase transition in which the material turns from a solid to a gas ideally involves no compound decomposition [24]. They report two small drops which occur at 85 and 125 ̊C, these are probably due to water loss and the larger mass drop which occurs near 600 ̊C is due to the decomposition of the lead iodide, Fig: 2.11[24]. Using DSC on MALI on a heating and cooling cycle there were peaks at 57.3

and 55.2 ˚C**,** which they attribute to the transition from the tetragonal to the cubic polymorph of MALI. The difference in temperature on heating and cooling was attributed to hysteresis [24].

Grain boundaries can play an important role in heat transport and rotation of the organic cation also plays an important role due to its interaction with phonon waves [25]. Pisoni et al [25] conducted thermal studies on both single crystals and polycrystalline MALI. Thermal conductivity is strongly dependent on the morphology of the material being examined, so single crystal and polycrystalline materials have different thermal conductivities. Because the solar cells incorporate thin films made from a solution of MALI, polycrystalline material is closer to the nature of MALI when in use in solar cells. Results for the thermal conductivity of single crystal and polycrystalline MALI samples vary with increasing temperature as shown in Fig: 2.12.

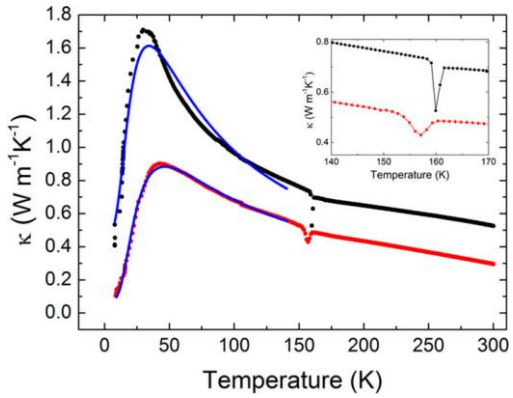

Figure 2.12. Variation of thermal conductivity with temperature, comparing single crystal (black) and polycrystalline (red) MALI samples. Blue lines (theoretical model). The inset shows the detail around the structural transition at 160 K. Figure reproduced from [25]**.**

Pisoni et al reported [25] single crystals of MALI to have very low thermal conductivity which might be due to the complex unit cell and the disordered MA^+ lattice. Room temperature values for the thermal conductivity of single crystal and polycrystalline MALI are 0.5 and 0.3 $Wm^{-1}K^{-1}$, these are considered to be very low. In the temperature dependence of the thermal conductivity a small drop at around -113 ˚C is observed which is associated with the polymorphic phase change [25]. Pisoni et al conclude the low thermal conductivity of the MALI is due to its particular crystal structure with the rotation of the MA^+ inside the unit cell. Lattice thermal conductivity dominates this temperature range rather than the electron conductivity [25]. This low thermal conductivity means that the solar radiation which is absorbed by MALI will induce heat that will spread or move along the material at a slow rate, which will, in turn, make the material more susceptible to thermal stresses and therefore mechanical tiring [25].

Defects and electrical conductivity

All crystals are imperfect. In some crystals the defect concentration is very high such that they are regarded as an important part of the structure [26]. Defects up to a certain concentration lead to a reduction in the free energy ($\Delta G < 0$), since the formation enthalpy of a defect is offset by an increase in entropy, primarily the configuration entropy [26]. Introducing a large level of defects has a smaller effect on entropy compared to the enthalpy required to make the defects, thus increasing the Gibbs free energy ($\Delta G > 0$) and this making high defect concentrations unfavourable [26].

The defect that dominates is the one easiest to form. There are stoichiometric and non-stoichiometric defects, also known as intrinsic and extrinsic defects. In ionic halides a Schottky defect is a stoichiometric defect where a pair of vacant sites, a cation and an anion vacancy are formed. An equal number of vacancies are formed to preserve electro neutrality [26].These defects may be present as clusters, pairs or randomly distributed. Frenkel defects involve an atom displaced from its original lattice site into an interstitial site, which is empty. Both of these are intrinsic defects. Defects can also occur as a consequence of variation in composition and these are often called extrinsic defects [26].

In metals the number of mobile electrons is essentially constant and their mobility decreases with increasing the temperature, so their conductivity decreases with increasing temperature. In semiconductors the number of mobile electrons is small. This can be increased by increasing the temperature so as to (exponentially) promote electrons from the valence band into the conduction band, or by doping, to provide electrons or holes [26]. Therefore, in the intrinsic regime the conductivity increases with temperature. A key parameter in electronic materials is the band gap. For promotion of electrons across this band gap, absorption of energy is required [26]. When electrons are promoted to the acceptor levels from the valence band, holes are left behind in the valence band so a p-type semiconductor is formed. When electrons move from the donor levels to the conduction band, electrons are introduced in the conduction band so a n-type semiconductor is formed. In many electronic devices the movement of charge carriers controls the speed at which the device operates. These are parameters such as the drift velocity, thermal velocity and diffusion [26].

In most ionic solids ions are trapped and vibrate at infrared frequencies and don't have sufficient thermal energy to migrate from their lattice sites. If they do have enough energy to move to an adjacent site then ionic conduction can take place [26]. Ionic movement is easier at higher temperatures, since the ions have higher thermal energy and more (thermally

generated) defects are present. So there needs to be some vacant sites where ion hopping can occur. More vacancies are created with increasing temperature or by chemical doping. For diffusion to occur a minimum energy barrier must be crossed, this is called the activation energy [26].

2.4. Electronic band structure

Experimental results tend to agree with the results from modelling about the direct band gap of these organic-inorganic perovskites [27], [28]. The optical absorption is related to the photoelectric transition, this is where the charges move from the valence to the conduction band. The optical absorption is therefore related to the electronic structure. For MALI the density of states close to the band edge is due to the s and p orbitals of the lead and the p orbitals of iodine (shown in Fig: 2.13). Although the organic cation doesn't contribute directly to the band edge (it has negligible contribution to the conduction and valence bands) it can create changes in the structure, eg: via tilting/distorting the octahedral cages or the presence of MA^+ dipoles can enhance carrier concentration, or even the rotation of the MA^+ extending the carrier lifetime. These could all invariably affect the electronic behaviour [29], [30]. The interesting properties however tend to be because of the electron lone pair on the Pb ions [31], [32]. The high optical transitions are due to both intra atomic transition between the iodine p and lead p orbitals and the inter atomic transition between the lead s and p orbitals. It is also because the material has a direct bandgap, the valence band maximum and conduction band minimum occur at the R point in the Brillouin zone (as shown in Fig: 2.13).

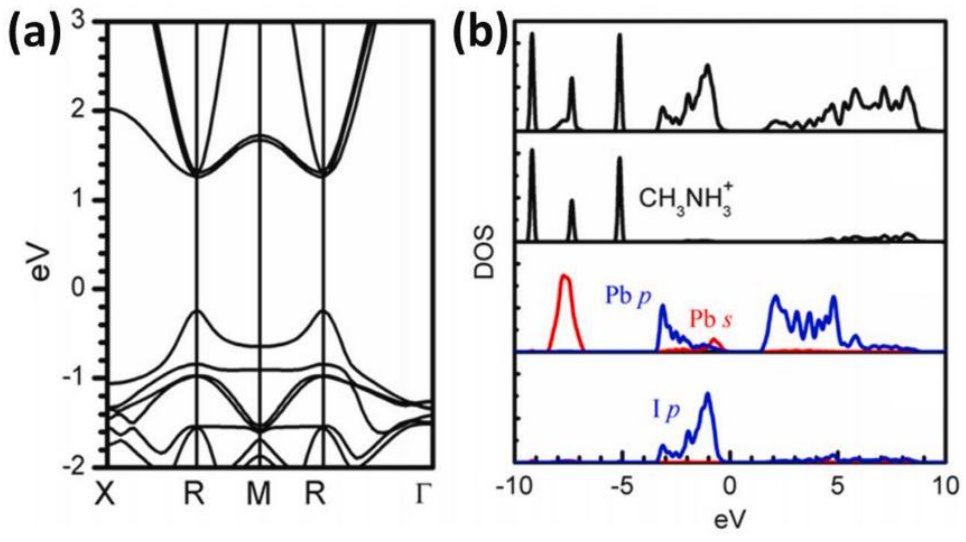

Figure 2.13. (a) The band structure of MALI and (b) the density of states versus eV [33]**.**

The electronic structure of these materials influences their band gap which cannot be assumed to be a constant because it is affected by different parameters, such as a structural phase change. Calculations of the band gap can therefore be challenging and shows some statistical dispersion [34]. This can be observed from Fig: 2.14 where experimental results for different halides in methylammonium lead halides can be compared to different theoretical models. The band gap for MALI is calculated as 1.57 eV and matches the experimental results and DFT; however, it had to cancel out the underestimation of the general gradient approximation and also disregard spin order coupling on the lead atoms [27].

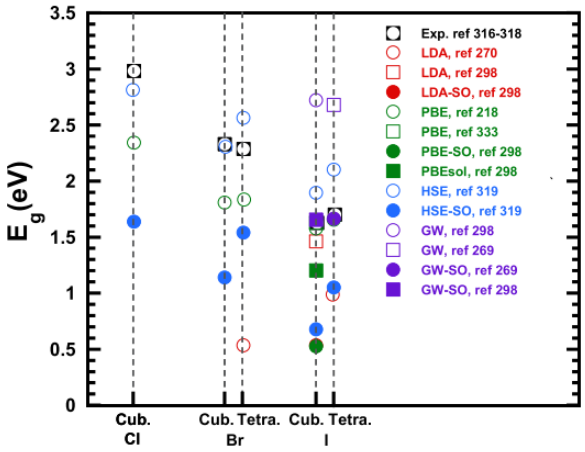

Figure 2.14. Experimental and theoretical results of the direct band gap of MAL(X), where X = halogen group. Figure reproduced from [35]**.**

Many different computational methods have been used to explore the electronic structure of MALI. The different methods don't show exactly the same results. This is primarily because of the spin order coupling of the heavy lead atom, whereas other effects which might be thought of complicating things like the dual bonding (ionic and covalent), or the lattice constant change because of the A (not a perfectly modelled sphere) site don't seem to show much of an effect [27], [36], [37]. Whereas, the role of electron phonon coupling could affect mobility but is unknown. MALI has good charge transport properties due to its long diffusion length, long range carrier, high mobility and balanced ambipolar conductivity. Although many of these are dependent on the processing conditions and when incorporated into a cell, on the film morphology.

2.4. Electronic and Ionic behaviour

For these perovskite materials to behave as a photovoltaics they need to produce electrons and holes which don't recombine easily, therefore giving rise to a current, which can be harvested into energy. The transport mechanism(s) in inorganic-organic halide

perovskites have been studied, they generally have large anion vacancy diffusion coefficients, with low activation energies. Frost and Walsh et al, through modelling, have looked at the energy required for MALI to produce full and partial Schottky defects and they concluded that it is quite low, at 0.14 eV per defect [14].

There is still a driving force in trying to make a certain concentration of lattice vacancies, even if the material is stoichiometric. The enthalpy required to form a defect is compensated by the increase in the entropy of formation. The band gap of the material, however, is devoid of forming any deep electronic states. This low formation energy of Schottky defects explains the low carrier concentration, because it minimizes the free energy of the crystal without generating extra charge carriers. This limits the charge density which otherwise will be raised by the configurationally entropy induced point-defects in other photovoltaic films absorbers. As a result, lower carrier concentrations ranging from 10^9 to 10^{14} cm^{-3} are observed in hybrid perovskites making the bulk greatly suppressed in its electron hole recombination. And also, why it might be difficult to dope the material extrinsically since these carriers are heavily compensated by the ionic defects. These charge point defects in the lattice could support an ionic current that might be produced by ionic movement. Their mobility depends on the activation energy and frequency at which the hopping occurs [14].

If the material is investigated under applied bias with electrodes that will block ion movement, the ions and electrons will then flow until ions transportation has stopped. However with this method the equilibrium point, where the ionic movement heavily relies on diffusion pathways can be very slow, and can also alter the current-voltage behaviour. It is this slow movement of ions that some attribute the current-voltage hysteresis behaviour of the material [14].

The ionic transport can be attributed to the diffusion of MA+, I^- or proton diffusion (possibly resultant from the preparation conditions), however, what determines the movement is the concentration of mobile ions present, the activation energy and the frequency of the ion at which it attempts to hop. In these hybrid perovskites, the pathway gets more complicated due to the disordered nature of the structure [14]. Proton diffusion seems unlikely as the MA^+ is a weak acid. The disorder of the A-site cation will also mean the long range diffusion will occur at a low rate since the transport mechanism would become more complex. If the attempt frequency is considered then it might be hypothesised that the iodide ions would have the largest attempt frequency since the anion transfer has the shorter distance for hopping [14]. The polarisability of the iodide ion and the ability for anions to have large

displacements at a higher temperature would also help iodide ions to be the main ionic conduction mechanism, considering that it also has the lowest activation energy. In contrast, long range diffusion of the organic cation will be slower due to its orientation disorder, thus lowering the attempt frequency of hopping. Ionic polarisation is slower compared to electronic mobility in hybrid perovskites, since they contain a molecular cation they also have a molecular polarisation. Fig: 2.15 shows the transport mechanism in MALI showing iodide ion vacancy migration obtained from DFT calculations, which indicates a curved path and local relaxation/tilting of the octahedra. The iodide ion migration along the octahedral edge, the lead migration along the diagonal <110> and the MA^+ into the next vacant A site, normal to the unit cell are all shown in Fig: 2.15.

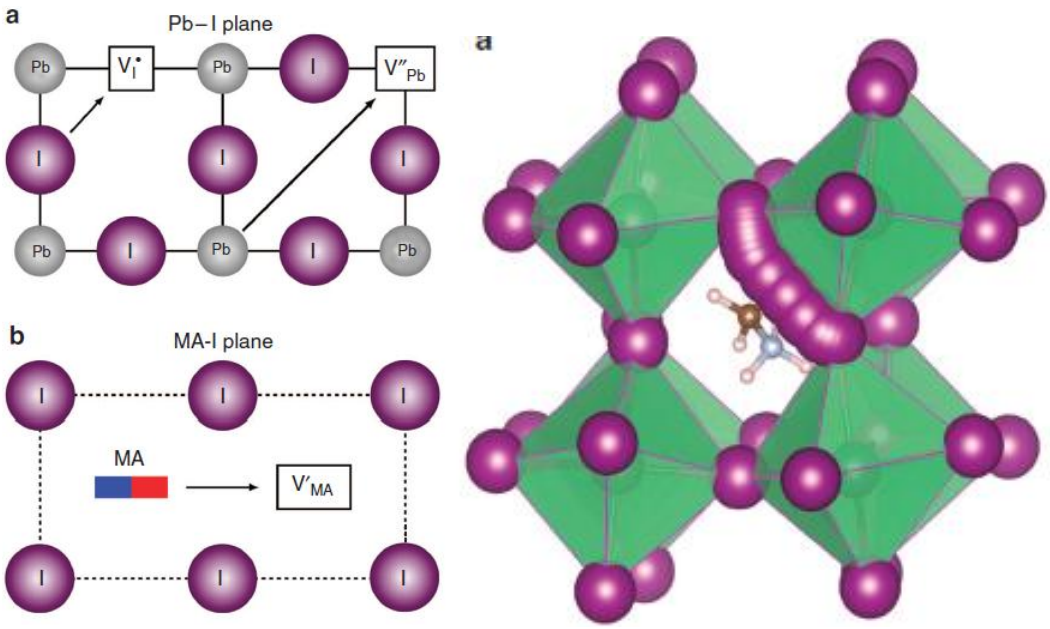

Figure 2.15. Transport mechanism in the hybrid perovskite. Figure reproduced from [9]**.**

Eames et al [9] conducted a computational and experimental study and concluded hybrid perovskites to have a mixed ionic and electronic conduction mechanism. MALI materials designed for solar cells seem to have unusual behaviour such as I-V hysteresis and a large dielectric response at low frequencies. The reason suggested for this behaviour is the ionic transport but the problem seems to be that the origin and the species of the transport do not seem to be fully known. They use first principles to derive the activation energy for conduction of MALI. The transport mechanism is identified as migration of iodide ions with E_a = 0.6 eV [9]. Defect studies suggest that Pb^{2+}, I^-, and MA^+ vacancies in the structure makes it possible for the creation of shallow donor or acceptor levels. It seems that ionic disorder might be favoured over electronic disorder. Hybrid perovskites have a uncharacteristic defect chemistry. Normally it is common for wideband gap materials to have ionic disorder. This is

where the charge point defects are arranged by self compensation. While the lower bandgap materials have a tendency to have electronic disorder. Where the carrier is distributed in the valence and conduction bands. But in this material the electron and holes are easily formed but still an ionic disorder is preferred. The defects here being shallow donors $V^{\cdot}_{I}$ or acceptors $V^{//}_{Pb}$ and $V^{/}_{MA}$. The concentration of electrons and holes are provided by the formation of charge-compensating lattice vacancies.

The values from both experimental [38]–[40],[41] and computational [41][42] studies show that MALI has low activation energy values for ionic diffusion coefficients for MA^{+} and I^{-}. The migration of these ions is seen to have a large effect on the device performance, especially the hysteresis behaviour in the ion migration from the perovskite layer to the charge extraction layer in the cell [42]. This also contributes to reducing the charge extraction efficiency. Table 2.1 shows the values of the activation energies for four different types of defect pathways, whereas Fig: 2.16 shows the diffusion pathway itself. The iodide ion vacancy moving from an equatorial to axial position has a low energy difference of 0.01 eV, see Fig: 2.16a. Fig 2.16b shows the hopping of the organic cation between adjacent cavities of the octahedra. Fig 2.16c shows the in-plane migration of a lead vacancy, whereas the migration of the interstitials along the c-axis is shown in Fig 2.16d.

From the activation energy it can be seen that the iodide vacancy and interstitials can easily move across the crystal with low energies of approximately 0.1 eV [42]. The other values from the table also show low energies for the X site, with both experimental and calculated values being in the range of 0.1-0.6 eV [33], [43]. The hopping of Iodide vacancies could be the dominant ion migration, the diffusion coefficient using electron and ion selective contacts was in the range of 10^{-8} - 10^{-7} cm^2s^{-1} [41], [44]. For iodide diffusion, values of $4.3x10^{-6}$ cm^2s^{-1} were reported whereas for the interstitial it was ~ $7.4x10^{-6}$ cm^2s^{-1} [45]. Defects can be brought about by grain boundary dislocations, space charge defects, i.e any type of boundary or by surface effects like interaction between the perovskite layer and other layers in the device or even interaction with the atmosphere such as water and/or oxygen. These could all affect the activation energy and therefore the rate of diffusion [46]–[49]. Ion migration is seen as a disadvantage for the stability of the material since it could change the electronic structure and device performance. For example, ion segregation of the mixed halide perovskite $MAPb(BrI)_3$ composition reduced the device performance due to segregation of iodine causing charge trapping [50].

Table 2.1. The type of possible defects in MALI and their relative activation energy both from experimental and computational sources for defect migration.

Defect migration in MALI	Experimental E_a (eV)	Calculated E_a (eV)
$V^{\cdot}_{I}$	0.2[42], 0.6[9], 0.3[51]	0.1[42], 0.2[52], 0.3[52], 0.6[9]
$V^{/}_{i}$		0.1[42]
$V^{/}_{MA}$	0.4[39]	0.5[42], 0.6[52], 0.8[9]
$V^{//}_{Pb}$		0.8[42], 0.9[52], 1.4[52], 2.3[9]

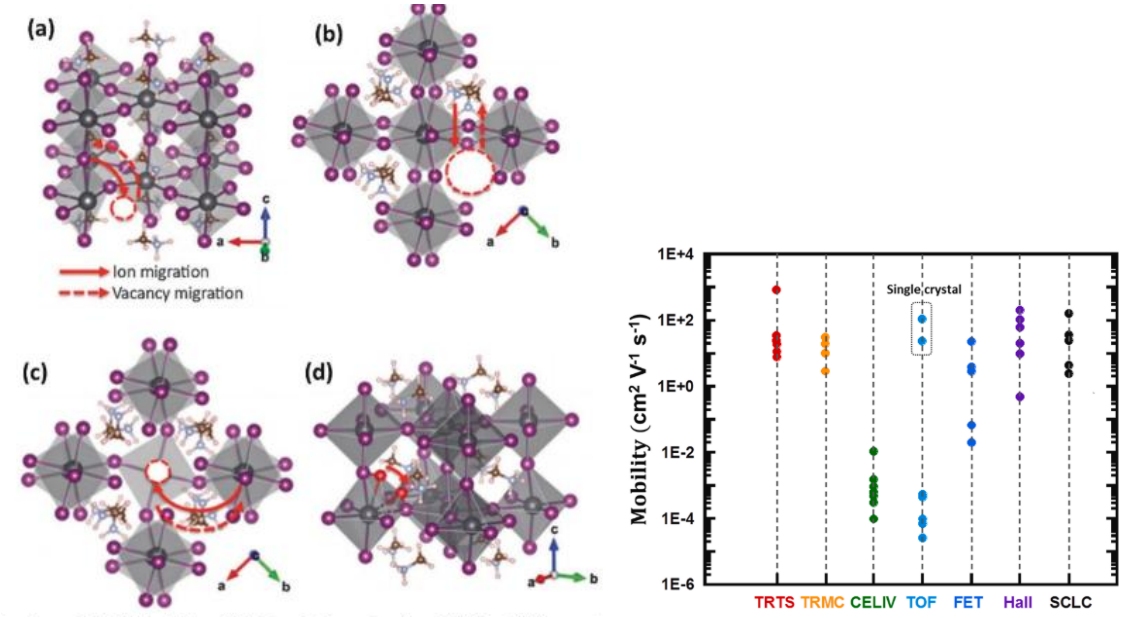

Figure 2.16. (a) The diffusion pathways of V_I, (b) of V_{MA}, (c) of V_{Pb} and (d) of I_i where the red atom refers to interstitial defects. Solid lines stand for migration and dashed for the path of the vacancy. (e) The charge carrier mobility in thin films and single crystals which is almost 4 orders of magnitude higher when the time of flight (TOF) technique is used. Transient absorption (TA) spectroscopy, Time-resolved photoluminescence (TRPL) spectroscopy, Time-resolved terahertz absorption spectroscopy (TRTS), Time-resolved microwave conductivity (TRMC) method, Charge extraction by linearly increasing voltage (CELIV) method, Field-effect transistor (FET) technique, Space charge limited current (SCLC) technique, Hall effect technique, Field-effect transistor (FET) technique. Figures reproduced from [42] **&** [53] **respectively.**

Defect sites can change the scattering of charge carrier transport, diffusion length and recombination rates within a material and therefore need to be taken into consideration [54]. MALI can have both p and n type behaviour dependent mostly on the processing conditions [55], [56]. The most common defects are seen to be interstitial and vacancy defects which introduce shallow states in the bandgap and influence charge movement. MALI can contain both Schottky and Frenkel defects as shown in Fig: 2.17. Schottky defects means the

formation of stoichiometric amounts of anion and cation vacancies. The equation for the Schottky defect for the full and partial disorder alongside PbI_2 reactions are shown below.

$$nil \rightarrow V_{MA}^{/} + V_{Pb}^{//} + 3V_I^{\cdot} + MAPbI_3 \text{ (Full Schottky)}$$

$$nil \rightarrow V_{MA}^{/} + V_I^{\cdot} + MAI \text{ (A site, X partial Schottky)}$$

$$nil \rightarrow V_{Pb}^{//} + 2V_I^{\cdot} + PbI_2 \text{ (B site, X partial Schottky)}$$

The net total charge is zero when all the charges have been summed at the macro level. Formation energy for the full Schottky defect is calculated to be 0.14 eV/defect, for the MAI a lower value of 0.08 eV/defect is reported. For PbI_2 (depending on the position energies) values are in the range of 0.027 - 0.073 eV, which seem lower than the average inorganic semiconductor [43]. The Schottky defects lower the free energy of the crystal without generating more charge carriers. The result is that there is lowering in the carrier concentration for these hybrid perovskites from 10^9 - 10^{14} cm^{-3} which decreases the bulk electron-hole recombination for solar cells [22], [57], [58]. The Frenkel defects being interstitial can be moved via an electrical field or a diffusion gradient as in the case of oxygen vacancy migration. The iodide vacancy can create n-type doping via shallow electron levels close to conduction band minimum, whereas at the valence band maximum lead and methylammonium vacancies produce p-type doping [43]. The physics of these materials can be complicated especially when most of the studies are conducted on solar cells, where many interfaces are present. However even polycrystalline samples have many different crystal grains, grain boundaries, possible impurities from precursors and different topographies which further complicates the defect physics. The coexistence of electron and ion conduction via various possible mechanisms makes the electron-hole generation, separation and recombination along with the conduction all mutually affect one another and the system becomes extremely complex.

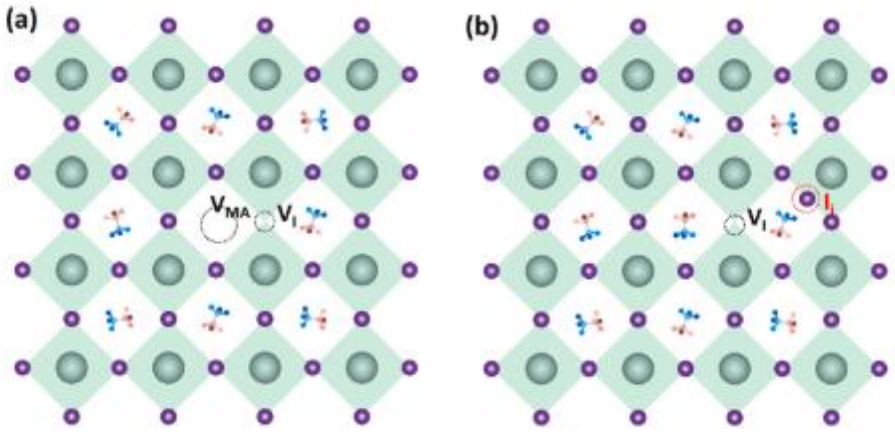

Figure 2.17. (a) A Schottky defect and (b) a Frenkel defect in MALI. Figure reproduced from [6].

In any ionic conducting material, it is known that the concentration and movement of the ionic transport is controlled by Schottky and/or Frenkel defects, non-stoichiometry and/or by aliovalent doping. In perovskite materials, the most common mechanism by which ions move is vacancy mediated diffusion. Eames also states the activation energy for each type of defect migration. It is stated that the iodide ions have a corresponding activation energy of 0.58 eV whereas for the methylammonium ion it is 0.84 eV and the lead ion it is significantly larger with a value of 2.31 eV. The path along which these ions move should be the one which has the shortest distance, as shown in Fig: 2.16 where the three different ionic means of transport are shown, i.e. the iodide ion along the octahedron, the lead ion in the diagonal direction and the organic cation into a neighbouring A site. Eames et al, however, suggest the actual migration route is not a linear path but a curved path between the I^- sites. The activation energy from experimental techniques showed values from 0.6-0.68 eV, which agrees with an activation energy of iodine movement which was calculated to be 0.58 eV. Whereas the E_a of the other ions is larger.

Yang et al also showed that MALI and FALI are mixed conductors with a significant amount of ionic conductivity, [14],[41]. The dielectric constant at low frequencies is ~ 10^3 (from perovskite thin films in solar cells) apart from hysteresis this was also attributed to ferroelectricity due to the dipolar nature of the molecular A-site cation. This was due to current-voltage curves on single crystals of MALI showing non-ohmic behaviour and above 113 ˚C the dipoles of the organic cation are disordered, while the frequencies at which this type of behaviour was observed are lower than what normally occurs for ferroelectric behaviour [41]. This behaviour could also be linked to slow charge carriers, however it seems that studies have not yet been done to identify this in any rigorous way. Yang et al studied MALI pellets with graphite electrodes in the dark and under argon gas and their results are

shown in Fig: 2.18. Distorted semi-circles were observed in Z* plots which were assigned to the bulk property with the dielectric constant being 34 at 30 ̊C and decreased with increasing temperature, [41]. The bulk conductivity is observed to increase with temperature with a corresponding E_a of 0.43 eV. The dielectric response at low frequencies increases with increasing temperature.

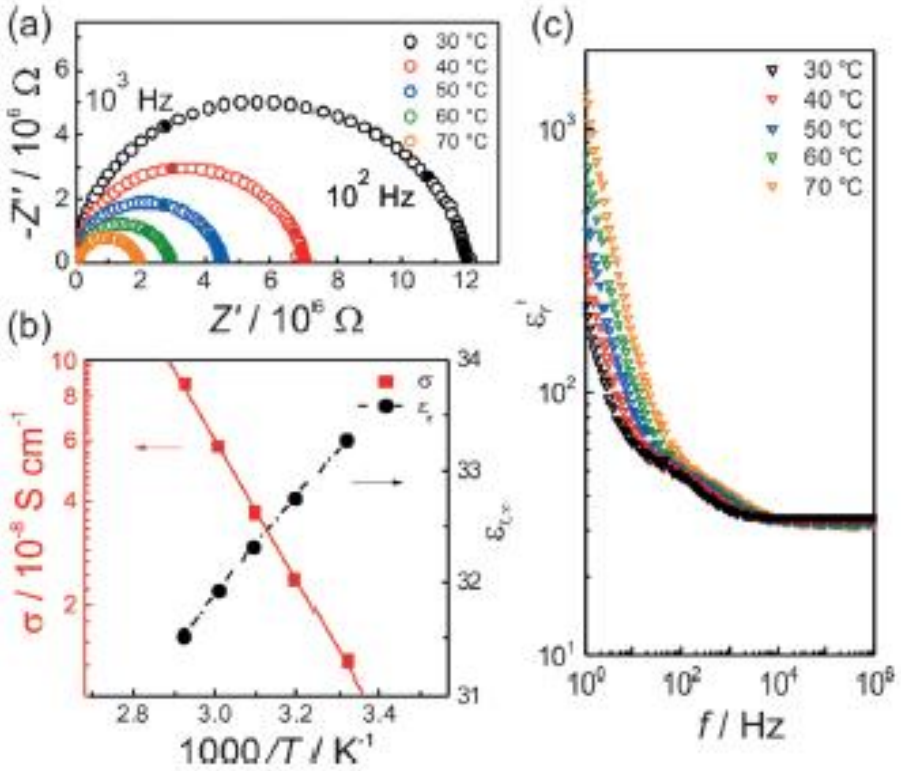

Figure 2.18. (a) Impedance spectroscopy results for a MALI pellet shown in the Z^* formalism. (b) The temperature dependence of the conductivity and the bulk dielectric constant. (c) The real part of the permittivity as a function of frequency at various temperatures. Figure reproduced from [41].

Hoque et al mention that the Warburg diffusion has not been considered in the IS results. The E_a associated with conduction changes at low and high temperatures, where the low temperature region was below 45 ̊C and the higher temperature region was above 45 ̊C. The E_a values were ~ 0.5 and 0.7 eV, respectively. They calculated these by using the Warburg element which has a Warburg time constant, which is related to E_a. These were fitted at different temperatures to produce plot Fig: 2.19b. The two lines intersect at 45 ̊C. The reason the value of 45 ̊C is important for Hoque et al is that all of the ionic and electrical studies indicate that the tetragonal to cubic transition occurs in this temperature region [16]. It is also indicated by Hoque et al that optical studies do not show the same type of changes in the properties of the material. It is important to note that the study was conducted on thin films of MALI which were deposited on FTO substrates, with the IS frequency going from 1 MHz to 0.1 Hz and voltage of 100 mV AC under 0 V DC bias and a temperature range from

15 to 70 ̊C [16]. The results (Fig: 2.19) show that as the temperature is increased there are two different charge transport regimes because the plot shows two semi-circles whose radii become smaller as temperature increases. The literature states that the two semicircles whose radii become smaller as the temperature increases, especially the second one which occurs at lower frequencies becomes more apparent at higher temperatures. The semi-circle which appears at higher frequencies i.e. those that occur at or close to the origin has been attributed to the transportation of free electrons. The behaviour in the low-frequency region is generally tied to different mechanisms such as hysteresis. Some have attributed this second semi-circle behaviour to a double layer capacitance which comes about from the trapping of electrons and their accumulation at the interface. The linear region which occurs between the two semicircles has not been addressed, where the charge accumulation might be due to the ionic diffusion and migration, where the diffusion part is ascribed to the Warburg diffusion [16].

It is true that generally the Warburg or ionic spike is attributed to the ionic behaviour of a material in standard electroceramics in polycrystalline form. This is due to the interface between the material and the electrode. However, since these results are from solar cells which contain many interfaces and the impedance data will show only the dominant mechanism(s) it seems quite hard to attribute this to any physical phenomenon with any confidence. Fig: 2.19 (a) shows the complex plot from impedance spectroscopy for MALI, with the model, used to fit the data, (c) shows the ionic conductivity and the activation energies. The circuit shows a mixed conductor system with both kinetic and mass transfer regions, which is represented by the Warburg element.

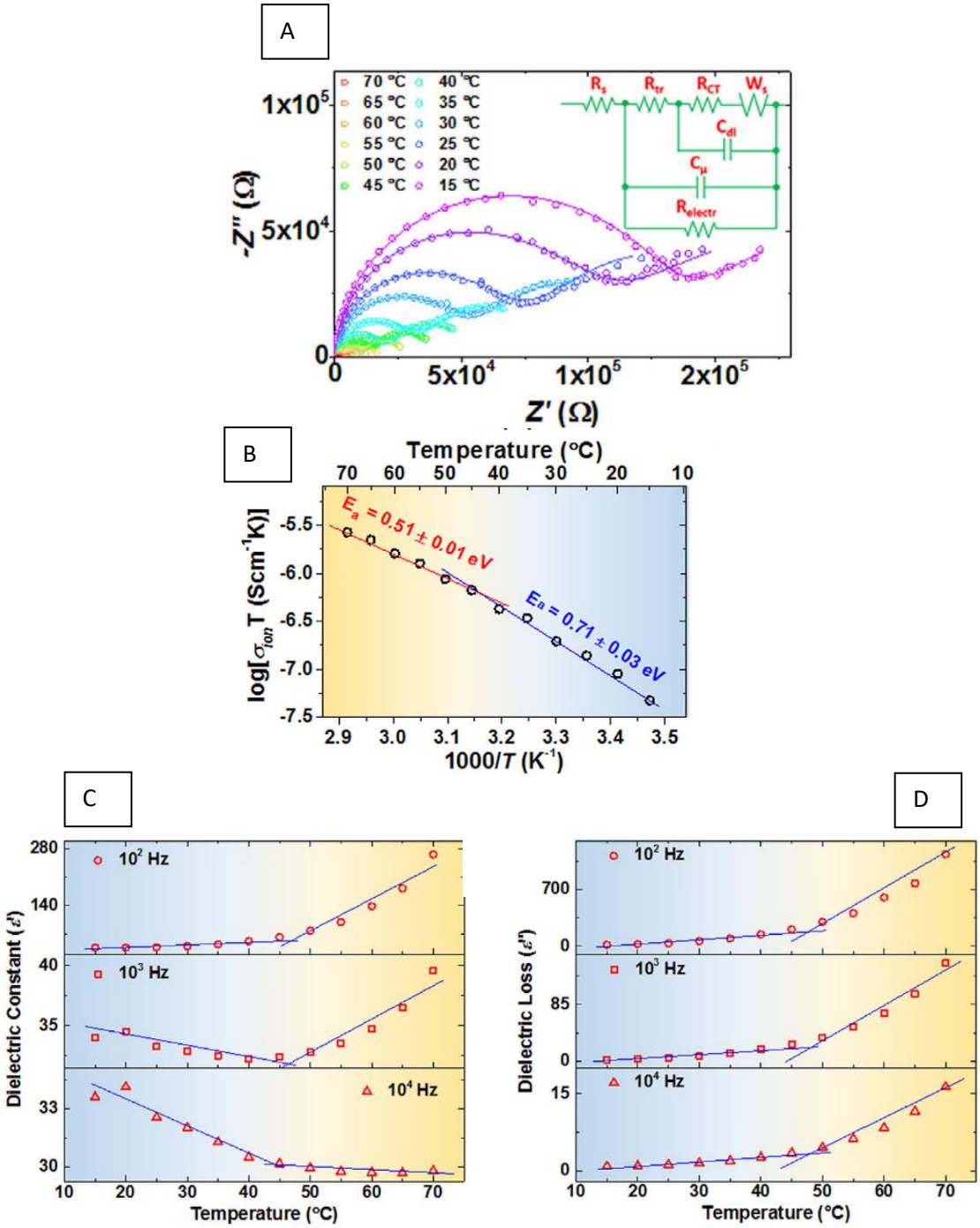

Figure 2.19. Plots from impedance spectroscopy, (A) shows the Nyquist plot. (B) Temperature dependent ionic conductivity. Plots from capacitance spectroscopy (C) temperature dependence of dielectric constant at different frequencies at 45℃ while (D) shows it at 47℃. Figure reproduced from [16]**.**

The ion conductivity from impedance can be used to find E_a when the temperature is varied. The two frequency peaks in the phase-frequency plot mean that two different transport regimes are present especially at high temperature. It has been indicated from other studies that the point defect ion migration is because of the iodide anions or the methylammonium cations.

Hoque et al used capacitance spectroscopy data where the model chosen was a parallel electrical circuit, shown in inset of Fig: 2.19a. From Fig: 2.19 it can be seen that at lower frequencies, higher temperatures show higher capacitance but at higher frequencies, higher temperatures show lower capacitance. At low frequencies the dielectric constant $\boldsymbol{\varepsilon'_r}$ increases with temperature, whereas at higher frequencies the ε'_r decreases with temperature. As was the trend with the capacitance, the conductivity is also higher with increasing temperature at lower frequency [16]. It can be observed from their capacitance vs. frequency plots that the geometry of the thin film is not mentioned so it can't be deduced as to what the actual values correspond to in terms of the material/device.

Lead halide perovskites have been known to be ferroelectric [59], [60], [61] non-ferroelectric[62], anti-ferroelectric [63] and ferro-elastic [64]. Direct measurement through ferroelectric (P-E) hysteresis loops are difficult to obtain due to the high electrical conductivity and low stability under high bias. Low temperature measurements of MALI crystals have however exhibited features such as inversion symmetry, polar domains and spontaneous polarization all consistent with ferroelectricity [65]. The dissociation of the electron-hole pair is caused by the electric field producing charge separation, so the spontaneous polarisation could be beneficial but in a ferroelectric material where ferroelectric domains are present these become unnecessary because once the electric field is applied their domains become readily orientated. These materials also have appreciable conductivity so the current is transferred quickly but this contradicts the capacitive ferroelectric behaviour which plays a role in charge separation [66]. Some studies suggest that domain walls can play a role in the high conduction, where they act as channels through which charge is transported [67], [68]. These domain walls have been offered as an explanation for high charge transport properties [69].

2.5. Doping: A, B and X site substitution

MALI can be modified by doping all three different sites, either separately or forming a mixture of different elements in different ratios, either to form solid solutions or in ratios which produce a combination of efficiency and stability.

One of the main limitations of the A-site organic cations compared to inorganic ions such as Cs^+ is their thermal decomposition at lower temperatures. Organic A site perovskites are therefore much more thermally unstable. When Cs^+ is incorporated into the A-site (giving $CsPbI_3$), due to its small size, it has a low tolerance factor. This means it is generally not in the range of 0.8-1, whereas it is for the MALI perovskite phase. So $CsPbI_3$ at room

temperature occurs as the yellow phase, which is not photovoltaic at room temperature and has an orthorhombic cell [5]. One of the advantages of doping, in this instance, is that due to the large size of the FA^+ cation, doping this for either MA^+ (in MALI) or Cs^+ (in $CsPbI_3$) or doping any of these with each other is going to change the tolerance factor and therefore make them more stable especially at room temperature, so a more easily sustained perovskite structure can be formed [13]. Fig 2.20 shows families of different hybrid perovskites and their tolerance factors.

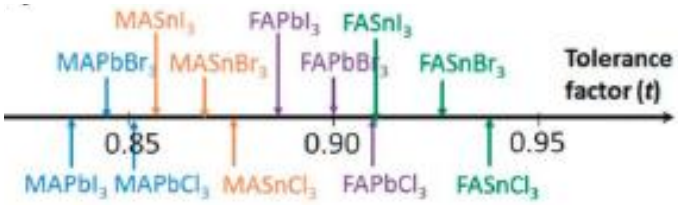

Figure 2.20. Changing A, B and X site and how it affects the tolerance factor. Figure reproduced from [5]**.**

The material that contains MA^+ as its A-site (MALI) is far more stable than FALI, since the FA^+ cation can readily dissociate into ammonia [22]. $CsPbI_3$ perovskite does have the ability to form the black phase (occurs upon heating to a higher temperature). Zhen et al reports this transition to be ~ 315 ℃, whereas Stoumpos et al state that it occurs at ~265 ℃ and that when cooled back to room temperature it reverts to the yellow phase. So unlike FALI, which upon cooling retains the black phase i.e. the photovoltaic phase, undoped $CsPbI_3$ is unstable as a photovoltaic material at room temperature or under operating conditions.

Unlike MA^+ and FA^+, Cs^+ can occupy the centre of the unit cell. The molecular structure of the organic cations tend to be more disordered due to the hydrogen bonding with an inability of the dipole moments to cancel [22]. An inorganic cation such as Caesium is much less volatile and is therefore more thermally stable, however, the major issue with $CsPbI_3$ is that it is not stable as a photovoltaic phase. In $CsPbI_3$, the solution method does not produce any black phases, yellow phases are created [22]. If the halide is changed to a bromide ($CsPbBr_3$) then the perovskite phase becomes stable at room temperature, however, the band gap is increased to almost 2.3 eV, which is too high since a higher band gap means that that the material is an inefficient photovoltaic [19].

A very large A site cation can make the structure of the perovskite unstable because of its larger ionic radius and therefore destabilise the 3D perovskite structure. Changing the A site cation or doping a mixture changes the structure, the bond lengths and angles (as seen from Fig: 2.21), which can have a large effect on the electronic properties [2]. Therefore,

perovskites such as MALI, FALI and $CsPbI_3$ can be investigated so as to predict their stability and by doping them into each other to create solid solutions. Properties such as band gap and photoluminescence can therefore be tuned to have an absorbance range across the visible light spectrum [2].

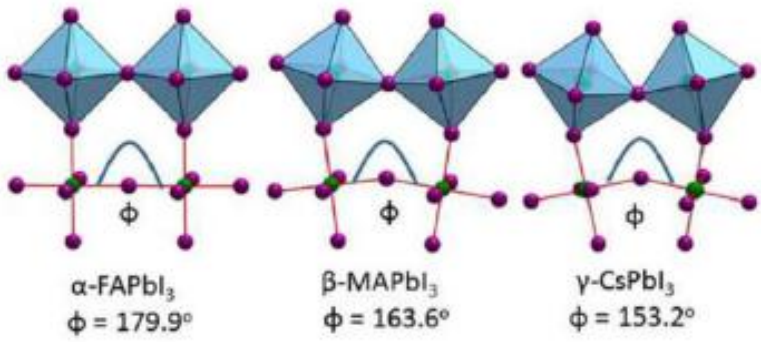

Figure 2.21. The octahedral tilting is increased as the A site is changed from formamidinium to methylammonium to Caesium. Figure reproduced from [2]**.**

Changing the X site has shown that some of the halides do not mix well together, therefore, there seems to be a small limit to the solid solutions being formed. It has been reported that chlorine in the iodide precursor matrix alters the crystallisation mechanism which can result in improved film morphology [2]. Substitution on the B site has also been reported to change the electronic properties of the material but has a small effect on the lattice parameters which are supposed to be mainly affected by the halide group on the X site. The B site generally tends to be lead but studies have been performed on tin, cadmium and calcium [2]. Replacing the A site or doping two or three different elements together alters the BX_6 bond angles which changes both the optical and electronic properties of the material. The use of many A-site cations can result in segregated phases but limited solid solutions can still be formed. For example, MA^+ and FA^+ can both be incorporated into the A site to form a perovskite structure when the B site is lead and the X site is iodine. These have shown better optical properties mainly by reducing the band gap. Changing the A site can alter the band gap. Eperon et al showed changing the A site from MA^+ to FA^+ to Cs^+ alters the band gap from 1.57, to 1.48 to 1.73 eV, respectively [70]. While other properties can also be seen to improve, one would be phase stabilisation where both MA^+ and Cs^+ ions can phase stabilise the FA^+-based perovskite.

FALI has the smallest band gap, however the black α phase is stable only at high temperatures of 150 ℃ and it reverts to the yellow δ phase below this temperature. Therefore, to maintain the black phase, FA^+ and MA^+ ions can be mixed to form a solid solution and to

form a stable black phase based on FA^+ at lower temperatures, however this is dependent on the synthesis conditions. The stabilisation of the black phase when a small amount of MA^+ is added is due to the strong dipole moment between the MA^+ and $[BX]^{3-}$, stabilising the 3D arrangement of the octahedra [71]–[78]. In this way MA-Cs, FA-Cs and even MA-FA-Cs systems have be investigated [72], [78].

In a similar manner the B site of the perovskite can be altered. This is done because lead is toxic but also the B site contributes to the conduction band. Therefore, changing the B site can not only make it lead-free but also to gauge how it changes the performance. However, altering the B site from lead has proven to be difficult since other elements do not give highly performant materials. This is for two reasons. Firstly, the density of states from the p orbitals in the lower conduction band is larger than a normal inorganic semiconductor such as gadolinium arsenide (GaAs) so higher optical absorption occurs for MALI. The second is there is strong s-p antibonding in MALI, which leads to smaller effective mass of electrons and holes and this results in good charge transport [79], [80]. Other elements such as Sn, Sr, Sb, Bi and Ge have been investigated, however they all have various issues. For example, Sn oxidises to 4+, Sr produces a large band gap and others give poor power conversion efficiency. Even in inorganic materials such as $CsSnI_3$ or $CsSnBr_3$ which are either easily synthesised or have high efficiency the Sn is readily oxidised to 4+. [80]–[86].

The X site can also be changed. In MALI the valence band minimum has strong s and p antibonding character between the lead and iodine. The conduction band minimum is contributed by the lead p states. The band gap of MALI decreases from chlorine to bromine to iodine down group 7, respectively. Because their valence orbitals change from 3p to 5p [32] the absorption spectra become narrow on going from iodine to chlorine. The halogen group therefore changes the optical properties of the material over a large wavelength. As the X species changes from chlorine to bromine to iodine the band gap changes from ~ 3.11 to 2.3 to 1.6 eV, respectively. X = chlorine generates a large band gap and is hard to synthesis whereas X= bromine has a smaller band gap with poor absorption at the near infra-red region. bromine and iodine can be substituted for each other at different percentages. This can lower the band gap to ~1.58 eV. A small amount of bromine can be substituted into MALI to change the structure from tetragonal to cubic. The different A, B and X elements can be used in appropriate fractions to produce a balance between stability and efficiency and be incorporated into tandem cell devices to reach their full potential.[87]–[96].

Table 2.2 shows a collection of band gap values and phase transitions from different papers for the main type of photovoltaic material being investigated.

Material (ABX_3)	Band gap (eV)	Phase change
[MA]PbI_3	1.46 [97], 1.5 [98],1.56 [99],1.59 [100]	[α -320K, cubic Pm3m, β>123K tetragonal (I4mcm), <123K - γ orthorhombic (Pnma) (162-172K)] [22]. [101] [-111C-57 tetragonal, >57C cubic] [102]
[MA]$PbCI_3$	2.65[97], 3.11[98], 3.1[103],3.1[100]	[Cubic from 178K - 450K until decomposition][104] [α >178.8 cubic Pm3m, β 173-178.8K tetragonal P4/mmm, γ < 172.9 orthorhombic P222] [101] [>-95 C cubic] [102]
[MA]$PbBr_3$	2.06 [97], 2.2 [98], 2.17 [99], 2.33 [105], 2.3 [100]	[α>236.9 cubic Pm3m, β 155.1-236.9 tetragonal I4/mcm, γ 149.5-155.1 tetragonal P4/mmm, δ <144.5 orthorhombic $Pna2_1$] [101] [-128C- -36C tetragonal, >-36 C cubic] [102]
[MA]SnI_3	0.66 [97], 1.1[98], 1.2-1.5 [105], 1.24 [100]	[α phase at -293K (tetragonal) P4mm, β 200K (tetragonal I4mcm)] [22] [α, P4mm tetragonal, 295K, β I4cm, tetragonal 190K] [106]
[MA]$SnCI_3$	2.56 [97], 2.2 [105], 3.5 [100]	[Pc monoclinic 318K, rhombohedral R3m, 350K, cubic Pm3m 533K] [106]
[MA]$SnBr_3$	1.36 [97], 1.1[105], 2.13[100]	[orthorhombic PmC21 200K, cubic Pm3m 295K][106]
[FA]PbI_3	1.40 [97], 1.48 [99], 1.4 [105], 1.51[100]	[α-293K trigonal P3m1, β-150K, trigonal P3, δ hexagonal][22]
[FA]$PbCI_3$	2.74[97], 3[105], 3[**100**]	cubic[100]
[FA]$PbBr_3$	2.0 [97], 2.23[99], 2.2[105], 2.25[100]	[Tetragonal: -98 - 2C, >2 cubic] [102]
[FA]SnI_3	0.94[97], 1.4[105], 1.24 [100]	[α-340K ,orthorhombic, Amm2 - β -180K orthorhombic - Imm2][22]
[FA]$SnCI_3$	3.1[97], 3.8 [105] ,3.6 [100]	cubic[100]
[FA]$SnBr_3$	2.34[97], 2.6 [105], 2.63[100]	cubic[100]
$CsPbI_3$	0.90 [97], 0.32 (cubic), 2.05 [99], 1.73, 1.8 [105], 1.6[100]	[δ 293K orthorhombic Pnma, 361C[22], orthorhombic <563K Pnma, cubic >602K, Pm3m] [101]
$CsPbCI_3$	2.0[97], 2.2 [105], 2.8 [103], 2.97 [107], 2.99 [100]	[Monoclinic < 315K, Pnma, orthorhombic 310-315K, Cmcm, tetragonal 315-320K,P4/mbm, cubic >320K Pm3m] [101] [monoclinic<38C, 38-42 orthorhombic, 42-47 tetragonal, >47C cubic] [102]
$CsPbBr_3$	1.01[97], 1.6 [105], 1.7 [107], 2.3[100]	[orthorhombic 305-360K Pbnm, tetragonal 368-399K P4/mbm, cubic 415 -505K, Pm3m] [101] [orthorhombic <82C, 82-132C tetragonal, >132C cubic] [102]
$CsSnI_3$	0.31[97], 1.4[105], 1.31 [108], 1.25 [100]	[78-153C (α-β,0.14ev, Pm3m) γ (rmt Pnam)] [22] [<170C γ phase, >170C α phase][109] [Black α cubic Pm3m 500K, Black-β-380K tetragonal P4/mbm, Black-γ orthorhombic Pnma, Y-yellow 300K orthorhombic Pnma][108]
$CsSnCI_3$	0.74[97], 1.4 [105], 2.8 [103], 2.9 [100]	[Monoclinic <117C transforms to cubic][110]
$CsSnBr_3$	0.28 [97], 1.6 [105], 1.81[100]	[Some tetragonal < 12C at >19C cubic][110]

Table 2.2. shows a collection of band gap values and phase transitions from different papers for the main type of photovoltaic material being investigated.

2.6. Processing conditions and degradation

One of the main challenges of these materials is their long term stability, which has a lot to do with the processing conditions. Most of the instability is induced through air or electrical charge. The processing conditions can introduce different local stoichiometries and some grains are more stable than others. For example, when a stoichiometric batch is prepared some grains have the ideal ABX_3 stoichiometry and others don't which then degrade faster. Kumar et al[111] used secondary electron hyperspectral imagining or SEHI to show variations in grain stoichiometry and that degradation pathways were dependent on the local stoichiometry. Grains present with excess MAI (therefore non-stoichiometric) degrade from the centre of the grain (shown by the black arrows in Fig: 2.22 (h)) and therefore with time, degradation moves towards the grain boundary. Whereas in stoichiometric grains the degradation onset occurs at the grain boundary (shown by the red arrows in Fig: 2.22 (b)). Therefore, precise control of the stoichiometry is required to improve the stability of MALI.

Alebrti et al[112] also studied lead clustering during perovskite degradation and reported that in polycrystalline MALI lead related defects aggregate into nanoclusters at the triple points of the grain boundaries. These lead clusters are detrimental to the integrity of MALI [112]. The ease at which this material starts degrading also caused creation of artefacts during experimental measurements which generally make it more challenging (at least in the beginning) to separate real phenomena from artefacts associated with characterisation. Pb-clustering is a surface phenomenon occurring in evaporated and also solution deposited layers. It occurs where the Pb related defects aggregate at the boundary of MALI grains after a volatile species is released during the dissociation process. This process can be triggered by many factors including local inhomogeneity in composition. Pb clustering on grain surfaces can be dramatic and can also occur under external factors like electric field, light and temperature and can even occur in the device architecture within the boundaries created by the electron transfer layer (ETL) and hole transfer layer (HTL). Lead clustering(s) are detrimental against MALI integrity since they agglomerate into the hosting matrix and can be easily activated by catalytic species like water [112].

The degradation of MALI also depends on many other factors like humidity, heat, trapped charge and UV light but the specific mechanism(s) and their related time scales are harder to determine because then it depends on multiple factors interacting with each other making it rather complex [111]. Previously it was thought that the local stoichiometry has a strong influence on the degradation process, however not much attention was paid to grain-

to-grain degradation processes. Three different compositions of MALI were used by Kumar et al [111] to study the effect of starting stoichiometry on MALI and its stability in air. They were stoichiometric MALI, and 5 mol% excess PbI_2 and 5mol% excess MAI. The standard morphological images of these pellets were collected for fresh pellets and aged pellets in air after 3 and 6 weeks, respectively. The results are shown in Fig: 2.22. The pellets exposed to air for 3 and 6 weeks had degraded and also show the formation of new phases. These new phases were determined by the change in contrast in the low voltage SEM images, which were also related to secondary electron spectra collected during the SEM process [111].

The as prepared stoichiometric MALI showed no signs of degradation, Fig 2.22 (a), whereas the aged MALI has signs of degradation at grain boundaries as shown by the red arrows in Fig 2.22 (b). Degradation continues until the microstructure looks visibly different by week 6, Fig 2.22 (c). The progress of degradation due to air is similar to MALI thin films under moist conditions as observed by Wang et al [113]. The starting composition seems to affect the degradation process with excess PbI_2 samples degrading faster than excess MAI or stoichiometric MALI, (i.e. compare Fig 2.22 (e) with (b) and (h)) and excess PbI_2 is shown by the bright light regions appearing on the surface edges of the grains, Fig 2.22 (d). The 6 week aged PbI_2 excess pellets have very high prevalence of sheet structures that appear in most grains (indicated by Fig: 2.22 (f) by the red arrow), so there could be a local distribution in composition for which SEHI was used because secondary electron spectra on a specific location can allocate a signature energy to each specific material component [111]. For example, a 14 - 2.0 eV energy window represents MAI rich perovksite or MALI itself, whereas ~ 2.7 - 3.3 eV represents pure PbI_2.

The excess MAI pellets showed different results (Fig: 2.22 (g-i)). They showed degradation at the centre of the grains rather than the edges adjacent to the grain boundaries. There is also a non-uniform manner in which the grains degrade. The dark region includes excess MAI by relating their contrast to SEHI spectra. Kumar et al also relate the degradation of different stoichiometries to the defect energies. Through computational studies they show that the loss of subsequent PbI_2 defects increases more than the subsequent losses of MAI defects, Therefore MAI defects loss is more favourable. Therefore, the further the material goes off-stoichiometry with making it PbI_2-rich, losses occur more easily. This agrees with the morphological results, where excess PbI_2 material degrade faster [111].

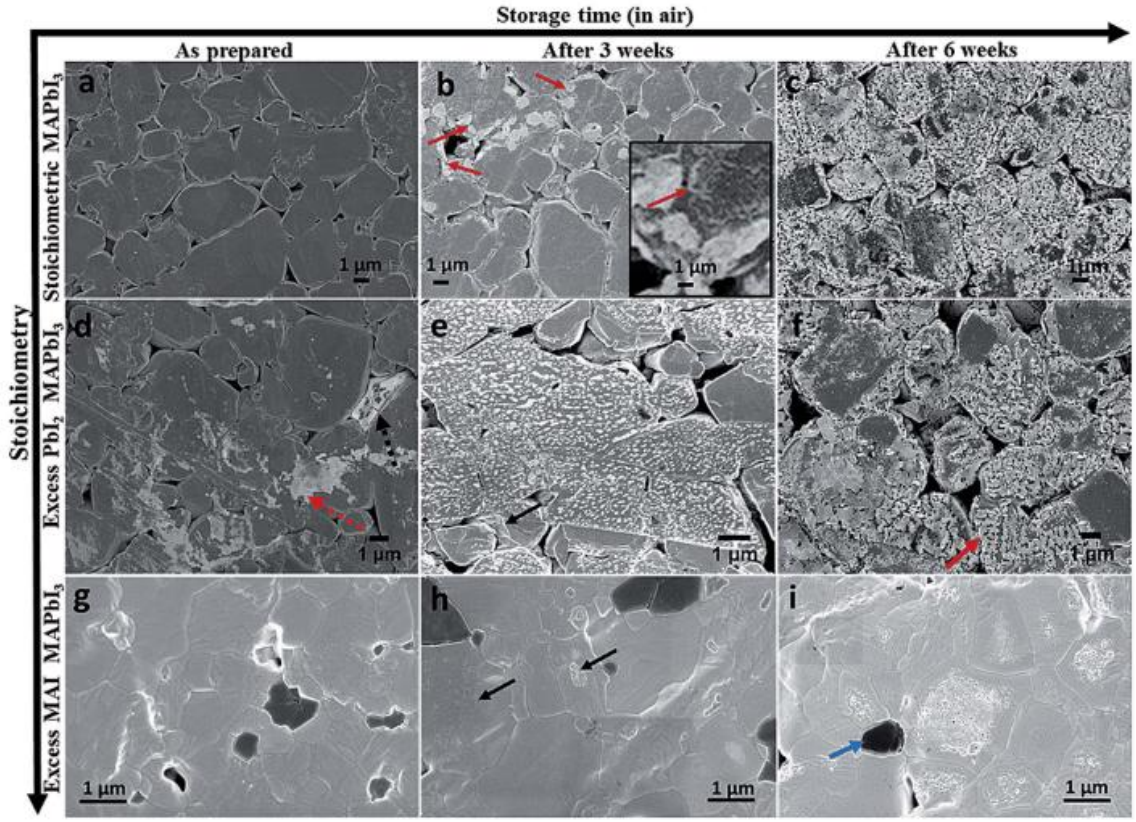

Figure 2.22. Low voltage SEM image of the surface of MALI pellets. (a) Stoichiometric MALI, (b) degraded stoichiometric pellets after 3 weeks, and (c) degraded stoichiometric pellets after 6 weeks. (d) A 5mol % excess PbI_2 pellet, (e) 5mol % excess PbI_2 pellets degraded after 3 weeks, and (f) 5mol % excess PbI_2 pellets degraded after 6 weeks. (g) A 5mol % excess MAI pellet, (h) 5mol % excess MAI pellets degraded after 3 weeks, and (I) 5mol % excess MAI pellets degraded after 6 weeks. Red arrows indicate the initial degradation emerging at the grain boundaries. The black arrows indicate excess MAI pellets having localised degradation at the centre of the grain. The blue arrow indicates local non stoichiometry of excess MAI grains. The dotted red and black arrows indicate the light regions of excess PbI_2. Figure reproduced from [111]**.**

The results show that degradation in air and its rate depends on the starting composition of the material and the local grain to grain structure can be very different within the synthesised material. This is not only the case for non-stoichiometric compositions but also within stoichiometric compositions and therefore their relative degradation rates will also differ.

Kumar et al [111] also performed bias experiments on solar cells prepared from these stoichiometric and non stoichiometric MALI compositions. When applied, the bias made the device less efficient and the non-stoichiometric device with 5% excess PbI_2 lost even more of its efficiency. The electrical bias degraded devices exhibit similar degradation to prolonged beam exposure where some grains degrade quickly and others are unaffected. Exposure to both bias and an electron beam increased the light region associated with PbI_2 rich regions of which some might be nanoclusters, which according to Alberti et al [112] can also be due to a phase change in the PbI_2 polytype. Therefore, any processing route which can improve the

local and macroscopic homogeneity of MALI should improve the resistance towards degradation.

Water has been shown to be either beneficial or detrimental on the device fabrication and the synthesis of MALI. Shoyama et al [114] examined the conversion of PbI_2 crystals to a polymer strip of a hydrated plumbate dimer and analysed the time course for the conversion of the fibre crystal of the hydrate to a perovskite. They proposed that when water is present as a minor constituent in either DMF or DMSO it acts as a catalyst in building of the Pb-I network and in the second step via quicker loss of the plumbate intermediate because of the lower hydrogen bond accepting ability than DMF and DMSO. They report a three stage conversion of sheet crystals of PbI_2 to a cubic perovskite via the organic solvent, where two of the steps are slow and require prolonged heating at 60 and 100 ˚C [114]. They label the product of these two steps as INT-F1 and INT-F2 where they are finally converted to a perovskite, Fig 2.23 (a). The basicity of the organic solvents are larger than water (hydrogen bond acceptor strength of water = 0.64, DMF = 2.10 and DMSO = 2.58) which probably accounts for the slower conversion rate into the final cubic perovskite phase [114].

The mechanisms of how lead iodide (PI) converts to the perovskite (PVK), Fig 2.23 (a) and how it can degrade back from a perovskite to lead iodide in the presence of water are shown in Fig: 2.23 (b) and 2.23C. PbI_2 degrades quickly to INT-W (this phase can be detected via XRD at 2θ = 8.5 and 10.5˚) assisted by the hydrated $MA^+.OH_2$ and further conversion from INT-W to the perovskite occurs at higher temperature and also due to the easy detachment of water from the crystal lattice [114], Fig: 2.23 (b). Water can act as a catalyst in both processes of formation and degradation of the perovskite. Water acts in the reaction in wet DMF or DMSO by converting the lead iodide to INT-W which goes through INT-F2 (DMF complex) and INT-S (DMSO complex) and this then either produces a cubic perovskite directly or via INT-W [114].

The perovskite degrades quickly into INT-W when exposed to water vapour just as it degrades into INT-F2 when exposed to DMF as shown in Fig: 2.23C. In these degradation processes both solvents act as a base to remove the methylammonium ion from the perovskite lattice, or when the perovskite is heated above 130 ˚C due to the loss of CH_3NH_3 and HI gases [114].

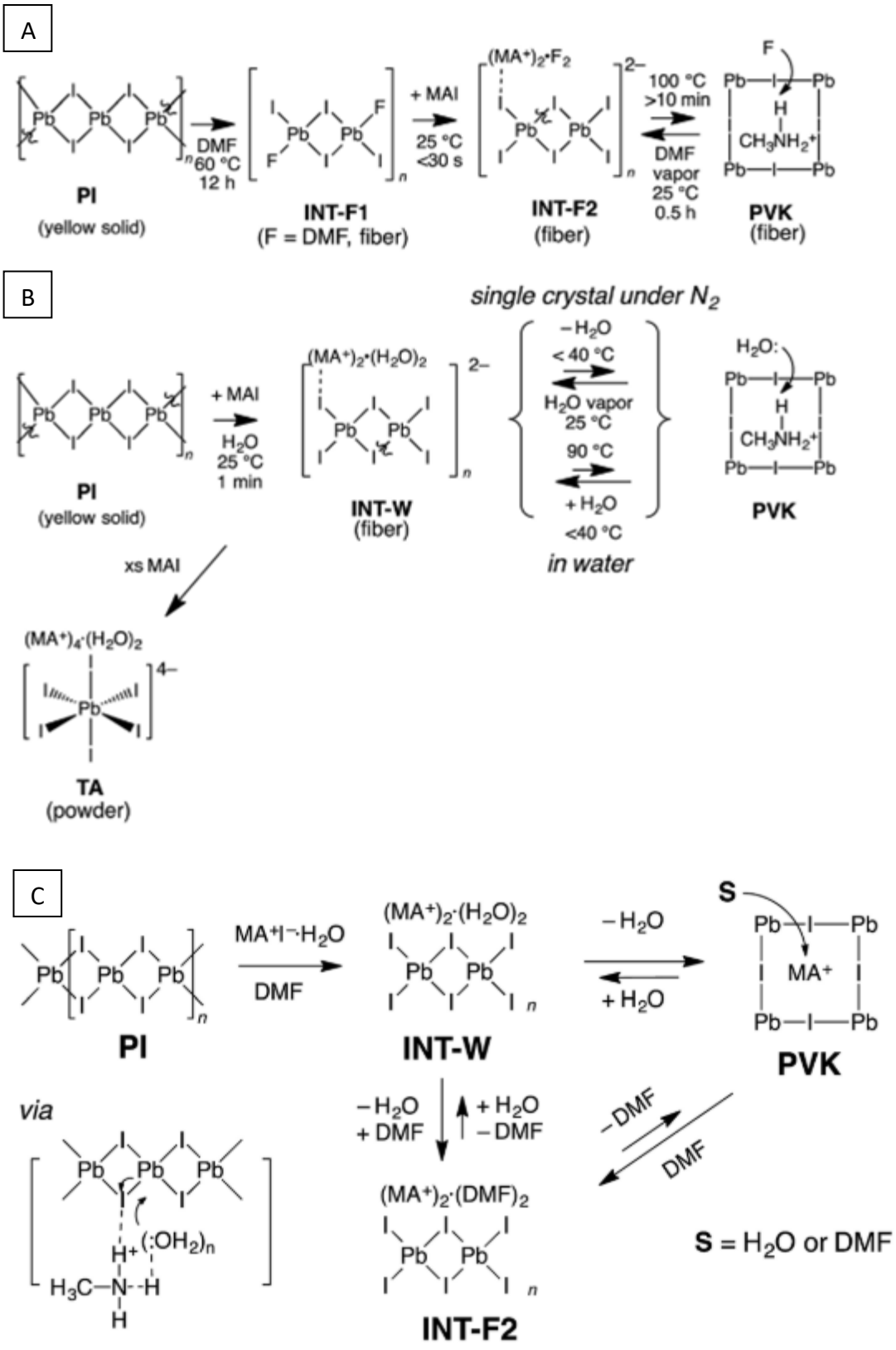

Figure 2.23. Lead iodide to perovskite conversion in DMF and in water. (A) DMF mediated conversion and (B) water mediated conversion in MAI solution. (C) shows the pathways involved in formation of MALI perovskite from INT-F2 or INT-S or the decomposition of perovskite to lead iodide in trace water shown by the reaction in moist DMF. Figure reproduced from [114]**.**

Aristidou et al [115] have investigated how oxygen can degrade MALI thin films by both experimental and computational techniques, stating that oxygen diffusion into MALI goes together with the formation of superoxide species. Thin films that have small crystals have more superoxide generation and a decrease in stability. From computational techniques the iodide vacancies are the sites where the photo-induced superoxides are located [115]. When iodine salts are deposited on MALI thin films (for example, MAI and trimethylsulfonium iodide spin coated onto MALI perovskite) this enhances the stability. Agents with bulky cations are to make sure that substitution with the MA^+ cation is unfavourable. The idea was to inhibit superoxide formation at iodide vacancies [115]. It is believed that the superoxide O_2^- de-protonates the MA^+ leading to the degradation of MALI into PbI_2, CH_3NH_2, H_2O, and iodine, as shown in Fig: 2.24. Where oxygen is incorporated into the lattice and upon exposure to light, electrons and holes are produced. Since the energy of the photon is higher than the band gap, this can induce the formation of O_2^-, which can lead to degradation.

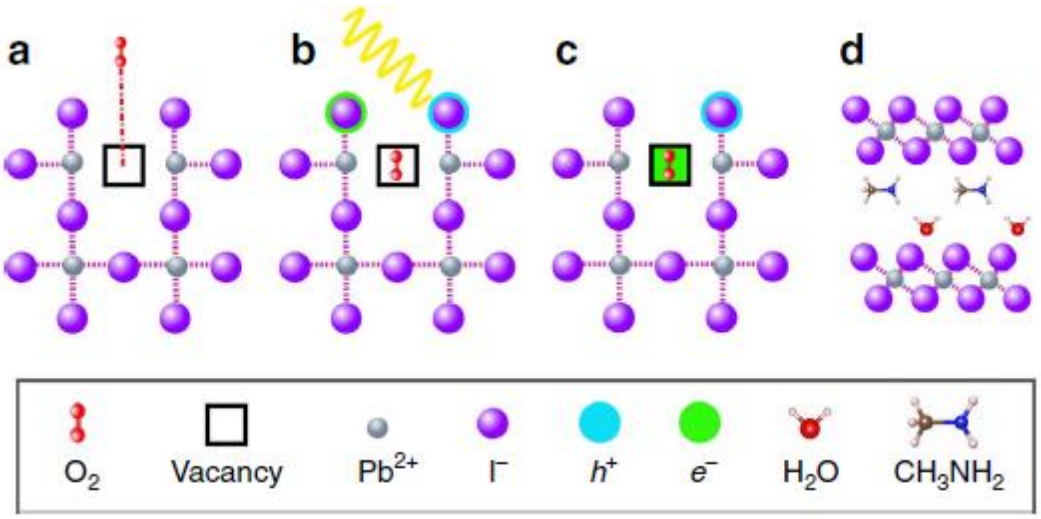

Figure 2.24. Diagram showing degradation due to O^2. Figure reproduced from [115].

Along with this mechanism, there is also the possibility of degradation being reduced with electron extraction [115]. Isothermal gravimetric analysis was used to incorporate O_2 into MALI thin films, corroborated with time-of-flight secondary ion mass spectrometry. The diffusion of oxygen into the thin film was uniform and happened at a very fast rate. A key factor might also be the particle size since MALI that has been made using a chlorine substitution step rather than just one-step where the only halogen is iodine produces larger crystals and this is a proposed reason why they are more stable.

When the effect of crystal size was further investigated it revealed that larger crystal sizes produce more stable solar cells and lowers the formation of the superoxide. It is important to state that it is not only the presence of oxygen but both oxygen and light that produces this effect. From their modelling, it was seen that when absorption of oxygen occurs the bond length increases and that it is the iodine vacancies where this reduction occurs. This is attributed to a study conducted on passing CH_3NH_3I in order to reduce iodide vacancies, by reducing the electron transfer [115].

2.7. Solar cells

The first reported use of MALI in a solar cell was reported when they were incorporated in dye-sensitized solar cells with a power conversion efficiency (PCE) of approximately 4%. As they were dye-sensitised with a liquid electrolyte the lifetime of these materials were limited to only a couple of minutes [14]. The big breakthrough came with the use of a solid hole conductor, which has now led to PCE's of up to 21%. A general structure for such a solar cell is shown in Fig: 2.25 where on a glass substrate, the fluorine doped tin oxide (FTO) layer is deposited on which an electron transport layer of TiO_2 is placed. Then the hybrid perovskite layer is added, then the hole transport layer is deposited and finally a gold layer on top.

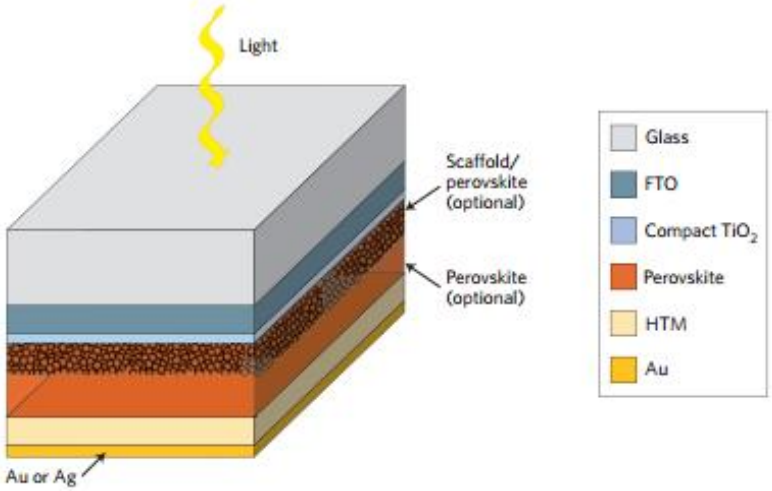

Figure 2.25. General structure of a perovskite solar cell. Figure reproduced from [8]**.**

The cells work due to the formation of electron and hole pairs. Once a photon hits the perovskite material, the separation and transference of the electrons and holes to an external circuit generate a current. The electron and hole transport layers make it possible for the separation of the electrons and holes at a much faster rate and therefore decreases the recombination mechanism so as to increase the cell efficiency.

The chemical and physical properties of these materials are highly dependent on their preparation method. For example, depending on the preparation methods the semiconducting behaviour of MALI can either be p- or n-type. Samples prepared with the lowest carrier concentration were from a solution based method and these tend to be n-type semiconductors, whereas p-type semiconductors are obtained from solid state reactions [116]. The A-site in the perovskite can be changed by either rubidium, caesium, methylammonium or formamidinium and a 3D structure is obtained; however, if the site is occupied by a larger cation then a 3D structure is not formed and either 2D or 1D structures are formed [22]. Altering the stoichiometry can also change the behaviour of these perovskites. Wang et al [116] conducted studies into varying the ratios of the precursors used in MALI, i.e. methylammonium iodide (MAI) and PbI_2.They report the behaviour of the MALI perovskite can change, being either p- or n-type depending on the ratio of the precursors used. They also reported (through Hall measurements) that annealing can convert MALI from p- to n-type. This occurs when the methylammonium iodide is removed, as shown in Fig: 2.26 [116].

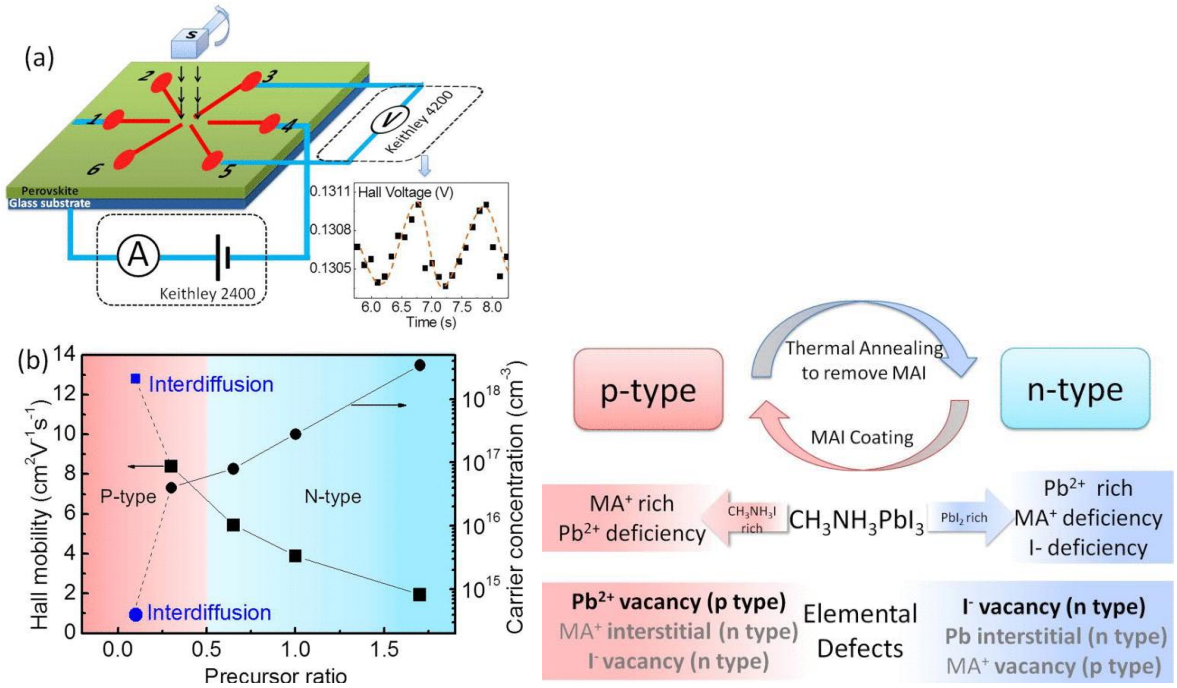

Figure 2.26. (A) The Hall effect measurement setup with the graph to the right showing the composition dependent carrier concentration (circle points) and mobility (square points) in MALI thin films. (B) The type of conductivity which is dependent on the precursor ratio. Excess MAI gives p-type behaviour whereas excess PbI_2 gives n-type behaviour. The elemental defects in bold (on the right hand of the figure) are more likely to form. Figure reproduced from [116].

The material can self-dope due to defects and changing the conditions of synthesis can produce either n- or p-type. By changing the amount of precursors a ratio of 0.52 led to a stoichiometric perovskite, the term precursor ratio means the molar ratio of PbI_2/MAI in the

precursor mixture solution. When the precursor ratio is set at 1.0 the material behaves as n-type. Reducing the precursor ratio to 0.65 reduced the electron concentration and increasing the ratio to 1.7 increased the electron concentration as shown in Fig: 2.26 (b) [116]. To produce a stoichiometric perovskite film, more MAI is needed than PbI_2. Wang et al show the n- to p-type transition occurring at a smaller ratio of 0.6 than 1 in the precursor solution. When the ratio is increased, meaning when less MAI is used, then the film turned n-type with high electron concentration almost six orders of magnitude higher than the hole concentration in the pristine film. Wang et al suggest MALI is not thermally stable above 150 ℃, which is due to the low dissociation energy of MALI. The carrier mobility of the high temperature annealed film was reduced due to the large density of defects caused by decomposition [116]. They comment that on increasing the MAI content relative to the PbI_2 content there will be more PbI_2 vacancies, and that its these lead vacancies that contribute to the p-type conductivity. However, when the starting precursors are changed and there is more PbI_2 than MAI it behaves like an n-type material [116].

References

[1] R.J.D. Tilley, Perovskites: Structure - Property Relationships, 1st edition. Chichester: John Wiley & Sons, 2016.

[2] J. S. Manser, J. A. Christians, and P. V. Kamat, 'Intriguing Optoelectronic Properties of Metal Halide Perovskites', *Chem. Rev.*, vol. 116, no. 21, pp. 12956–13008, 2016.

[3] A. Kojima, K. Teshima, Y. Shirai, and T. Miyasaka, 'Organometal Halide Perovskites as Visible-Light Sensitizers for Photovoltaic Cells', *J. Am. Chem. Soc.*, vol. 131, no. 17, pp. 6050–6051, May 2009.

[4] M. M. Lee, J. Teuscher, T. Miyasaka, T. N. Murakami, and H. J. Snaith, 'Efficient Hybrid Solar Cells Based on Meso-Superstructured Organometal Halide Perovskites', *Science*, vol. 338, no. 6107, pp. 643 – 647, Nov. 2012.

[5] H.-S. Kim et al., 'Lead Iodide Perovskite Sensitized All-Solid-State Submicron Thin Film Mesoscopic Solar Cell with Efficiency Exceeding 9%', *Sci. Rep.*, vol. 2, no. 1, p. 591, 2012.

[6] Z. Fan, K. Sun, and J. Wang, 'Perovskites for photovoltaics: a combined review of organic-inorganic halide perovskites and ferroelectric oxide perovskites', *J. Mater. Chem. A*, vol. 3, no. 37, pp. 18809–18828, 2015.

[7] K. Wang, 'Progress in Materials Science Recent progress in fundamental understanding of halide perovskite semiconductors', *Prog. Mater. Sci.*, vol. 106, no. June, p. 100580, 2019.

[8] M. A. Green, A. Ho-Baillie, and H. J. Snaith, 'The emergence of perovskite solar cells', *Nat. Photonics*, vol. 8, no. 7, pp. 506–514, 2014.

[9] C. Eames, J. M. Frost, P. R. F. Barnes, B. C. O'Regan, A. Walsh, and M. S. Islam, 'Ionic transport in hybrid lead iodide perovskite solar cells', *Nat. Commun.*, vol. 6, no. May, p. 7497, 2015.

[10] J. Byun et al., 'Efficient Visible Quasi-2D Perovskite Light-Emitting Diodes', *Adv. Mater.*, vol. 28, no. 34, pp. 7515–7520, 2016.

[11] H. Zhu et al., 'Lead halide perovskite nanowire lasers with low lasing thresholds and high quality factors', *Nat. Mater.*, vol. 14, no. 6, pp. 636–642, 2015.

[12] Y.-H. Kim, H.J. Kim, M. Osada, B.-W. Li, Y. Ebina, and T. Sasaki, '2D Perovskite Nanosheets with Thermally-Stable High-κ Response: A New Platform for High-Temperature

Capacitors', ACS Appl. Mater. *Interfaces*, vol. 6, no. 22, pp. 19510–19514, Nov. 2014.
[13] Z. Li, M. Yang, J. S. Park, S. H. Wei, J. J. Berry, and K. Zhu, 'Stabilizing Perovskite Structures by Tuning Tolerance Factor: Formation of formamidinium and Cesium Lead Iodide *Solid-State Alloys*', Chem. Mater., *Vol.* 28, no.1, pp. 284–292 2016.
[14] M. G. Nam-Gyu Park and Miyasaka Tsutomu, Organic- Inorganic Halide Perovskite Photovoltaics. 2016.
[15] K. P. Ong, T. W. Goh, Q. Xu, and A. Huan, 'Structural Evolution in methylammonium Lead Iodide $CH_3NH_3PbI_3$', *J. Phys. Chem. A,* vol. 119, no. 44, pp. 11033–11038, Nov. 2015.
[16] M. N. F. Hoque, N. Islam, Z. Li, G. Ren, K. Zhu, and Z. Fan, 'Ionic and Optical Properties of methylammonium Lead Iodide Perovskite across the Tetragonal Cubic Structural Phase Transition', *ChemSusChem,* Vol. 9, no. 18, pp. 2692-2698, 2016.
[17] P. S. Whitfield et al., 'Structures , Phase Transitions and Tricritical Behavior of the Hybrid Perovskite methylammonium Lead Iodide', Scientific reports 6, Article number 35685, pp. 1–16, June 2016.
[18] P. Nandi, C. Giri, B. Joseph, S. Rath, U Manju, and D. Topwal, '$CH_3NH_3PbI_3$, A Potential Solar Cell Candidate: Structural and Spectroscopic Investigations', *J Phys Chem A,* Vol, 120, no. 49, pp. 9732-9739, 2016.
[19] R. E. Beal et al., 'Fully inorganic cesium lead halide perovskites with improved stability for tandem solar cells' *J Phys Chem Lett,* Vol, 7, no. 5, pp. 746-751, 2016..
[20] Z. Song, S. C. Watthage, A. B. Phillips, B. L. Tompkins, R. J. Ellingson, and M. J. Heben, 'Impact of Processing Temperature and Composition on the Formation of methylammonium Lead Iodide Perovskites', *Chem. Mater.,* vol. 27, no. 13, pp. 4612–4619, 2015.
[21] D. P. Nenon et al., 'Structural and chemical evolution of methylammonium lead halide perovskites during thermal processing from solution', *Energy Environ. Sci.,* vol. 9, p. 10.1039, 2016.
[22] C. C. Stoumpos, C. D. Malliakas, and M. G. Kanatzidis, 'Semiconducting tin and lead iodide perovskites with organic cations: Phase transitions, high mobilities, and near-infrared photoluminescent properties', *Inorg. Chem.,* vol. 52, no. 15, pp, 9019-9038, 2013.
[23] A. D. Jodlowski, A. Yepez, R. Luque, L. Camacho, and G. de Miguel, 'Benign-by-Design Solventless Mechanochemical Synthesis of Three-, Two-, and One-Dimensional Hybrid Perovskites', *Angew. Chemie* - Int. Ed., vol. 56, no.45, pp. 13929-13929 2016.
[24] A. Dualeh, P. Gao, and M. Grätzel, 'Thermal Behavior of methylammonium Lead-trihalide Perovskite Photovoltaic Light Harvesters' *Chem Mater,* vol. 26, no. 21, pp. 6160-6164, 2014
[25] A. Pisoni et al., 'Ultra-low thermal conductivity in organic-inorganic hybrid perovskite $CH_3NH_3PbI_3$', J. Phys. Chem. Lett., *J. Phys. Chem. Lett,* vol. 5, no. 14, pp. 2488-2492, 2014.
[26] A. West, Solid State Chemistry and its Applications, 2nd Edition, Student Edition. 2014.
[27] J. Even, L. Pedesseau, J.-M. Jancu, and C. Katan, 'Importance of Spin–Orbit Coupling in Hybrid Organic/Inorganic Perovskites for Photovoltaic Applications', *J. Phys. Chem. Lett.,* vol. 4, no. 17, pp. 2999–3005, Sep. 2013.
[28] P. Umari, E. Mosconi, and F. De Angelis, 'Relativistic GW calculations on $CH_3NH_3PbI_3$ and $CH_3NH_3SnI_3$ Perovskites for Solar Cell Applications', *Sci. Rep.,* vol. 4, no. 1, p. 4467, 2014.
[29] C. Motta, F. El-Mellouhi, S. Kais, N. Tabet, F. Alharbi, and S. Sanvito, 'Revealing the role of organic cations in hybrid halide perovskite $CH_3NH_3PbI_3$', *Nat. Commun.,* vol. 6, no. 1, p. 7026, 2015.
[30] F. Brivio, A. B. Walker, and A. Walsh, 'Structural and electronic properties of hybrid perovskites for high-efficiency thin-film photovoltaics from first-principles', *APL Mater.,* vol. 1, no. 4, p. 42111, Oct. 2013.
[31] A. Walsh and G. W. Watson, 'The origin of the stereochemically active Pb(II) lone pair: DFT calculations on PbO and PbS', *J. Solid State Chem.,* vol. 178, no. 5, pp. 1422–1428, 2005.
[32] A. Walsh, D. J. Payne, R. G. Egdell, and G. W. Watson, 'Stereochemistry of post-transition metal oxides: revision of the classical lone pair model', *Chem. Soc. Rev.,* vol. 40, no. 9, pp. 4455–4463, 2011.
[33] W.-J. Yin, T. Shi, and Y. Yan, 'Unusual defect physics in $CH_3NH_3PbI_3$ perovskite solar cell absorber', *Appl. Phys. Lett.,* vol. 104, no. 6, p. 63903, Feb. 2014.
[34] M. R. Filip, G. E. Eperon, H. J. Snaith, and F. Giustino, 'Steric engineering of metal-halide

perovskites with tunable optical band gaps', *Nat. Commun.*, vol. 5, no. 1, p. 5757, 2014.
[35] S. T. A. G. Melissen, F. Labat, P. Sautet, and T. Le Bahers, 'Electronic properties of CH_3NH_3 PbX_3 (X = Cl{,} Br{,} I) compounds for photovoltaic and photocatalytic applications', *Phys. Chem. Chem. Phys.*, vol. 17, no. 3, pp. 2199–2209, 2015.
[36] L. Lang, J.-H. Yang, H.-R. Liu, H. J. Xiang, and X. G. Gong, 'First-principles study on the electronic and optical properties of cubic ABX_3 halide perovskites', *Phys. Lett. A*, vol. 378, no. 3, pp. 290–293, 2014.
[37] M. H. Du, 'Efficient carrier transport in halide perovskites: theoretical perspectives', *J. Mater. Chem. A*, vol. 2, no. 24, pp. 9091–9098, 2014.
[38] M. N. F. Hoque et al., 'Polarization and Dielectric Study of methylammonium Lead Iodide Thin Film to Reveal its Nonferroelectric Nature under Solar Cell Operating Conditions', *ACS Energy Lett.*, vol. 1, no. 1, pp. 142–149, Jul. 2016.
[39] Y. Yuan et al., 'Photovoltaic Switching Mechanism in Lateral Structure Hybrid Perovskite Solar Cells', Adv. Energy Mater., vol. 5, no. 15, pp. 1500615, 2015.
[40] M. Bag et al., 'Kinetics of Ion Transport in Perovskite Active Layers and Its Implications for Active Layer Stability', *J. Am. Chem. Soc.*, vol. 137, no. 40, pp. 13130–13137, Oct. 2015.
[41] T. Y. Yang, G. Gregori, N. Pellet, M. Gratzel, and J. Maier, 'The Significance of Ion Conduction in a Hybrid Organic-Inorganic Lead-Iodide-Based Perovskite Photosensitizer', *Angew. Chemie* - Int. Ed., vol. 54, no. 27, pp. 7905–7910, 2015.
[42] J. M. Azpiroz, E. Mosconi, J. Bisquert, and F. De Angelis, 'Defect migration in methylammonium lead iodide and its role in perovskite solar cell operation', *Energy Environ. Sci.*, vol. 8, no. 7, pp. 2118–2127, 2015.
[43] J. Kim, S. Lee, J. H. Lee, and K. Hong, 'The Role of Intrinsic Defects in methylammonium Lead Iodide', *J. Phys. Chem. Lett*, Vol. 5, no. 8, pp. 1312-1317, 2014.
[44] Y. Zhang et al., 'Charge selective contacts, mobile ions and anomalous hysteresis in organic–inorganic perovskite solar cells', *Mater. Horiz.*, vol. 2, no. 3, pp. 315–322, 2015.
[45] P. Delugas, C. Caddeo, A. Filippetti, and A. Mattoni, 'Thermally Activated Point Defect Diffusion in methylammonium Lead Trihalide: Anisotropic and Ultrahigh Mobility of Iodine', *J. Phys. Chem. Lett.*, vol. 7, no. 13, pp. 2356–2361, Jul. 2016.
[46] D. Bryant et al., 'Observable Hysteresis at Low Temperature in "Hysteresis Free" Organic–Inorganic Lead Halide Perovskite Solar Cells', *J. Phys. Chem. Lett.*, vol. 6, no. 16, pp. 3190–3194, Aug. 2015.
[47] O. S. Game, G. J. Buchsbaum, Y. Zhou, N. P. Padture, and A. I. Kingon, 'Ions Matter: Description of the Anomalous Electronic Behavior in methylammonium Lead Halide Perovskite Devices', *Adv. Funct. Mater.*, vol. 27, no. 16, p. 1606584, 2017.
[48] Y. Shao et al., 'Grain boundary dominated ion migration in polycrystalline organic–inorganic halide perovskite films', *Energy Environ. Sci.*, vol. 9, no. 5, pp. 1752–1759, 2016.
[49] J. S. Yun et al., 'Critical Role of Grain Boundaries for Ion Migration in formamidinium and methylammonium Lead Halide Perovskite Solar Cells', *Adv. Energy Mater.*, vol. 6, no. 13, p. 1600330, 2016.
[50] E. T. Hoke, D. J. Slotcavage, E. R. Dohner, A. R. Bowring, H. I. Karunadasa, and M. D. McGehee, 'Reversible photo-induced trap formation in mixed-halide hybrid perovskites for photovoltaics', *Chem. Sci.*, vol. 6, no. 1, pp. 613–617, 2015.
[51] S. Meloni et al., 'Ionic polarization-induced current–voltage hysteresis in CH3NH3PbX3 perovskite solar cells', *Nat. Commun.*, vol. 7, no. 1, pp. 10334, 2016.
[52] J. Haruyama, K. Sodeyama, L. Han, and Y. Tateyama, 'First-principles study of ion diffusion in perovskite solar cell sensitizers', *J. Am. Chem. Soc.*, vol. 137, no. 32, pp. 10048–10051, 2015.
[53] J. Peng, Y. Chen, K. Zheng, T. Pullerits, and Z. Liang, 'Insights into charge carrier dynamics in organo-metal halide perovskites: from neat films to solar cells', *Chem. Soc. Rev.*, vol. 46, no. 19, pp. 5714–5729, 2017.
[54] W. A. Laban and L. Etgar, 'Depleted hole conductor-free lead halide iodide heterojunction solar cells', *Energy Environ. Sci.*, vol. 6, no. 11, pp. 3249–3253, 2013.
[55] L. Etgar et al., 'Mesoscopic $CH_3NH_3PbI_3/TiO_2$ Heterojunction Solar Cells', *J. Am. Chem. Soc.*, vol. 134, no. 42, pp. 17396–17399, Oct. 2012.

[56] J. You et al., ‘Low-Temperature Solution-Processed Perovskite Solar Cells with High Efficiency and Flexibility’, *ACS Nano*, vol. 8, no. 2, pp. 1674–1680, Feb. 2014.
[57] Z. Xiao and Y. Yan, ‘Progress in Theoretical Study of Metal Halide Perovskite Solar Cell Materials’, *Adv. Energy Mater.*, vol. 7, no. 22, p. 1701136, 2017.
[58] G. Landi et al., ‘Correlation between Electronic Defect States Distribution and Device Performance of Perovskite Solar Cells’, *Adv. Sci.*, vol. 4, no. 10, p. 1700183, 2017.
[59] J. M. Frost, K. T. Butler, F. Brivio, C. H. Hendon, M. van Schilfgaarde, and A. Walsh, ‘Atomistic Origins of High-Performance in Hybrid Halide Perovskite Solar Cells’, *Nano Lett.*, vol. 14, no. 5, pp. 2584–2590, May 2014.
[60] H. Röhm, T. Leonhard, M. J. Hoffmann, and A. Colsmann, ‘Ferroelectric domains in methylammonium lead iodide perovskite thin-films’, *Energy Environ. Sci.*, vol. 10, no. 4, pp. 950–955, 2017.
[61] Z. Fan et al., ‘Ferroelectricity of $CH_3NH_3PbI_3$ Perovskite’, *J. Phys. Chem. Lett.*, vol. 6, no. 7, pp. 1155–1161, Apr. 2015.
[62] S. G et al., ‘Is $CH_3NH_3PbI_3$ Polar?’, *J. Phys. Chem. Lett.*, vol. 7, no. 13, pp. 2412–2419, Jul. 2016.
[63] G. A. Sewvandi, K. Kodera, H. Ma, S. Nakanishi, and Q. Feng, ‘Antiferroelectric Nature of $CH_3NH_3PbI_3$−xClx Perovskite and Its Implication for Charge Separation in Perovskite Solar Cells’, *Sci. Rep.*, vol. 6, no. 1, p. 30680, 2016.
[64] I. M. Hermes et al., ‘Ferroelastic Fingerprints in methylammonium Lead Iodide Perovskite’, *J. Phys. Chem. C*, vol. 120, no. 10, pp. 5724–5731, Mar. 2016.
[65] Y. Rakita et al., ‘Tetragonal $CH_3NH_3PbI_3$ is ferroelectric’, *Proc. Natl. Acad. Sci.*, vol. 114, no. 28, pp. E5504--E5512, 2017.
[66] L. Pintilie, "Charge Transport in Ferroelectric Thin Films", in Ferroelectrics - Physical Effects. London, United Kingdom: IntechOpen, 2011 [Online]. Available: https://www.intechopen.com/chapters/16751 doi: 10.5772/18165
[67] J. Seidel et al., ‘Conduction at domain walls in oxide multiferroics’, *Nat. Mater.*, vol. 8, no. 3, pp. 229–234, 2009.
[68] J. Guyonnet, I. Gaponenko, S. Gariglio, and P. Paruch, ‘Conduction at Domain Walls in Insulating $Pb(Zr_{0.2}Ti_{0.8})O_3$ Thin Films’, *Adv. Mater.*, vol. 23, no. 45, pp. 5377–5382, 2011.
[69] T. S. Sherkar and L. Jan Anton Koster, ‘Can ferroelectric polarization explain the high performance of hybrid halide perovskite solar cells?’, *Phys. Chem. Chem. Phys.*, vol. 18, no. 1, pp. 331–338, 2016.
[70] G. E. Eperon, S. D. Stranks, C. Menelaou, M. B. Johnston, L. M. Herz, and H. J. Snaith, ‘formamidinium lead trihalide: a broadly tunable perovskite for efficient planar heterojunction solar cells’, *Energy Environ. Sci.*, vol. 7, no. 3, pp. 982–988, 2014.
[71] Hyosung Choi, Jaeki Jeong, Hak-Beom Kim, Seongbeom Kim, Bright Walker, Gi-Hwan Kim, Jin Young Kim, Cesium-doped methylammonium lead iodide perovskite light absorber for hybrid solar cells, *Nano Energy*, Volume 7, pp. 80-85, 2014
[72] Y. Sun, J. Peng, Y. Chen, Y. Yao, and Z. Liang, ‘Triple-cation mixed-halide perovskites: towards efficient, annealing-free and air-stable solar cells enabled by $Pb(SCN)_2$ additive’, *Sci. Rep.*, vol. 7, no. 1, p. 46193, 2017.
[73] K. T. Cho et al., ‘Highly efficient perovskite solar cells with a compositionally engineered perovskite/hole transporting material interface’, *Energy Environ. Sci.*, vol. 10, no. 2, pp. 621–627, 2017.
[74] Bai-Xue Chen, Wen-Guang Li, Hua-Shang Rao, Yang-Fan Xu, Dai-Bin Kuang, Cheng-Yong Su, Large-grained perovskite films via $FA_xMA_{1-x}Pb(I_xBr_{1-x})_3$ single crystal precursor for efficient solar cells, *Nano Energy*, Volume 34, pp. 264-270, 2017
[75] Y. Fu et al., ‘Nanowire Lasers of formamidinium Lead Halide Perovskites and Their Stabilized Alloys with Improved Stability’, *Nano Lett.*, vol. 16, no. 2, pp. 1000–1008, Feb. 2016.
[76] C. Mu, J. Pan, S. Feng, Q. Li, and D. Xu, ‘Quantitative Doping of Chlorine in formamidinium Lead Trihalide ($FAPbI_{3-x}Cl_x$) for Planar Heterojunction Perovskite Solar Cells’, *Adv. Energy Mater.*, vol. 7, no. 6, p. 1601297, 2017.
[77] N. Pellet et al., ‘Mixed-Organic-Cation Perovskite Photovoltaics for Enhanced Solar-Light Harvesting’, *Angew. Chemie Int. Ed.*, vol. 53, no. 12, pp. 3151–3157, 2014.

[78] A. Binek, F. C. Hanusch, P. Docampo, and T. Bein, 'Stabilization of the Trigonal High-Temperature Phase of formamidinium Lead Iodide', *J. Phys. Chem. Lett.*, vol. 6, no. 7, pp. 1249–1253, Apr. 2015.
[79] P. Guo et al., 'decoupled organic and inorganic sublattices', Nat. Commun., no.10, 2019, pp. 1–8.
[80] W.-J. Yin, T. Shi, and Y. Yan, 'Unique Properties of Halide Perovskites as Possible Origins of the Superior Solar Cell Performance', *Adv. Mater.*, vol. 26, no. 27, pp. 4653–4658, 2014.
[81] J. Navas et al., 'New insights into organic–inorganic hybrid perovskite $CH_3NH_3PbI_3$ nanoparticles. An experimental and theoretical study of doping in Pb^{2+} sites with Sn^{2+}, Sr^{2+}, Cd^{2+} and Ca^{2+}', *Nanoscale*, vol. 7, no. 14, pp. 6216–6229, 2015.
[82] B. Saparov et al., 'Thin-Film Preparation and Characterization of $Cs_3Sb_2I_9$: A Lead-Free Layered Perovskite Semiconductor', *Chem. Mater.*, vol. 27, no. 16, pp. 5622–5632, Aug. 2015.
[83] J.-C. Hebig, I. Kühn, J. Flohre, and T. Kirchartz, 'Optoelectronic Properties of $(CH_3NH_3)_3Sb_2I_9$ Thin Films for Photovoltaic Applications', *ACS Energy Lett.*, vol. 1, no. 1, pp. 309–314, Jul. 2016.
[84] T. J. Jacobsson, M. Pazoki, A. Hagfeldt, and T. Edvinsson, 'Goldschmidt's Rules and Strontium Replacement in Lead Halogen Perovskite Solar Cells: Theory and Preliminary Experiments on $CH3NH_3SrI_3$', *J. Phys. Chem. C*, vol. 119, no. 46, pp. 25673–25683, Nov. 2015.
[85] P. V Kamat, J. Bisquert, and J. Buriak, 'Lead-Free Perovskite Solar Cells', ACS Energy Lett., vol. 2, no. 4, pp. 904–905, Apr. 2017.
[86] P. P. Boix, S. Agarwala, T. M. Koh, N. Mathews, and S. G. Mhaisalkar, 'Perovskite Solar Cells: Beyond methylammonium Lead Iodide', *J. Phys. Chem. Lett.*, vol. 6, no. 5, pp. 898–907, Mar. 2015.
[87] S.-H. Wei and A. Zunger, 'Electronic and structural anomalies in lead chalcogenides', *Phys. Rev. B*, vol. 55, no. 20, pp. 13605–13610, May 1997.
[88] E. Mosconi, A. Amat, M. K. Nazeeruddin, M. Grätzel, and F. De Angelis, 'First-Principles Modeling of Mixed Halide Organometal Perovskites for Photovoltaic Applications', *J. Phys. Chem. C*, vol. 117, no. 27, pp. 13902–13913, Jul. 2013.
[89] Y. Fang, Q. Dong, Y. Shao, Y. Yuan, and J. Huang, 'Highly narrowband perovskite single-crystal photodetectors enabled by surface-charge recombination', *Nat. Photonics*, vol. 9, no. 10, pp. 679–686, 2015.
[90] Kenichiro Tanaka, Takayuki Takahashi, Takuma Ban, Takashi Kondo, Kazuhito Uchida, Noboru Miura, Comparative study on the excitons in lead-halide-based perovskite-type crystals $CH_3NH_3PbBr_3$ $CH_3NH_3PbI_3$, *Solid State Communications*, Volume 127, Issues 9–10, Pages 619-623, 203.
[91] E. Edri, S. Kirmayer, M. Kulbak, G. Hodes, and D. Cahen, 'Chloride Inclusion and Hole Transport Material Doping to Improve methylammonium Lead Bromide Perovskite-Based High Open-Circuit Voltage Solar Cells', *J. Phys. Chem. Lett.*, vol. 5, no. 3, pp. 429–433, Feb. 2014.
[92] E. Edri, S. Kirmayer, D. Cahen, and G. Hodes, 'High Open-Circuit Voltage Solar Cells Based on Organic–Inorganic Lead Bromide Perovskite', *J. Phys. Chem. Lett.*, vol. 4, no. 6, pp. 897–902, Mar. 2013.
[93] B. Cai, Y. Xing, Z. Yang, W.H. Zhang, and J. Qiu, 'High performance hybrid solar cells sensitized by organolead halide perovskites', *Energy Environ. Sci.*, vol. 6, no. 5, pp. 1480–1485, 2013.
[94] H.-S. Kim et al., 'Mechanism of carrier accumulation in perovskite thin-absorber solar cells', *Nat. Commun.*, vol. 4, no. 1, p. 2242, 2013.
[95] S. Ryu et al., 'Voltage output of efficient perovskite solar cells with high open-circuit voltage and fill factor', *Energy Environ. Sci.*, vol. 7, no. 8, pp. 2614–2618, 2014.
[96] A. Walsh, G. W. Watson, The origin of the stereochemically active Pb(II) lone pair: DFT calculations on PbO and PbS, *Journal of Solid State Chemistry*, Volume 178, Issue 5, Pages 1422-1428, 2005.
[97] W. A. Saidi, W. Shadid, and I. E. Castelli, 'Machine-learning structural and electronic

properties of metal halide perovskites using a hierarchical convolutional neural network', npj C*omput. Mater*., vol. 6, no. 1, p. 36, 2020.
[98] B. Wang, X. Xiao, and T. Chen, 'Perovskite photovoltaics: a high-efficiency newcomer to the solar cell family', *Nanoscale,* vol. 6, no. 21, pp. 12287–12297, 2014.
[99] W. Wang, M. O. Tadé, and Z. Shao, 'Research progress of perovskite materials in photocatalysis- and photovoltaics-related energy conversion and environmental treatment', *Chem. Soc. Rev*., vol. 44, no. 15, pp. 5371–5408, 2015.
[100] S. Tao et al., 'Absolute energy level positions in tin- and lead-based halide perovskites', *Nat. Commun*., vol. 10, no. 1, p. 2560, 2019.
[101] Z. Zhu et al., 'Metal halide perovskites: stability and sensing-ability', *J. Mater. Chem. C*, vol. 6, no. 38, pp. 10121–10137, 2018.
[102] T. Haeger, R. Heiderhoff, and T. Riedl, 'Thermal properties of metal-halide perovskites', *J. Mater. Chem. C*, vol.8, pp.14289-14311, 2020
[103] Q. Sun, W.-J. Yin, and S.-H. Wei, 'Searching for stable perovskite solar cell materials using materials genome techniques and high-throughput calculations', *J. Mater. Chem. C*, vol. 8, no. 35, pp. 12012–12035, 2020.
[104] G. M. Bernard et al., 'methylammonium lead chloride: A sensitive sample for an accurate NMR thermometer', *J. Magn. Reson*., vol. 283, pp. 14–21, 2017.
[105] I. E. Castelli, J. M. García-Lastra, K. S. Thygesen, and K. W. Jacobsen, 'Bandgap calculations and trends of organometal halide perovskites', *APL Mater*., vol. 2, no. 8, p. 81514, 2014.
[106] M. Ha et al., 'Phase Evolution in methylammonium Tin Halide Perovskites with Variable Temperature Solid-State Sn NMR Spectroscopy', *J. Phys. Chem. C*, vol. 124, no. 28, pp. 15015–15027, 2020.
[107] L. Peedikakkandy and P. Bhargava, 'Composition dependent optical, structural and photoluminescence characteristics of cesium tin halide perovskites', *RSC Adv*., vol. 6, no. 24, pp. 19857–19860, 2016.
[108] I. Chung et al., '$CsSnI_3$: Semiconductor or Metal? High Electrical Conductivity and Strong Near-Infrared Photoluminescence from a Single Material. High Hole Mobility and Phase-Transitions', *J. Mater. Chem. C*, vol.8,no. 3, pp. 14289-14311, 2012.
[109] A. G. Kontos et al., 'Structural Stability , Vibrational Properties , and Photoluminescence in CsSnI 3 Perovskite upon the Addition of SnF_2', *J. Am. Chem. Soc*, vol. 134, no.20, pp. 8579-8587, 2017.
[110] D. E. Scaife, P. F. Weller, and W. G. Fisher, 'Crystal preparation and properties of cesium tin(II) trihalides', *J. Solid State Chem*., vol. 9, no. 3, pp. 308–314, 1974.
[111] V. Kumar et al., 'Stoichiometry-dependent local instability in $MAPbI_3$ perovskite materials and devices', *J. Mater. Chem. A*, vol. 6, no. 46, pp. 23578–23586, 2018.
[112] A. Alberti, C. Spinella, C. Bongiorno, E. Smecca, I. Deretzis, and A. La Magna, 'degradation', *Nat. Commun.*, no.10, pp. 2196, 2019.
[113] Q. Wang et al., 'Scaling behavior of moisture-induced grain degradation in polycrystalline hybrid perovskite thin films', *Energy Environ. Sci.*, vol. 10, no. 2, pp. 516–522, 2017.
[114] K. Shoyama, W. Sato, Y. Guo, and E. Nakamura, 'Effects of water on the forward and backward conversions of lead (II) iodide to methylammonium lead perovskite', sp - 482, vl - 10, Is -1, pp. 23815–23821, 2017.
[115] N. Aristidou et al., 'Fast oxygen diffusion and iodide defects mediate oxygen-induced degradation of perovskite solar cells', *Nat. Commun*., vol. 8, SP. 15218, IS. 1, pp. 1–40, May 2017.
[116] Q. Wang et al., 'Qualifying composition dependent p and n self-doping in $CH_3NH_3PbI_3$', *Appl. Phys. Lett*., vol.105, no.16, pp.163508, 2014

3. Experimental Procedures

3.1. Synthesis of materials

The materials were synthesised using conventional solid-state synthesis using mortar and pestle along with ball milling and solution synthesis, where organic solvents were used. The precursor powders used were methylammonium iodide, CH_3NH_3I (MAI) (99%, Greatcell Solar, Elanora, Australia) and Lead Iodide, PbI_2 (99%, Sigma Aldrich, Gillingham, UK). PbI_2 and MAI were mixed in stoichiometric amounts to produce methylammonium lead iodide (MALI, $CH_3NH_3PbI_3$). The PbI_2 content was reduced to produce organic-rich compositions of formula, $CH_3NH_3Pb_{(1-x)}I_{(3-2x)}$, and the MAI content was reduced to produce PbI_2-rich compositions of formula $(CH_3NH_3)_{(1-y)}PbI_{(3-y)}$. x and y in these compositions were varied and synthesised using the three different methods described below to establish their structure-property relations and to investigate how (or if) the differing synthesis conditions affected their properties.

3.1.1. Solid-state method

The precursor powders were weighed according to their nominal composition and ground together in a mortar and pestle for 30 minutes under ambient conditions in a fume hood to produce 5g batches. The resultant mixtures were analysed using X-ray diffraction (XRD). The mixtures were then annealed (for 12 hours) at a higher temperature of 80 ˚C and ground again. The powders were characterised using XRD and repeated cycles of grinding and annealing until no changes in the XRD data were observed. Samples were then heated at 120 ˚C and XRD data subsequently collected. The process was repeated four times until no change in the XRD data was observed. This process was limited to 120 ^{o}C because above 140 ˚C there were concerns about the onset of decomposition of the organic species.

3.1.2. Ball milling method

Ball milling was used to mix the precursor powders (in order to produce a 5g batch size) in a 125 mL HDPE bottle with ethanol (filling the bottle half way, so as to cover all the precursor powder) used as a solvent, and with 25, 10.5 mm yttria-stabilised zirconia milling media beads. The ball milling time was varied between 1-12 hours to see its effect on the material. After several trials, compositions were generally milled for 6 hours; however, three different ball milling times were investigated, 1, 6 and 12 hours. Increasing the ball milling time from 1 to 6 hours produced MALI with reduced PbI_2 peaks, whereas after 12 h no change was observed. The resultant mixture of material and ethanol was then poured into a

beaker, with further washing of the bottle and milling media with ethanol to acquire all the material that had been processed. The resultant solution was placed in an 80 ̊C drying oven (placed inside a fume hood). The beaker was covered with aluminium foil which was then pierced to allow evaporation of the ethanol (this took 24 hours) and obtain the resultant MALI material. The powder was ground in a mortar and pestle and heated further at 80 ̊C for 6 hours. The resultant powders were then characterised. The powders were ground again and heated at higher temperatures and characterised again.

3.1.3. Solvent method

The solution synthesis involved mixing the precursors (to obtain ~3g of final product) with 5 mL of either dimethylformamide (DMF) or dimethylsulfoxide (DMSO) in a beaker. A magnetic stirrer was added and the top covered with aluminium foil. The beaker was placed on a hot plate and the temperature was set to 60 ̊C. It was left on the hot plate inside a fume hood for 30 minutes. Once a yellow solution was formed the top of the foil was pierced and the beaker placed in a drying oven set at 80 ̊C. The beaker was left until all the solvent had evaporated and only powder remained; this took ~48 hours. The resultant powders were then ground in a mortar and pestle and placed back in a drying oven at 80 ̊C for 6 hours. The resultant materials were characterised and the powders further annealed at higher temperatures with further characterisation.

3.2. X-ray Diffraction, XRD

X-ray diffraction (XRD) was used to identify the phase(s) present in samples as the composition was altered and under different synthesising conditions. XRD data were collected for samples measured under different annealing temperatures for all of the synthesis methods described above.

The powder was placed on a Brucker D2 sample holder and pressed with a glass slide to ensure a flat surface. This was then placed in a D2 Brucker XRD machine using copper (Cu) radiation with scans being measured between 2θ of 5-50̊, with a step size of 0.3 to check for phase purity. To obtain lattice parameters, a Stoe Cu PSD was used between 5-90̊ 2-theta with a step size of 0.1, including an internal standard of silicon being mixed with the powders. The Silicon was used to calibrate the measured peaks to obtain accurate lattice parameters with low errors. The XRD data from the Brucker D2 were analysed using Eva Diffrac software, whereas Stoe data were analysed using WinX^{pow} software (version 2.10, STOE & Cie GmbH, Germany) [1].

3.3. Scanning Electron Microscopy, SEM

Pellets of each composition was pressed to obtain an even surface and were placed on an aluminium sample holder, attached via a carbon coated sticker. The surface of the pellet was not coated. A NOVA nano SEM 450 was used to analyse the material surface, with an accelerating voltage of 1 kV and using a through lens detector (TLD). The spot size was set to 3 A.U (arbitrary units) and the sample was 4 mm away from the lens.

When using conventional SEM with a high voltage between 15-20 kV decomposition of the perovskite material was apparent. The problem with imaging MALI perovskite is that in both thin film devices and bulk powders there are observed amorphous impurities, and nanoscale phase segregation and that within grain-to-grain analysis, stoichiometry can vary [2]. To be able to detect such variations other groups have implemented the use of fast hyperspectral imaging techniques based on secondary electrons in low voltage SEM [3]. This is where conventional imaging is used together with spectroscopy for both spatial and spectral information. Energy Dispersive X-ray (EDX) analysis is also limited due to its spatial resolution and is not suitable in environments where the beam energy is as low as 1 kV as the characteristic X-rays are not excited.

From these studies it was observed that when there is an excess of MAI or PbI_2 in the samples there is an observed difference in contrast. For example, an excess MAI composition appears to have regions that are darker than the rest of the pellet surface. This was determined by secondary electron hyperspectral Imagining (SEHI), when SEM was carried out at low voltage using a TLD. The main peak for secondary electron emission spectra for stoichiometric and excess-MAI MALI overlap, there are also additional peaks (in the organic-rich composition) which are absent in stoichiometric and excess PbI_2 compositions. Therefore, they must be due to excess MAI/MAI-rich perovskite. MAI regions appear dark when images are collected in the energy window of 10 eV, so MAI-rich regions emit low energy secondary electrons that can't be detected selectively in standard SEM. Pellets with excess PbI_2 showed energy spectra that matched with stoichiometric MALI peaks and also contained additional peaks which corresponded to PbI_2 peaks. In these compositions, the PbI_2 regions appear light compared to the darker contrast of the MALI perovskite phase.

3.4. Inductance-Capacitance-Resistance (LCR) Meter

The pellet sides were wrapped with tape and placed in a sputter coater to electrode samples. Au was sputtered onto the two major surfaces of the pellets. The tape was then removed and the pellet placed inside an alumina jig which was then placed inside a tube

furnace, making sure the pellet was placed in the centre of the furnace. The LCR results were then measured using a Hewlett Packard 4284A Precision LCR meter (Hewlett-Packard GmbH, Böblingen, Germany) and by programming the furnace to the required temperature with a set heating and cooling ramp rate of 1 ^{o}C/min. Measurements of capacitance and dielectric loss (tan δ) were taken at set frequencies of 1, 10, 100 and 250 kHz and 1 MHz.

The relative permittivity (ε_r) of the material was extracted from capacitance data by dividing the measured capacitance (C') by the permittivity of free space (ε_0) and then applying a geometric factor for the normalised shape of the pellet.

The geometric factor was calculated by treating the pellet as a perfect cylinder, with a thickness, t and radius r. The geometric factor was calculated using the equation 3.1.

$$G_f = \frac{t}{\pi r^2} \qquad \text{Equation: 3.1}$$

ε_r could therefore be calculated by the equation 3.2.

$$\varepsilon_r = \frac{C'}{\varepsilon_0} \cdot \frac{t}{\pi r^2} \qquad \text{Equation: 3.2}$$

3.5. Impedance Spectroscopy (IS)

3.5.1. Methodology

Impedance spectroscopy (IS) is an electrical characterisation technique used to determine the electrical properties of various materials and devices. IS applies an ac voltage being across a frequency range from 10^{-2} - $1x10^{6}$ Hz. It can be used to separate different electro-active responses in a material. These can be the bulk (this is the response of the material itself, i.e. individual grains in a polycrystalline material), grain boundaries, electrode-sample interfaces etc.

The measured response being available only in the frequency range mentioned previously, temperature can be used as a variable, either by heating or cooling the sample to be able to observe all the various responses that might be present in a material. Other experimental variables include, oxygen partial pressure, changing the electrode material and/or applying a DC bias.

The reason for applying an ac voltage and measuring the impedance of a sample is because measuring the dc voltage response, where the frequency is 0 Hz gives only the total

resistance of the sample. The total resistance of the sample however could be dominated by many different regions of the sample microstructure and/or electrode contact resistance. impedance being the ac analogue of resistance has the ability to provide a more in-depth picture of the electrical behaviour of a sample. The applied voltage is low, typically 100 mV. This is to ensure the measurement is in the linear I-V (ohmic) regime, since the sample can also be affected by the magnitude of the applied voltage.

Samples were prepared with electrodes in the same way as described in the LCR section. They were then placed in a jig, inside a tube furnace. An Agilent E4980A Precision LCR Meter (Agilent Technology, California, USA) was used with a frequency range of 20 Hz to 1 MHz. For lower frequency measurements, a Solartron SI 1260 impedance analyser (Solartron Group Ltd, Farnborough, Hampshire, UK) with a frequency range of 0.01 Hz to 1 MHz was used and after data collection the geometric factor, G_f was applied. The measured impedance data were also jig corrected. This is where the resistance and capacitance contributions from the jig (cables) are subtracted from the sample response. This is carried out by measuring closed and open circuit measurements. In a closed circuit measurement, the sample is short circuited with the two jig electrodes made from platinum being in contact, and the impedance response measured. Due to the low resistance of when the two electrodes are in contact, a large current passes through the cables and the response is dominated by resistive and inductive elements. The open circuit measurement is when the two platinum electrodes of the jig are separated and a measurement of the air gap is taken. The high resistance of the air gap causes little current to pass through the cables, so the resistive and inductive components are negligible. The response is therefore dominated by the empty jig capacitance. The closed and open measurement values are then subtracted from the sample response using an excel spreadsheet, leaving only the sample response. Data were analysed using Zview (Scribner Associates, USA) [4].

3.5.2. Background, theory and analysis of IS data

IS is a widely used technique in characterising electroceramics due to its ability to establish an electrical microstructure. Electroceramics are produced in various forms and can be electrically homogenous or heterogeneous, often depending on the method of fabrication. In homogenous materials the electrical properties are dominated by the bulk material even if grain boundaries are physically present, however, sample-electrode effects may also be present in the IS response. Ideally, the bulk electrical response in the ceramic should be close

to that of a corresponding single crystal. In such cases, composition-structure-property relations can be studied using ceramics without the need for preparing single crystals.

An example of a heterogeneous material is where the electrical properties can be controlled by core-shell microstructures, grain boundaries or surface layers. In this case, low levels of dopants/impurities can have a significant effect on the electrical properties of ceramics. For example, core-shell structures, as in the case of $BaTiO_3$-based capacitors, can produce desirable electrical properties [5]. Generally, IS can be easily carried out, however the interpretation of the results can be challenging since it requires prior knowledge about the material being investigated. Furthermore, precautions must be taken about the quality of the sample, such as the density, electrode-material interactions and temperature range at which the sample can and should be investigated.

During IS measurements when a sinusoidal voltage is applied, the current sinusoid may not have its maximum value (I_{max}) at the same time (t) as the voltage maximum (V_{max}). This creates a phase difference, θ between the measured current and the applied voltage. This is expressed in equations 3.3 and 3.4 respectively.

$$V_t = V_{max} sin(\omega t) \qquad \text{Equation: 3.3}$$

$$I_t = I_{max} sin(\omega t + \theta) \qquad \text{Equation: 3.4}$$

where ω is the angular frequency in rad/s and is expressed as:

$$\omega = 2\pi f \qquad \text{Equation: 3.5}$$

and f is the frequency in Hz.

Using the ac equivalent of Ohms law, gives the impedance, Z^* as:

$$Z^* = \frac{V_t}{I_t} = \frac{V_{max} sin(\omega t)}{I_{max} sin(\omega t + \theta)} \qquad \text{Equation: 3.6}$$

For a pure resistor, there is no phase difference between the voltage and current, since they both achieve their maximum, minimum and zero values at the same time. This simplifies the above equation 3.6 as follows:

$$Z^* = \frac{V_t}{I_t} = \frac{V_{max} sin(\omega t)}{I_{max} sin(\omega t + 0)} = \frac{V_{max} sin(\omega t)}{I_{max} sin(\omega t)} = \frac{V_{max}}{I_{max}} = R \qquad \text{Equation: 3.7}$$

As impedance is a complex number it can be defined as:

$$Z^* = Z' - jZ''$$

The impedance of an ideal resistor is:

$Z_R^* = R - j(0)$ Equation: 3.8

where Z' is the real component, Z" is the imaginary component and j is the imaginary number $\sqrt{-1}$. This equation 3.8 shows an ideal resistor has only a real component, R with no imaginary component.

Complex numbers are used because to mathematically represent any sinusoidal behaviour a real number is not enough, therefore complex numbers are introduced which have a real number plane and an imaginary plane giving rise to four quadrants as shown in Fig: 3.1A. The j operator, when multiplied by itself (j^2) gives the real number -1, J^3 gives -j and j^4 gives the real number 1. This allows an anticlockwise rotation to be represented in the two dimensional imaginary axis. The reason why the imaginary part of the impedance is defined as -jZ" is so that the data are represented in the top right hand quadrant of the complex number plane.

Capacitors store energy between two conductive plates in the form of electrical charge. The electrical charge is built up due to an applied voltage, the charge between the plates is maintained as long as a voltage is present. For an ac voltage however, there is constant charging and discharging dependent on the frequency. The current meanwhile is opposed to the voltage at a rate of change of charge stored onto the plates. In a capacitor the current leads the voltage by 90 degrees.

This is expressed as:

$I_t = C\left(\frac{dV(t)}{dt}\right)$ Equation: 3.9

substituting V(t) into the equation above and solving for I(t), gives the impedance as:

$$Z^* = V_t/I_t = 1/j\omega C$$

Giving the impedance of a pure capacitor as:

$Z_C^* = 0 - j\frac{1}{\omega C}$ Equation: 3.10

The impedance of an ideal capacitor has only an imaginary component, as shown in equation 3.10, which is inversely proportional to the capacitance, C and frequency, f.

$$Z_C^* = -\frac{j}{2\pi f C}$$

The impedance of an inductor is obtained from the equation 3.11.

$V_t = L\left(\frac{dI(t)}{dt}\right)$ Equation: 3.11

Since an inductor induces a voltage when a sinusoidal current pass through it. Solving the above equation, gives the impedance of the inductor as expressed in equation 3.12.

$Z_L^* = j\omega L$ Equation: 3.12

$$Z_L^* = j2\pi f L$$

Therefore, for an inductor the impedance increases with increasing frequency. In an ideal inductor, current lags voltage by 90 degrees. Fig: 3.1A shows how an impedance measurement can be represented as a vector |Z| on a Nyquist plot for a single frequency, when the response is deconvoluted into the individual impedance contributions from R, C and L elements. Fig: 3.1B shows how each component impedance varies with frequency starting from the low frequency region (where impedance is dominated by resistive components) to the higher frequency ac response (where capacitive elements are more dominant). Fig: 3.1A and B show that R of a resistor is independent of frequency with current and voltage being in-phase. So measurements of impedance for a pure resistor are always on the real axis. Resistive elements are more predominant in conductors, since they deal with long range migration of charge carriers via electrons and/or ions, therefore charge is transferred in an inelastic process.

The impedance of an ideal capacitor decreases with increasing frequency and the current leads the voltage by 90°, therefore data are always on the imaginary axis. Capacitors become more leaky with increasing frequency, since their impedance decreases. The physical origins of the capacitive element are related to the polarisation mechanism(s) present in a sample. Polarisability is the extent to which the positive/negative nuclei are displaced relative to the surrounding negative/positive charge when an electrical field is applied. There are four different polarisability mechanisms, electronic, ionic, dipole reorientation and space charge [5]. Capacitive elements represent elastic processes and tend to be more dominant in insulators, where the charge is recoverable.

The impedance of an inductor increases with frequency. Inductors become more resistive with increasing frequency and also have a response only on the imaginary axis. Inductor elements deal with storage of energy in magnetic fields generated by high current.

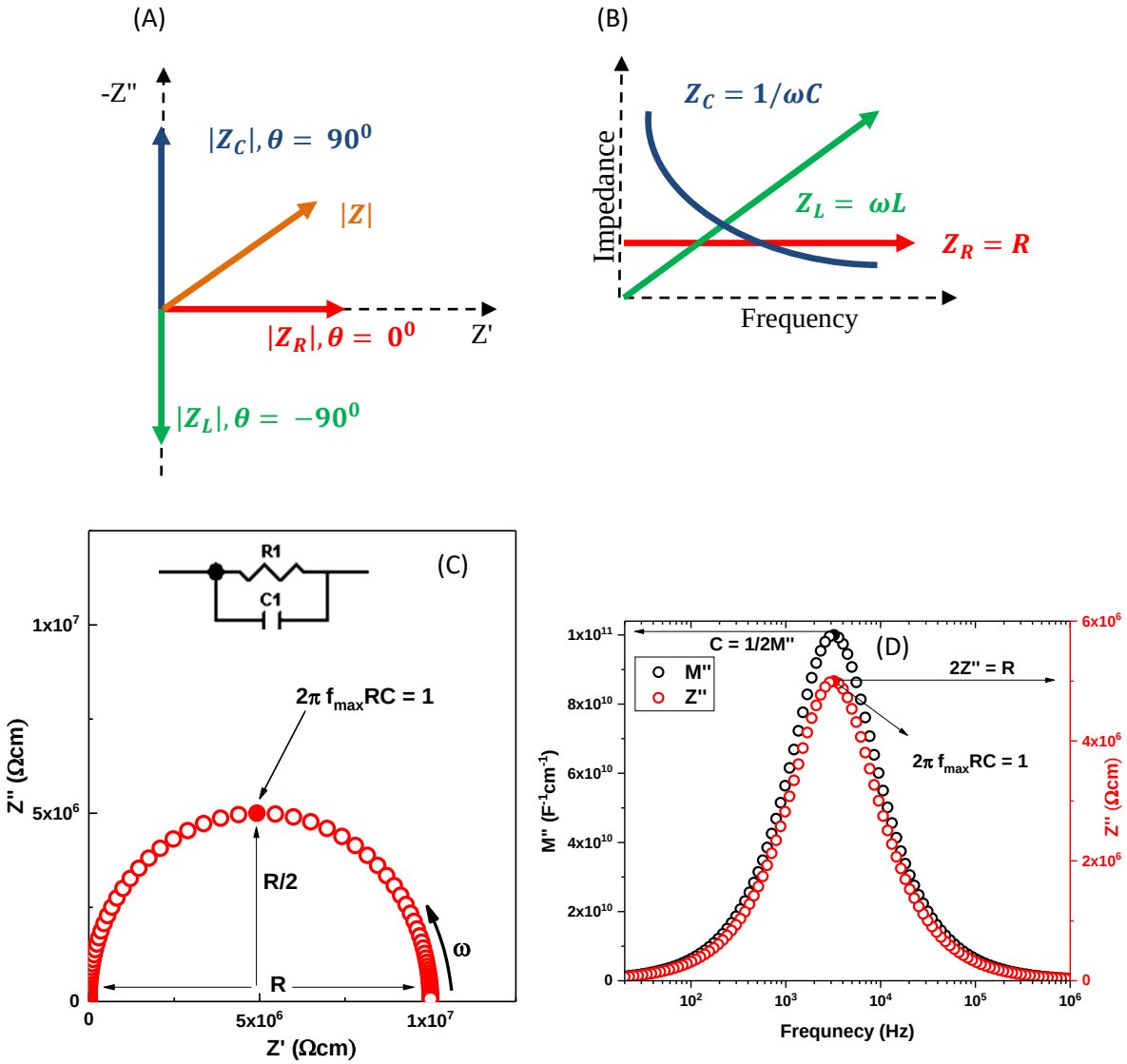

Figure 3.1. Plot(A) shows how each individual element of impedance can be represented as a vector when deconvoluted. Plot(B) shows the impedance response of single R, C and L elements along the frequency domain. Plot(C) shows the Z^* plot where the real part of impedance is plotted against the imaginary part for a parallel RC element. Plot(D) shows the M'', Z'' spectroscopic plot for a parallel RC element.

Impedance in most materials can be modelled by combining R and C elements in parallel to each other (inset of Fig: 3.1C). The parallel RC element will have an overall impedance response made up of its individual resistance and capacitance components. The different components (bulk, grain boundaries, secondary phases) within a materials microstructure will have individual R and C values. These can be separated by having their own unique time constant (τ) with a unit of seconds. This allows an electrical microstructure to be constructed which can be different to the physical microstructure.

To find the total impedance of the circuit shown in Fig: 3.1C, is as follows.

$$Z_R^* = R,\ Z_C^* = j\frac{1}{\omega C}$$

Adding impedance in parallel $Z(\text{total}) = \frac{1}{Z_R} + \frac{1}{Z_C} = \frac{1}{R} + 1/j\frac{1}{\omega C}$

Simplifying and separating the real and imaginary component gives:

$$Z' = \frac{R}{1 + (\omega RC)^2}$$

$$Z'' = R \cdot \frac{(\omega RC)}{1 + (\omega RC)^2}$$

At low frequencies, the real part has a limit towards R, with no imaginary component. At high frequency, the real part converges towards 0 and the imaginary component also tends towards 0, as seen from fig: 3.1C.

The imaginary part Z'', contains the Debye function, and at the Debye frequency, where $\omega\tau = 1$, the voltage applied is equal to the maximum voltage and where the dielectric relaxation occurs indicated by a peak shown in fig: 3.1D. This denotes the maximum loss frequency, also known as the Debye frequency.

The time constant (τ) is given by the following equation.

$\tau = RC$ Equation: 3.13

Therefore, substituting terms in equation 3.13 gives:

$$\frac{1}{\tau} = RC = \omega_{max}$$

$$f_{max} = \frac{1}{2\pi RC}$$

At the Debye frequency, the imaginary component reduces to R/2, therefore the resistance can either be estimated by the x intercept from fig: 3.1C or from the Z''_{max} peak.

Since:

$$2 \cdot Z''_{max} = R$$

The frequency maximum is geometry independent and is related to the permittivity of the material via the capacitance value, and its conductivity via the resistance, R.

The impedance data can be analysed in four different formalisms; these are impedance (Z^*), admittance (Y^*), electric modulus (M^*) and permittivity (ε^*). impedance data are collected in ZView in the impedance formalism, Z but can be converted to the other formalisms. impedance was already defined previously as

$$Z^* = Z' - jZ''$$

Admittance is the inverse of impedance, therefore defined as

$$Y^* = \frac{1}{Z^*} \qquad \text{Equation: 3.14}$$

$$= \frac{1}{Z' - jZ''} = Y' + jY''$$

The electric modulus is defined as follows

$$M^* = j\omega C_0 Z^* \qquad \text{Equation: 3.15}$$

$$\frac{M^*}{C_0} = M' + jM''$$

$$\frac{M^*}{C_0} = j\omega Z^* = j\omega \cdot \left[\frac{R}{1 + (\omega RC)^2} + R \cdot \frac{(\omega RC)}{1 + (\omega RC)^2}\right]$$

where C_0 is the capacitance of cell in a vacuum.

$$C_0 = \frac{\varepsilon_0}{G_f} \qquad \text{Equation: 3.16}$$

simplifying gives the real and imaginary component as:

$$M' = \frac{1}{C}\frac{\omega^2 R^2 C^2}{1 + (\omega RC)^2}, \qquad M'' = \frac{1}{C}\frac{\omega RC}{1 + (\omega RC)^2}$$

The M" contains the Debye functions and when at the Debye frequency, $\omega RC = 1$

$$M''_{max} = \frac{1}{2C}$$

The permittivity (ε^*) is defined as

$$\varepsilon^* C_0 = \frac{1}{M^*} = \varepsilon' - j\varepsilon''$$

The different formalisms show dominant responses from either resistive or capacitive elements. Z^* is dominated by large resistances, while the admittance Y^* being the inverse of impedance is dominated by small resistances. The M^* and ε^* formalisms are used to examine capacitances, where ε^* is dominated by large capacitances, M^* is dominated by small capacitance values. This is the main reason the M" peak is used to extract conductivity values for the bulk, since the bulk component generally has the lowest capacitance values due to high volume fraction present in a ceramic sample. Although the different formalisms are related mathematically, it is best practice to observe data in multiple formalisms due to their dependence on frequency [6]. Analysing the data in these four formalisms can assist in choosing an appropriate equivalent circuit for data analysis.

Conductivity is defined as:

$$\sigma = \frac{1}{R}$$ Equation: 3.17

where R has been corrected for sample geometry. Therefore, when the resistance for a particular response is estimated from the impedance data the conductivity can be calculated. The impedance response when measured as a variable of temperature will change the resistance of the sample, not only the overall resistance but the individual electro-active components resistance (if they are able to be distinguished). The R values can be estimated from the M''_{max}, Z''_{max} equations stated above, or the Z' real-axis intercept on the Z^* plot. Using the Debye frequency equation can also give the associated capacitance value, therefore a capacitance vs. temperature plot can also be constructed.

When the conductivity is plotted against inverse temperature, T, then using the Arrhenius relationship, the activation energy of a conduction process can be calculated from the gradient of the log(σ) vs. 1/T graph, as shown by the following algebraic manipulation:

$$k = Ae^{-\frac{E_a}{k_b T}}$$ Equation: 3.18

$$\sigma = \sigma_0 e^{-\frac{E_a}{k_b T}}$$

$$\log(\sigma) = \log(\sigma_0) + \log(e^{-\frac{E_a}{k_b T}})$$

$$\log(\sigma) = \log(\sigma_0) - \frac{E_a}{k_b T}\log(\mathrm{e})$$

$$\log(\sigma) = \log(\sigma_0) - \frac{1}{T}\frac{E_a}{k_b}\log(\mathrm{e})$$

equating to:

$$y = c + mx \qquad \text{Equation: 3.19}$$

$$\frac{E_a}{k_b}\log(\mathrm{e}) = \text{gradient}$$

$$E_a = \frac{gradient\ x\ k_b}{\log(\mathrm{e})}$$

$$\log(\mathrm{e}) = constant$$

$$k_b = 8.617x10^{-5}\ eVK^{-1}$$

$$E_a = 1.984x10^{-4}\ x\ \ gradient\ (eV) \qquad \text{Equation: 3.20}$$

The circuit shown in the inset of Fig: 3.1C, would be for an electrically homogenous material, ideally an electronically conducting single crystal with non-blocking electrodes. However, most materials do not behave electrically in a way to be described by such a circuit. A material response might also appear as a single electrical response; however, it might be two or more responses with similar time constants, as shown in Fig: 3.2. If the time constants are similar to each other, the arcs in the Z^* plot can merge towards each other and may also become depressed. This is where equivalent circuit fitting is used as a tool to separate out the different processes. It must be kept in mind however that an equivalent circuit can be fitted to any data, therefore the processes must be related back to some physical phenomenon/a occurring in the sample.

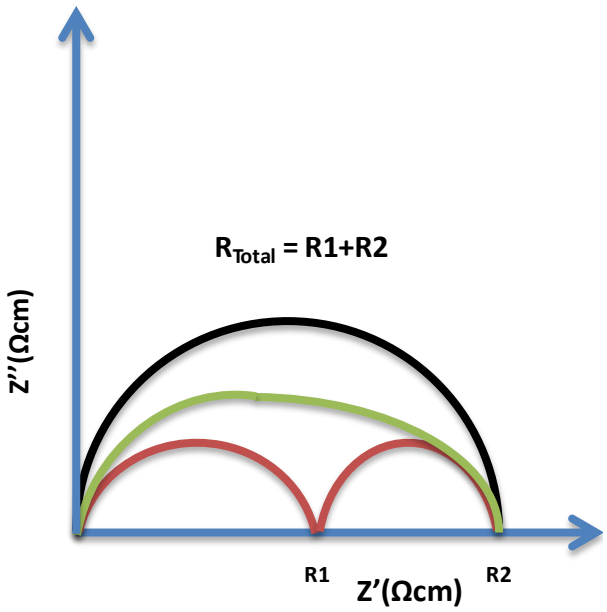

Figure 3.2. Diagram shows how the Z^* plot appears when the time constants of two RC elements become similar to each other. Plot in red shows two responses that are well separated. Green shows the response when the time constants become close to each other but the separation could be specified visually. The black line shows either one response or two responses where the time constants are nearly identical to each other.

For an IS response such as that shown by the red or green line in Fig: 3.2, where either or at least two responses are observed, a single RC circuit can't be used to model such a response. The next step may therefore be to use to multiple parallel RC elements in series as shown in Fig: 3.3A. If the time constants of the two elements are separated out adequately, a response as shown in Fig: 3.3B is observed, where R2 > R1, and C2 > C1.

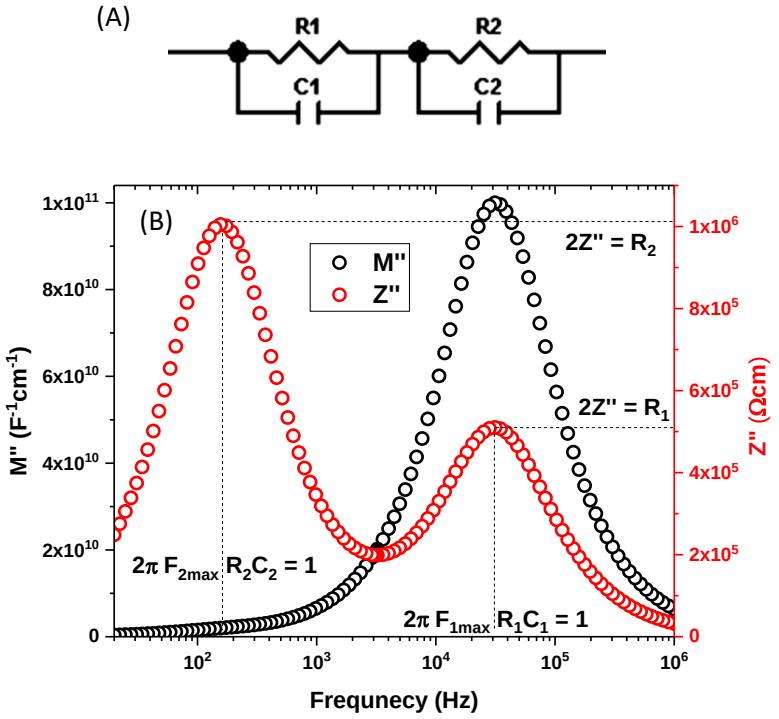

Figure 3.3. (A) Diagram of two parallel RC elements connected in series. (B) M'' and Z'' spectroscopic plots for two parallel RC elements connected in series.

Since the overall impedance is given as:

$$Z^* = \frac{R - j\omega R^2 C^2}{(1 + \omega RC)^2}$$

Then the impedance of the two parallel RC elements connected in series is given as the following:

$$Z^* = \frac{R_1 - j\omega R_1^2 C_1^2}{(1 + \omega R_1 C_1)^2} + \frac{R_2 - j\omega R_2^2 C_2^2}{(1 + \omega R_2 C_2)^2}$$

Considering the real part, Z' at low frequency, where the limit converges to 0, Z' = R1 + R2. whereas at high frequency where frequency converges towards infinity, Z' = 0. When R2 and C2 are both larger than R1 and C1, respectively then the Debye frequency of the second element will occur at a lower frequency. The imaginary part, Z'' is given as:

$$Z^* = R_1 \cdot \frac{\omega R_1 C_1}{(1 + \omega R_1 C_1)^2} + R_2 \cdot \frac{\omega R_2 C_2}{(1 + \omega R_2 C_2)^2}$$

Giving two Debye functions, and when the frequency matches to F_{1max} and F_{2max}, peaks occur at $R_1/2$ and $R_2/2$, the peaks are only distinctly separated if the time constants are sufficiently

different. Considering the M^* formalism, the two parallel RC element circuit gives the equation:

$$M^* = \frac{1}{C_1} \cdot \frac{\omega^2 R^2{}_1 C^2{}_1 + j\omega R_1 C_1}{(1+\omega R_1 C_1)^2} + \frac{1}{C_2} \cdot \frac{\omega^2 R^2{}_2 C^2{}_2 + j\omega R_2 C_2}{(1+\omega R_2 C_2)^2}$$

The real part, M' at low frequency converges to 0, while at high frequency, M' has a value of $\frac{1}{C_1} + \frac{1}{C_2}$. The imaginary part is expressed as:

$$M^* = \frac{1}{C_1} \cdot \frac{\omega R_1 C_1}{(1+\omega R_1 C_1)^2} + \frac{1}{C_2} \cdot \frac{\omega R_2 C_2}{(1+\omega R_2 C_2)^2} \qquad \text{Equation: 3.21}$$

At their relative Debye frequencies, the peaks occur at $\frac{1}{2C_1}$ and $\frac{1}{2C_1}$, respectively. In this way the two RC element circuit and its M" and Z" responses can be used to estimate the R and C values of both components in a sample, if the RC elements are connected in series. It must be stressed that equivalent circuits based on other connections of parallel RC elements can also give rise to similar responses in IS data and proving a unique equivalent circuit remains a challenge in many cases. Nevertheless, this series type equivalent circuit is commonly used in the study of electroceramics.

A material response also varies with frequency. Therefore, for a non-ideal response, where the Z* plot seems depressed, the M" and Z" relaxation peak are misaligned, or there is a rise in the Y' spectroscopic plot at high frequency (as shown in Fig: 3.4). Such frequency dependent behaviour can be modelled by a constant phase element (CPE). The CPE's impedance is defined as:

$$Z^*{}_{CPE} = [A(j\omega)^n]^{-1} \qquad \text{Equation: 3.22}$$

A and n are frequency independent parameters that could either change with temperature or stay constant depending on the materials response. n is the gradient of the slope of the high frequency dispersion in the Y' plot, whereas A is the intercept on the y-axis. The value of n ranges from 0 to 1, where n = 0 for the CPE simplifies to an ideal resistor whereas for n = 1, it simplifies to an ideal capacitor.

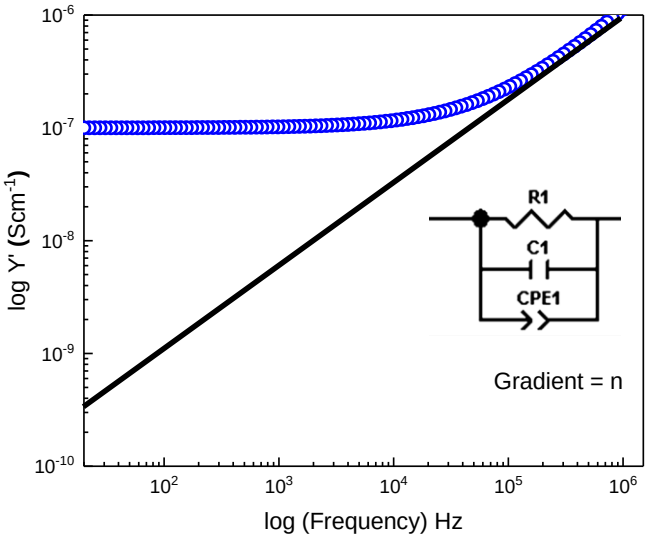

Figure 3.4. Y' spectroscopic plot with a high frequency dispersion, which needs a CPE in the RC circuit for the data to be fitted.

ZView was used with its data fitting method. This is where the experimental data for a sample at a specific temperature is selected and an equivalent circuit model based on the sample behaviour is chosen. Some hand fitting estimated R and C values are inserted as starting values. If a CPE is used then a value for A and n is inserted and through a complex non-linear least squares fit the R, C, A and n values can be optimised. Repeating the process for the variable being altered, such as temperature, the electrical parameters across the temperature range can be obtained. When circuit fitting, it is best practice to utilise the different formalisms obtained via IS, since a circuit might fit well for a Z^* plot, but not very well in Y^* or ε^*. Another factor that needs to be taken into account when fitting is frequency, since a real material response is not constant within the measured frequency domain. So the equivalent circuit data must fit the real and imaginary components over the entire frequency range. The general method followed in this work is to look at log(M''/Z'') vs. log (frequency), log(C') vs. log(frequency), log(Y^*) vs. log(frequency) and the Z^* plot. The reason log-log plots are inspected is that the fitted data can be easily compared to the experimental data and where the two diverge can be easily pinpointed.

Once an equivalent circuit is selected, the experimental data are fitted over the measured temperature range. The R and C values can be extracted from the fitted data and Arrhenius conductivity plots and capacitance vs. temperature plots can be constructed for each specific R and C element in the circuit and the trends with temperature investigated.

In summary, IS is a powerful technique and can be used to investigate the frequency dependent electrical microstructure of electroceramics. AC frequency is used because it provides more information than DC, or a response at a single (fixed) frequency. Temperature

is used to obtain activation energies of various conduction processes and to access time constants that are out of the measured frequency window (due to material either being too resistive or conductive) at room temperature.

References

[1] https://www.stoe.com/product/software-powder-xrd/

[2] A. Alberti, C. Spinella, C. Bongiorno, E. Smecca, I. Deretzis, and A. La Magna, 'degradation', *Nat. Commun.*, no. 10, article number. 2196, 2019.

[3] V. Kumar *et al.*, 'Stoichiometry-dependent local instability in $MAPbI_3$ perovskite materials and devices', *J. Mater. Chem. A*, vol. 6, no. 46, pp. 23578–23586, 2018.

[4] https://www.scribner.com/software/68-general-electrochemistr376-zview-for-windows/

[5] A. R. West, *Solid State Chemistry and its Applications, 2nd Edition, Student Edition*. *Wiley and Sons*, 2014.

[6] J. T. S. Irvine, D. C. Sinclair, and A. R. West, 'Electroceramics : Characterization by impedance Spectroscopy', *Adv. Mater.*, vol. 2, no. 3, pp. 132–138, 1990.

4. Introduction and Aims

Methylammonium lead iodide (MALI) is a hybrid perovskite compound used as a photovoltaic material in solar cells. It is an attractive photovoltaic material due to its large range of light absorption, it has a low electron-hole recombination mechanism, its bandgap alteration is easy compared with silicon and its manufacturing is cheap and easy. There are, however, significant challenges. Firstly, it contains lead which is a toxic element and there is a general impetus to reduce such toxic elements in devices. Secondly, MALI is unstable in conditions where there is moisture present along with oxygen and UV radiation which causes the organic group to degrade and reduces the efficiency of the solar cell. The initial aim of this project was based on preparing MALI by different processing routes as this can influence the phase assemblage and resulting properties of the materials. The work is conducted on bulk ceramics rather than thin film devices. Although thin film devices are more useful to test performance they are more challenging to investigate the fundamental properties of MALI. On this basis, and due to the lack of literature on the bulk properties of MALI this study was undertaken.

4.1. Executive Summary of Chapter 4.

This chapter summarises the synthesis and characterisation for a range of $CH_3NH_3Pb_{(1-x)}I_{(3-2x)}$ (MALI) compositions (x = 0.00 to 0.50) using a solid state reaction. The precursor powders were mixed together in a mortar and pestle and heated at various temperatures (up to 140 ^{o}C). This provided both a solventless procedure and allowed phase analysis to be conducted from room temperature. The reaction mechanism involved is described in section 4.1. The formation of MALI requires little initial energy because some MALI is formed at room temperature, however all samples also contain the precursor phases. These steadily reduce in content when annealing the powders at higher temperatures, however heating above 140 ^{o}C initiates the process of decomposition of the organic content. All samples in this series were shown to have reached thermodynamic equilibrium at 120 ̊C by XRD. At this temperature, x = 0.00 has both MALI and PbI_2 phases present. With increasing x, 0.05 and 0.10 have clean XRD patterns and appear single-phase, however samples with x > 0.10 have MALI and crystallised MAI in their XRD patterns.

SEM data showed that the different phases could be distinguished due to differences in their back scattering contrast and that SEM was more sensitive for phase analysis compared to XRD. MAI-organic rich phase(s) appear as dark-black regions, PbI_2 appears as

light-white regions and the perovskite phase appears as gray. SEM results for x = 0.05 and 0.10 revealed the samples to contain a MAI organic-rich phase that was not detected by XRD and therefore no samples in this series were single-phase. It is unclear whether these MAI organic-rich regions are crystalline (but of low volume fraction and therefore not detected by XRD) or are amorphous in x = 0.05 and 0.10. There was no systematic trend in lattice parameters across this series suggesting no appreciable level of solid solution based on this synthetic procedure.

LCR and IS results showed all powders are susceptible to intake of moisture which occurs both during sample processing and when stored. This was most concisely shown by the hysteresis behaviour in data during an initial heating and cooling cycle. Hysteresis was easily observed in permittivity and dielectric loss versus temperature scans using LCR data and via conductivity data from IS via an Arrhenius-type relationship. Cycling experiments showed that once the moisture is removed during the first heating cycle, it can take 1-2 weeks of storing samples in a lab environment before similar hysteresis effects can be reproduced in LCR measurements. Initial heating LCR permittivity results showed that the moisture loss mostly occurred at around 90 ℃ and was complete by ~ 100 ^{o}C and interestingly there was a peak in permittivity at 60 ℃ (for x = 0.10 to 0.30) associated with the tetragonal (β) to cubic (α) MALI phase transition. IS results showed that increasing the value of x slightly above 0.00, i.e. for x = 0.05 and 0.10 the conductivity of the samples increased slightly on both heating and cooling cycles. These higher x samples, which are MAI-rich also showed higher dielectric losses and increases in permittivity at higher temperatures. To avoid issues associated with proton conduction, IS data are most reliable for analysis based on cooling cycle data; however, even then some increases in conductivity (presumably due to water uptake) are possible below ~ 60 ^{o}C in the cooling cycle.

Correlating the physical and electrical microstructures of this series (after the removal of moisture) remains a challenge. The physical microstructure, as determined by XRD and SEM results supports a main phase of MALI but depending on the value of x, could either have some excess PbI_2 (x = 0.00) or MAI-rich phases (x > 0.00), whereby the latter could be amorphous or poorly crystalline for x ~ 0.05 - 0.10 but is well crystallised for x > 0.10. The IS results showed clear signs of electrical heterogeneity in this series of samples with enhanced conductivity apparent for x = 0.05 and 0.10. To determine the electrical microstructure, equivalent circuit fitting was carried out. For all samples, the circuit fitting results showed a series circuit based on a parallel R-C-CPE element connected with a parallel

RC element provided a better model than a single, parallel R-C-CPE circuit. The R-C-CPE element was attributed to the response of MALI but the origins of the additional RC element remain unknown and could be consistent with the existence of an α' MALI phase, organic-rich regions and/or the development of a core-shell type microstructure.

4.2. Solid state reaction mechanism

The formation of MALI varies greatly with the preparation method. Both its physical and chemical properties can be significantly altered, whether it's the homogeneity, crystallinity, phase purity, morphology, surface area or grain size [1]. The solid state method, whether it's by mortar and pestle or by ball milling should provide similar powders provided they are well mixed and similar (or no) solvents are used.

Some groups have synthesised MALI using ball milling with and without solvent. Those who haven't used a solvent have generally synthesised MALI in a glove box with a single large milling media rather than many smaller ones. Stoumpos et al [2] was the first to synthesis MALI in a mortar and pestle with heat treatment and compared the results to a solution-based method. Their solution-based MALI was prepared by adding a reducing agent based on a mixture of HI/H_3PO_2 solution to suppress oxidation. This occurs during exposure of MALI solution to air, which oxidises $(I^3)^-$ to I^-. Visually this is seen by a dark red colour forming on the surface of the bright yellow powder, when it is exposed to air. When treated with HI/H_3PO_2 no oxidation product is present (so no dark red colour) during precipitation and when heat treated, it turns into the black photovoltaic phase. Stoumpos et al [2] showed the solid-state material was stable for months although the surface (as opposed to the bulk) was affected by humidity after a few weeks. Prochowicz et al [1] synthesised MALI using ball milling producing highly crystalline MALI with no detectable precursors of MAI or PbI_2. Their synthesis method consisted of mixing the precursors in an agate jar with one 10 mm agate ball and milling for 30 minutes. Manukyan et al [3] also conducted solventless ball milling synthesis and showed the gradual change of colour from a white/yellow mixture to black with the formation of MALI confirmed by XRD.

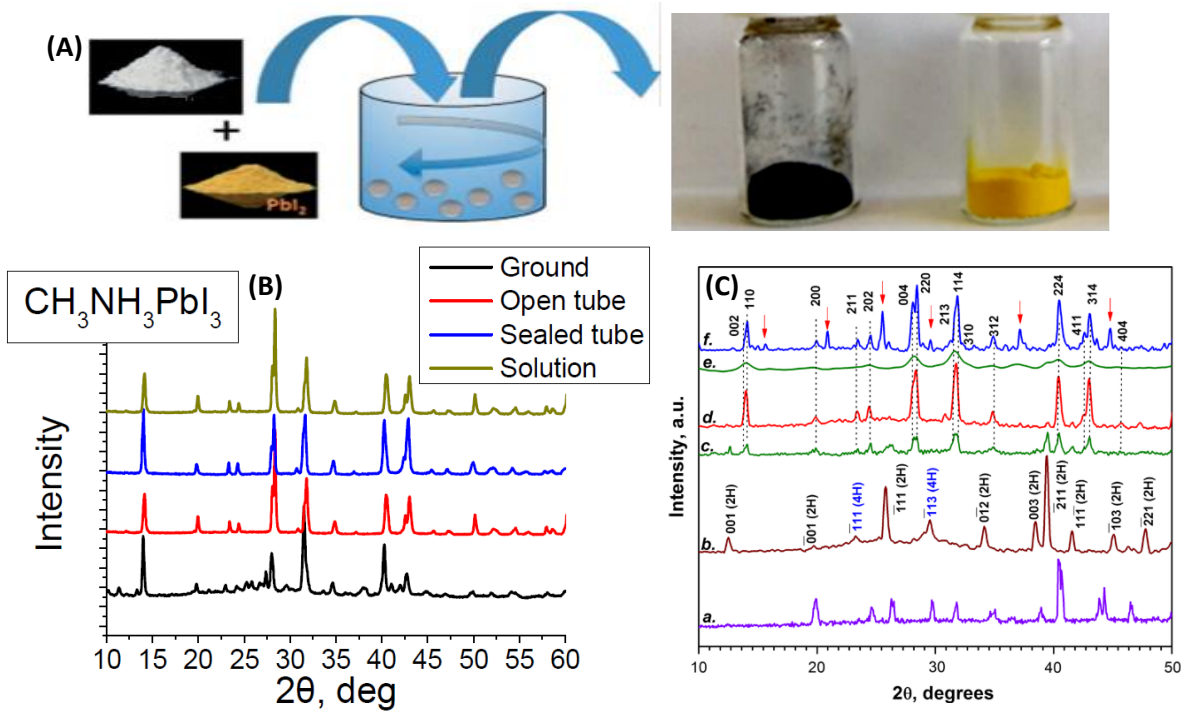

Figure 4.1. (A) shows yellow MALI not fully reacted and Black MALI which is the photovoltaic fully reacted MALI. (B) compares the ground MALI synthesised in a mortar and pestle with solution prepared MALI. (C) shows XRD of the precursors MAI (a), PbI_2 (b), MALI prepared by ball milling after 10 min (c) and 45 min (d) and compared to a solution synthesised MALI (f). Figures reproduced from [2]–[4] **respectively.**

Fig: 4.1A (right hand side) shows the black phase-pure MALI and the not fully reacted MALI which appears yellow due to PbI_2. XRD data from Stoumpos et al [2] shows the ground MALI synthesised by mortar and pestle along with solution-processed MALI, Fig: 4.1B. The MALI synthesised by mortar and pestle forms mainly the perovskite phase but with a significant amount of unreacted precursors and other unidentified phases, Fig: 4.1B. XRD data from Manukyan et al [3] in Fig: 4.1C show that as the precursor was milled for a longer time more of the perovskite formed. However, some precursor peaks remain present along with unindexed/not-assigned low angle peaks. These results showed that MALI can be formed by a solventless solid state route although the products aren't phase pure. Precursor phases are present and there are also extra unidentified peaks associated with additional phases(s). The solvent method produced a phase pure material and also reduced oxidation of the material during synthesis, Fig: 4.1B.

There are two mechanism pathways suggested for the mechanosynthesis although both can occur simultaneously depending on the preparation circumstances. Firstly, temporary structures are formed when mechanical mixing of precursors occurs and these temporary structures depend on the mechanical properties of MAI and PbI_2. In the first pathway, a reaction starts in a particular area when a collision occurs between the precursors

and milling media and the localised temperature increases [3]. This is typical for an exothermic reaction during product formation. The second pathway includes a gradual formation of the product by diffusion of reactants through a mobile amorphous solid phase. The microstructural transformation indicates that MAI is plastically deformed due to shearing which leads to cracking and rupture in this ductile phase and produces reactive dislocations. The brittle PbI_2 is fragmented and then penetrates the deformed MAI phase [3]. The diffusion of PbI_2 into MAI crystals leads to nucleation and eventual growth of the perovskite phase. This perovskite surface itself can break further and when exposed to fresh reactants this can increase the rate of reaction. For the organic reaction to occur mechanically its reaction kinetics depends strongly on the PbI_2 surface area since it's the diffusion of the PbI_2 into the MAI that has to occur [3].

4.3. Experimental procedures

The synthesis process for methylammonium lead iodide ($CH_3NH_3PbI_3$, MALI) has been altered and the materials characterised to see if and how the methods produce any changes in phase assemblage and behaviour. In this chapter, preparation is via solid state synthesis using a mortar and pestle.

4.3.1. Solid state synthesis - Mortar and pestle

The precursor powders were weighed according to their final composition and ground together in a mortar and pestle for 30 minutes under ambient conditions in a fume hood. The resultant mixture was analysed using X-ray diffraction, XRD. The mixture was then annealed (for 12 hours) at a higher temperature of 80 ˚C and ground again. The powders were characterised using XRD and repeated cycles of grinding and annealing were performed until no changes in the XRD data were observed. Samples were then heated at 120 ˚C and XRD data subsequently collected. The process was repeated four times until no changes in the XRD data were observed.

4.3.2. Experimental results

Once the material (MALI) was synthesised different characterisation techniques were used for investigation. The resultant dried powder was ground in a mortar and pestle until a fine powder was produced. The powders themselves were characterised or pressed in a 6 mm die with a pressure of 350 MPa applied to form pellets.

4.4. Solid state (mortar and pestle) synthesis

A range of $CH_3NH_3Pb_{(1-x)}I_{(3-2x)}$ compositions were synthesised by varying the PbI_2 content, from x = 0.00 giving the nominally stoichiometric composition to x = 0.30. Initially, synthesis for all powder compositions was carried out at ambient conditions, and then incrementally annealed at higher temperatures. Fig: 4.2 shows a room temperature phase assemblage diagram of the region where x is varied from 0.00 to 0.30 over an annealing range from room temperature to 130 ^oC.

Fig: 4.2 shows that at room temperature, when the precursors are mixed and ground together in a mortar and pestle, all compositions have the same phase assemblage. These are the perovskite phase, the precursor phases and lower dimensional perovskite (LDP) phase(s). Once these compositions are annealed at a higher temperature of 80 ˚C the LDP phase(s) disappear and only the precursor phases and the perovskite phase remain. Along the x series, the same phases are present. The samples were then annealed at 120 ˚C. At this temperature, the phase assemblage altered for the different compositions. For x = 0.00, perovskite and PbI_2 were present. For x = 0.05 and 0.10 only the perovskite phase was observed whereas x = 0.20 and 0.30 showed the perovskite and MAI precursor phase were present.

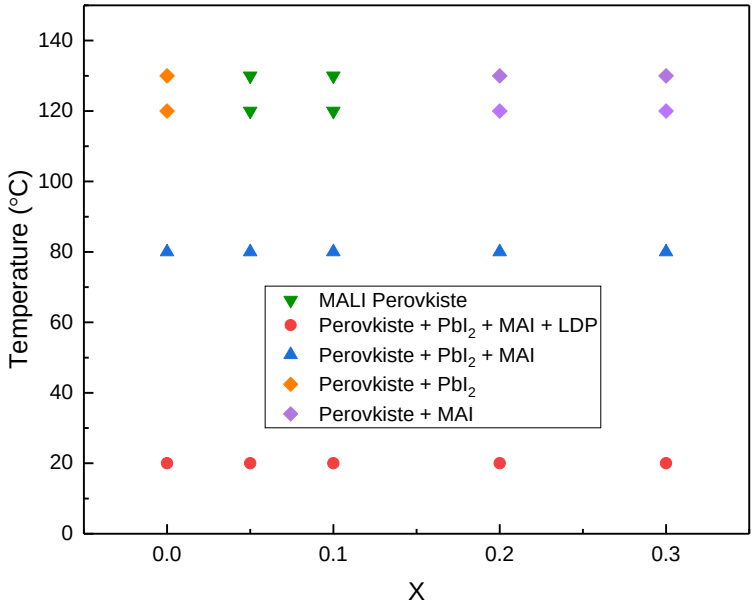

Figure 4.2. Room temperature phase assemblage diagram for the x series of MALI samples heated at various temperatures (y-axis).

Fig: 4.3 shows XRD data for all compositions after 30 minutes of grinding in a mortar and pestle at room temperature. All compositions have three phases present. They are MALI and the precursor phases; PbI_2 and methylammonium iodide (MAI). The diffraction patterns clearly show that by grinding the precursors together at room temperature some MALI

perovskite phase is formed. The diffraction patterns from Fig: 4.3 show the peaks attributed to MAI increase in intensity with increasing x.

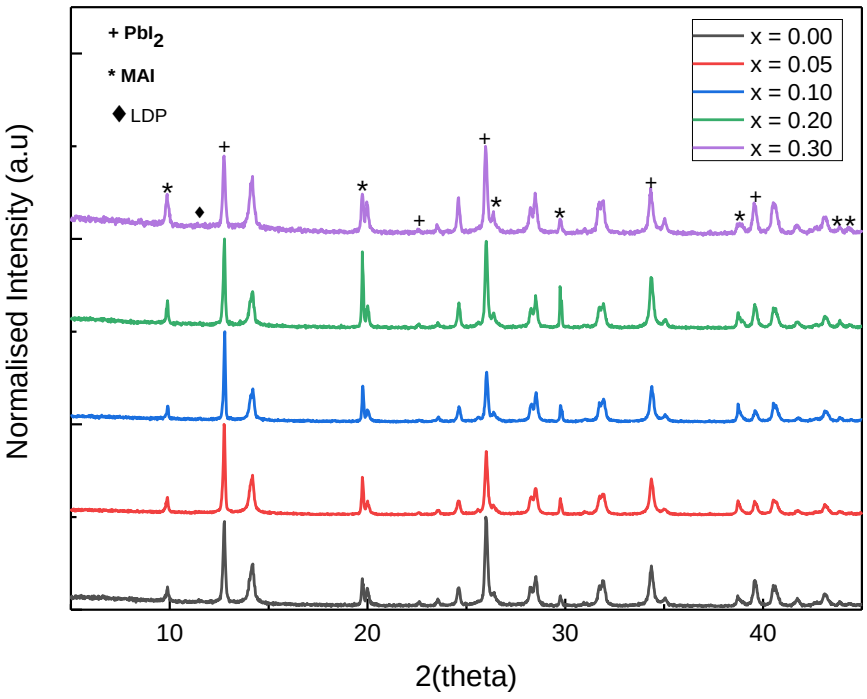

Figure 4.3. X-ray diffraction patterns for stoichiometric and PbI_2 deficient MALI compositions synthesised using a mortar and pestle at room temperature.

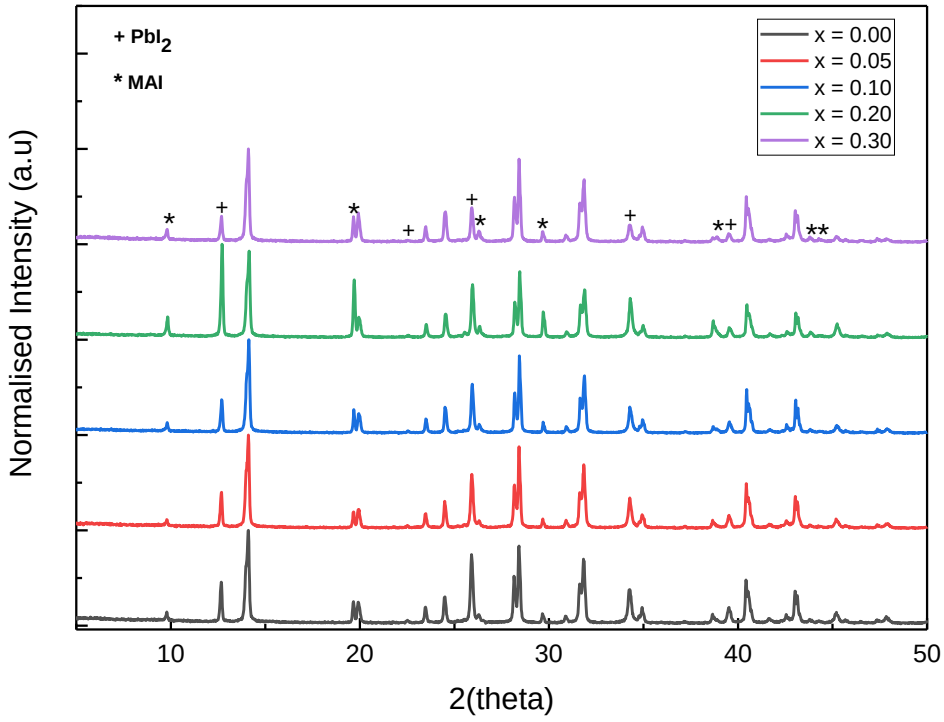

Figure 4.4. X-ray diffraction patterns for stoichiometric and PbI_2 deficient MALI compositions synthesised using a mortar and pestle and annealed at 80 °C.

The powders were then annealed at 80 ̊C and their resultant XRD diffraction patterns analysed, as shown in Fig: 4.4. These also have the same three phases present in all compositions. As the different compositions are annealed at this temperature, there is not a clear trend that can be observed among them regarding the intensities of the precursor peaks. The relative intensity of peaks associated with the perovskite phase increased when compared to the diffraction patterns collected at room temperature.

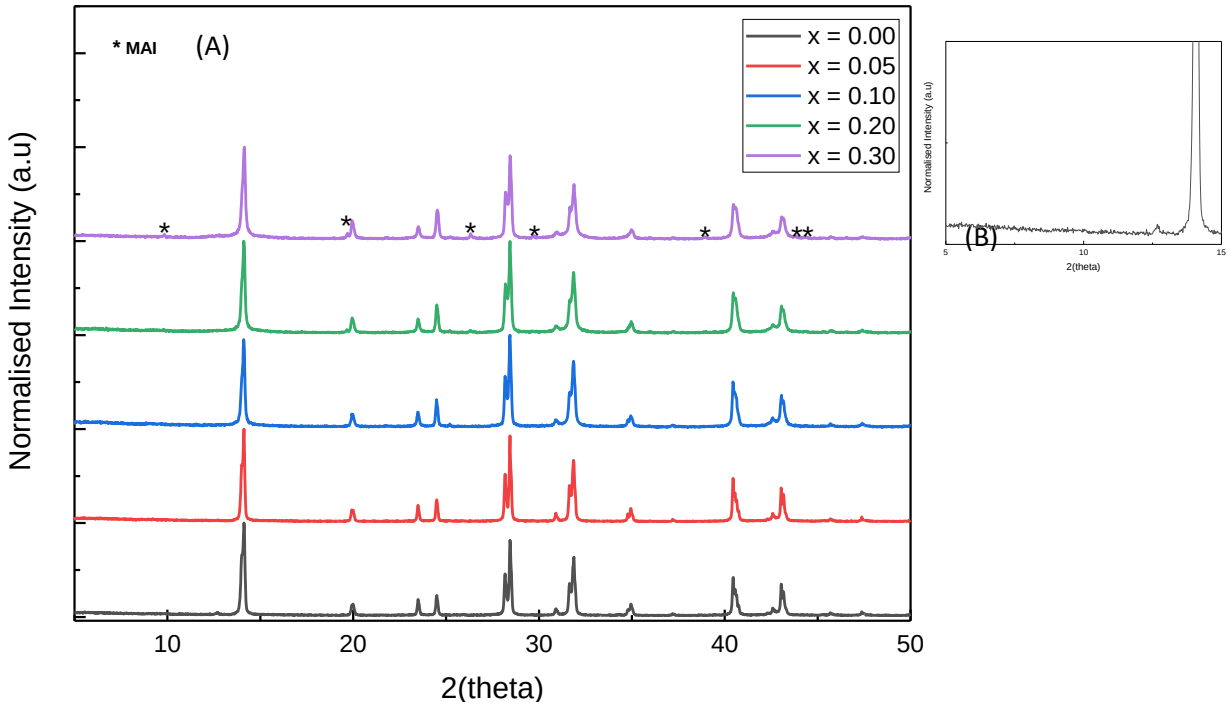

Figure 4.5. (A) shows X-ray diffraction patterns for stoichiometric and PbI_2 deficient MALI compositions synthesised using a mortar and pestle and annealed at 120 ̊C. (B) shows inset of x = 0.00 between 2θ = (5-15̊) in order to show a PbI_2 peak.

The powders were ground further and then annealed at 120 ̊C. This process was repeated on four occasions in attempts to achieve equilibrium, as indicated by no further changes in the XRD patterns. The final patterns from annealing at 120 ̊C are shown in Fig: 4.5.

Fig: 4.5 shows, x = 0.00 has a small amount of PbI_2 as shown by the peak at 12.6 ̊ two theta, whereas x = 0.05 and 0.10 samples appear phase-pure. The pattern for x = 0.20 shows the presence of a small amount of MAI; the peak intensities for this phase increase as x increased to 0.30. The perovskite phase formed is tetragonal MALI with space group I4/mcm.

Fig: 4.6 shows the room temperature lattice parameters of MALI for the x-series annealed at 120 ̊C and show little change in the a, c and V (when considered within the error range) values.

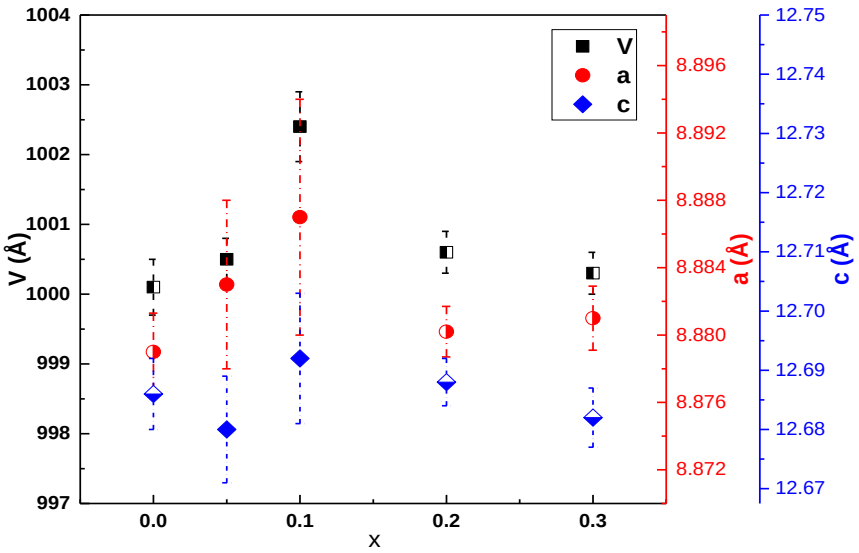

Figure 4.6. Variation in lattice parameters and cell volume for the x series. The samples were annealed at 120℃ four times with grinding steps between each anneal. Filled symbols indicate phase purity by XRD and half-filled symbols indicate phase mixtures by XRD.

4.5. Scanning electron microscopy (SEM) - Low voltage

The nature of the hybrid perovskite material, especially the organic cation makes it an unstable material under high temperatures or energies. Therefore, when conducting experiments on such materials, the experimental conditions may alter the material. One such case is when performing electron microscopy on these materials. The operating voltage of 20 kV normally used during routine SEM can easily damage the surface of the material. Energy dispersive X-ray spectroscopy (EDX) is also limited due to these voltages. Therefore, low voltages were required to observe the surface of these samples to avoid any surface damage/decomposition and without the application of any conductive (surface) layer coating.

Fig: 4.7 shows surface images gathered from pellets of x = 0.00 when synthesised at room temperature, 80 and 120 ℃. The images in Fig: 4.7 show three distinct regions of contrast, one is the grey region (red arrows), another is a darker region (black arrows) and the third is the light region (orange arrows).

The combination of secondary electron hyperspectral imaging (SEHI) carried out at a low voltage of 1 kV, and using a through lens detector (TLD) has been used to distinguish the different contrast regions observed on the surface of these pellets. The darker regions are attributed to organic-rich regions i.e. MAI-rich or MAI itself. The grey regions have been attributed to the perovskite MALI phase. Under these low energy conditions, PbI_2 is attributed to regions which appear bright or light compared to the dark MAI regions or grey perovskite regions.

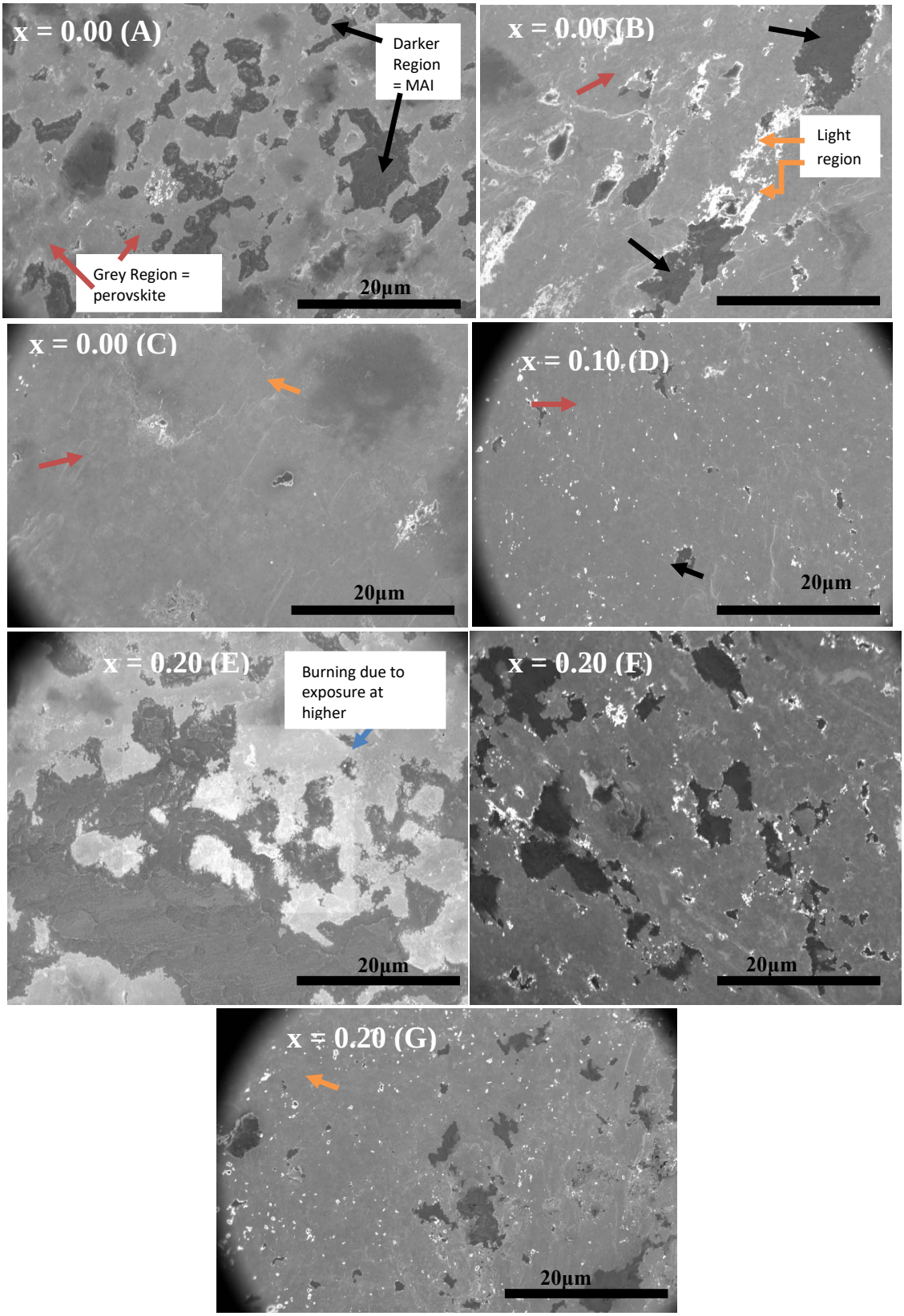

Figure 4.7. SEM images of x=0.00 MALI synthesised using the solid-state method at room temperature (A), 80 ˚C (B) and 120 ˚C (C). (D) shows the SEM image of x=0.10 synthesised using the solid-state method and annealed at 120 ˚C. SEM images of x=0.20 synthesised using the solid-state method at room temperature (E), 80˚C (F) and 120˚C (G).

From Fig: 4.7, as x = 0.00 is annealed at higher temperatures the fraction of darker MAI regions decreases whereas the grey perovskite regions become more dominant across the pellet surface. After annealing at 120 ̊C, Fig: 4.7(C), there is no sign of regions attributed to MAI. The phase assemblage diagram in Fig: 4.2 shows that x = 0.00 at room temperature and annealed at 80 ̊C have precursor phases co-existing with the perovskite phase. Fig: 4.7(A) and (B) show regions of the grey perovskite, light PbI_2 and dark MAI-rich whereas, in Fig: 4.7(C), there is no sign of distinct organic-rich regions. From other studies, which used a combination of SEHI with low voltage microscopy, the light regions indicated by the orange arrows are attributed to PbI_2. These regions are predominantly seen in Fig: 4.7B, however, it is not certain whether this is due to PbI_2 or associated with surface charging. Using a combination of XRD and SEM it can't be concluded with certainty that these regions can be attributed to PbI_2. The relative XRD peak intensities and SEM regions of the samples do not correlate very well.

Fig: 4.7D shows an SEM image of x = 0.10 after being annealed at 120 ̊C. Three distinct regions of grey perovskite, dark MAI regions and light PbI_2 regions are observed. From Fig: 4.5 the corresponding XRD pattern shows it to be phase-pure. The SEM image from the pellet surface shows there are small regions that can be attributed to the precursor phases of PbI_2 and MAI; however, most of the region examined is attributed to the perovskite phase.

Fig: 4.7(E-G) shows x = 0.20 after being annealed at three different temperatures. With increasing temperature, the darker MAI-rich regions decrease in area and more of the grey perovskite regions are observed on the pellet surface. The same trend is observed from the XRD data (Fig: 4.3- 4.5), Fig: 4.7G shows two distinct regions corresponding to the perovskite and MAI phases which is consistent with XRD results. Although the SEM image shows light regions which might be PbI_2, this is not observed by XRD.

When collecting images, the exposure time can cause some surface damage as shown by the blue arrow, Fig: 4.7A. When images are gathered at higher magnification or a certain region is magnified, to adjust focus and stigmatism, the surface of a pellet can be subjected to damage. This can easily be detected as rectangular regions from lower magnification with slightly different contrast.

Fig: 4.7 show that for synthesis at room temperature or after annealing at 80 ̊C, there is little to distinguish the different compositions along the x-series: they all show the same distinct features and phases. As they can't be quantified no trend can be distinguished

between them. After annealing at 120 ̊C; however, a trend across the x series is more easily observed.

Using solid state synthesis and grinding at room temperature produces some perovskite phase. Therefore, little energy is needed for perovskite formation but precursor phases are also present, alongside low dimensional perovskites. Heating to a higher temperature of 80 ̊C, increases the intensity of XRD peaks associated with the perovskite phase. Precursor phases are still present until 120 ̊C. x = 0.00 is a two-phase mixture (perovskite and PbI_2) but x = 0.05 and 0.10 are phase-pure based on XRD (although it takes four cycles of heating and grinding to reach this stage). At higher x, too much reduction in the starting PbI_2 content results in MAI precursor being present. Similar results/trends in the XRD data are seen when heated at 135 ̊C, whereas heating over 140 ̊C starts decomposition of the organic cation. Therefore, via solid state, x = 0.00 is not phase pure, but 0.05 and 0.10 are clean based on XRD data. SEM shows that along the x series, the dark organic-rich region increases in volume fraction on pellet surfaces and with heating to higher temperatures their volume fraction decreases. Even when XRD data suggest a sample is phase-pure (in the case of x = 0.05 and 0.10), SEM data indicates differing regions of contrast, therefore different phases are present.

4.6. Density of samples

The density of the samples used for electrical measurements was calculated using sample geometry and weight and treating the pressed pellets as cylinders. This was then divided by the theoretical density (calculated from atomic weight and unit cell dimensions) to get the percentage density. Since density is measured only via geometry (which can be quite inaccurate), three pellets for each composition of different diameters were pressed with varying amounts of powder. The average density was calculated, with variation in pellet size producing a 5% error in the calculated geometric density. Fig: 4.8 shows pellet density across the x series. The samples have a relatively high density (this agrees with the SEM images since the pellet surfaces have a small amount of visible porosity). All samples are > 90% dense with no significant variation in density across the series, within errors.

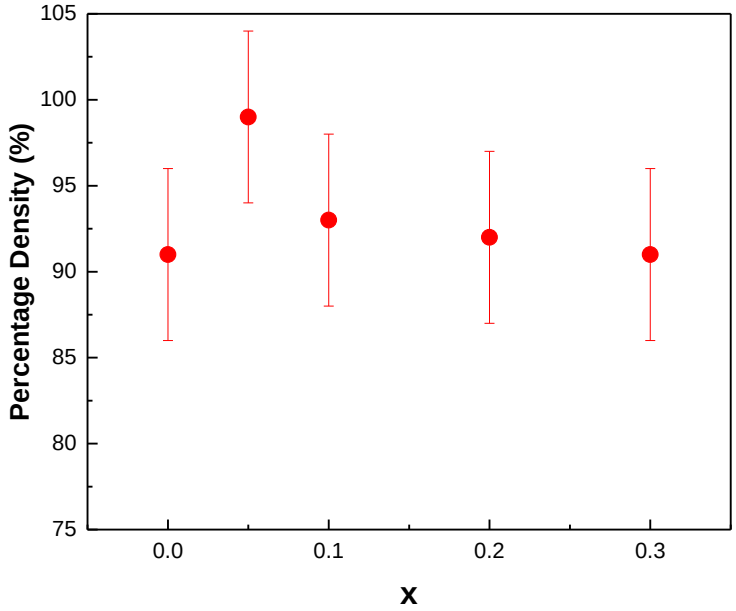

Figure 4.8. Percentage density of ceramics from x = 0.00 to 0.30 powders annealed at 120 ℃ and then pressed at room temperature.

4.7. LCR

An inductance capacitance resistance meter (LCR) was used to measure the capacitance vs. temperature relationships. The permittivity (ε_r) was extracted from the measured capacitance value and plotted against temperature for the x series. The capacitance response is also shown at different frequencies. Fig: 4.9, shows the permittivity-temperature relationship at frequencies of 100 kHz, 250 kHz and 1 MHz.

The LCR data for x = 0.00 in Fig: 4.9A shows ε_r at 250 kHz and 1 MHz to decrease with increasing temperature. The initial ε_r at room temperature is ~ 64, with a final value of ~ 52 at 120 ℃. On cooling, the trend shows reversible behaviour. At a lower frequency of 100 kHz, the same trend is observed but there is a plateau region observed between 70-90 ℃ on the heating cycle. On the cooling cycle during the aforementioned temperature range, ε_r has a slightly lower value. For the higher frequency of 1 MHz, this discrepancy between heating and cooling is less obvious.

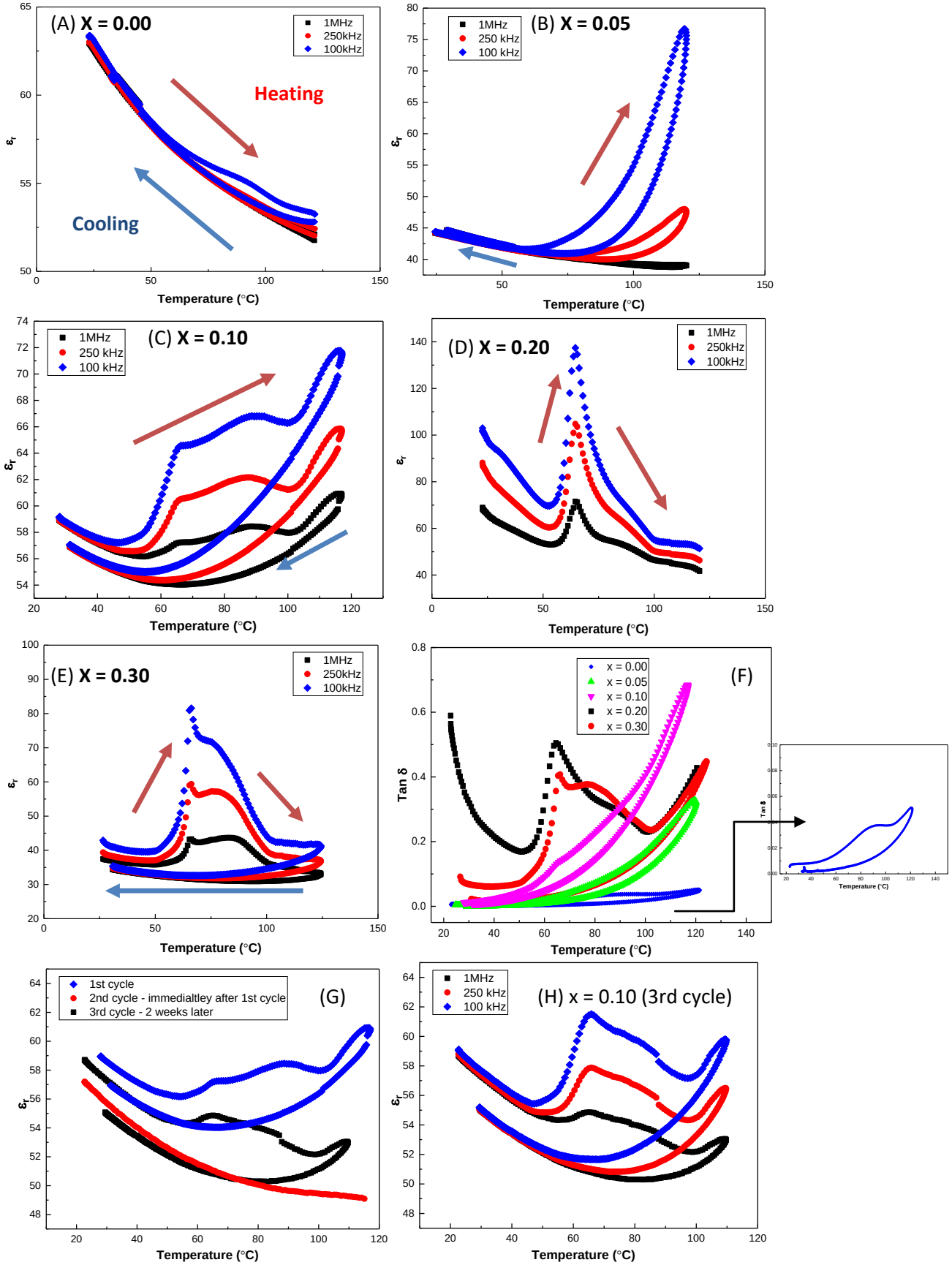

Figure 4.9. Permittivity vs. temperature for x = 0.00 (A), 0.05 (B), 0.10 (C), 0.20 (D) and 0. 30 (E), tan δ of x series (F). Permittivity vs. temperature of x = 0.10 on 1st, 2nd and 3rd cycles at different time periods at 1 MHz (G), and permittivity vs. temperature on 3rd cycle of x = 0.10 at different frequencies (H).

For x = 0.05 (Fig: 4.9B) ε_r shows a similar response to x = 0.00 at 1 MHz with an initial value of 45 although at lower frequencies there is a greater rise in the permittivity (as seen after 65°C for 100 kHz). On cooling, the permittivity is reversible (final ε_r of ~45) but there is a larger difference in permittivity between the heating and cooling cycles at lower frequencies.

In Fig: 4.9C, for x = 0.10, ε_r starts decreasing upon heating from room temperature, until 50 °C. At higher temperatures, there is an increase in ε_r with a peak appearing at 65 °C. Above 65 °C, there is a steady increase in ε_r with another peak appearing at 90 °C. Temperatures above 90 °C show a rise in ε_r, until the final temperature of 120 °C. On the cooling cycle, the peaks observed on heating are not observed and permittivity reverses back towards the room temperature value. x = 0.20 and 0.30 (Fig: 4.9D and E, respectively) show similar behaviour.

tan δ (Fig: 4.9F) shows that for x = 0.00 the loss is very low with a slight increase above 65 °C (seen from inset), and then on cooling it decreases. x = 0.05 shows the loss increases with temperature, with a steeper rise above 80 °C. For x = 0.10, the loss starts to increase, and there is a small peak at around 65 °C, after which the loss starts to increase more rapidly. On cooling, the loss decreases with no peaks appearing. For x = 0.20 the loss is initially very high and then it decreases with heating. After 50 °C it starts increasing again with a peak at ~65 °C, corresponding to the peak in Fig: 4.9D. The loss then decreases but with a plateau region between ~70-90 °C, after which it starts increasing again. x = 0.30 shows a similar trend as x = 0.20, and on cooling the loss decreases, however without the phenomena observed on the heating cycle but with a final loss that is slightly lower than the initial loss value at room temperature.

The LCR data show that on the heating cycle there are two temperature regions where the samples go through some change. These are at ~65 °C, where a peak in the permittivity occurs, and the temperature region between ~70-90 °C, where there is another peak. The peak at 65 °C is not observed for x = 0.00 and 0.05. For x = 0.10-0.30, the peak at 65 °C is easier to distinguish. For the second peak between ~70-90 °C, it is harder to be exact about the temperature due to the broadness of the peak. Only for x = 0.10 is there a clearer indication that it might be around ~90 °C.

On the cooling cycle both ε_r and tan δ decrease with decreasing temperature. The rate of decrease is higher during the temperature range 120 - 60 °C, whereas below 60 °C it tends to stay more or less constant. The peaks observed at 65 and 90 °C are not observed on the cooling cycle, therefore the ε_r and tan δ behaviour is not reversible.

If ε_r is remeasured soon after the 1st LCR cycle, then the behaviour observed on the first heating cycle is not observed, and a response similar to the initial cooling cycle is obtained as shown in Fig: 4.9G as the 2nd cycle. x = 0.10 was measured on three separate occasions and after leaving the sample longer between measurements. The behaviour seen on the 1st heating cycle is observed again on the 3rd cycle. The peak at 65 ˚C is observed again as is the plateau region between 70-90 ˚C. These are seen more clearly at lower frequencies from Fig: 4.9H as well as the subsequent rise in ε_r, with increasing temperature above 90 ˚C. Therefore, the initial heating permittivity behaviour is repeatable but only after a substantial time between measurements with the samples being stored at room temperature in ambient conditions.

4.8. Impedance spectroscopy (IS)

The samples annealed at 120 ˚C were characterised using IS. Measurements were performed on heating from room temperature to 120 ˚C and then on cooling back to room temperature. Fig: 4.10(A) shows the impedance response of four different compositions at ~ 62 ^{o}C on the heating cycle.

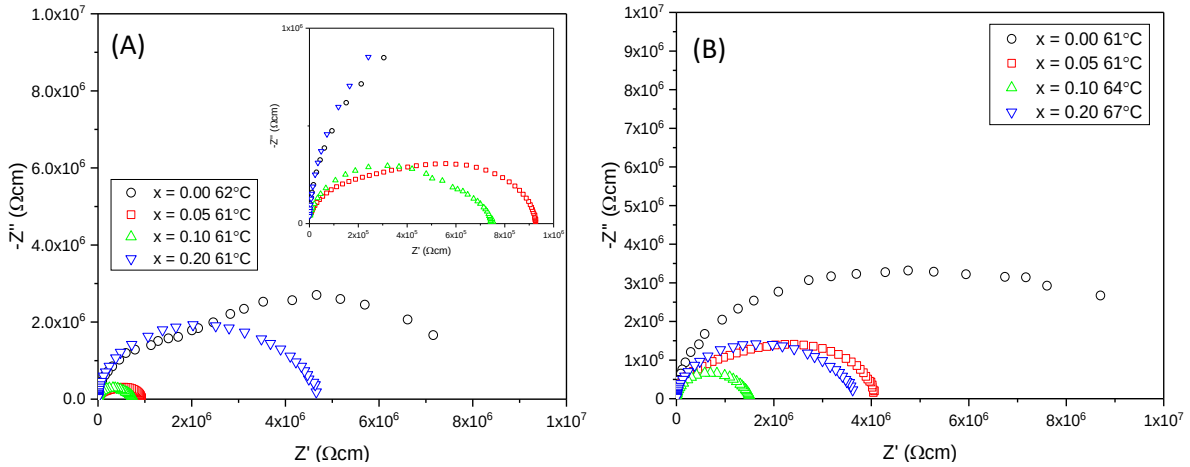

Figure 4.10. (A) Z* plots showing the response of x = 0.00 - 0.20 on the heating cycle. (B) Z* plots showing the response of x = 0.00 - 0.20 on the cooling cycle.

x = 0.00 shows the presence of two clear arcs in the Z^* plot. This trend is also observed for x = 0.05 and 0.10 (seen more clearly in the inset) but these samples have a lower total resistivity compared to x = 0.00 as shown by the low frequency, x-axis intercept. The individual R and C values of the first (higher frequency) and second (lower frequency) arcs were estimated by hand fitting the individual arcs based on an equivalent circuit of two parallel RC elements connected in series. These are shown in table 4.1, concentrating first on the heating data, via hand fitting. For x = 0.00, R1 is 2.9 MΩcm, and for 0.05 and 0.10, R1 is smaller, with values of 0.53 and 0.64 MΩcm, respectively. x = 0.20 shows a more depressed

singular arc rather than two distinct arcs. This is shown to have an R1 value of 4.0 MΩcm, which is higher than all other samples.

C1 for the x series during the heating cycle shows that x = 0.00 and 0.05 have similar values of $2.5x10^{-12}$ and $2.3x10^{-12}$ F/cm, respectively corresponding to ε_r of ~28 and 26. The C values of x = 0.10 and 0.20 are similar to each other and higher than 0.00 and 0.05, corresponding to ε_r of ~46 and 45, respectively.

The second arc's resistance and capacitance (R2 and C2) show that for x = 0.00, where it is the most clearly separated second arc, it has a corresponding resistance of 4.9 MΩcm. R2 for x = 0.05 and 0.10 are much smaller (0.4 and 0.1 MΩcm). The corresponding ε_r from C2 for x = 0.00, 0.05 and 0.10 are ~293, 170, and 203, respectively. x= 0.20 does not show a clear enough separation between the two responses, therefore R2 and C2 are harder to estimate but with hand fitting, R2 is ~ 0.8 MΩ with a very high permittivity of 2824.

For the heating cycle, the first arc can be associated with a bulk response due to its permittivity being attributed to that of MALI (although C1 for 0.00 and 0.05 are slightly low) and the second response has a much higher (effective) permittivity, which tends to be more similar along the x series. Except for x = 0.20, where C2 is an order of magnitude higher than C2 of x = 0.00-0.10, however it is also harder to separate out the two responses for x = 0.20. The total resistance (R_T) across the x series from 0.00-0.10, decreases. For x = 0.20 its higher. R of the second response is similar for x = 0.05 - 0.20 but is much larger for x = 0.00. This could be due to the smaller error in hand fitting for x = 0.00, due to the clear separation between the two responses in the Z^* plots.

Table 4.1. Estimated R and C values from Z^*plots of the first and second arc, on both heating and cooling cycles for the x series.

Sample (cycle)	R1 (M Ωcm)	C1 (pF/cm)	R2 M (Ωcm)	C2 (pF/cm)	ε_r (C1)	ε_r (C2)	R_T (M Ωcm)
X = 0.00 (Heating)	2.9	2.5	4.9	26	28	293	7.8
(Cooling)	6.2	3.2	8.8	22	36	249	15
X = 0.05 (Heating)	0.24	2.3	0.69	15	26	170	0.93
(Cooling)	2.1	1.9	2	14	22	158	4.1
X = 0.10 (Heating)	0.64	4.1	0.1	18	46	203	0.75
(Cooling)	1.4	4.6	0.1	21	52	237	1.5
X = 0.20 (Heating)	4.0	4.0	0.8	250	45	2824	4.8
(Cooling)	3.1	3.4	0.6	330	38	3729	3.7

Fig: 4.10(B) shows the Z^* response at a similar temperature but on the cooling cycle. On cooling, x = 0.00 shows only a single depressed arc from which the two different responses observed on heating become harder to separate. R1is now higher than during heating, with a

value of 6.2 MΩcm with ε_r of ~36. R2 is estimated by subtracting R1 from the total resistance (R_T = 15 MΩcm) with a value of ~8.8 MΩcm.

R1 for x = 0.05 and 0.10 on cooling are also higher, with values of ~2.1 and 1.4 MΩcm but ε_r remains relatively similar to that shown during heating, with values of ~22 and 52, respectively. The second response, R2 and C2 can be extracted for x = 0.05 and 0.10, although again it is more difficult to estimate the values on the cooling cycle. An overall increase in R2 for x = 0.05 is seen, with a value of 2 MΩcm, whereas for x = 0.10 it stays similar with a value of ~ 0.1 MΩcm. C shows little change for x = 0.05 with ε_r ~158 and ~237 for x = 0.10.

The resistance for the samples (x = 0.00-0.10) tends to be higher on the cooling cycle compared to the heating cycle. The Z^* semicircles are also more depressed and appear more like a single semi-circular arc rather than two clear responses observed on the heating cycle. Although there is an increase in the resistance of the samples on the cooling cycle, the overall resistance still tends to be smaller for the PbI_2 deficient samples than for x = 0.00 since R_T (on cooling) still decreases with x for x = 0.00-0.10.

Using the Z^* plot can be difficult to separate the two different components, more so during the cooling cycle. Especially knowing when the arcs of the first and second responses start and end, therefore the errors for extracted R and C values are high and with the errors probably increasing with x. M", Z" spectroscopic plots were therefore used in an attempt to obtain better estimates of the various R and C values. Fig: 4.11 and 4.12 show M", Z" spectroscopic plots on the heating and cooling cycles along the x series, again at a similar temperature.

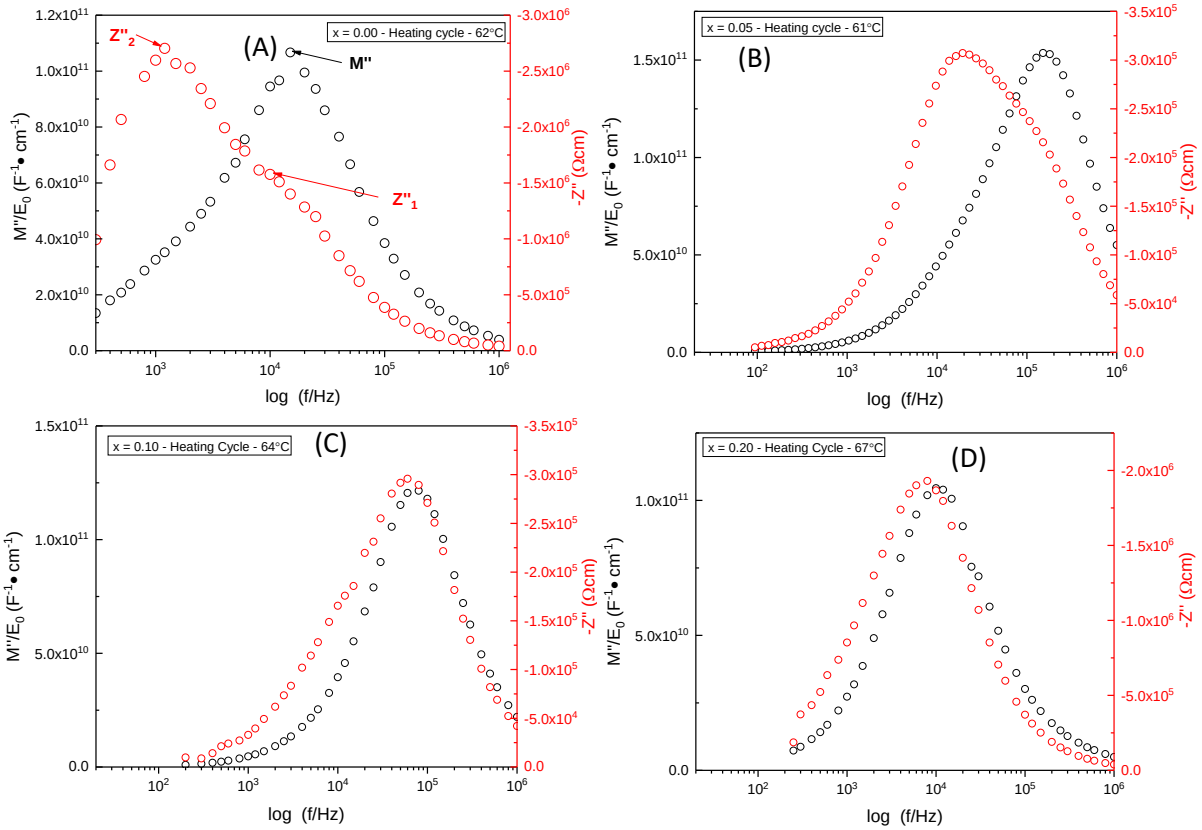

Figure 4.11. Combined M'' and Z'' spectroscopic plots on the heating cycle for x = 0.00 (A), x = 0.05 (B), x = 0.10 (C) and x = 0.20 (D).

Fig: 4.11 shows combined M" and Z" spectroscopic plots for the four compositions on the heating cycle. x = 0.00 shows a single low frequency M" peak and two Z" peaks, in plot A. This agrees with the two arcs observed in the impedance response shown in Fig: 4.10A and signifies at least two electro-active responses in this sample. A resistive component which occurs at a lower frequency (1.2 kHz) and a more conductive component (shown by the peak heights where R1 < R2), which has the time constant closer to the M" Debye peak. The response for x = 0.05 (plot B) has a similar number of components. Plots C and D show data for x = 0.10 and 0.20, respectively; their relative M", Z" plots each show one peak. There is little difference in the time constants of ($Z"_1$, $Z"_2$), compared to x = 0.00 and 0.05.

Table 4.2, shows the extracted R and C values using hand fitting from M" and Z" peaks of plots in Fig: 4.11. The M" peak appears at a higher frequency than $Z"_1$, this means the resistance extracted from M" is smaller than from $Z"_1$. This is seen to be true for all x series on heating. $Z"_2$ occurs at a lower frequency, and for x = 0.00 and 0.05 they are more resistive than both $Z"_1$ and M". For x = 0.10, $Z"_2$ has a smaller resistance than $Z"_1$, (a similar trend seen from Z^* values in table 4.1) although again using the M", Z" spectroscopic plots along the x series $Z"_1$, $Z"_2$ peaks become harder to distinguish (which is why there are no

extracted R and C values for Z''_2 for x = 0.20). Errors in R and C therefore increase using hand fitting.

Looking at the extracted capacitance responses, values from M'' and Z''_1 are similar to each other, with the corresponding ε_r of ~53, 57 from M'', Z''_1 for x = 0.00. For x = 0.05, ε_r ~37 and 35, for x = 0.10 ε_r ~47 and 51 and for x = 0.20 ε_r ~54 and 58, respectively. Therefore, there is not a large difference between them, and they all come in the range of bulk MALI ε_r. The capacitance from Z''_2 is higher, with ε_r for x = 0.00 - 0.10 being ~277, 151 and 426, respectively.

Table 4.2. Estimated R and C values and f_{max} from M'', $Z''_{1,2}$ Debye peaks, on a heating cycle for the x series.

Sample		R (M Ωcm)	C' (pF/cm)	f_{max} (kHz)	ε_r (C')
X = 0.00	M''	2.3	4.7	15	53
	Z''_1	3.2	5.1	10	57
	Z''_2	5.4	25	1.2	277
X = 0.05	M''	0.32	3.3	150	37
	Z''_1	0.5	3.1	107	35
	Z''_2	0.6	13	19	151
X = 0.10	M''	0.5	4.1	80	47
	Z''_1	0.6	4.5	60	51
	Z''_2	0.35	38	12	426
X = 0.20	M''	3.3	4.8	10	54
	Z''_1	3.9	5.2	8	58
	Z''_2	-	-	-	-

Fig: 4.12 shows the M'', Z'' spectroscopic plots for the x series on the cooling cycle, at a similar temperature to the heating cycle shown in Fig: 4.11.

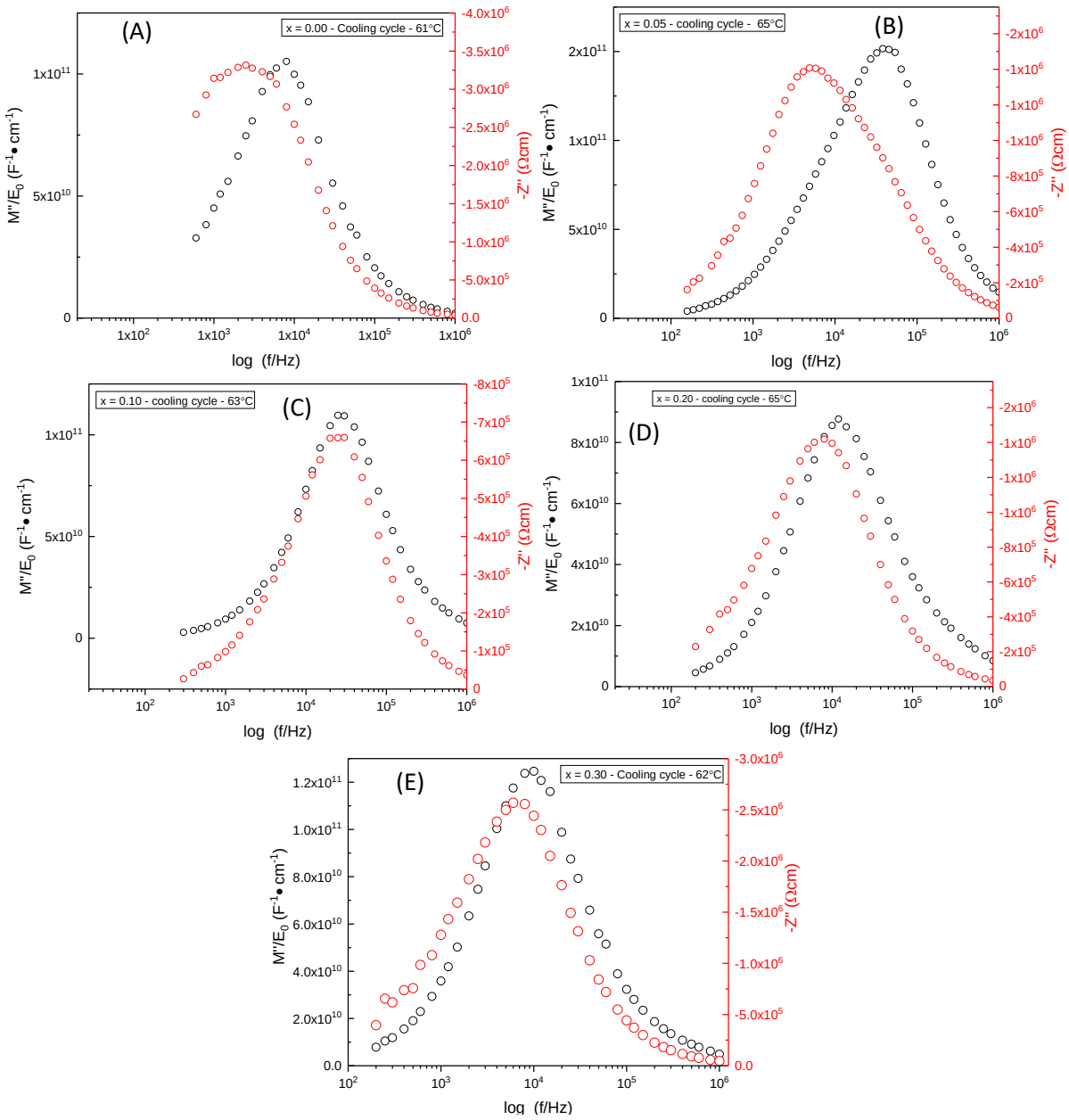

Figure 4.12. Combined M'' and Z'' spectroscopic plots on the cooling cycle for x = 0.00 (A), x = 0.05 (B), x = 0.10 (C), x = 0.20 (D) and x = 0.30 (E).

The M", Z" plots in Fig: 4.12(A) for sample x = 0.00 has one broad Z" peak rather than two distinct peaks (as seen on the heating, Fig: 4.11A). The Z" peak's time constant no longer aligns with the M" peak. Plots B-E for x = 0.05 - 0.30, show a similar M", Z" response on cooling as that on heating, where there are two different responses; however, it is even harder now to distinguish the $Z"_1$ and $Z"_2$ peaks from each other. The f_{max} for all peaks has decreased, as shown in table 4.3 when compared to table 4.2, even though the temperature at which the measurement is taken is almost the same on the two cycles.

The resistances extracted from M" and $Z"_1$ on cooling are higher for x = 0.00-0.10 than during heating. This is also true for $Z"_2$ for x = 0.00 and 0.05 where there is still some

difference between the two Z" peaks for the values to be extracted. For x = 0.10 and 0.20, the Z" peaks are too close so they can't be separated. This could be why the M", $Z"_1$ resistances for x = 0.20 are smaller on the cooling cycle (same trend seen when Z^* plots are used, table 4.1).

Table 4.3. Estimated R and C values and f_{max} from M'', $Z''_{1,2}$ Debye peaks, on the cooling cycle for the x series.

Sample		R (M Ωcm)	C' (pF/cm)	f_{max} (kHz)	ε_r (C')
X = 0.00	M''	4.2	4.8	8	54
	Z_1''	6.6	8.1	3	92
	Z_2''	6.4	17	1.5	186
X = 0.05	M''	1.1	3.3	46	37
	Z_1''	2	2.9	27	32
	Z_2''	2.8	9.8	5	110
X = 0.10	M''	1.2	4.6	30	52
	Z_1''	1.3	4.8	25	55
	Z_2''	-	-	-	-
X = 0.20	M''	2.3	6	12	64
	Z_1''	2.8	7	8	79
	Z_2''	-	-	-	-

The C values extracted from M", $Z"_1$ for x = 0.05 and 0.10 still remain similar to each other, with corresponding ε_r for x= 0.05 being ~37 and 32, respectively, whereas for x= 0.10 being ~52 and 55, respectively. Therefore, compared to the heating cycle the ε_r extracted from both peaks seem to have increased although by a small amount. This is prominent for x = 0.10 and 0.20 whereas for x = 0.00, M"(C') remains similar ε_r ~54, but there is a large increase in the ε_r extracted from $Z"_1$, now having a value of ~92. For x = 0.20, M"(C') being ~64 and $Z"_1$ (C') being ~79, both increased during the cooling cycle. The capacitance from the second response $Z"_2$ remains high, where for x = 0.00 ε_r ~186 and for x = 0.05 ε_r ~110. A decrease in both on the cooling cycle compared with the heating cycle but having a similar magnitude.

Comparing R and C values extracted from Z^* and M", Z" spectroscopic plots show the same trends although there are slight variations in the final extracted values. R1 values from Z^* on heating and cooling generally resemble $Z"_1$ well, except for x = 0.20, where the two responses are harder to separate. Depending on where on the arc the points are chosen from, using hand fitting to separate the two responses, there could be some difference in extracted values. For example, from Z^* for x = 0.00, R2 is 8.3 MΩcm, whereas from the M", Z" plot peak, $Z"_2$ it is 5.4 MΩcm.

For x = 0.05 and 0.10 there is less of a difference. For x = 0.10, on heating R2 is 0.1 MΩcm from Z^* and from Z''_2 its 0.35 MΩcm, therefore there is a smaller difference between the resistances (R1 and R2 extracted from Z^* and M", Z" peaks) of two responses in x = 0.05, and 0.10. This could be more a case of difficulty in extracting values from hand fitting, or one response dominating (due to similar time constants) rather than an actual trend.

This can be seen from the C' value of x = 0.00. If extracted from the Z^* arc, ε_r is estimated to be ~29 but from M", Z" it is ~53 and 57, respectively, so closer to the permittivity of MALI. The exact value of R and C from the two responses might be hard to distinguish but their magnitudes can be differentiated. C2 is significantly higher than C1, and it is easier to distinguish between them than R1 and R2 estimated from Z''_1 and Z''_2, respectively.

4.8.1. Hand fitting impedance data

The Z''_1, Z''_2 responses for x = 0.00 are clearly separated by different time constants. Therefore, their R and C values on the heating and cooling cycles can be estimated. Their conductivity (1/R) Arrhenius behaviour and capacitance vs. temperature relationships are shown in Fig: 4.13A and B, where R is estimated from both the M" peak and Z''_1, Z''_2 peaks, and their C values are shown in Fig 4.13C.

In Fig: 4.13A, the conductivity estimated from the M" peak is slightly higher than that estimated from the Z''_1 peak. The conductivity for both decreases slightly after 60 ˚C (1000/T = 3). The Z''_2 associated conductivity is lowest. As the sample is heated, the conductivity associated with Z''_2 increases and at around 110 ˚C, the time constants of both Z" peaks converge and their conductivity estimated through hand fitting become similar. The cooling data values shown in Fig: 4.13B still indicate a higher conductivity from the M" peak. The peaks in Z" converge and becomes broad, (as seen in Fig: 4.11A), therefore distinguishing between the two responses becomes harder and therefore their conductivities remain similar on cooling. The activation energy, E_a from the Z" data on cooling is calculated to be 0.65 eV.

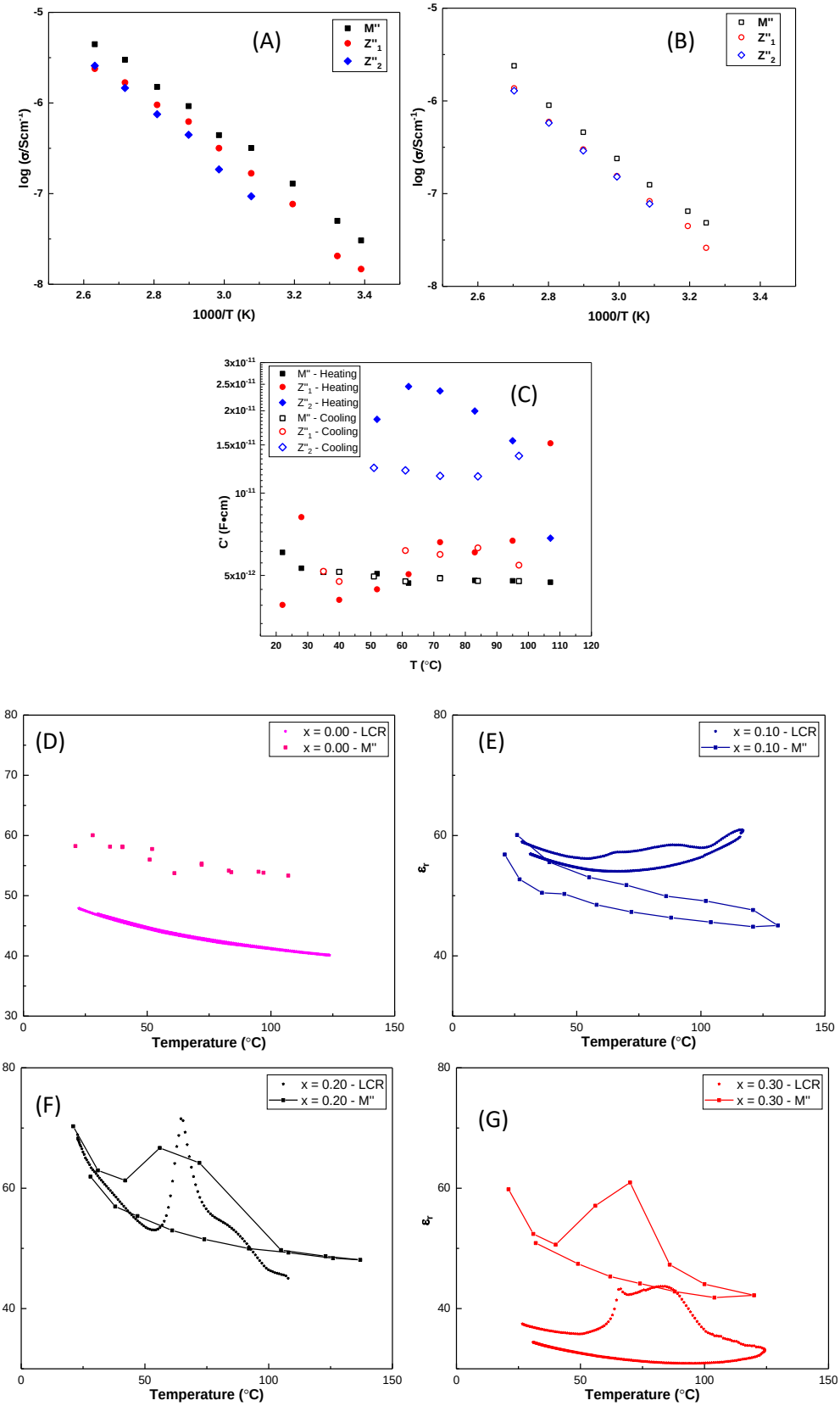

Figure 4.13. (A) Arrhenius conductivity plot on the heating cycle for x = 0.00, where the resistances are estimated from the M'', Z''$_1$ and Z''$_2$ peaks, and (B) Arrhenius conductivity plot for the same sample on the cooling cycle. (C) Capacitance vs. temperature behaviour on heating and cooling cycle for x = 0.00. Plots D to G shows comparison of permittivity estimated from the M'' peak to LCR measurement at 1 MHz, for x = 0.00 (D), x = 0.10 (E), x = 0.20 (F) and x= 0.30 (G).

Fig: 4.13C shows how the capacitance extracted from M", $Z"_1$, $Z"_2$ varies with temperature on both cycles. C' from M" stays constant with temperature on both cycles. C' from $Z"_1$ is lower than M" and starts to rise with temperature until 70 ˚C, where it then stays constant until 100 ˚C. At 110 ˚C it has a higher value, although the difference in Z" peaks are harder to distinguish and therefore it is harder to estimate. On cooling $Z"_1$ remains constant, however, below 60 ˚C, there is a slight decrease in the permittivity value, now resembling more the capacitance from the M" peak. C' from $Z"_2$ is higher and with an increase in temperature there is a decrease in C. On cooling, C remains higher than $Z"_1$(C') and doesn't vary significantly with temperature.

Fig: 4.13D shows ε_r estimated from the M" peak for x = 0.00 follows the same trend as the LCR measurements; however, ε_r is higher by about 10. From Fig: 4.13D-G, the trends in ε_r along x, between M" and LCR data remain the same, with the rise in ε_r seen at ~65 ˚C, which becomes clearer along x. On cooling ε_r rises steadily as the temperature is decreased without the peak occurring during the heating cycle. However, there are some variations in the magnitudes of ε_r and this is attributed to the method of impedance analysis employed to extract R and C values.

Fig: 4.14A shows the Arrhenius plot (when the resistances are extracted from the M" peak) for the x series on the heating cycle. x = 0.00 shows a near-linear relationship between conductivity and temperature. The other compositions where the PbI_2 content is reduced show higher conductivity which decreases at higher temperature; this starts to occur above 70 ˚C. Fig: 4.14B shows the conductivity Arrhenius plot on the cooling cycle, the relationship appears linear at high temperatures when compared to the heating cycle; however, below 50 ˚C the trend is generally non-linear and in some cases the conductivity rises towards room temperature. The conductivity values on cooling for x = 0.05 and 0.10 are higher by about half an order of magnitude, this difference being more pronounced in the higher temperature region.

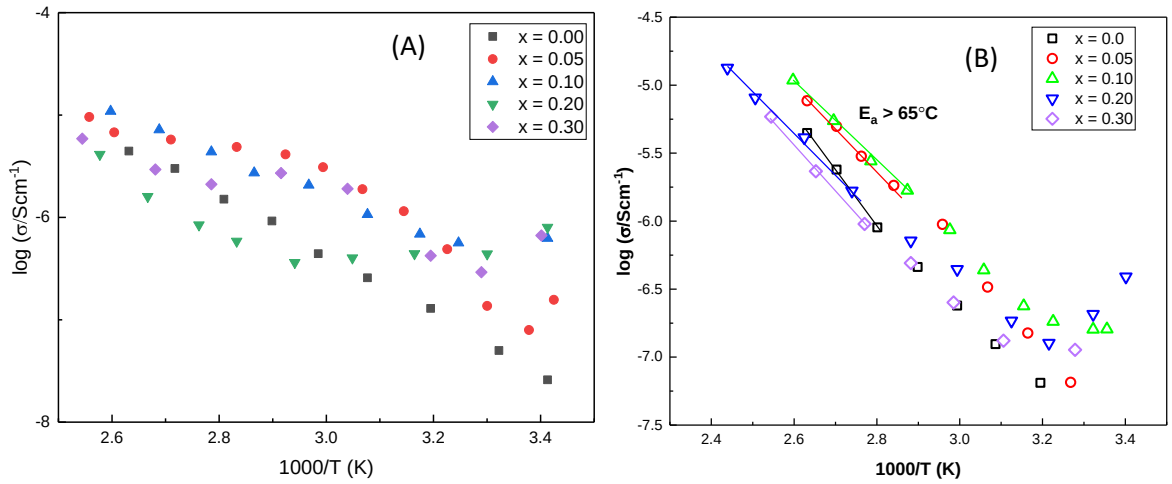

Figure 4.14. (A) Arrhenius conductivity plot for the x series on heating. (B) Arrhenius plot of conductivity for the x series on cooling. The resistance for the x series is extracted from the M'' peak.

The activation energy (E_a) values for conduction associated with the M'' response above 65 ˚C (on cooling) as indicated by the solid lines in Fig: 4.14B are tabulated in table 4.4. The values remain similar for x = 0.05-0.20, E_a being in the region of ~0.56-0.60 eV, whereas, there is a significant increase in E_a for x = 0.00 and 0.30 with values of ~ 0.89 and 0.69 eV, respectively. It was not feasible to extract E_a values in the low-temperature region (below 65 ˚C) because of deviations from linearity and in some cases a rise in conductivity near room temperature, eg x = 0.10 and 0.20, Fig: 4.14B.

Table 4.4. Conductivity Activation energy values above 65˚C extracted from the M'' peak data as shown in Fig: 4.14B.

Sample	$E_{a\,(2)}$ > 65˚C (eV) (M'')
X = 0.00	0.82 (±0.03)
X = 0.05	0.60 (±0.03)
X = 0.10	0.59 (±0.02)
X = 0.20	0.58 (±0.03)
X = 0.30	0.69 (±0.03)

4.8.2. Equivalent circuit fitting

The difficulty in extracting data from hand fitting for the x series is due to the poor resolution of the overlapping responses in the impedance formalism on heating, which becomes even harder on the cooling cycle. In an attempt to extract more accurate R and C values equivalent circuit fitting was attempted. An equivalent circuit composed of two parallel R and C elements connected in series was used (as a first approximate). Hand fitted R and C data were initially used as input values and through an iterative process and inclusion of appropriate Constant Phase Elements (CPEs) an equivalent circuit was

developed that could simulate the experimental data and allow refined R and C values to be obtained.

Hand-fitting showed that for x = 0.00, two parallel R-C elements connected in series should be the starting point, with a constant phase element (CPE) connected in parallel to an RC element. A CPE is used during circuit fitting due to the high-frequency dispersion in the Y' spectroscopic plot and the non-ideal arcs in the Z^* plot. The impedance of a CPE contains two parameters, these are n and CPE-T. The constant n is in between 0 and 1, where 0 is for an ideal resistor and 1 is for an ideal capacitor. All four formalisms in various formats, i.e. M'', Z'', Y' and C' spectroscopic, and Z^* plots, were analysed to ensure the best fit.

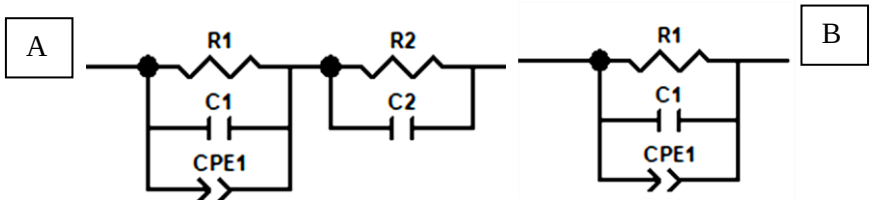

Figure 4.15. (A) RQC-RC equivalent circuit containing two RC elements in series, with the first element also having a CPE in parallel with R1, C1. (B) RQC circuit, containing one RC element with a CPE in parallel with R1 and C1.

The circuit used to analyse and fit the experimental data is shown in Fig: 4.15A. The comparison between fitted and experimental data is shown in Fig: 4.16. Data on the heating cycle (Fig: 4.16A & B) show a better fit than that on the cooling cycle (Fig: 4.16C and D), where the discrepancy at high frequency is enhanced during the cooling cycle. This is most clearly seen in the Y' plot. The fitted data deviates more during cooling, although even on heating at the highest frequency the fit is not perfect.

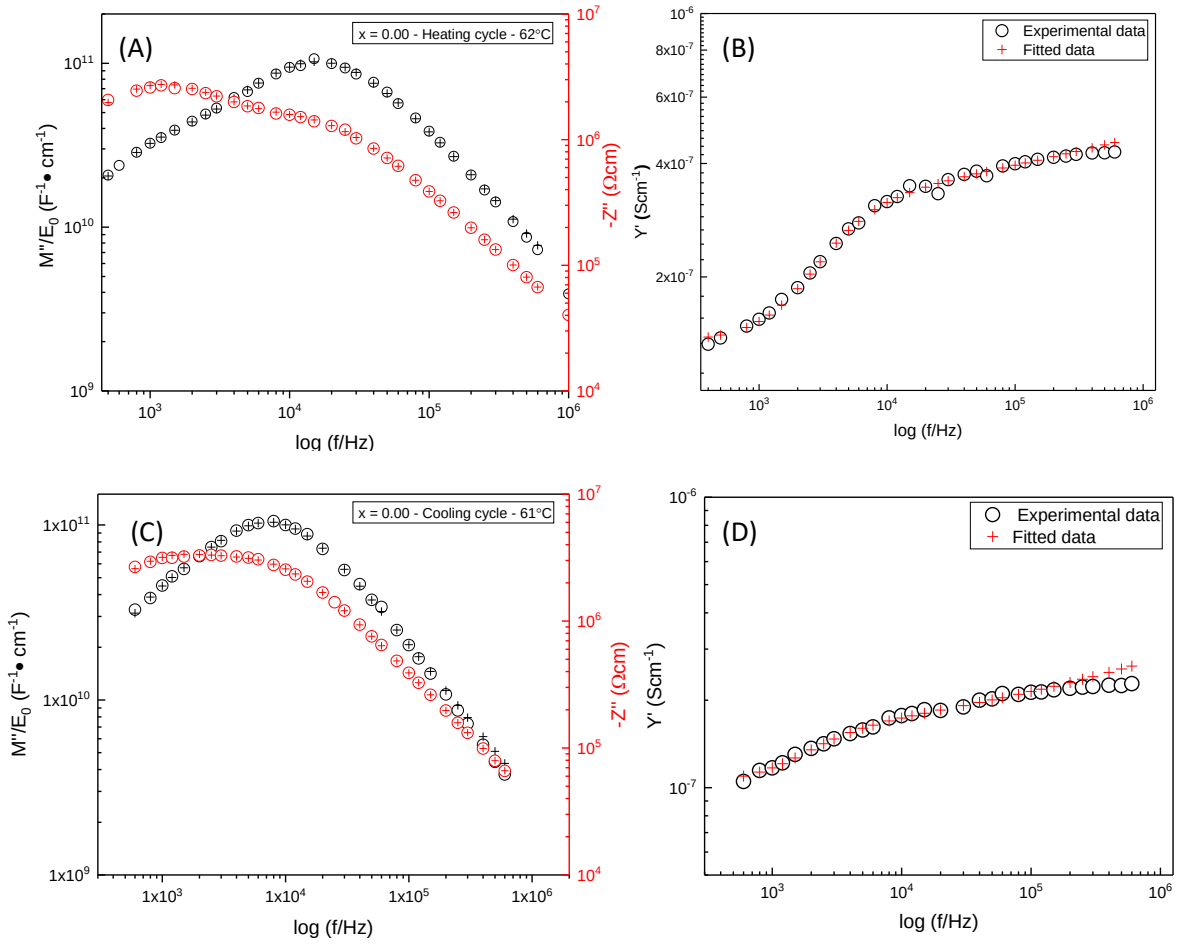

Figure 4.16. Circuit fitting (RQC-RC) for x = 0.00 compared to experimental data during the heating and cooling cycle. (A) log-log M''/Z'' spectroscopic plot during heating. (B) Y' spectroscopic plot during heating. (C) log-log M''/Z'' spectroscopic plot during cooling. (D) Y' spectroscopic plot during cooling.

The different R, C, and CPE circuit components during fitting could either be constrained or set free. This depends on how well the experimental and equivalent circuit data fit together, whilst attaining realistic R and C values from the equivalent circuit. The cooling data for x = 0.00 was modelled to the equivalent circuit shown in Fig: 4.17A, first where all the parameters were set free. This resulted in realistic values in the R and C values; however, there was no trend in n with temperature, although most were close to a value of ~ 0.3. The data were then fitted again, but this time, n was set to 0.3, this resulted in worse fitting, especially conductivity at high frequency in the Y' spectroscopic plot. However, it can be seen from Fig: 4.17A and B that R1 and R2 values both gave very similar final results whether n was free to refine or was set to 0.3.

Fig: 4.17C shows the CPE-T values when n was free to refine or was set to 0.3. There does not seem to be a great difference except at 72 ℃. The trend shows the CPE-T value increases with temperature linearly, more so for n = 0.3. Data fitting is also constrained by good quality data being available over a given frequency window. At low temperatures, the

low-frequency data tends to be noisy. Most of the data need to be cropped (between 20 Hz-400/600 Hz), increasing the error in the low-frequency RC component of the equivalent circuit. This is especially the case during the cooling cycle where the material is less conductive, f_{max} is lower, therefore fewer data are available in the lower frequency range (as seen by comparing Fig: 4.16A and B to 18C and D, respectively). At high frequency, the dispersion can move out of the frequency range during the heating cycle as the sample becomes more conductive.

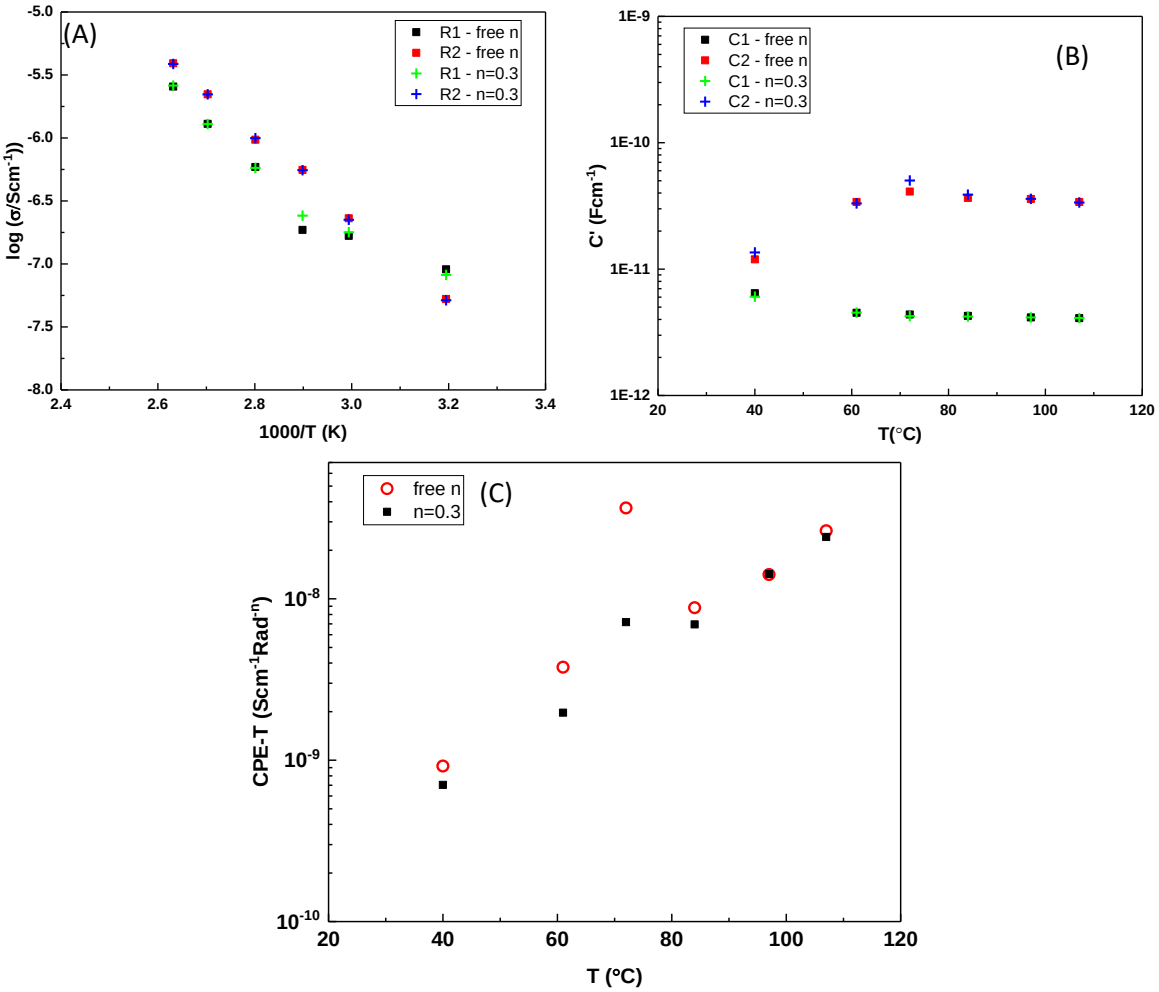

Figure 4.17. (A) Comparison of R1 and R2 values when n is set free and for n = 0.3. (B) C1 and C2 values when n is set free and for n = 0.3. (C) CPE-T values for when n is free compared to n = 0.3. All for when the equivalent circuit is fitted to x = 0.00 cooling data.

x = 0.00 appears to have at least two separate responses, however along the x - series the Z''_1, Z''_2 time constants become similar. If x = 0.30 is observed from Fig: 4.12E, it is harder to distinguish between the two separate responses. Therefore, two different circuits were tried to fit the experimental data. The first circuit was the one shown in Fig: 4.17A and second circuit is shown in Fig: 4.17B. This was attempted to distinguish if there are two separate responses

in the impedance data or one singular response. Due to the data appearing as if it has one response when judged visually.

Fig: 4.17B represents a single RC element with a CPE (Q) connected in parallel. Fig: 4.18 shows the experimental and fitted data (for x = 0.30 and 0.10) for both circuits, Fig 4.17A and B. The comparison between the plots show the data in Fig: 4.18A (RQC-RC) fit much better than the one shown in 4.18B (RQC), where the low-frequency data does not fit. This is most clearly seen in Fig: 4.18C for x = 0.30 and Fig: 4.18D and E for x = 0.10, where both the high and low capacitance region fit well with the RQC-RC circuit from Fig: 4.17A but not with the RQC circuit from Fig: 4.17B.

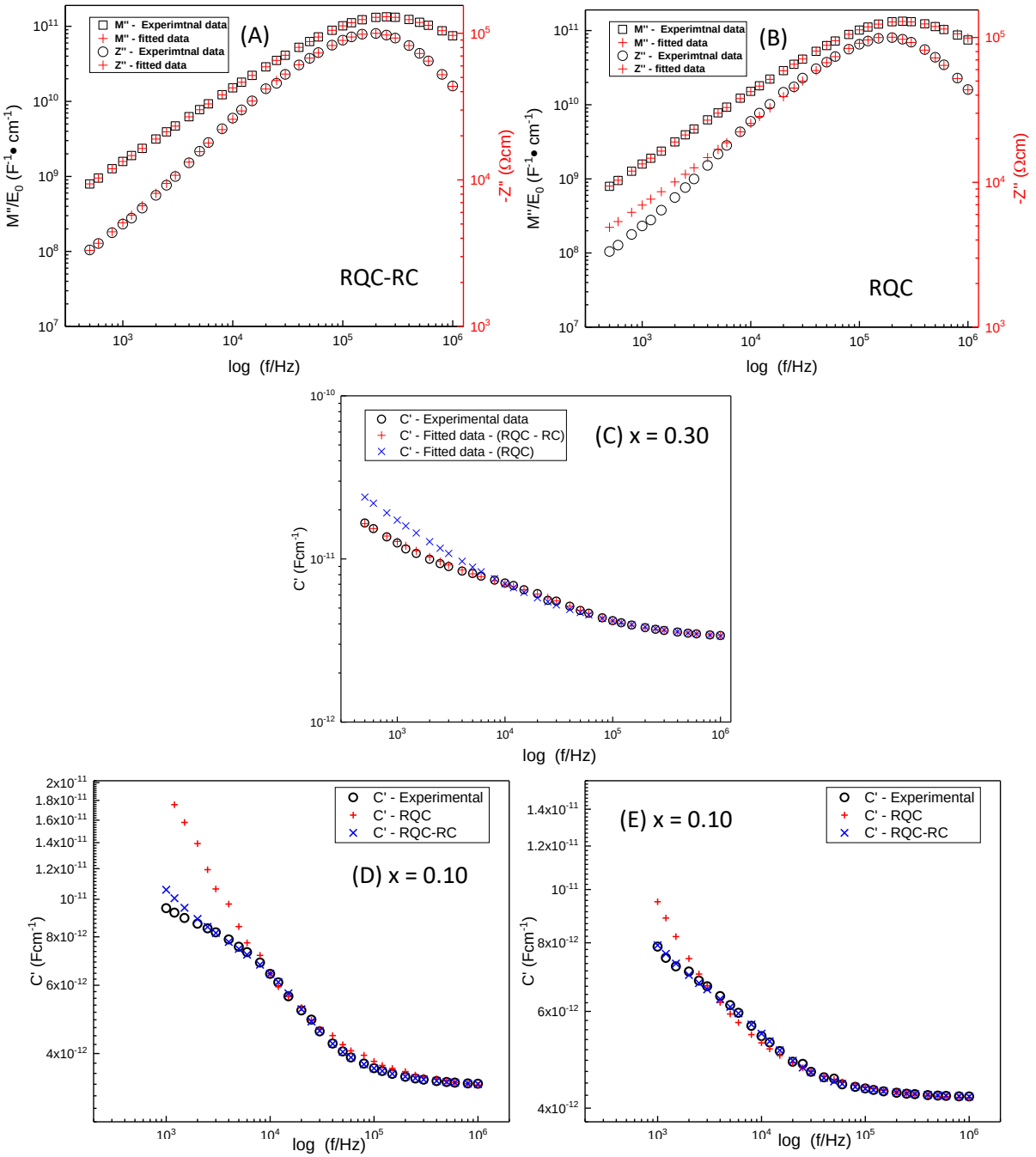

Figure 4.18. Comparing RQC-RC and RQC circuit fitting for x = 0.30 at 120 ℃. (A) log-log M'', Z'' spectroscopic plot for an RQC-RC circuit compared to experimental data. (B) log-log M'', Z'' spectroscopic plot for an RQC circuit to experimental data. (C) Capacitance plot comparing RQC-RC and RQC circuit fit to experimental data. (D) Capacitance spectroscopic plot for x = 0.10 comparing RQC-RC and RQC circuit fits experimental data on heating at 76 ℃. (E) Capacitance spectroscopic plot for x = 0.10 comparing RQC-RC and RQC circuit fits experimental data on cooling at 75 ℃.

Although the samples in the x series might visually look to have one IS response, as observed in Fig: 4.11 and 4.12 when subjected to equivalent circuit analysis, better-fitted data are produced for two RC elements connected in series (RQC-RC), as shown in Fig: 4.18. Therefore, all samples in the x-series were fitted to the circuit shown in Fig: 4.17A.

Once the equivalent circuit is chosen and fitted to the experimental data at each temperature, both during the heating and cooling cycle, individual resistance and capacitance values can then be extracted for R1, C1 and R2, C2 from the equivalent circuit. These values were compared to the hand-fitted R and C values extracted from the M" and Z" peaks to get a broader picture of sample behaviour with temperature and how the various values changed during the heating and cooling cycle.

Fig: 4.19 shows these parameters being compared to each other during the heating and cooling cycle for x = 0.00. The heating data in Fig: 4.19A shows that initially R1 and M" values are closer to each other and have slightly higher conductivity values than those from R2 and Z". There is a slight decrease in the 1/R1 value at ~ 60°C after which 1/R1 starts to increase again with increasing temperature. At higher temperatures, however, 1/R1 is now similar in magnitude to Z" conductivity values.

Conductivity from 1/R2 is initially similar to Z" and after 60 °C there is a slight increase in 1/R2 values. A conductivity Arrhenius plot for cooling data in Fig: 4.19B shows that after the heating cycle, R1 and Z" values are closer together whereas R2 and the M" value are closer in magnitude to each other.

The capacitance plot on heating shown in Fig: 4.19C, shows that C1 resembles the bulk capacitance extracted from M". At lower temperatures they match well, however above 60 °C, there is a slight increase in the M"(C') value, diverging slightly from C1, however, M" and C1 remain similar. The capacitance extracted from the Z" plot is higher with the value of C2 also being higher. An increase in temperature increases the value of C2, deviating from Z" (C').

On cooling, Fig: 4.19D shows C extracted from the M" and C1 are similar, there again seems to be a very small drop in the M" capacitance below 70 °C, whereas C2 and Z" values have a higher magnitude. When the extracted values from the equivalent circuit are compared to the hand fitting estimated values there is good correlation for the C values where C1 resembles the M" peak capacitance and C2 being higher and closer to the Z" capacitance although it is not as high, as seen from Fig: 4.19D. The conductivity, calculated from the resistance values indicates a change in slope for both R1 and R2 on heating (Fig: 4.19A) whereas the hand fitting data shows a more linear response, where distinguishing this change in slope is difficult to pinpoint. Especially comparing hand-extracted M" conductivity values to that calculated from R1 of the equivalent circuit.

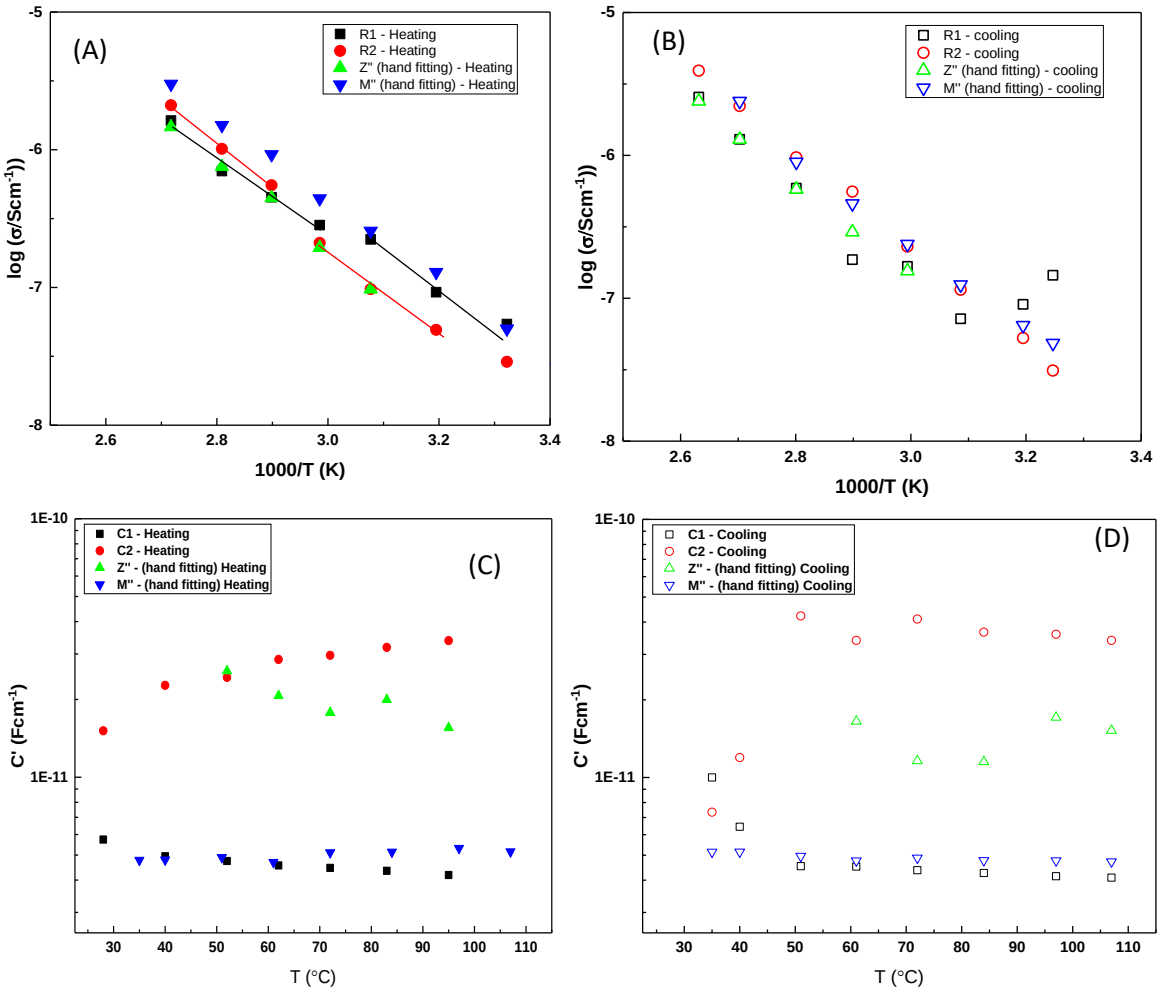

Figure 4.19. Extracted R and C values from the fitted equivalent circuit (RQC-RC) for x = 0.00 on heating and cooling. (A) Arrhenius plot of conductivity comparing R1 and R2 values from the equivalent circuit to hand fitting values from M'' and Z'' spectroscopic peaks on the heating cycle. (B) Conductivity Arrhenius plot comparing R1 and R2 values from the equivalent circuit to hand fitting values from M'' and Z'' spectroscopic peaks on the cooling cycle. (C) Capacitance vs. temperature comparing C1 and C2 values from the equivalent circuit to hand fitting values from M'' and Z'' spectroscopic peaks on the heating cycle. (D) Capacitance vs. temperature, comparing C1 and C2 values from the equivalent circuit to hand fitting values from M'' and Z'' spectroscopic peaks on the cooling cycle.

Fig: 4.20 shows the extracted values when an RQC-RC circuit is fitted to x = 0.10 on both the heating and cooling cycle. Unlike the x = 0.00 sample, in x = 0.10, there is only one distinguishable Z" peak. Fig: 4.20A shows that M" and Z" along with 1/R1 conductivity values are all close to each other in magnitude, whereas 1/R2 is higher. For R1, M", and Z", there is a slight change in slope that can be seen after ~ 60 ˚C (1000/T = 3.0), whereas for R2 there is a decrease in conductivity above ~ 40 ˚C (1000/T = 3.2) and then a slight increase after ~ 85 ˚C (1000/T = 2.8). The conductivity between 40 ˚C-85 ˚C being linear with temperature. Fig: 4.20B also shows the same trend on cooling, with R1, M" and Z" conductivities being the same, whereas 1/R2 is about an order of magnitude higher.

The trend in the capacitances on heating and cooling can be seen from Fig: 4.20C and D, respectively, where the C values extracted from Z" and M" are lower in magnitude and resemble C1, whereas the C2 values are higher. There is again a small increase in the C extracted from M" and Z" above 60 ̊C and a decrease in C below that temperature during the cooling response, similar to the trend shown for x = 0.00 discussed earlier.

Similar trends are observed for x = 0.20 and 0.30. R values extracted and then converted to conductivities from the M" and Z" peaks are close to each other and resemble R1. The 1/R2 values are higher. The capacitance C1 is closer to M" and Z" extracted capacitance values whereas C2 is higher.

Equivalent circuit fitting across the temperature on both heating and cooling cycles then indicates that R1 values match well with the M", Z" peak resistances and capacitances. Where there is a clear indication of the second $Z"_2$ peak as in x = 0.00, C2 matches closely to it. For the rest of the x series, a better fit is obtained from the RQC-RC circuit indicating another electro-active element is contributing to the IS response. Where there is a clear separation of time constants of $Z"_1$ and $Z"_2$ as in x = 0.00, C1 resembles the M" peak and C2 is closer to $Z"_2$. However, when the time constants are similar, R1 and C1 resemble the M", hand-fitting data of bulk MALI. Whereas R2 and C2 have higher conductivity and capacitance values.

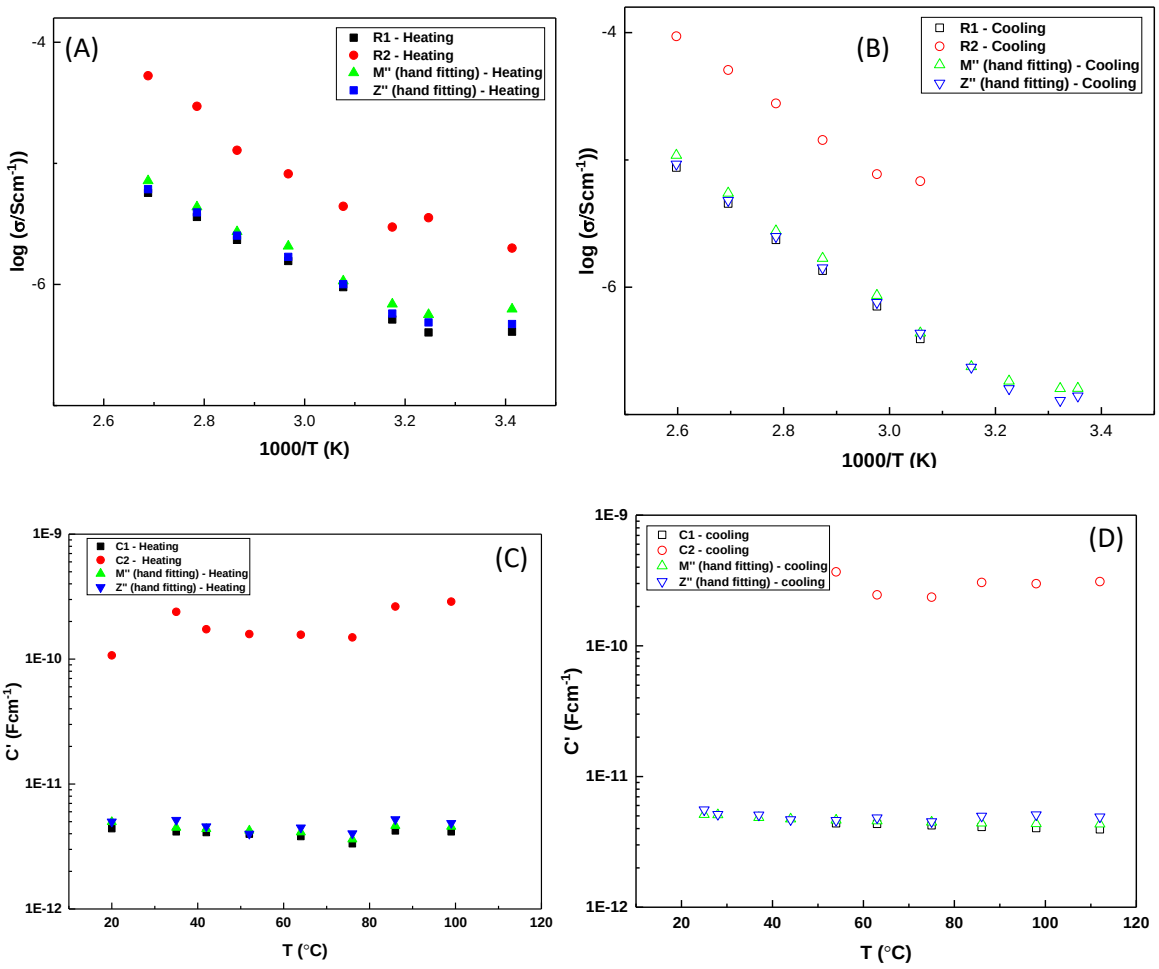

Figure 4.20. Extracted R and C values from the fitted equivalent circuit (RQC-RC) for x = 0.10 on heating and cooling. (A) Arrhenius conductivity plot comparing R1 and R2 values from the equivalent circuit to hand fitting values from M'' and Z'' spectroscopic peaks on the heating cycle. (B) Conductivity Arrhenius plot comparing R1 and R2 values from the equivalent circuit to hand fitting values from M'' and Z'' spectroscopic peaks on the cooling cycle. (C) Capacitance vs. temperature comparing C1 and C2 values from the equivalent circuit to hand fitting values from M'' and Z'' spectroscopic peaks on the heating cycle. (D) Capacitance vs. temperature comparing C1 and C2 values from the equivalent circuit to hand fitting values from M'' and Z'' spectroscopic peaks on the cooling cycle.

4.8.3. Extracted R and C values from circuit fitting

Fig: 4.21 shows the extracted R and C values on a heating cycle when the x series has been fitted to the equivalent circuit shown in Fig: 4.17A. Fig: 4.21A and B show 1/R1 and 1/R2 values, respectively. The conductivity from R1 values shows similar behaviour to the conductivity estimated from M" values. On heating a decrease in conductivity occurs for x = 0.00, 0.20 and 0.30 above ~60 ˚C (1000/T = 3.0), whereas for 0.10 it shows little change.

For 1/R2 however (Fig: 4.21B), there is an initial decrease (for x = 0.10 - 0.30) above 40 ˚C (1000/T = 3.2) as mentioned before, whereas for x = 0.20 and 0.30 there is another drop in conductivity observed, occurring at a slightly higher temperature of ~85 ˚C (1000/T = 2.8).

The R2 values show higher conductivity than R1 for x = 0.10, 0.20 and 0.30, but for x = 0.00 it is similar to R1.

The capacitance response on heating (Fig: 4.21C) shows that C1 values for the x series remain constant with ε_r in the range of 37-49, with the lowest values for x = 0.30. C2 values are higher, with the highest C2 corresponding to the most conductive sample, x = 0.10. The other samples (x=0.00, 0.20 and 0.30) show that as x increases so does C2. The C2 values also show there is an increase at ~90 ˚C.

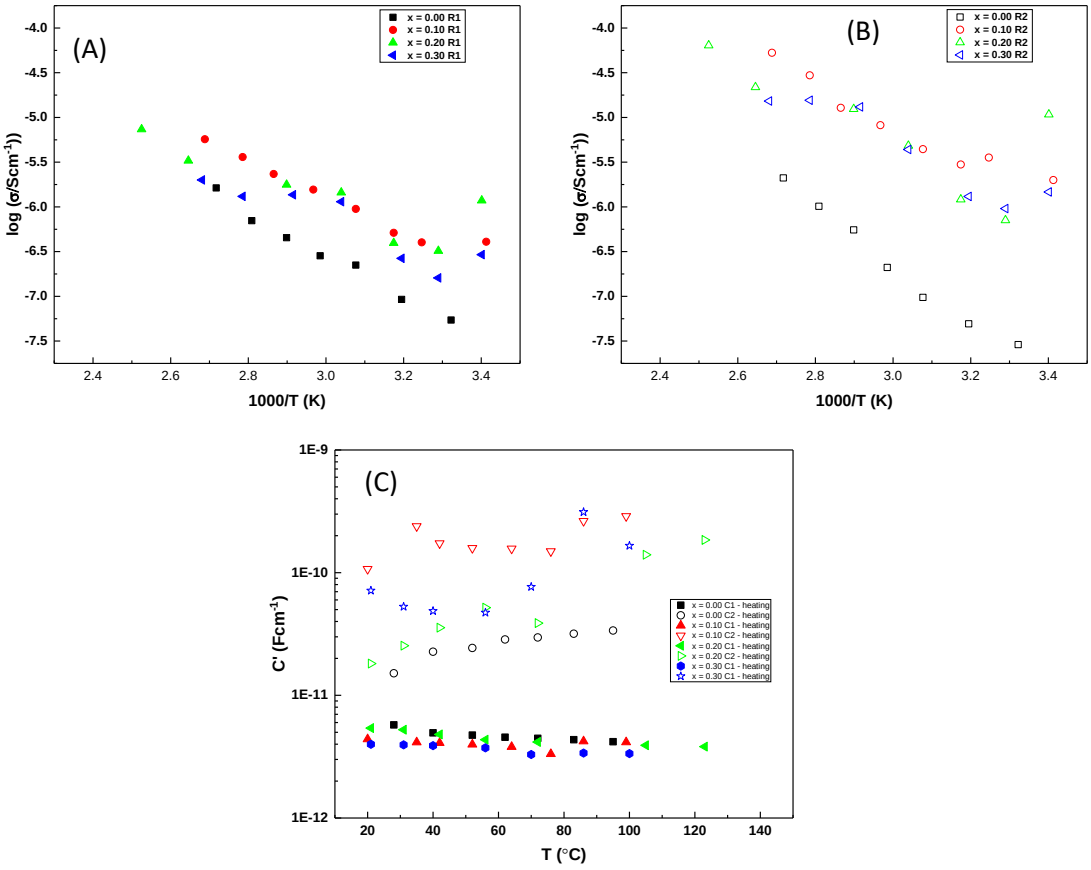

Figure 4.21. Extracted R and C values from the fitted equivalent circuit (RQC-RC) for x = 0.00 - 0.30 on heating. (A) Arrhenius conductivity plot comparing 1/R1. (B) Arrhenius conductivity plot from 1/R2 values. (C) Capacitance vs. temperature response comparing C1 and C2 values from the equivalent circuit.

Fig: 4.22A, shows the cooling data, where 1/R1 values for x = 0.00,0.20 and 0.30 remain similar but for x = 0.10 the conductivity is half an order of magnitude higher. Fig: 4.22B shows the 1/R2 values, x = 0.00 are the lowest, with x = 0.20 and 0.30 being almost half an order of magnitude higher, with the highest 1/R2 values being those for x = 0.10. Fig: 4.22C shows that during cooling, C1 values are very similar for x = 0.00 - 0.20, corresponding to ε_r of ~49 but for x = 0.30 they are slightly lower with ε_r of ~38. C2 remains high, with the

highest C2 for the conductive x = 0.10, whereas for x = 0.00, 0.20 and 0.30 C2 increases with x.

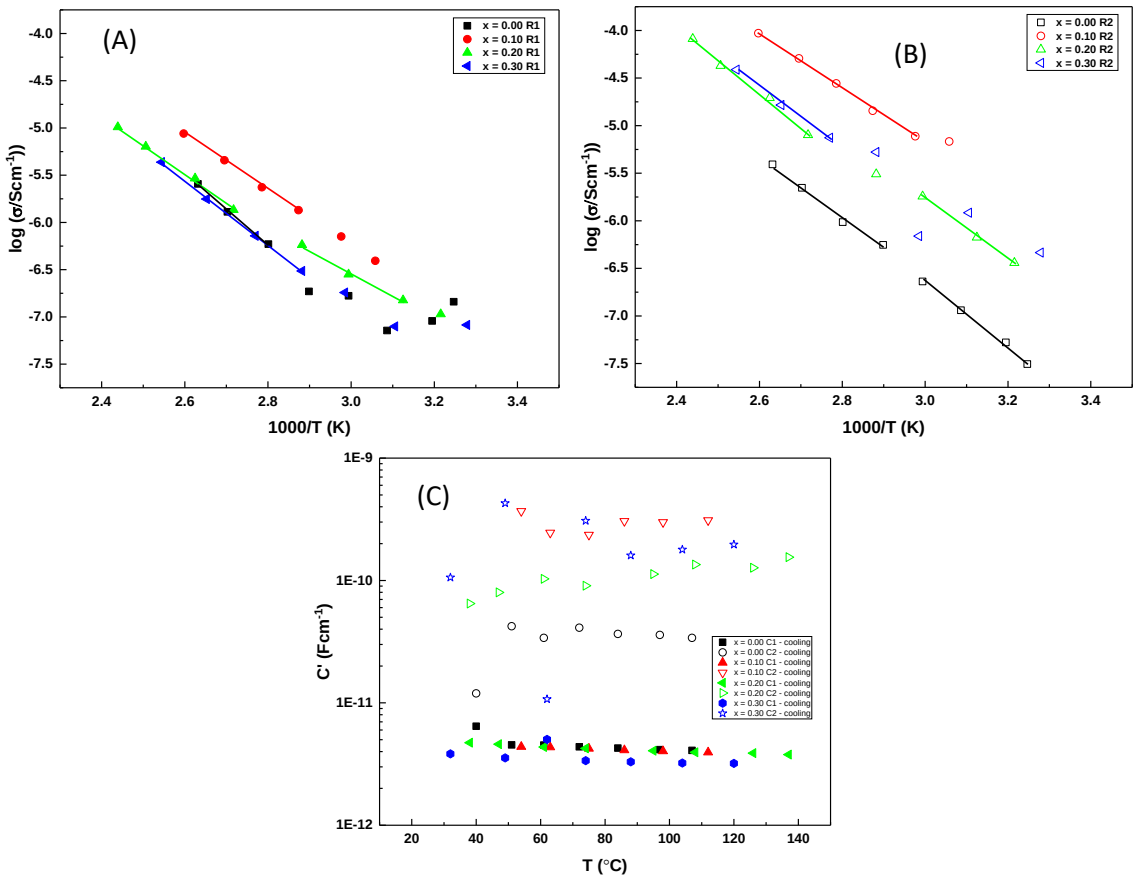

Figure 4.22. Extracted R and C values from the fitted equivalent circuit (RQC-RC) for x = 0.00 - 0.30 on cooling. (A) Arrhenius conductivity plot comparing 1/R1. (B) Arrhenius conductivity plot from 1/R2 values. (C) Capacitance vs. temperature response, comparing C1 and C2 values from the equivalent circuit.

Table 4.5 shows the E_a associated with 1/R1 and 1/R2 from the cooling cycle shown in Fig: 4.22A and B. For x = 0.00 1/R1 at higher temperatures has an E_a of 0.74 eV, at a lower temperature the conductivity rises, therefore an E_a cannot be obtained. For x = 0.10, E_a is 0.59 eV, for x = 0.20 the high temperature E_a is 0.62, whereas the lower temperature E_a is 0.48 eV. Finally, for x = 0.30 the high temperature E_a is 0.68 eV.

The E_a estimated from Fig: 4.22B for 1/R2 shows that x = 0.00 and 0.20 in the high temperature region have an E_a of 0.71 and 0.70 eV, respectively. Whereas, for the lower temperature region E_a is 0.68 and 0.63 eV, respectively. For x = 0.10 the high temperature region has an E_a of 0.58 eV, and for x = 0.30 it is 0.63 eV.

Table 4.5. Activation energy values, E_a, for 1/R1 and 1/R2 from Fig: 4.22A and B respectively, for the higher and lower temperature ranges.

Sample	R1 (high temperature)	R1 (low temperature)	R2 (high temperature)	R2 (low temperature)
0.00	**0.74 (±0.04)**		**0.71 (±0.04)**	**0.68 (±0.03)**
0.10	**0.59 (±0.01)**		**0.58 (±0.02)**	
0.20	**0.62 (±0.02)**	**0.48 (±0.04)**	**0.70 (±0.04)**	**0.63 (±0.02)**
0.30	**0.68 (±0.04)**		**0.63 (±0.03)**	

Fig: 4.23A shows the value of n for the x series on the heating cycle. For x = 0.00 n starts low at ~ 0.2, with high error. As the temperature is increased n remains similar when considering the errors involved. n for x = 0.10 has an initial value of ~ 0.31 and with an increase in temperature seems to remain constant within error (although there appears a peak for both x = 0.00 and 0.10 at ~55 ˚C but with high errors), however above 65 ˚C it increases linearly with temperature and since the errors are very small this seems to be a real trend. x = 0.20 and 0.30 show similar trends, increasing the temperature rapidly increases the value in n with a peak appearing for both at 70 ˚C, after which n starts to decrease.

On the cooling cycle, n for x = 0.30 almost stays constant, with little change within error. For x = 0.20, n stays constant at higher temperatures (~ 0.4) but below 100 ˚C, n starts to decrease (to a value of ~ 0.25) and below 60 ˚C errors become too high for any trend to be implied. Although the last cooling temperature at ~30 ˚C, n once again has a high value of 0.45. For x = 0.10, n seems to decrease with lowering temperature, below ~60 ˚C, n is linear within error and for x = 0.00 n stays constant, within error.

The general trend in n seems to be an increase in n with temperature, while at lower temperatures the errors are larger and at higher temperatures, the errors are either very small or minuscule. The changes in n along the temperature profile occur at the same temperatures where the data from LCR and impedance show a change in ε_r and conductivity values, i.e. ~60 and ~90-100 ˚C.

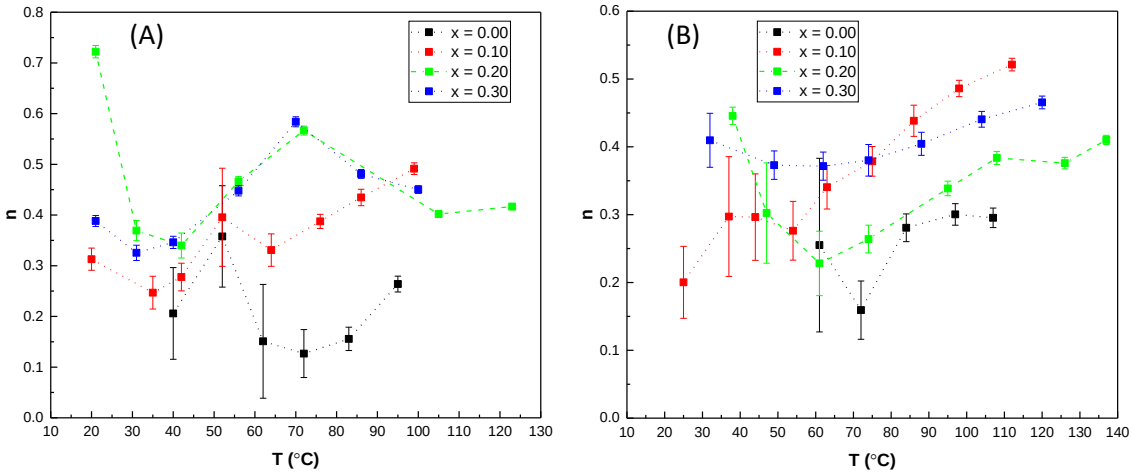

Figure 4.23. Variation of n for the CPE with temperature for the x series on heating (A) and cooling (B) cycles.

4.9. Discussion

4.9.1. Discussion of XRD/SEM and comparison to literature

The effects of varying the starting stoichiometry with temperature can be observed from the phase assemblage diagram shown in Fig: 4.2. Considering some MALI was synthesised at room temperature this showed there is a low formation energy associated with this perovskite phase. x = 0.00 has some perovskite being formed in the presence of the two precursors, therefore the reaction does not go to completion even with multiple grindings. Some new phase(s) are also formed and were attributed to LDPs. Based on XRD results, this trend remains similar for all samples in this series.

Comparing these results to the phase assemblage diagram formed from Song et al [5] for thin films shows that in thin films one could form a pure phase stoichiometric MALI at lower temperatures. The range of x for which MALI can be prepared as a single phase is also larger at higher temperatures as seen from Fig: 4.24. They also remain stable at temperatures up to ~ 180 ̊C, although this is because they were able to control the loss of MAI at higher temperatures by conducting experiments under a MAI-rich environment in attempts to control for its ease of evaporation, especially in thin-film form. TGA on MALI generally shows weight loss at temperatures above 200 ̊C, when synthesised using a solution or solid-state method [2]. However, this could be due to the heating rate and the short amount of time spent at a particular temperature. Although others showed that depending on conditions and temperature the range can vary between 140-240 ^{o}C, mainly by the release of HI and CH_3NH_2 gases [6].

XRD diffractograms for x = 0.05 and 0.10 agree with the thin film phase diagram, so the XRD patterns appear the same, however they attribute this MALI phase as an α' form based on stacked perovskite sheets as opposed to the pure cubic form of the α phase. These layered perovskites as discussed in the literature review, have the same crystallographic structures and are not distinguishable by XRD due to the long-range periodicity of the 3D framework but they are MAI-rich as based on energy dispersive x-ray spectroscopy [2].

This can also be backed up by the low-voltage SEM results in this work. Albeit the SEM results in Fig: 4.7, show that none of the samples at 120 ℃ are phase pure, due to there being excess MAI-rich regions present. These are distinguished by using low voltage SEM where the difference in contrast, corresponds to a different phase and or composition. The fraction of the darker regions attributed to an organic-rich phase increases with x. Therefore, the XRD sensitivity is insufficient to pick up the small amount of organic-rich regions that are present in x = 0.05 and 0.10 and/or the XRD patterns of the two phases are indistinguishable. The samples seem dense from the surface images and their calculated density from Fig: 4.8 is also high, however, this was calculated using only the geometry of the pellets and not a more accurate method such as Archimedes due to the ease of degradation of MALI in water. Although x = 0.05 and 0.10 'appear' phase pure via XRD from Fig: 4.6 there does not seem to be any trend in the lattice parameters when their errors are taken into account.

Song et al [5] were also able to observe the LDP phase but at much higher x values and also at higher temperatures. After 75% X_{MAI}, there only seems to be LDP present. The results from this work show that at higher x, there are perovskite peaks alongside the precursor MAI. Furthermore, the XRD peak intensities of the MAI phase increases with increasing x. The thin film work only shows MAI peaks when the nominal starting composition is close to a composition with 100% MAI. Therefore, what they attribute the LDP phase too could be a feature of the thin film procedure, or that the reaction is not complete and it's an intermediate phase in the reaction and due to the nature of MAI which can appear amorphous when dissolved in solution and reacted with PbI_2. This could be why they do not observe any MAI peaks in XRD data even at rather high x values.

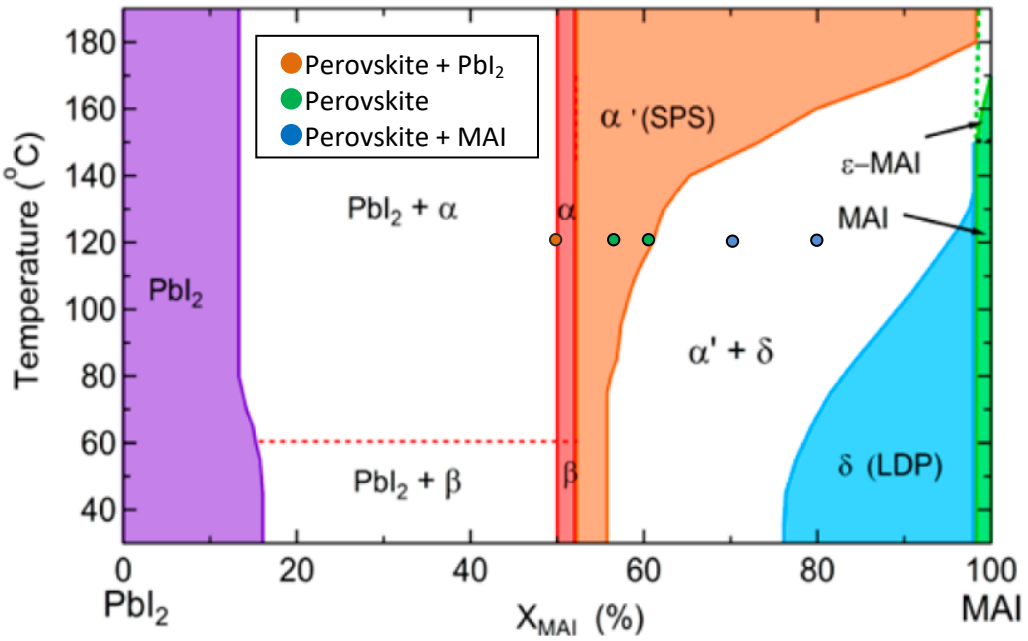

Figure 4.24. Thin film solution phase diagram with results from this work (prepared at 120 °C but measured at RT) included. Figure reproduced from [5].

The main conclusion is that although at least some MALI is formed at room temperature showing its ease of formation, solid state synthesis cannot supply enough energy prior to the loss of MA^+ ions to form phase pure MALI, even when heated to temperatures as high as 135 ˚C. Incomplete mixing of the precursors using solid state synthesis could also be a reason why LDP phase(s) are seen at lower x values.

The advantage of solid-state synthesis is that the effect of solvents can be eliminated. The XRD and SEM results showed some MALI can be formed at room temperature; however, due to the poor mixing method associated with hand grinding and without any heating applied to the process the reaction is incomplete. As a consequence, most of the precursors are not converted into the final product. The LDP formation at these low temperatures also limits the reaction towards the formation of pure MALI. The phase assemblage diagram via the XRD results shows elimination of these low temperature LDP phases with increasing temperature; however, the risk of MAI loss increases due to increasing reaction temperature. A nominal excess of MAI is required to obtain XRD patterns that contain peaks associated only with MALI. This loss of MAI need not only be due to elevated temperature but also because of the processing conditions. This involved multiple heating and grinding steps prior to XRD of the powders being performed without any solvent and this always resulted in some loss of the powders. This is especially true at 120 ˚C where the powders were subjected to four cycles of heating and grinding to ensure no subsequent change in the XRD patterns, in attempts to ensure reaction equilibrium.

The increasing amount of MAI into the MALI system shown by higher x values in the phase diagram does not result in any substantial non-stoichiometry within a single matrix as all lattice parameters seem similar, Fig: 4.6. Taking into consideration SEM, the results provide a more complex picture of the MALI system, where materials that had 'clean' XRD patterns showed the presence of organic-rich (possibly amorphous or poorly crystalline) regions.

Combining the data from XRD, SEM and the electrical data and comparing it to the thin film diagram, we can see that because the XRD is conducted at room temperature (RT), the MALI perovskite can be labelled as a β phase, due to it being the tetragonal polymorph. From section 2.2.2 in the literature review, the thin film study stated that increasing the MAI content brings about another phase labelled as α'. These stacked perovskite sheets, SPS (α') are a transitional phase between a 3D and a 2D structure where there are a limited number of stacking faults present to the extent that it can still withhold a 3D crystal. Although they are indistinguishable from XRD, (the amorphous or the poorly crystalline region are probably due to MAI in the material) they dominate the MAI-rich samples since it is the excess MAI that introduces the stacking faults in the crystal structure that generate the SPS phase. However, these can't be related to the dark regions in the SEM because they are related to MAI-rich regions/grains rather than the α' phase itself. Therefore, if α' exists it is seen as part of the grey regions in the SEM images. This is similar to what the thin film diagram in Fig: 4.24 shows because the MAI-rich sample region is not labelled as (α + α'), or (α + α' + δ), but as (α'), or (α' + δ) respectively, thus indicating that introducing more MAI changes the MALI itself due to staking faults being present. In conclusion, the dark regions are just amorphous organic material or crystalline MALI (either MAI, or MAI-rich grains) and that β and SPS MALI coexist in the grey perovskite areas but the contrast is insufficient to separate them in SEM but there seems to be evidence of their existence from the IS results.

Thin films have a rapid heat transfer and larger surface to volume ratio and these results could be different when working with bulk powders. It could also be that the grey perovskite region, which is the tetragonal, β MALI phase could contain some α' phase which could explain some of the inhomogeneity in the IS results. The complexity of the IS results leads to the necessary use of a two element circuit, even if the time constants of the two elements are quite close. The use of R1C1 and R2C2 could be due to the mixture of the tetragonal β MALI and SPS, α' phase in the perovskite. Another possibility is of core-shell microstructure but the volume fractions and distribution of β and α' may be complex and beyond the detection of the low voltage SEM.

This possibility of both being present in the grey perovskite region in SEM images could also explain some of the other electrical results. For example, it might be that the tetragonal β MALI and α' have different moisture sensitivity which could play a factor in the enhanced permittivity/conductivity of the material but this would only be on the heating cycle. This apparent higher permittivity might be related to incorrect correction for the sample geometry as α' has a low volume fraction compared to β MALI. It might also be related to space charge effects in α'due to much higher conductivity on the initial heating due to a higher uptake of water. The results from the circuit fitting showed the C2 data to have a peak at ~ 90 ̊C, whereas C1 remained constant, it could therefore be that there is significant dehydration associated with the SPS α' phase. However, it must be stated that since it is hard to distinguish between β and α' in XRD, and in SEM the darker regions are observed for MAI-rich samples, this explanation is mostly derived from the more complicated electrical response. Further work is required is substantiate this hypothesis.

4.9.2. Discussion of the electrical data

4.9.2.1. LCR

The samples across this series were tested using LCR to establish any permittivity vs. temperature relationships. The results for x = 0.00 which only has MALI and PbI_2 based on XRD data and has no sign of dark organic-rich regions from SEM, are shown in Fig: 4.9A and F. The results will therefore not be influenced by any excess organic precursor and since PbI_2 is electrically resistive in this temperature region the results should be dominated by the MALI phase(s). x = 0.00 shows near reversible permittivity behaviour on heating and cooling but with some indications of possible changes at lower frequencies, shown in Fig: 4.9A. tan δ is low but it is not completely reversible on thermal cycling, Fig: 4.9F. This indicates there may be MALI-related moisture issues in the electrical properties of x = 0.00. This becomes borne out in the impedance data. There is no evidence of a peak in permittivity or tan δ at the tetragonal-cubic phase transition associated with MALI.

As x increases the permittivity and loss behaviour becomes more complex, even at 1 MHz. This is only on the heating cycle, whereas no peaks are observed on the cooling cycle. This is clearly shown from the tan δ plots in Fig: 4.9F, and at these higher x samples of x = 0.10 - 0.30, two distinct events become clear, one at ~ 61 ̊C and the other at ~91 ̊C. At 61 ̊C there is a peak, which is attributed to the tetragonal to cubic transition of the MALI perovskite (so goes from β to α). For the event at 91̊C, it could be due to water-loss, since the powders have already been heated multiple times at 120 ̊C but stored at room temperature

prior to electrical measurements. Further chemical reaction between MALI, PbI_2, MAI and LDP's is ruled out and the temperature (~ 90 ^oC) is too low for decomposition.

To investigate the irreversibility, x = 0.10 was tested thrice at different time intervals, as shown in Fig: 4.9G. The first heating LCR cycle showed the complex permittivity phenomena, the second heating cycle immediately after the first heating/cooling cycle showed no peaks at either temperature or the rise of permittivity with temperature. When the same sample was tested again after 2 weeks, a similar trend to the first heating cycle was observed. This indicates the presence of space charge, which is both higher on the first cycle and also across the x series with higher organic content and is related to resting/ageing and enhanced moisture sensitivity. This also appears to make the tetragonal to cubic transition temperature in MALI detectable by LCR measurements. The moisture sensitivity makes proton uptake possible, and with higher x, because the more organic material there is, the more moisture can be absorbed and the clearer the tetragonal to cubic transition phase change can be observed. When the moisture is driven off the same phenomena are not seen on the cooling cycle.

Space charge also makes the phenomenon occurring at 91℃, easier to observe. Since no solvent is used it can't be due to solvent and also the use of solvent makes the material pick up water more easily from the atmosphere [7]. The absence of solvent in the synthesis implies additional moisture can be picked up by the excess organic-rich phases present in x>0. x = 0.00 had the least amount of MAI in the starting composition and evidence of MAI-rich regions, with both x = 0.05 and 0.10 having more MAI in the starting composition and evidence of more darker regions associated with MAI-rich regions present on the surface. The results for x = 0.00 at 1 MHz are a smooth trend of decreasing permittivity with increasing temperature. In contrast, for the other two there is an increase in both permittivity and loss. Making the materials from an organic-rich starting composition can therefore increase the level of SPS (α') moisture content and this increases the space charge contribution, which elucidates the ease with which another phenomenon in the material (such as the tetragonal to cubic phase transition in MALI) is observed.

4.9.2.2. Impedance

The impedance results from Fig: 4.10 and table 4.1, show that on heating and cooling C1 can be attributed to the bulk MALI permittivity, since C2 has a much larger magnitude (~250). Although on heating C1 is low (~28) compared to values reported in the literature (range from 38 - 45) [8],[9],[10]. On cooling, however, it shows more of a resemblance, with

a value of 36. Once again, the cooling results show a closer response to bulk MALI. This is presumably related to the irreversible water-loss on the initial heating cycle.

Samples are more conductive on heating than on cooling, with x = 0.00 having the largest total resistance on both cycles. Their Z^* and M"/Z" plots in Fig: 4.11 and 4.12 show there are (at least) two-components present. Their presence becomes harder to observe by hand fitting as x increases and also as the measurements are conducted on the cooling cycle. From the hand fitting data tabulated in Tables 4.2 and 4.3, it can be deduced that M" and $Z"_1$ peaks both correspond closer to the bulk MALI behaviour whereas the $Z"_2$ corresponds to a secondary element due to it much higher permittivity value, and as discussed previously, it could be due to some α' present alongside the β MALI in the grey regions of the SEM results. MALI is reported to be a mixed conductor [11], however the low frequency response doesn't show any evidence of a high capacitance Warburg or electrode related response. The magnitude of the capacitance for the lower frequency element is more closely related to the presence of a secondary phase. These results possibly correlate with the SEM results, where different phases are present. In addition to the possibility of the second element being associated with α' it could also be due to a secondary phase (most likely to be MAI, or partially reacted MAI-PbI_2 that is MAI rich), or possibly a grain boundary (constriction) response.

The impedance and LCR results are readily linked, firstly from Fig: 4.13 where the permittivity from the LCR measurements as superimposed on the capacitance values obtained from Impedance. These show general agreement, except the magnitudes slightly differ probably due to the non-ideal M" Debye peak used to extract C values from the impedance results. Also, from the impedance results x > 0.00 are more conductive. Unlike the resistive x = 0.00 where both elements are clearly observed due to there being sufficient separation of their f_{max} values for x > 0 the resolution of the two responses is not so apparent. However, the M" peak in all samples seems to be dominated by the MALI response. From the XRD and SEM results, precursors can remain present (MAI or PbI_2) in addition to MALI perovskite itself. Although its feasible that the secondary response (R2C2) may be attributed to MAI or PbI_2, this is deemed unlikely as PbI_2 is electrically resistive and MAI very conductive and the f_{max} values for R2C2 for x = 0 and > 0, respectively do not corroborate with the precursors. As mentioned previously in section 4.8.1, this second response could be due to another type of MALI like the SPS phase (α').

The impedance results also illustrate it is the addition of excess organic precursor in the starting composition that causes the electrical response to be more complicated. This is seen even more so by the conductivity Arrhenius plots from Fig: 4.14. Increasing x > 0.00 increases the conductivity of the material slightly, which remains intact for some like x = 0.10 on the cooling cycle. This indicates when moisture is removed the conductivity still remains higher than x = 0.00 and this may be related to the increase in MAI content.

The activation energy from hand fitting cooling Arrhenius plot data in Fig: 4.14 is high for x = 0.00 at 0.82 eV whereas in the literature it is reported to be ~ 0.45-0.5 eV [8][12]. For x = 0.05-0.20 their activation energy tends to be closer at ~ 0.59 eV whereas for 0.30 it increases again. It could be high for x = 0.00 due to the excess PbI_2 and incomplete reaction, whereas adding some excess MAI in the starting composition makes the samples more conductive, adding too much decreases the conductivity. This variation in conductivity could be either due to the ease of loss of powders through the grinding and heating process. It could also be that if both β and α' phases coexist, especially in the off-stoichiometric samples, then an increase in the volume fraction of α' may result in an overall increase in the conductivity of the samples; however, adding too much excess MAI results in distinct MAI precursor being retained as opposed to forming α' MALI and the overall conductivity starts to decrease.

From the circuit fitting results the activation energy values shown in table: 4.5 for R1 and R2 have similar values above 65 ̊C. This suggest a similar conduction mechanism in these phases. This is where linear behaviour is obtained and therefore the values obtained are more reliable. The slight rise in conductivity during the cooling cycle at lower temperature is attributed to the pickup of moisture again. The only difference seems to be for the values between x = 0.00 when comparing hand to circuit fitting. For x = 0.00 both R1 and R2 have E_a of ~0.74 eV if errors are taken into account, whereas for hand fitting it is larger at ~0.82eV. But for x = 0.10-0.30 they are all very similar. Although for x = 0.00 the activation energy had decreased when using the circuit fitting data, it is still higher than what is expected for MALI. The similarity in E_a for R1 and R2, at least in the higher temperature region could indicate that both the MALI and the secondary phase have similar electrical behaviour. As discussed previously with the possibility of β and α' coexisting, the two responses could be attributed to these phases.

4.9.2.3. Equivalent circuit

Equivalent circuit fitting was used because the IS data showed the need for more than one element and because the time constants are so close that IS cannot be applied. This makes it harder to distinguish between the two responses using only hand fitting. When both circuits shown in Fig: 4.15A and B are applied to the raw data in fitting, it's clearly shown in Fig: 4.16 and 4.18 that for all the samples an RQC-RC circuit provides a better fit to the data. This agrees with the combined XRD and SEM data, where none of the samples are completely homogenous.

Fig: 4.21 and 4.22 show the extracted R and C plots vs. temperature, on heating and cooling cycles, respectively. The R1 and C1 element can be easily attributed to the bulk MALI response whereas R2 and C2 correspond to the secondary response. And it is in the C2 data that a peak at ~ 90 ˚C (as seen in the LCR results) is clear, whereas C1 is temperature invariant with a magnitude corresponding to the permittivity of MALI. The tetragonal to cubic phase transition (β to α) is hard to pinpoint due to the number of data points, as seen by Fig: 4.13. As has been mentioned before, the possibility of both β to α' existing together simultaneously could explain the existing need of the two elements R1C1, and R2C2, even though in some samples the time constants for both are very close.

In general, the circuit fittings show when slightly excess MAI is present the conductivity is increased (and this phenomenon is enhanced in subsequent chapters where synthesis is more controlled) and remains so on cooling, Fig: 4.21 and 4.22A. Controlling the stoichiometry can be challenging and some studies show that in order to produce a stoichiometric perovskite film, more MAI is needed than PbI_2. This type of self-doping can change the semiconductor type, when there is more MAI present this could lead to p-type semiconduction [13].

The C1 values remains similar to bulk MALI. Based on permittivity that C1 and R1 are the MALI response then it is only at higher temperatures on the heating cycle (Fig 4.21 A) and on the cooling cycle above 1000T/K =2.8, (Fig 4.22 A) that there is a good agreement for 1/R1. At lower temperatures on cooling and on the heating cycle, the values are variable. This could be a strong indicator of moisture sensitivity interfering with the electrical measurements. At these lower temperatures during the cooling cycle the conductivity rises again, especially because IS data collection take a minimum of 35 minutes for temperature equilibration on the heating cycle and longer on the cooling cycle. Therefore, there could be sufficient time to pick up water from the atmosphere during cooling cycle impedance measurements, especially at temperatures close to room temperature.

The second component R2 and C2 could be a secondary phase related to organics, grain boundary or where β and α' type MALI coexist (either as an intimate mixture or as a core-shell microstructure). If it is purely due to organic-excess matter then the conductivity might have been even higher for x = 0.20 and 0.30 than x = 0.05 and 0.10. As C2 for x = 0.00 is an order of magnitude lower than when x is > 0.00, what C2 may be attributed to might change depending on adding of excess MAI. It could be a grain boundary in x = 0.00 but linked to secondary phases in x > 0.00. It might also be that if it's a core-shell phenomenon, its thickness might change with variation of MAI content. This may be possible depending on how MALI grows, as discussed in the solid state reaction mechanism, it could lead to a heterogeneous microstructure. The heating data for 1/R2 seems to mirror 1/R1 for their temperature dependence (Fig 4.21B) which is odd for a GB (unless it's a constriction resistance) but would make some sense for a shell.

4.9.3. Conclusions

Solid state synthesis shows that MALI has a low formation energy. Although XRD data may show a phase-pure region over a variable range of nominal starting compositions that are MAI-rich, SEM clearly shows that none of the samples are phase pure. This means that low levels and/or amorphous MAI-rich phases are not detectable by laboratory XRD. Although MAI or MAI-rich regions are hard to detect by XRD below x < 0.20 (probably because they are amorphous/poorly crystalline or generate XRD patterns similar to 3D MALI) at x = 0.20 crystalline MAI appears and remains at higher x. In conclusion, there is no substantial evidence for any significant non-stoichiometry in 3D MALI (or at least it is too low to detect by the methods employed in this thesis). Instead, it appears that coexistence of various dimensionalities of MALI is possible.

At this stage, sample inhomogeneity is attributed to hand grinding and heating to a maximum temperature of 135 ̊C which are insufficient to prepare a phase pure material. The inability for complete mixing to occur has a dramatic effect on the electrical properties especially if they are made more organic-rich, since there might be different types and distribution of secondary phases depending on x, eg MAI, LDP, SPS.

From LCR and impedance data x = 0.00 is not electrically homogenous, although the LCR data are close to being reversible on heating/cooling albeit with some evidence of moisture loss/uptake on thermal cycling. There is no evidence of the tetragonal/cubic polymorphic phase transition. Excess organic matter in the starting composition makes the samples more conductive especially on the first heating cycle and possibly makes them more susceptible to pick up water on ageing at room temperature as seen from Fig: 4.9H.

Compositions of x > 0.00, show evidence of two electrical phenomena at 61 and 91℃, probably due to space charge associated with moisture-pick up in the samples. One is attributed to the tetragonal to cubic MALI transition at 61 ℃. This is seen again in the capacitance vs. temperature analysis of impedance data extracted from equivalent circuit analysis. The phenomenon at 91 ℃ which is more pronounced for x> 0 seems most likely to be associated with water loss as there is more organic-rich phase(s) present in those samples.

Excess MAI in MALI samples can have a large influence on the electrical data. The impedance showed that higher x of 0.05 and 0.10 increases the conductivity. This remained high on both heating and cooling cycles, and even above 65 ℃. The higher x values of 0.20 and 0.30, show a drop in conductivity at temperatures of higher than 65 ℃. On the cooling cycle the conductivity remains low, therefore excess MAI (when $x \geq 0.20$) seems to decrease the overall conductivity. LCR data show more information because data are collected over smaller temperature intervals. The LCR collects data every minute by increasing the temperature by 1degree unit, and the heating and cooling cycle takes on average about 4 hours. In contrast, impedance measurements take 35 minutes to equilibrate at each change in temperature and each time the temperature is changed by about 15 degrees. LCR data can therefore readily identify temperatures of interest and aspects of reversibility. impedance spectroscopy for these materials is also hampered by the poor separation of the time constants between at least two responses. The hand-fitted IS data, however, showed good M" and LCR C versus T relationships as seen from Fig: 4.13, so the bulk MALI properties could be extracted from the M" peak. The discrepancy in some values is attributed to the broad, non-ideal M" peak.

The difficulty of separation between the different electrical responses of the two elements using hand fitting could not be relied upon to elucidate the electrical microstructure, therefore circuit fitting analysis had to be undertaken. This was due to the second (higher capacitance) response, which is present in all samples. Circuit fitting suggested this component to be less resistive than bulk MALI for x> 0.00. This may be consistent with the existence of an α' phase, organic rich regions and/or the development of an interfacial region between the phases that can give enhanced conductivity when moisture has been absorbed in the ceramics. However even this proved to be problematic because the resistance values were variable with temperature and cycling (for x = 0.00, 0.20 and 0.30 with similar magnitudes, whereas it was higher for 0.05 and 0.10) and C1 and C2 differed by a maximum of ~ 2 orders

of magnitude, therefore, the time constants weren't particularly favourable for impedance analysis.

Overall, LCR and low voltage SEM appear more favourable to elucidate the material quality and properties of MALI than XRD and Impedance, unless equivalent circuit fitting is used. This is because the material is very sensitive to temperature and time, either during heating or during the measurements. Artefacts can be introduced during measurements as was seen when using SEM where the surface can be damaged if too much time/too high a voltage is taken to record data from a selected area. Also, local regions in the microstructure, of either non-stoichiometry or secondary phases can have significant effects on the electrical data, however, XRD and impedance measure average rather than local properties.

References

[1] D. Prochowicz, M. Franckev, A. M. Cié Slak, S. M. Zakeeruddin, M. G. Atzel, and J. Lewí, 'Mechanosynthesis of the hybrid perovskite $CH_3NH_3PbI_3$: characterization and the corresponding solar cell efficiency', *J. Mater. Chem. A Mater. energy Sustain.*, vol. 3, issue. 41, pp. 20772-20777, 2015.

[2] C. C. Stoumpos, C. D. Malliakas, and M. G. Kanatzidis, 'Organic Tin and Lead Iodide Perovskites with Organic Cations : Unique Semiconductors , with Phase Transitions and Near-infrared Photoluminescent Properties', *Inorg. Chem.*, vol. 52, no. 15, pp. 9019–9038, 2013.

[3] K. V Manukyan, A. V Yeghishyan, D. O. Moskovskikh, J. Kapaldo, A. Mintairov, and A. S. Mukasyan, 'Mechanochemical synthesis of methylammonium lead iodide perovskite', *J. Mater. Sci.*, vol. 51, no. 19, pp. 9123–9130, 2016.

[4] A. D. Jodlowski, A. Yepez, R. Luque, L. Camacho, and G. de Miguel, 'Benign-by-Design Solventless Mechanochemical Synthesis of Three, Two, and One-Dimensional Hybrid Perovskites', *Angew. Chemie Int. Ed.*, vol. 55, no. 48, pp. 14972–14977, 2016

[5] Z. Song, S. C. Watthage, A. B. Phillips, B. L. Tompkins, R. J. Ellingson, and M. J. Heben, 'Impact of Processing Temperature and Composition on the Formation of methylammonium Lead Iodide Perovskites', *Chem. Mater.*, vol. 27, no. 13, pp. 4612–4619, 2015.

[6] A. Latini, G. Gigli, and A. Ciccioli, 'A study on the nature of the thermal decomposition of methylammonium lead iodide perovskite, $CH_3NH_3PbI_3$: an attempt to rationalise contradictory experimental results', *Sustain. Energy Fuels*, vol. 1, no. 6, pp. 1351–1357, 2017.

[7] K. Shoyama, W. Sato, Y. Guo, and E. Nakamura, 'E ff ects of water on the forward and backward conversions of lead (II) iodide to methylammonium lead perovskite', vol. 5, no.45, pp. 23815–23821, 2017.

[8] M. N. F. Hoque, N. Islam, Z. Li, G. Ren, K. Zhu, and Z. Fan, 'Ionic and Optical Properties of methylammonium Lead Iodide Perovskite across the Tetragonal Cubic Structural Phase Transition', *ChemSusChem*, vol. 9, no. 18, pp. 1864-5631, 2016

[9] M. N. F. Hoque *et al.*, 'Polarization and Dielectric Study of methylammonium Lead Iodide Thin Film to Reveal its Nonferroelectric Nature under Solar Cell Operating Conditions', *ACS Energy Lett.*, vol. 1, no. 1, pp. 142–149, Jul. 2016.

[10] I. Anusca *et al.*, 'Dielectric Response : Answer to Many Questions in the methylammonium Lead Halide Solar Cell Absorbers', vol.7, no. 19, pp. 1–12, 2017.

[11] A. Senocrate *et al.*, 'The Nature of Ion Conduction in methylammonium Lead Iodide : A Multimethod Approach', Angew. chem. int., vol. 55, no. 27, pp. 7755-7759, 2017

[12] O. S. Game, G. J. Buchsbaum, Y. Zhou, N. P. Padture, and A. I. Kingon, 'Ions Matter: Description of the Anomalous Electronic Behavior in methylammonium Lead Halide Perovskite Devices', *Adv. Funct. Mater.*, vol. 27, no. 16, p. 1606584, 2017.

[13] Q. Wang *et al.*, 'Qualifying composition dependent p and n self-doping in $CH_3NH_3PbI_3$', *Appl. Phys. Lett.*, vol.105, no.16,pp.163508, 2014

5. Ball milled synthesis of MALI

5.1. Executive Summary of Chapter 5.

This chapter summarises the results from ball milling synthesis but for a wider range of x, i.e from -0.90 (PbI_2-rich) to 0.90 (MAI-rich). The reaction mechanism is similar to the solid state synthesis using a mortar and pestle (chapter 4); however, the process has increased energy input due to using a mill, along with the use of ethanol. The resultant powders showed some differences to that obtained in chapter 4. The structural and morphological results from XRD and SEM showed all samples to be impure and contain additional phase(s) to MALI. PbI_2-rich samples ($x < 0.00$) and $x = 0.00$ and 0.05 contained excess PbI_2, which appear both in the XRD patterns and in the SEM images as light regions. MAI-rich samples ($x > 0.20$) appear with crystallised MAI in their XRD patterns and as dark regions in SEM. At x values of 0.10 and 0.20, the samples appear clean from XRD patterns but SEM reveals dark regions among the gray perovskite phase. The milling process along with the annealing at 80 ˚C in order to evaporate the ethanol produces powders that don't show any change in their phase assemblage upto annealing at 140 ^{o}C. The phase assemblage diagram shows that MALI starts decomposing above 140 ˚C, as most samples in the MAI-rich region show phase assemblage changes due to the decomposition of the organic cation.

The LCR and IS electrical data for the ball milled samples show broadly similar behaviour to the solid state samples in chapter 4. However, due to better processing conditions, in which more energy is put into the mixing of the reagents in the ball mill the resulting powders are more homogenous. Samples still show hysteresis in the LCR data on an initial heating and cooling cycle associated with uptake of water however the presence of well-defined peaks in permittivity and/or dielectric loss at 60 and 90 ^{o}C are less pronounced. The electrical data of samples along x from both the LCR and IS measurements show the same general trend as that observed in chapter 4. PbI_2-rich (low or negative x) samples have low dielectric losses and low conductivity, intermediate x-samples ($x = 0.10$ and 0.20) that have clean XRD patterns but show existence of MAI-rich regions via SEM have enhanced conductivity and those with high x values ($x > 0.20$) that contain crystallised MAI in their XRD patterns have lower conductivity.

IS analysis based on equivalent circuit fitting of the data showed that MAI-rich samples are more electrically heterogeneous than PbI_2-rich samples. The series circuit combination of a parallel R-C-CPE with a parallel RC element still provides a better fit than a

single R-C-CPE circuit for all samples; however, for PbI_2-excess samples the difference between the two circuits becomes harder to distinguish/justify.

IS measurements near room temperature on pellets of the precursor phases PbI_2 and MAI showed PbI_2 and MAI to be electrically insulating and more conductive than the MALI dominated x-series samples, respectively. This shows the variation in the electrical properties based on variable MAI/PbI_2 precursor ratios (x values) may be related to the development of composite microstructures. For $-0.20 \leq x \leq 0.05$ the β-form of MALI (tetragonal) dominates the electrical properties whereas there is compositional range of $x \sim 0.10$ to 0.20 where the β- and α' phases of MALI can coexist and as discussed in chapter 4 this can give rise to much higher conductivity. However, for $x = 0.50$ when the excess MAI is crystallised as a secondary phase, the samples revert to more insulating behaviour.

5.2. XRD

The samples synthesised via ball milling were heat treated at higher temperatures and their RT XRD patterns collected. This was used to analyse the phases present at RT and to establish the influence of the annealing temperature on the phase assemblage. This information was used to plot the phase assemblage diagram shown in Fig: 5.1. The diagram shows annealing temperature versus x, where x is varied on the positive axis to reduce the PbI_2 content and have MAI-rich compositions, of formula $CH_3NH_3Pb_{(1-x)}I_{(3-2x)}$. On the negative axis, the MAI amount is reduced, producing PbI_2-rich compositions of formula $(CH_3NH_3)_{(1+x)}PbI_{(3+x)}$.

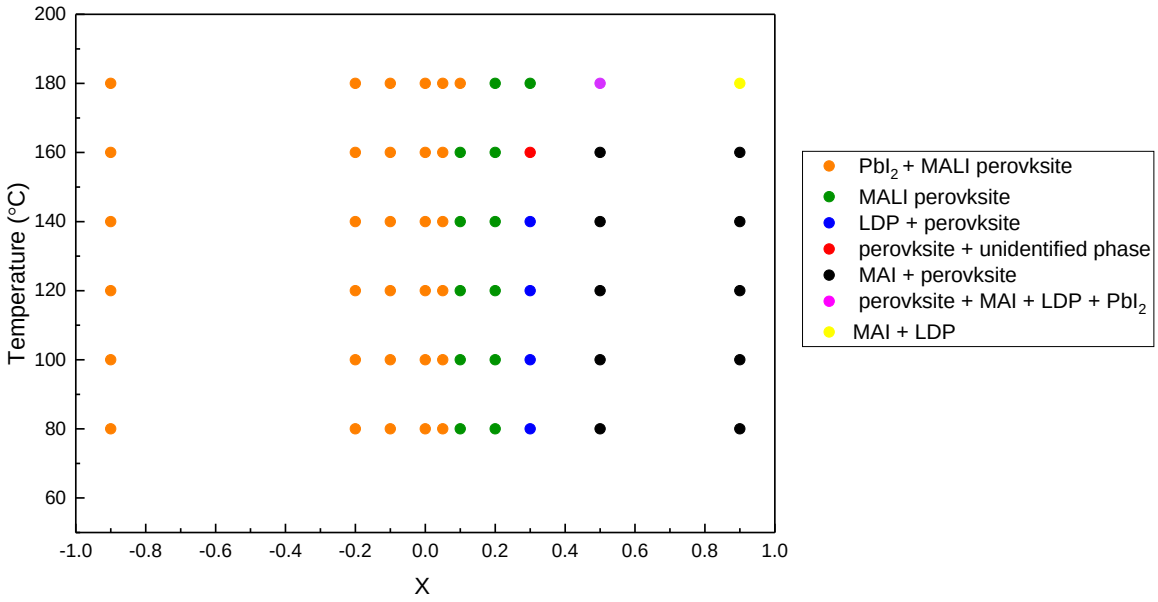

Figure 5.1. The room temperature phase assemblage diagram for samples prepared by ball mill synthesis at various annealing temperatures.

x = -0.90 was first annealed at 80 ˚C and RT XRD showed it to contain PbI_2 and the MALI perovskite phase. The same phases were retained after subsequent heat treatments between 80 and 180 ˚C. x = -0.20, -0.10, 0.00, and 0.05 all contain a two-phase mixture of PbI_2 and the MALI perovskite phase. No changes in the phase assemblage were observed for higher temperature anneals in these samples. After x = 0.10 and 0.20 were annealed at 80 ˚C only the perovskite phase was present via RT XRD. After annealing the powders up to 180 ˚C, x = 0.10 shows the emergence of PbI_2 whereas x = 0.20 retains only the perovskite phase.

Reducing the PbI_2 content further and therefore making the composition more MAI-rich, x = 0.30 displays another phase in addition to the perovskite. After annealing at 80 ˚C the RT XRD shows lower dimensional perovskite(s) (LDP) which are present in addition to MALI for anneals up to 160 ˚C. At this point the peak in the RT XRD attributed to the LDP is no longer present but other broad peaks occur which are associated with an unidentified phase(s). Further annealing to 180 ˚C shows only the perovskite phase to be present via XRD.

After annealing x = 0.50 at 80 ˚C RT XRD shows two phases present, perovskite and MAI. These are present after higher heat treatments until 160 ˚C. After 180 ˚C annealing, at least four phases are present. These are perovskite, MAI, LDP and PbI_2. A composition with greatly reduced PbI_2, i.e. x = 0.90, shows similar phases to be present (MAI + perovskite) as for x = 0.50, until 160 ˚C. After 180 ˚C annealing, however the perovskite peaks disappear in the RT XRD data and only the MAI and LDP phases are present.

5.2.1. Stoichiometric MALI

A nominally starting stoichiometric MALI composition was synthesised using the ball milling route. The resulting powders were then characterised using XRD. The results of this are shown in Fig: 5.2, where the precursors were ball milled for 1 hour, showing PbI_2 was always present, even when the powders were annealed at higher temperatures up to 150 ̊C.

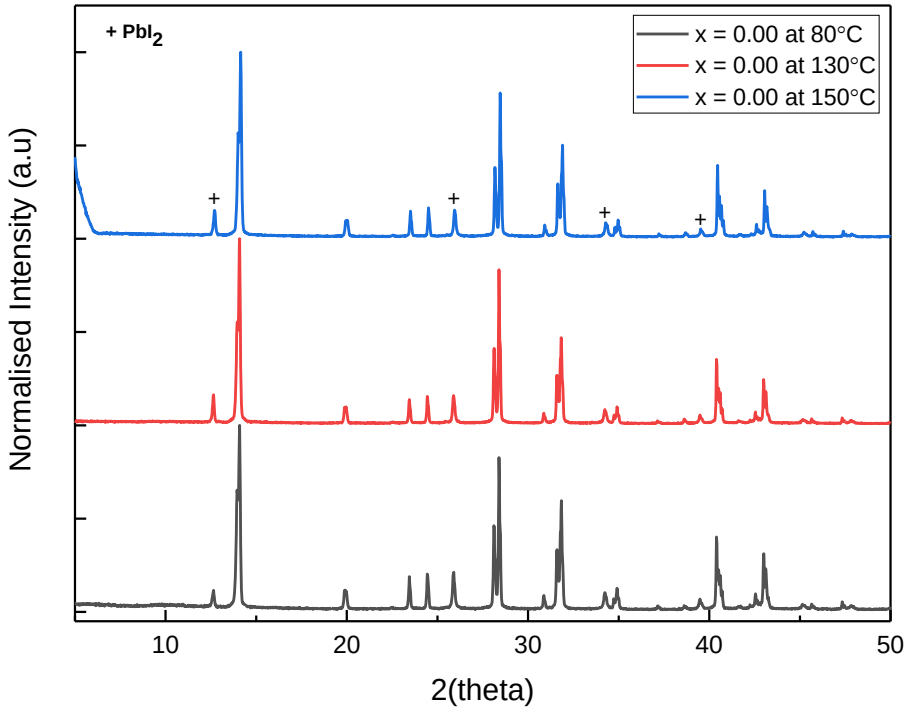

Figure 5.2. XRD patterns for nominally stoichiometric MALI synthesised via ball milling in ethanol for 1hr. Oven dried at 80℃ and powders further heat treated at 130 and 150℃.

The ball milling time was increased from 1 to 6 hrs to test if this might reduce the level of PbI_2 secondary phase and form a phase pure MALI sample. The results for this are shown in Fig: 5.3. The powders were then annealed at higher temperatures to see if it had any effect on the presence of the PbI_2 content. XRD showed that it was still present and therefore phase-pure MALI could not be prepared from a nominally stoichiometric starting composition via ball milling. Compared to the main perovskite peak observed in XRD, the PbI_2 peaks decreased in intensity when the ball milling time increased.

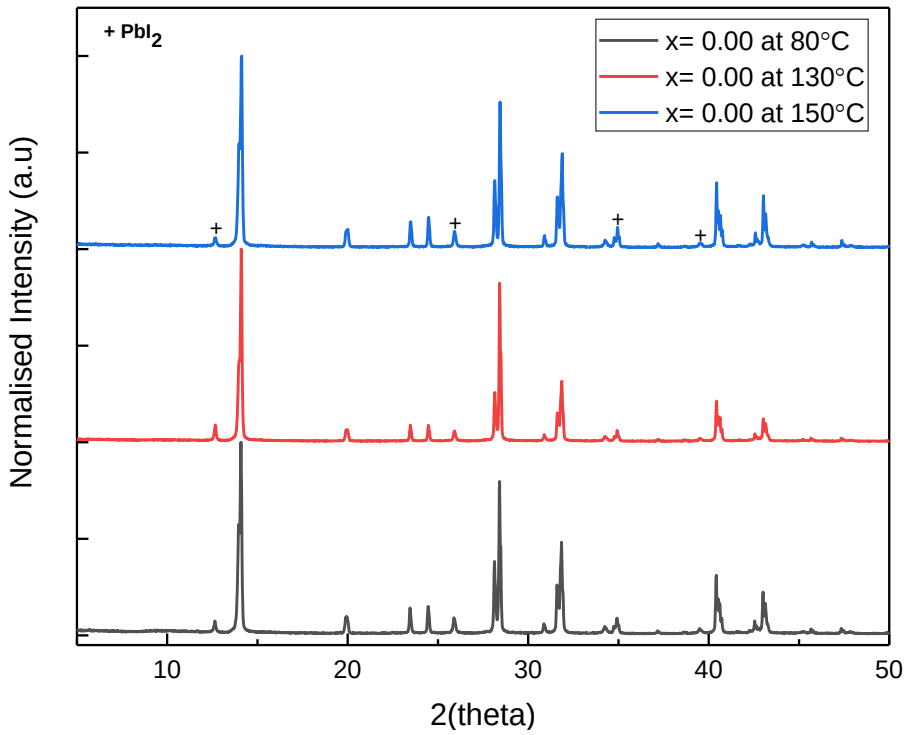

Figure 5.3. XRD patterns for nominally stoichiometric MALI synthesised via ball milling in ethanol for 6 hr. Oven died at 80℃ and powders further heat treated at 130 and 150℃.

5.2.2. PbI_2-deficient MALI - Ball Milling

The PbI_2 content in the starting composition was reduced (x > 0.00), because via the ball milling route phase-pure MALI could not be synthesised based on a nominally stoichiometric starting composition (x = 0.00). As the secondary phase present was PbI_2, reducing the starting PbI_2 content may produce phase pure MALI via ball milling. Fig: 5.4 shows the range of compositions of MALI for which the PbI_2 content was reduced.

PbI_2 was still present as a secondary phase for x = 0.05 and 0.07, respectively; however, x = 0.10 and 0.20 were phase-pure based on XRD. x = 0.30 showed extra peaks corresponding to lower dimensional perovskites (LDP) in addition to the perovskite phase. x = 0.50 and 0.90 did not show the LDP phase but the emergence of MAI precursor peaks, with their peak intensities increasing with x.

The ball milling route also tends to give results that are not reproducible, at least for x = 0.05, despite the same nominal preparation procedures being followed. This can be seen from Fig: 5.5, where three different batches of x = 0.05 were synthesised under the same nominal conditions. The first batch produced a sample that was phase-pure by XRD; however, the 2nd and 3rd batches contained additional PbI_2.This phase could not be removed on further grinding and annealing at the same temperature of 80 ℃. For other compositions such as x = 0.10, where x is higher, the initial XRD pattern for a sample might not be phase

pure. Further heating and grinding however produced a phase pure sample via XRD. For lower x values such as x = 0.05, the results were more processing sensitive.

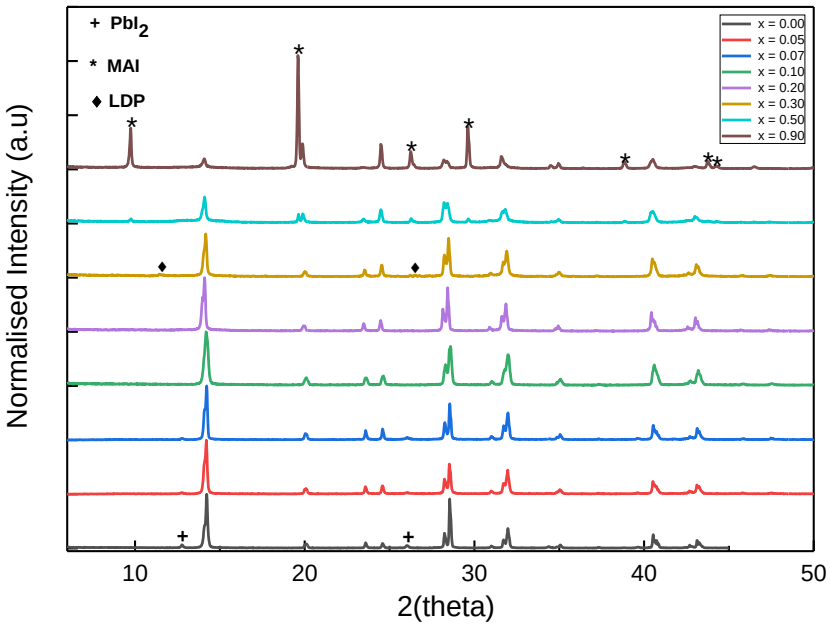

Figure 5.4. XRD patterns for the x series between the range of 0.00 - 0.90, powders annealed at 80℃.

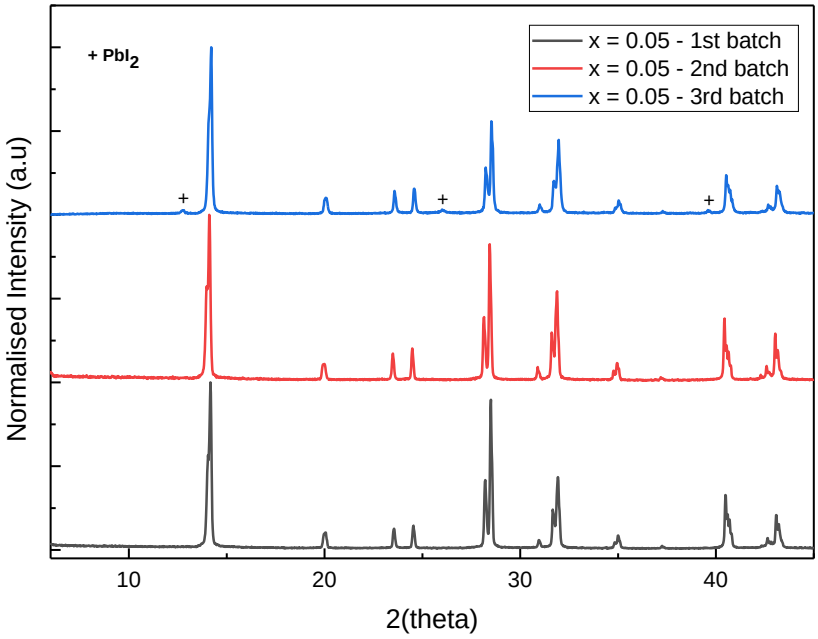

Figure 5.5. XRD patterns for x = 0.05 synthesised via ball milling on three occasions and annealed at 80℃.

5.2.3. Methylammonium iodide (MAI) deficient MALI - Ball Milling

Examining the effects of both stoichiometric and PbI_2 deficient MALI, it was decided to investigate how reducing the organic precursor would affect the phase assemblage in the same system. Compositions were made of $(CH_3NH_3)_{(1+x)}PbI_{(3+x)}$, where $x < 0$ was varied. Fig: 5.6 shows the variation in the RT XRD patterns with x produced from such compositions. In

all three compositions two phases are always present, these are the MALI perovskite phase and PbI_2. The trend in x from -0.10 to -0.90 shows the PbI_2 peaks increase in intensity relative to those of the perovskite phase.

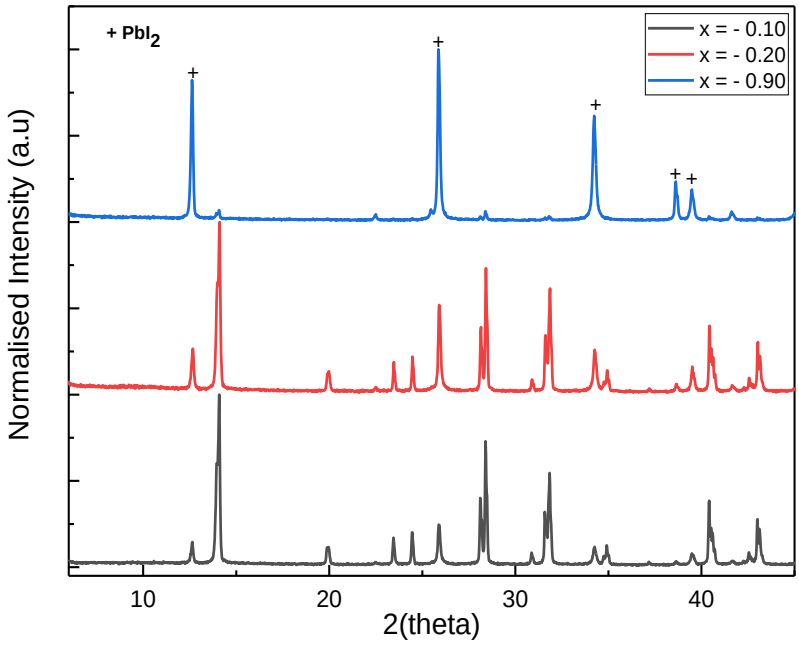

Figure 5.6. XRD patterns showing organic deficient samples in the x series, powders annealed at 80 ˚C.

Fig: 5.7 shows how the RT lattice parameters of the MALI phase change along the x series for $0.00 \leq x \leq 0.20$. a and c both generally increase with x; however, there are only small variations in a, c and V for the two samples that are single-phase based on XRD.

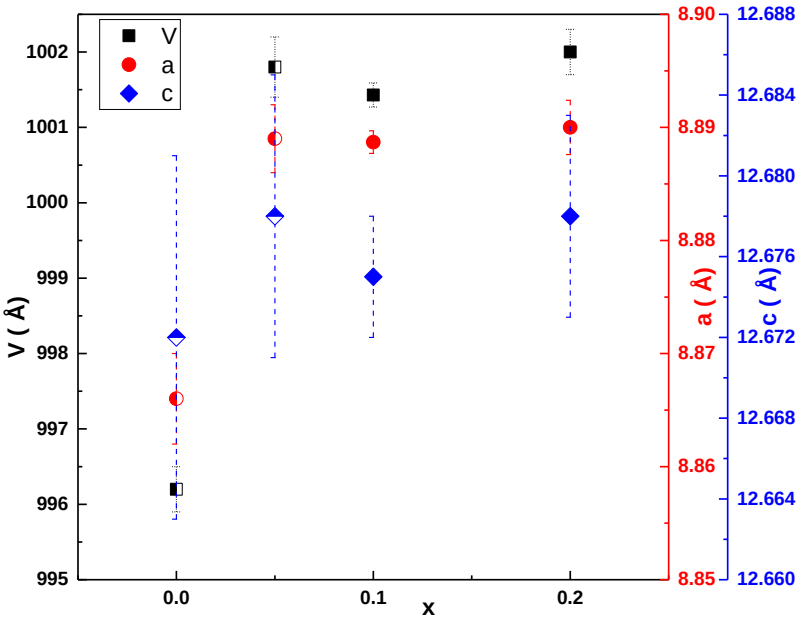

Figure 5.7. Lattice parameters for ball milled samples along the x series of 0.00 ≤ x ≤ 0.20 for powders annealed at 80℃.

5.3. SEM

LV SEM was carried out on the x series of ball milled samples. Fig: 5.8 shows the initial SEM images from pellet surfaces of the x series that were annealed at 80 ℃. These were shown not to be phase pure from XRD. The images show three different regions, which are the light regions associated with PbI_2, the dark regions associated with MAI-rich phases and the grey regions associated with MALI.

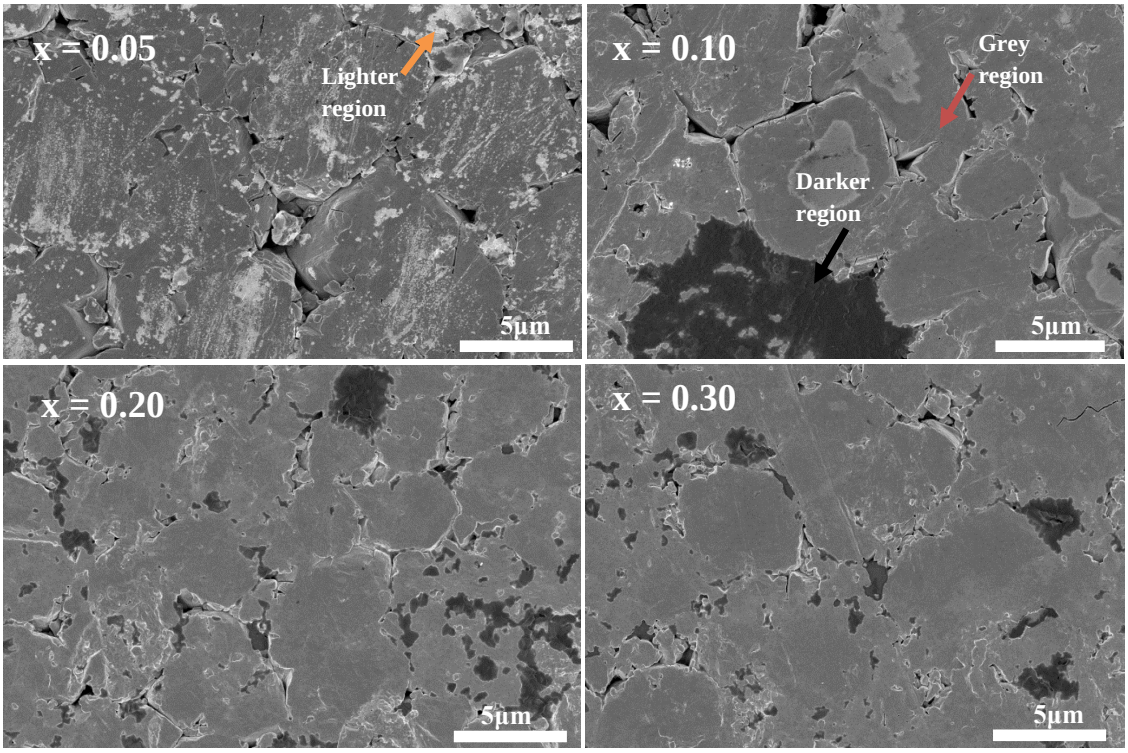

Figure 5.8. SEM images of x = 0.05 (A), x = 0.10 (B), x = 0.20 (C) and x = 0.30 (D) samples which had to be reground and annealed further to reach phase purity.

After further regrinding and reheating, x = 0.10 and 0.20 were shown to be phase pure from XRD, whereas x = 0.05 still had PbI_2 present. SEM was carried out again and surface images of the pellets were taken for x = 0.00 - 0.30 (shown in Figs: 5.9). SEM images of the x = 0.00 sample are shown in Fig: 5.9

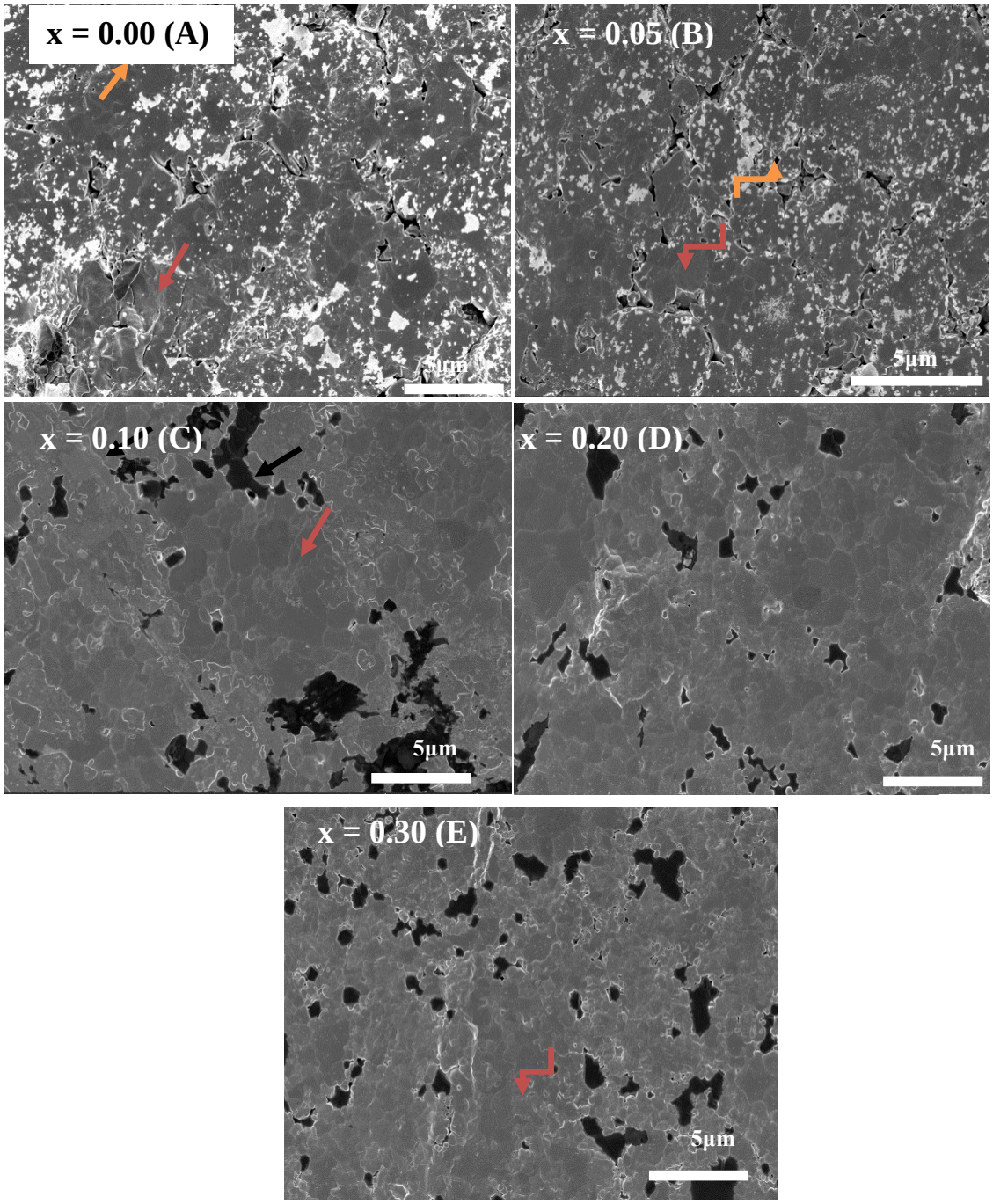

Figure 5.9. (A) SEM images of x = 0.00. (B) SEM images of x = 0.05. (C) SEM images of x = 0.10 (D) SEM image of x = 0.20 and (E) SEM image of x = 0.30

Fig: 5.9 shows the lighter regions attributed to PbI_2 and the grey regions attributed to MALI perovskite, confirming the XRD results that two phases are present in x =0.00. For x = 0.05, the SEM images (Fig: 5.9B) show there are still two phases, PbI_2 and perovskite; however, when compared to Fig: 5.9 there is less of the lighter regions (PbI_2) present. The grey (perovskite) regions in x = 0.05 are also higher in surface area fraction than x = 0.00.

SEM images for x = 0.10 are shown in Fig: 5.9C. Compared to the previous compositions there seems to be almost no light (PbI_2) regions present. The corresponding

XRD patterns for this sample are shown in Fig: 5.4 and also show no evidence of PbI_2; however, there are still two different regions present. They constitute mostly of the grey (perovskite) regions with darker (MAI-rich) regions located in-between. XRD data for this sample suggest a phase pure material with only peaks that can be indexed on the perovskite phase.

Surface SEM images are shown in Fig: 5.9D and 5.9E, respectively for when the PbI_2 content is reduced further in x = 0.20 and 0.30. Both show similar results to x = 0.10, i.e. no light (PbI_2) regions, whereas the darker (MAI-rich) regions become more significant in content. The XRD data for x = 0.20 suggests it is phase-pure whereas for x = 0.30 there are peaks which correspond to the LDP phase(s). The SEM data indicate that even when the composition appears phase pure via XRD, they are not phase pure via SEM. Comparing the SEM images in Fig: 5.8 to their relative compositions in Fig: 5.9 it appears that further regrinding and reheating does not alter the different phases that are present but may influence the microstructure.

The XRD and SEM results show that as x is varied from -0.90 to 0.07 there are two phases present, PbI_2 and MALI perovskite. The peak intensity of the PbI_2 phase in RT XRD data increases as x is varied from 0.00 to -0.90, since the compositions have reduced amounts of the organic cation and are synthesised to be PbI_2 rich. Even up to x = -0.90 the perovskite is formed, although the relative XRD peak intensities decrease as x becomes more negative. For the range $-0.90 \leq x \leq 0.07$, once the composition is synthesised at 80 ˚C, there is no change in the phases present, even for powders that are annealed up to 180 ˚C.

Increasing x to 0.10 produces the first phase-pure material based on XRD and this remains the case for x = 0.20. This remains the case up to 160 ˚C, after which (at 180 ˚C) x = 0.10 shows PbI_2 and the perovskite phase. In contrast, x = 0.20 remains phase pure.

Increasing x (at 80 ˚C) further produces new phases in addition to the perovskite phase, meaning that the solid solution limit (if it exists) is small. At x = 0.30, an LDP phase is present with the perovskite phase, and from x = 0.50 onwards only MAI and perovskite phases are observed. When nominal compositions are therefore made to be too organic-rich the MAI precursor appears in the XRD. Using ball milling synthesis, the LDP phase(s) are formed with the perovskite phase in a narrow organic-rich region, but not excessively so. Since when x is increased from 0.30 to 0.50, the LDP phase is no longer observed for the 80 ˚C annealed samples. In the organic-rich region ($x \geq 0.30$) the phase assemblage remains the same up to 140 ˚C, after which it starts to show some unidentified peaks in addition to that of the perovskite, and at 180 ˚C, a phase-pure pattern emerges. Therefore, when such materials

are prepared, the synthesis temperature should not exceed 140 ̊C to avoid the effects of decomposition.

When x is increased to 0.50 and annealed at 180 ̊C, compositions show MAI, LDP, MALI perovskite and PbI_2 phases are present. MAI and perovskite phases are observed for x = 0.90. At these higher temperatures more of the organic cation decomposes and therefore compositions move off-stoichiometry compared to the nominal starting composition. These new phases being present at higher temperatures (such as LDP), when they weren't present at lower temperatures indicates that it is present only in a certain region of the diagram when the nominal compositions are not too organic-rich (i.e. x is not too high, $0.2 < x < 0.5$).

As the SEM images of the compositions are observed from x = 0.00 - 0.30, the surface area fraction of the light (PbI_2) regions is highest for x = 0.00 and decreases with increasing x, whereas after x = 0.10 the dark (MAI-rich) regions increase. Although x = 0.10 and 0.20 appear to be phase-pure from XRD, SEM indicates these dark MAI-rich regions are present on the surface of the pellets. The surface images also indicate a dense surface with little porosity.

5.4. Density

Three different pellets of each composition were pressed in an 8 mm die, their diameter and thickness measured and volume calculated. Measuring the weight of the pellet allowed the density of the pellets to be estimated. This calculated density was then divided by the theoretical density to obtain the average percentage density. Fig: 5.10 shows the percentage density along the x-series. The percentage density for all samples is ~ 90 - 93%, with no change across the series for x = 0.00, 0.07, 0.10 and 0.20. x = 0.05 has the highest value of 93% but based on the errors involved there is no systematic trend and all have similar values.

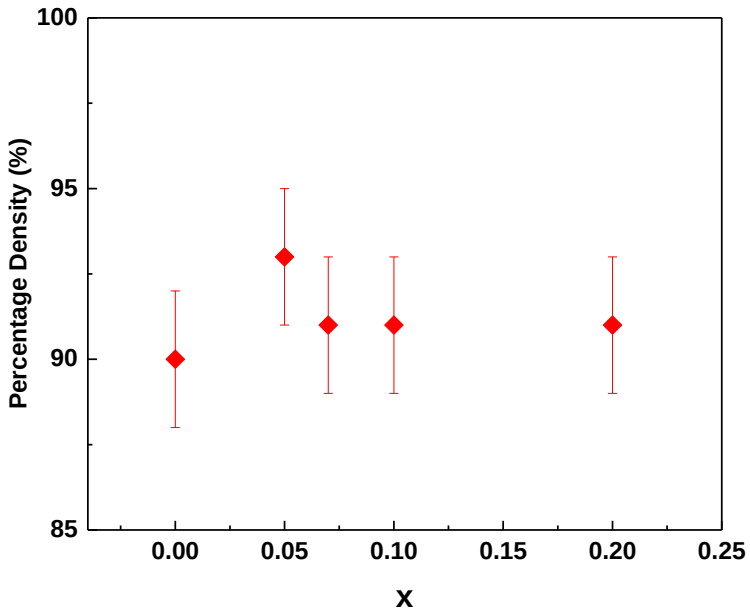

Figure 5.10. Variation in percentage density of pellets along the x series powders annealed at 80℃.

5.5. LCR

LCR was performed on these samples and permittivity, ε_r vs. temperature plots were constructed. Fig: 5.11 shows the permittivity response at a frequency of 1 MHz.

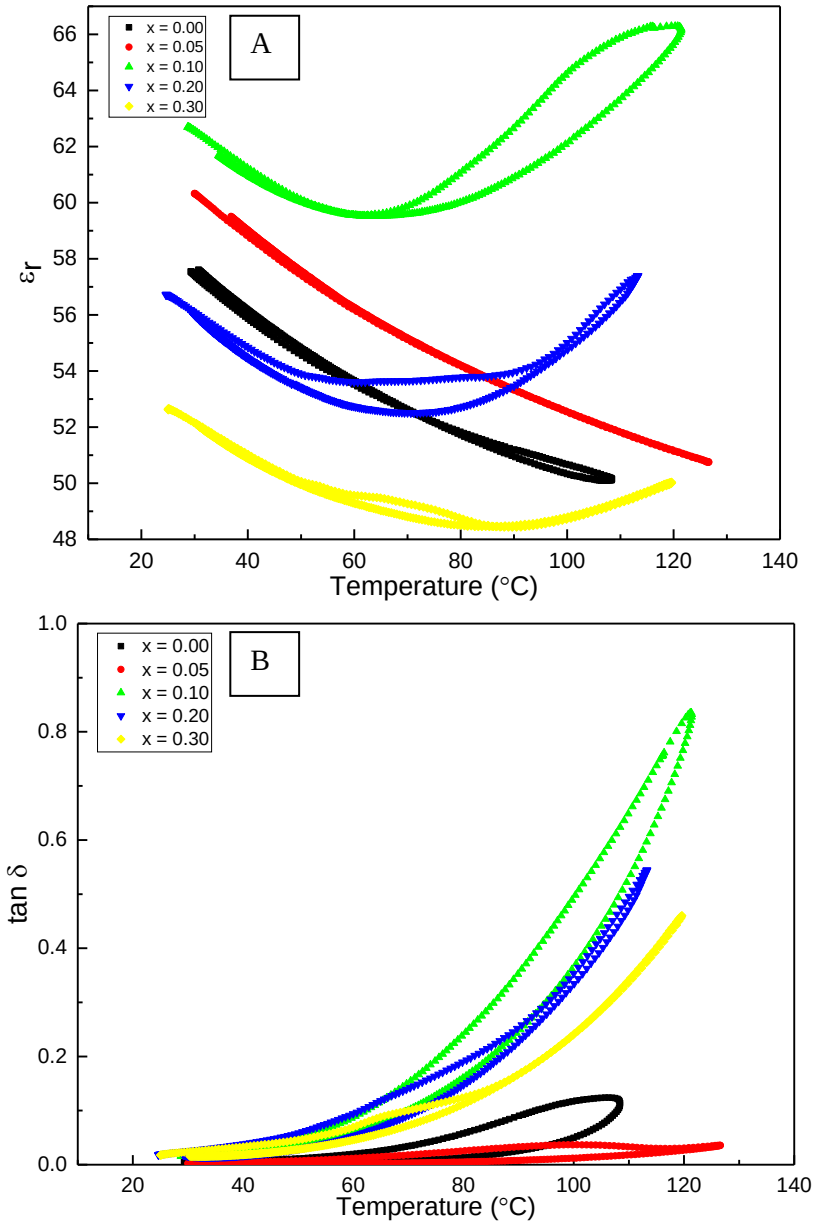

Figure 5.11. (A) shows the permittivity (at 1 MHz) vs. temperature on heating and cooling of ball milled x series annealed at 80 ˚C. (B) shows the tan δ (at 1 MHz) vs. temperature on heating and cooling for the ball milled x series annealed at 80 ˚C.

Fig: 5.11A shows that initial room temperature ε_r for the series are different. x = 0.00 has ε_r ~ 58, whereas for x = 0.05 and 0.10, it increases to ~60 and 63, respectively. ε_r of x = 0.20 is ~57 but for x = 0.30 it decreases to ~53. Therefore, there is little difference in the room temperature ε_r between x = 0.00-0.20, since it is in the range of ~ 57- 63.

x = 0.00 and 0.05, show decreasing permittivity with increasing temperature. There is also limited hysteresis in the permittivity of the samples during a heating and cooling cycle. The other members of the series, x = 0.10, 0.20, and 0.30 show that in the heating cycle, initially there is a decrease in permittivity with increasing temperature, until 50 ˚C. At higher

temperatures, for x = 0.10 ε_r increases with temperature after 65 ˚C. On the cooling cycle ε_r decreases, with the final room temperature ε_r matching the initial value of ~63. x = 0.20 shows almost constant ε_r between 50-90 ˚C, after which, there is an increase in ε_r. The cooling cycle shows an initial decrease in ε_r, then in the 50-90 ˚C region ε_r has a slightly lower value (therefore indicating a divergence between the heating and cooling ε_r). On final cooling to room temperature, ε_r matches the initial room temperature value. For x = 0.30 there is again a rise in ε_r after 90 ˚C, with the region between 60-80 ˚C again having a slightly lower ε_r on cooling.

Fig: 5.11B shows tan δ of these samples at a frequency of 1 MHz. tan δ values for x = 0.00 and 0.05 start at a very low value of ~0.004 at RT and increase to 0.12 and 0.035, respectively at their maximum heated temperatures. Although from Fig: 5.11A there is not a significant discrepancy in their permittivity values between the heating and cooling cycle, from the tan δ values there is a slight difference in the two cycles, with the loss on cooling being lower. x = 0.05 shows a maximum at about 100 ˚C, after which the loss decreases and then starts to rise again with temperature. It is in this region that the difference in the loss is most pronounced since the loss on the cooling cycle is lower. This is also observed for x = 0.20 and 0.30, but with these, the temperature at which this discrepancy is observed is lower, occurring at 65 - 70 ˚C. The losses for x = 0.10, 0.20, and 0.30 increase more rapidly with temperature, their values being ~ 0.82, 0.5, and 0.48, respectively at their highest heated temperatures.

The ε_r and tan δ results show that samples which contain PbI_2 (x = 0.00 and 0.05) show a reasonable ε_r response, where it decreases with increasing temperature and little difference between the heating and cooling cycle is observed. Although there is little change between the heating and cooling cycle in ε_r their tan δ plots show more of a difference between these two cycles.

For x = 0.10-0.30 after 50 ˚C two regions can be pinpointed. First, between 60 ˚C-80 ˚C where ε_r remains constant or there is a slight increase and after 80 ˚C where there is a sharp rise in ε_r. This is also observed in the loss for the samples, where it is higher than x = 0.00 and 0.05 and rises rapidly after 80 ˚C. There is also more of a disparity between the heating and cooling response of the samples especially as they become electrically leakier, most clearly seen for x = 0.10. There is no clear indication of a peak that may correspond to the tetragonal to cubic MALI phase transition with the possible exception of x = 0.30.

5.6. Impedance Spectroscopy

5.6.1. x = 0.00 annealed at 80 and 130 ˚C

The impedance responses for x = 0.00 annealed at 80 and 130 ˚C were measured and shown in Fig: 5.12. Both samples had a very similar electrical response, the capacitances (within errors) are the same throughout the frequency range, with similar time constants and their overall RT resistances were very close to each other, with values of 8.4 and 9.5 MΩcm for the 80 and 130 ˚C annealed samples, respectively.

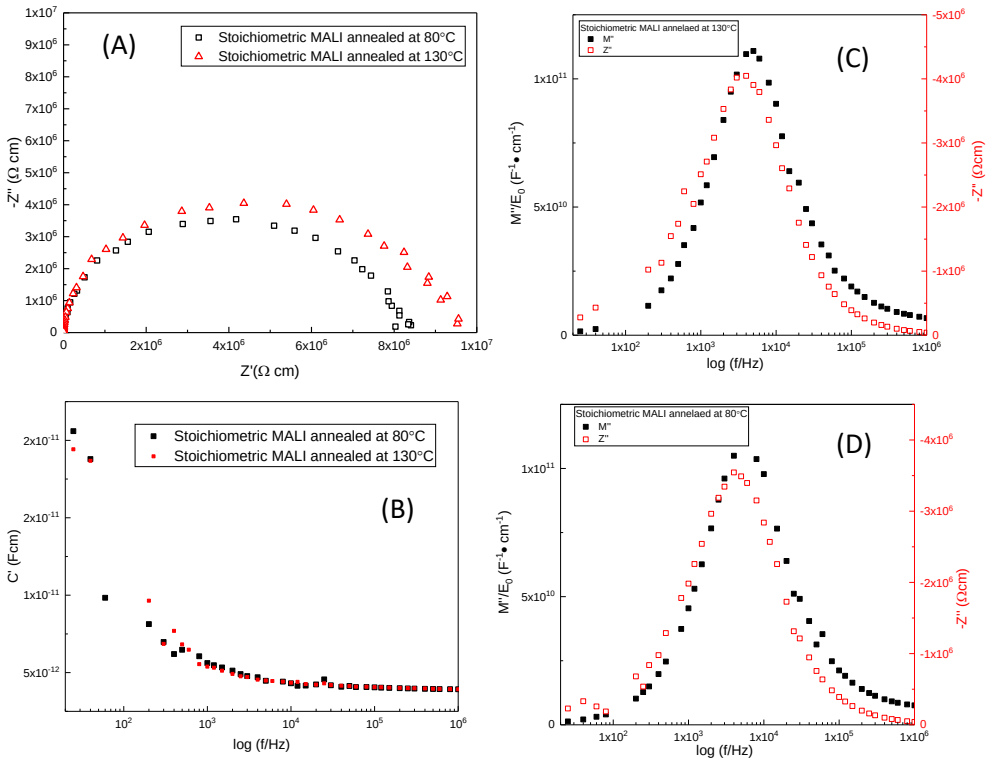

Figure 5.12. Z* (A), real capacitance (B) and combined M''/Z'' spectroscopic (C) and (D) plots comparing the stoichiometric sample annealed at 80 and 130 ˚C at ~91 ˚C on a cooling cycle respectivly.

Table 5.1 shows the estimated R and C values from Fig: 5.12, the R values from the M'' peaks are the same, with a value of 7.1 MΩcm whether x = 0.00 is annealed at 80 or 130 ˚C. The R values estimated from Z'' peaks is 1 MΩcm higher for the 80 ˚C annealed sample. The capacitance values from both M'' peaks are the same with $\varepsilon_r \sim 51$, with C' values from the Z'' peaks being slightly higher with $\varepsilon_r \sim 55$ for the 80 ˚C annealed sample and ~ 63 for the 130 ˚C annealed sample.

The R values from Z^* plots show the total resistance for a 130 ˚C annealed sample is higher by ~ 1.1 MΩcm, but their capacitance values are similar with a corresponding ε_r of ~ 51. Therefore, from the impedance data both the M'' and Z'' peaks correspond to a bulk-type MALI response with both R and C values estimated from the M'' peaks remaining the same when the sample is annealed at different temperatures. Although there is a slight difference in the R and C values extracted from the Z'' peaks and the Z^* plots when a sample is annealed at different temperatures this could indicate a second response that is harder to separate out due to the bulk component dominating the overall response.

Table 5.1. Estimated R and C values from Z^*, M'' and Z'' peaks from Fig: 5.12. For x = 0.00 when annealed at 80 ˚C and 130 ˚C

	80 ˚C	130 ˚C
Z^* - Total R (MΩcm)	8.4	9.5
M'' - R (MΩcm)	7.1	7.1
Z'' - R (MΩcm)	8.1	7.1
Z^* - C' (pF/cm)	4.5	4.6
M'' - C' (pF/cm)	4.5	4.5
Z'' - C' (pF/cm)	4.9	5.6

5.6.2. PbI_2 deficient samples - annealed at 80 ˚C

Fig: 5.13 shows Z^* and M''/Z'' spectroscopic plots for the $x \geq 0$ series.

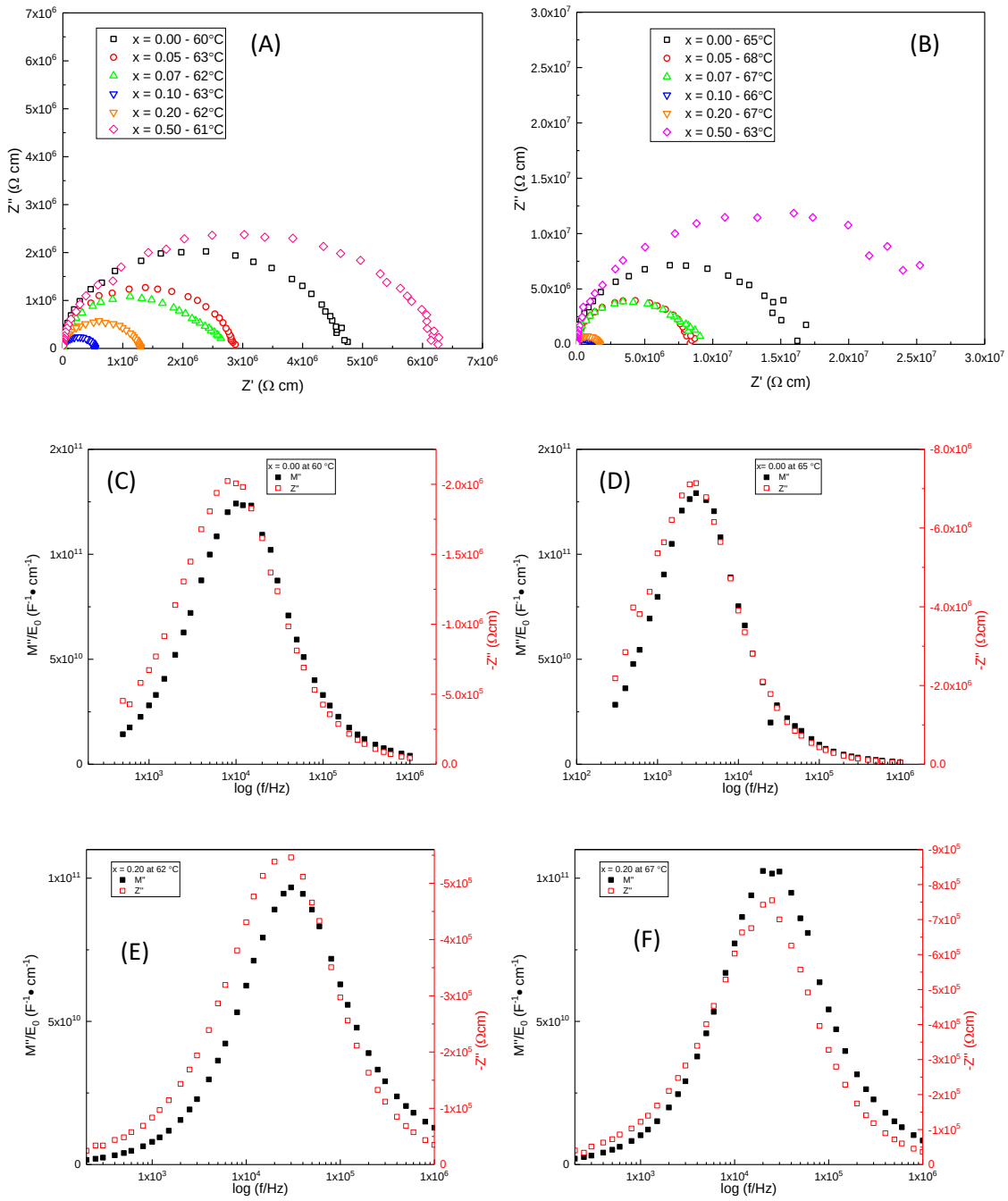

Figure 5.13. Z* plots on heating (A) and cooling (B) for x series. M''/Z'' spectroscopic plots for x = 0.00 (C) on heating, (D) on cooling. M''/Z'' spectroscopic plots for x = 0.20 (E) on heating, (F) on cooling.

Fig: 5.13A and B show the heating and cooling Z^* plots, respectively for this x series. The heating cycle plot shows that x = 0.50 has the highest total resistance, as seen from the x-axis intercept. x = 0.05 - 0.2 all have smaller total resistance values than x = 0.00. The cooling cycle results (Fig: 5.13B) show the total resistance for all has increased. The trend along x remains the same, with x = 0.50 having the highest total resistance and from x = 0.00 to 0.20, the total resistance decreases.

Table 5.2 shows the estimated R and C values from the Z^* plots, Fig 5.13A and B. The Z* arcs look as if they correspond to one response, therefore the data were hand fitted from the highest frequency (1 MHz) up to the Debye frequency maximum. This estimated the R value to be slightly less than R_{Total} of the arc, as seen from table 5.2 by comparing R and R_{Total}. As there is no definite evidence of a second response, if there is, the time constants are very similar and it's not reasonable to assign (R_{Total} - R) to another element. The R values decrease along the series with R being 4.3, 2.6, 2.2, and 0.51 MΩcm for x = 0.00, 0.05, 0.07, and 0.10, respectively. R for x = 0.20 is still lower than x = 0.00 - 0.07 but slightly higher than x = 0.10 with a value of 1.2 MΩcm. When x is increased to 0.50, R has the highest value with 5.2 MΩcm.

Table 5.2. Estimated values of R and C on both heating and cooling cycles from the Z^* plot, for the x-series.

Sample	R (M Ωcm) Heating / (Cooling)	C (pF/cm) Heating / (Cooling)	ε_r (C) Heating / (Cooling)	R_{Total} (M Ωcm) Heating / (Cooling)
X = 0.00	4.3 / (14)	4.6 / (3.7)	52 / (42)	4.7 / (15.7)
X = 0.05	2.6 / (8.1)	5.1 / (4.9)	58 / (55)	2.9 / (8.2)
X = 0.07	2.2 / (7.9)	4.7 / (4.0)	53 / (45)	2.7 / (8.2)
X = 0.10	0.51 / (1.0)	5.2 / (5.1)	59 / (58)	0.53 / (1.1)
X = 0.20	1.2 / (1.5)	5.1 / (3.5)	58 / (40)	1.3 / (1.7)
X = 0.50	5.2 / (26)	2.0 / (3.1)	23 / (35)	6.3 / (27)

The cooling data show the same trends in R and R_{Total} across the series, however all resistances have increased, more so for x = 0.00-0.07 and 0.50 than for 0.10 and 0.20.

ε_r on the heating cycle from x = 0.00 - 0.20 remains similar. Values range from ~52-59 but for x = 0.50 it is lower having a value of ~23. Similar to the LCR results, ε_r on the cooling cycle can be lower than during the heating cycle. This trend is also seen in table 5.2, where ε_r is either very similar or lower for x = 0.00 - 0.20, but is higher for 0.50.

Table 5.3 shows the estimated values of R and C from M"/Z" spectroscopic plots. First looking at R and C values estimated from the Z" peak, they match very closely to the values in table 5.2, either being the same or slightly lower. This is true for both cycles, where the trend in R decreasing across this series is maintained, as well as R for each sample having increased on the cooling cycle.

From Fig: 5.13 C-H, it can be seen that on the heating cycle there is a small offset between the M" and Z" peaks and this difference in the f_{max} of the peaks increases across the series. Fig: 5.13C, E and G for x = 0.00, 0.20 and 0.50, respectively show this trend whereas on cooling the difference in f_{max} between the two peaks becomes smaller. From table 5.3 it

can be observed that the largest separation is when x = 0.10, with a difference of 20 kHz between M''_{max} and Z''_{max}.

The R and C values estimated from the M" peaks show the R values to be smaller than when estimated from Z" peaks, however the trend across the series remains the same with R decreasing with x with the least resistive sample being x = 0.10 having a resistance of 0.38 MΩcm with x = 0.20 being slightly more resistive at 1.0 MΩcm. On the cooling cycle the trend remains the same but with the magnitude of the resistance increased for all.

The permittivity estimated from both M" and Z" spectra are quite similar to each other with the biggest difference being for x = 0.50. ε_r from M" data increases slightly as x increases from 0.00 - 0.10 (with ε_r ~ 44, 52, 53 and 58, respectively), for higher x of 0.50 ε_r decreases to ~41.

The impedance results for the x series annealed at 80 ℃ show that estimated values for R and C from the Z" peak and Z* match. The arcs on the Z^* plot are depressed and if hand fitted from 1 MHz to the frequency of the arc maximum, it does not fit all the circle, so R_{Total} is larger than R. This could possibly indicate a secondary response, however it's hard to say with any certainty. If present, the time constants for the two elements are too close to each other to allow hand fitting of the data. This could also be hinted at by the difference in the M" and Z" f_{max} values which are larger across the x series and more so during the heating than on the cooling cycle. The resistance (R and R_{Total}) across the series goes through a minimum. Samples become less resistive from x = 0.00 - 0.10, with x = 0.20 being slightly more resistive and for x = 0.50, the resistance being even higher than x = 0.00. The same trend is observed across the series on cooling, both from Z* and M"/Z" data, however all samples become more resistive after going through the heating cycle. x = 0.10 and 0.20 have much lower resistance than the other samples and this remains so on cooling. These samples are phase-pure from XRD analysis, although they contain MAI-rich dark regions on their surfaces from SEM images. x = 0.10 also has the largest difference between the M" and Z" f_{max} values.

The permittivity from both M"/Z" peaks correspond well with bulk MALI, with the permittivity being slightly lower during cooling than on the heating cycle. This is also seen from the LCR results especially for the 60 - 80 ℃ range, and the impedance data shown is in this range as well.

Table 5.3. Estimated values of R and C on both heating and cooling cycles from the M''/Z'' spectroscopic plot, along with f_{max} value of both peaks, for the x-series.

Sample		R (M Ωcm)	C' (pF/cm)	f_{max} (kHz)	ε_r (C')
X = 0.00	M'' - Heating/ (cooling)	3.3 / (13.7)	4.1 / (3.9)	12 / (3)	46 / (44)
	Z'' - Heating/ (cooling)	4.0 / (14.3)	4.9 / (3.7)	8 / (3)	55 / (42)
X = 0.05	M'' - Heating/ (cooling)	2.2 / (8.6)	4.8 / (4.6)	15 / (4)	54 / (52)
	Z'' - Heating/ (cooling)	2.5 / (7.9)	5.2 / (5.1)	12 / (4)	59 / (58)
X = 0.07	M'' - Heating/ (cooling)	2.2 / (6.8)	4.7 / (4.7)	15 / (5)	53 / (53)
	Z'' - Heating/ (cooling)	2.2 / (7.7)	4.9 / (4.1)	15 / (5)	55 / (46)
X = 0.10	M'' - Heating/ (cooling)	0.38 / (1.0)	5.2 / (5.1)	80 / (30)	59 / (58)
	Z'' - Heating/ (cooling)	0.47 / (1.0)	5.6 / (6.2)	60 / (25)	63 / (70)
X = 0.20	M'' - Heating/ (cooling)	1.0 / (1.3)	5.2 / (4.9)	30 / (25)	59 / (55)
	Z'' - Heating/ (cooling)	1.2 / (1.5)	5.5 / (4.2)	25 / (25)	62 / (47)
X = 0.50	M'' - Heating/ (cooling)	1.4 / (18)	7.4 / (3.6)	15 / (2.5)	84 / (41)
	Z'' - Heating/ (cooling)	4.8 / (24)	5.6 / (5.6)	6 / (1.2)	63/ (63)

5.6.3. x-series annealed at 120 ˚C

Although the XRD data and phase assemblage of the x series remained similar when annealed at 120 ˚C, impedance was performed to observe if there were any differences in the electrical behaviour of the samples. Fig: 5.14A and B shows the response from Z^* plots on both cycles. It shows a single depressed arc for all of this series with the total resistance decreasing for x = 0.00 to 0.20. The cooling cycle shows the same trend but the total resistances have increased.

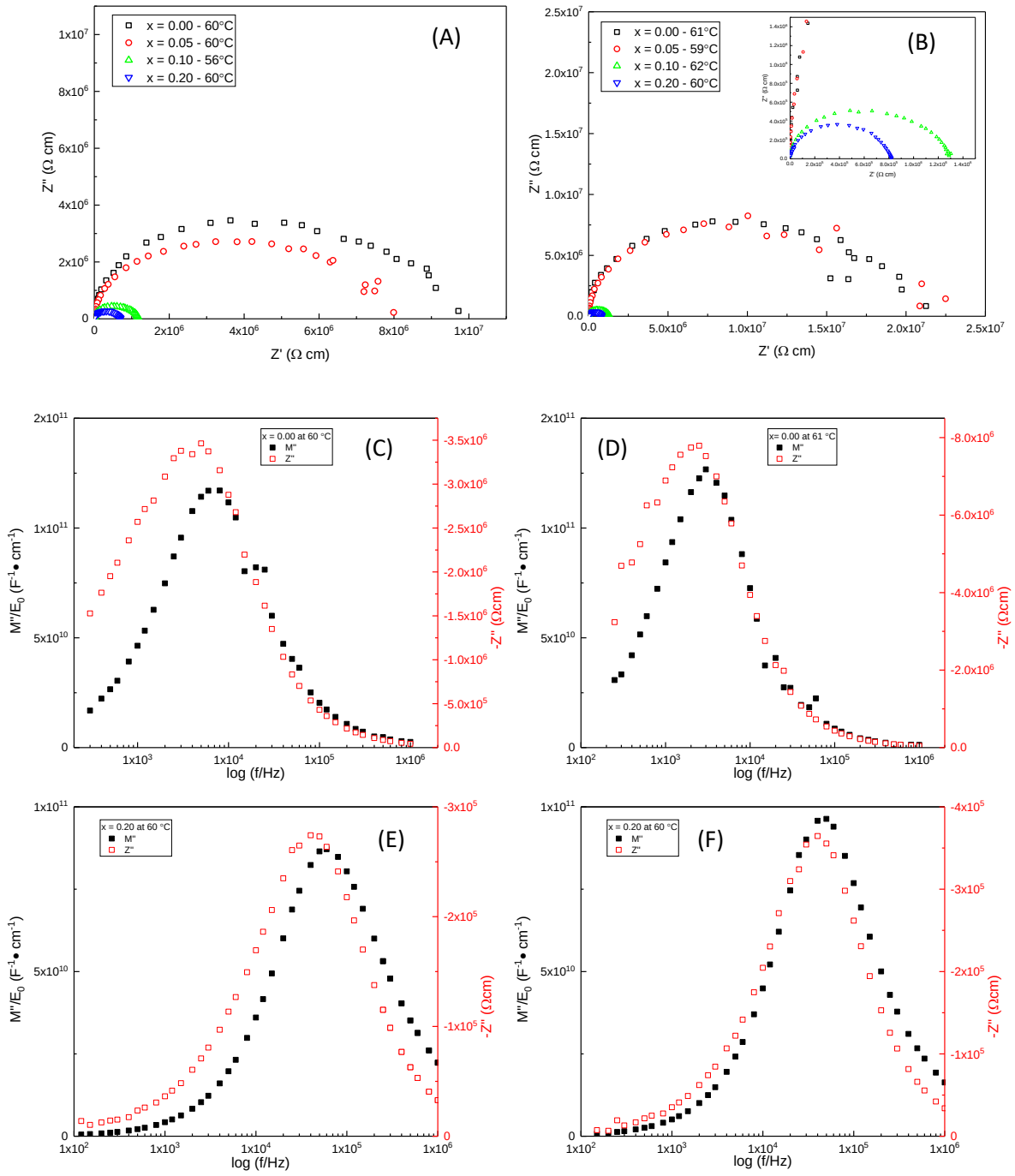

Figure 5.14. Z* plots on heating (A) and cooling (B) for x series. M''/Z'' spectroscopic plots for x = 0.00 (C) on heating, (D) on cooling. M''/Z'' spectroscopic plots for x = 0.20 (E) on heating, (F) on cooling.

The M''/Z'' spectroscopic plots also show a similar trend, where on the heating cycle, Fig: 5.14C and E the time constants between the M'' and Z'' peak is larger than on the cooling cycle, Fig: 5.14D and F. The f_{max} also shifts towards higher frequency across the x series. These trends can be more readily observed from tables 5.4 and 5.5, showing the estimated R and C values from the Z^* and M''/Z'' spectroscopic plots, respectively.

The trends (from table 5.4) in R and C for 120 ˚C annealed samples remain similar to the 80 ˚C annealed samples (from table 5.2). From x = 0.00 to 0.20, R decreases, with the total resistance also decreasing. This trend remains the same on the cooling cycle but the total resistance values have increased. The permittivity is again slightly higher during the heating cycle than the cooling cycle. Comparing estimated R and R_{Total} from Z^* plots of the 80 and 120 ˚C annealed samples shows that when annealed at higher temperature the resistances have a higher magnitude on both cycles for x = 0.00 - 0.20 and the permittivity tends to be of similar value especially on the cooling cycle.

Table 5.4. Estimated values of R and C on both heating and cooling cycles from the Z^* plot, for the x-series.

Sample	R (M Ωcm) Heating / (Cooling)	C (pF/cm) Heating / (Cooling)	ε_r (C) Heating / (Cooling)	R_{Total} (M Ωcm) Heating / (Cooling)
X = 0.00	**7.3 / (16)**	**4.4 / (4.1)**	**50 / (46)**	**9.5 / (20)**
X = 0.05	**6.0 / (15)**	**6.6 / (4.3)**	**75 / (49)**	**7.7 / (17)**
X = 0.10	**0.94 / (1.1)**	**5.6 / (5.0)**	**63 / (57)**	**1.2 / (1.3)**
X = 0.20	**0.62 / (0.77)**	**6.4 / (5.1)**	**72 / (58)**	**0.7 / (0.82)**

Table 5.5 shows R and C values estimated from M" and Z" peaks. The M" peak occurs at a higher frequency than the Z" peak on both heating and cooling, although the difference is larger on the heating cycle. This indicates that the time constants separate out more across the series and that the resistance estimated from the M" peak is lower than from the Z" peak. R decreases with x and for the less resistive samples (x = 0.10 and 0.20) the difference in the M" and Z" associated resistivity becomes smaller.

ε_r from the M" peak is lower than from the Z" peak on both cycles and for an increase in x ε_r tends to increase. The bulk ε_r for MALI is most closely resembled to the one estimated using the M" peak for x = 0.00 and ε_r from the Z" data tends to be particularly high especially for x= 0.05-0.20 with values as high as ~ 111. Comparing values from table 5.5 to table 5.3, again shows the 80 ˚C annealed samples have a smaller resistance on both cycles and the f_{max} of both M" and Z" peaks appear at higher frequency.

The trends in the 120 ˚ C annealed samples are similar to the 80 ˚C annealed samples, except their resistance is higher. However, a more interesting difference is seen in the ε_r extracted from the Z" peak. Whereas for the 80 ˚C annealed samples they resemble the bulk MALI permittivity, in the 120 ˚C annealed samples it is higher especially for x = 0.05-0.20 with values being in the range of ~ 83-111.

Table 5.5. Estimated values of R and C on both heating and cooling cycles from the M''/Z'' spectroscopic plot, along with f_{max} value of both peaks, for the x-series.

Sample		R (M Ωcm)	C' (pF/cm)	f_{max} (kHz)	ε_r (C')
X = 0.00	M'' - Heating/ (cooling)	4.7 / (13)	4.3 / (4.0)	8 / (3)	47 / (45)
	Z'' - Heating/ (cooling)	6.7 / (16)	6.0 / (4.1)	4 / 2.5)	68 / (46)
X = 0.05	M'' - Heating/ (cooling)	3.7 / (12)	5.4 / (5.3)	8 / (2.5)	61 / (60)
	Z'' - Heating/ (cooling)	5.4 / (16)	9.8 / (8)	3 / (1.5)	111 / (90)
X = 0.10	M'' - Heating/ (cooling)	0.71/ (0.72)	5.6/ (5.5)	40/ (40)	63 / (62)
	Z'' - Heating/ (cooling)	0.87 / (0.99)	7.4/ (6.4)	25/ (25)	84 / (72)
X = 0.20	M'' - Heating/ (cooling)	0.46 / (0.61)	5.7 / (5.2)	60 / (50)	64 / (59)
	Z'' - Heating/ (cooling)	0.55 / (0.73)	7.3 / (5.5)	40 /(40)	83 / (62)

5.6.4. MAI-deficient samples

Impedance was carried out on x = -0.10 and -0.20 and compared to x = 0.00. Fig: 5.15 (A) shows the Z^* plots showing a single arc for all in this series with the response of x = -0.20 being more depressed than the others. Fig: 5.15B shows the M" spectroscopic plots, where all samples have a single M" peak with similar f_{max} although there is a difference in their peak height.

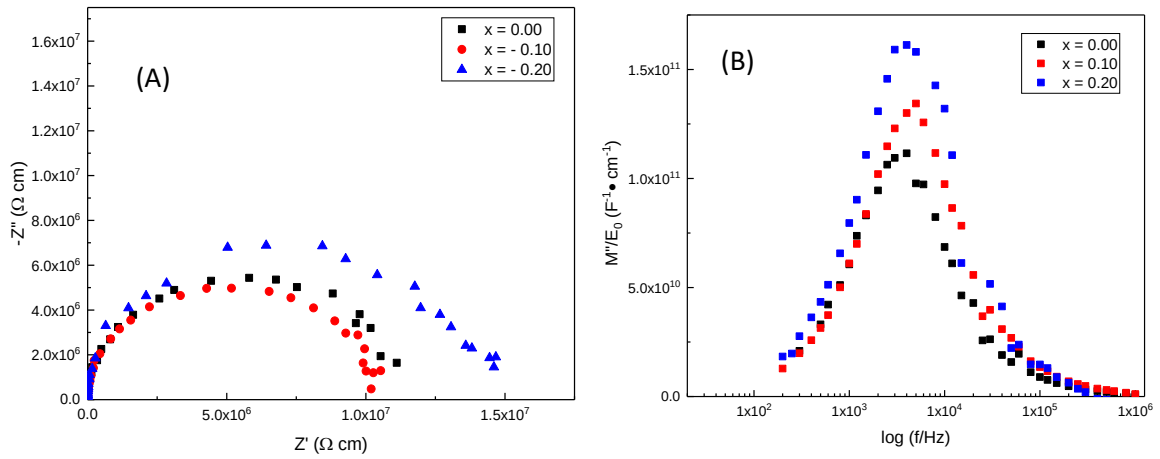

Figure 5.15. Plot (A) shows the Z* response, (B) shows the M'' spectroscopic plot, for the x series in the negative direction. x = 0.00 and -0.10 are at 65 ˚C, and x = -0.20 is at 60 ˚C, all on the cooling cycle.

The estimated values from both Z^* and M", Z" spectroscopic plots are shown in table 5.6, there does not seem to be any clear trend in R in this series, they all remain quite similar. The f_{max} of all samples are very close, including the permittivity of x = 0.00 and 0.10, although there is a slight drop for x = 0.20. ε_r values match the bulk permittivity of MALI when R is estimated from Z^* by hand fitting between the highest frequency and the Debye peak maximum at ωRC =1. R is the same as the total resistance, unlike the PbI_2 deficient samples where R_T tends to be slightly higher than R.

Table 5.6. Estimated values of R and C on cooling cycles from the M''/Z'' spectroscopic plot and Z^*, along with f_{max} value of both peaks, for x = -0.20 - 0.00.

Sample		R (M Ωcm)	ε_r (C')	f_{max} (kHz)	R_{Total} (M Ωcm)
X = 0.00	M''	14.1	43	3	-
	Z''	13.2	45	3	-
	Z^*	13.4	44	-	14
X = 0.10	M''	10.3	45	4	-
	Z''	10.0	45	4	-
	Z^*	10.0	45		10
X = 0.20	M''	12.8	35	4	-
	Z''	13.8	33	4	-
	Z^*	15.0	32	-	15

5.6.5. Arrhenius plots of x-series from hand fitting

Pellets of x = 0.00 powder annealed at 80 ˚C from different batches were characterised using IS. Fig: 5.16A shows the conductivity (estimated from M" peaks) of these samples on the heating cycle. Two pellets were analysed from separately synthesised batches; a sample from batch 1 was analysed twice using IS. This showed that conductivity (1/R) initially increased with temperature, however there is then a decrease, after 70 ˚C, after which conductivity increased again. The samples from batch 1 showed the same conductivity behaviour on the heating cycle, after IS was performed for the second time. The batch 2 sample showed the same type of conductivity trend with temperature; however, the initial conductivity is almost one order of magnitude higher than batch 1. At higher temperature, eg ~130 ˚C, once the drop in conductivity has occurred it has a similar magnitude as batch 1.

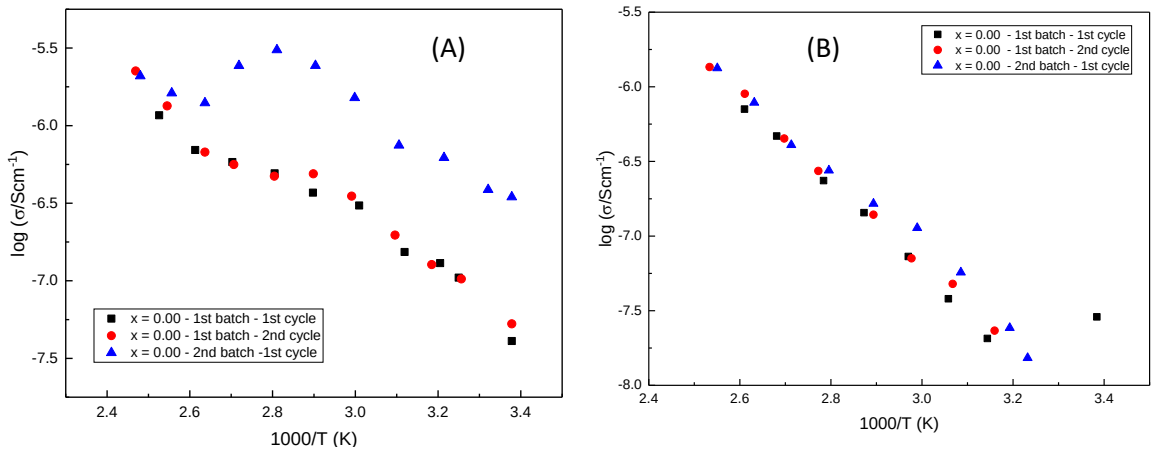

Figure 5.16. Arrhenius conductivity plots showing x = 0.00 response on the heating cycle for two different batches with measurements being repeated on a batch 1 pellet. (B) Conductivity Arrhenius plots of x = 0.00 on the cooling cycle for the two different batches.

The conductivity Arrhenius plots on the cooling cycle are shown in Fig: 5.16B, this indicates that both samples from batch 1 have the same conductivity response with

temperature. The conductivity during the heating cycle is higher than the cooling cycle. During the cooling cycle measurements, the conductivities at higher temperatures are more similar to each other than at lower temperatures where there is a slight variation in the trend(s). This is also shown by the room temperature measurement of the 1st batch,1st cycle. There is a sudden increase in conductivity and the point deviates from the linear trend. The response from batch 2 on the cooling cycle is similar to the 1st batch, more so at the higher than the lower temperature region.

These results show that during heating, the conductivity is higher than on cooling. This is true when measurements are repeated on the same sample. It also shows there is a large variation in conductivity of samples from the same starting composition but from different batches during the initial heating stage, after which their responses become similar.

Figs: 5.17A and B show the conductivity relationship on heating and cooling, respectively for samples annealed at 80 ℃ and C and D show the values for samples annealed at 120 ℃.

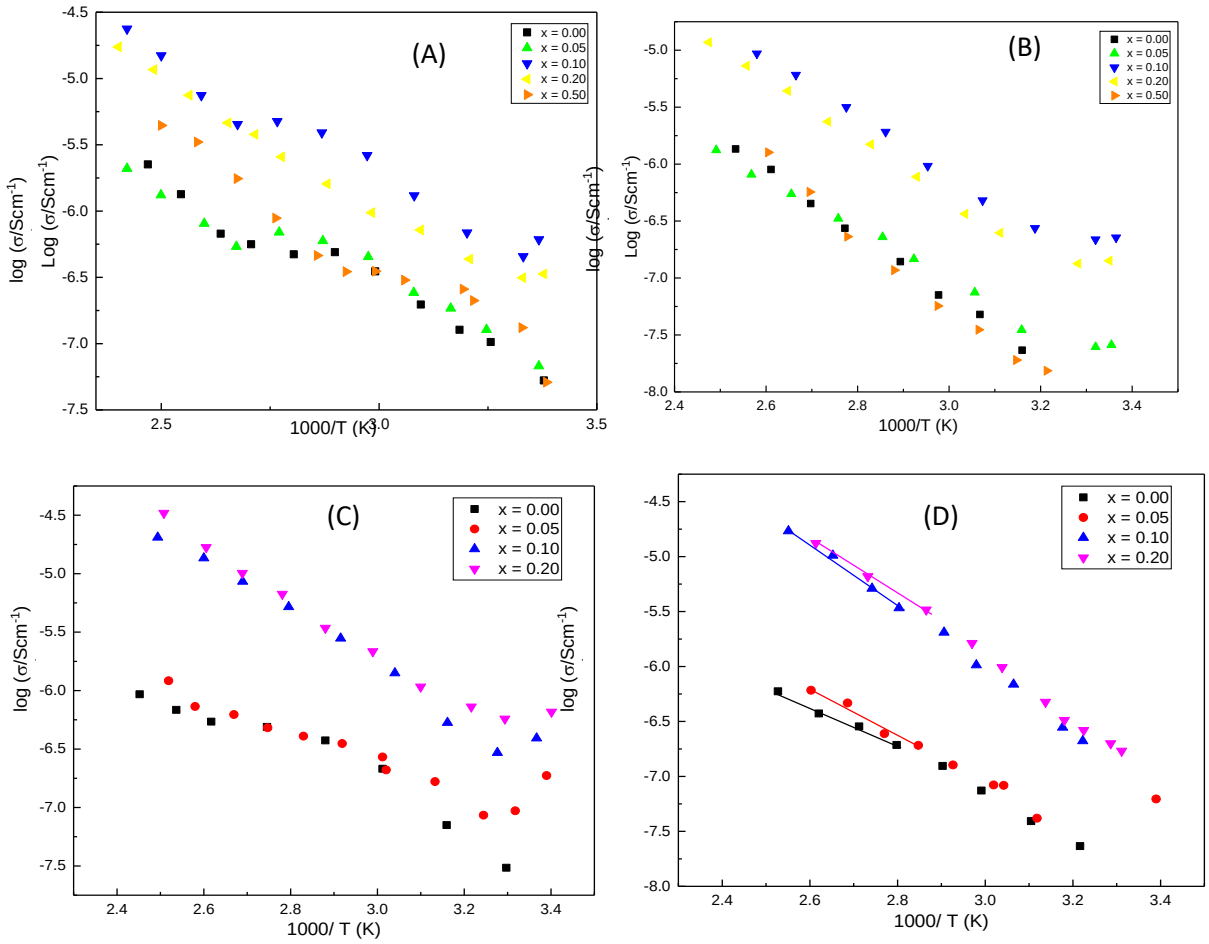

Figure 5.17. Arrhenius conductivity plot on the (A) heating cycle and (B) cooling cycle for x series when powders were annealed at 80℃. Arrhenius conductivity plot on the (C) heating cycle and (D) cooling cycle for the x series when powders were annealed at 120℃.

Fig: 5.17A shows that x = 0.00 and 0.05 both have similar conductivities on heating, with a drop in their conductivity occurring at a similar temperature of ~ 85 ℃. x = 0.07 has similar conductivity in the initial heating stage but at higher temperature the conductivity is higher than x = 0.00 and 0.05. When x is increased to 0.10 and 0.20, they both have higher conductivity than x = 0.00, 0.05 and 0.07. When the drop in conductivity occurs for x = 0.10 (at a similar temperature), the subsequent conductivity values still remain about an order of magnitude higher. x = 0.50 initially shows increasing conductivity with temperature, however from 40 - 80 ℃ it remains constant with temperature after which it starts to increase again.

Fig: 5.17B shows the conductivity values for the x series tend to be linear based on an Arrhenius format. As the temperature approaches room temperature, the conductivity values deviate from linearity. Therefore, the ball milled samples also show this difference in conductivity behaviour between a heating and cooling cycle. There is however still the increase in conductivity by an order of magnitude for x = 0.10 and 0.20. x = 0.07 has a slightly higher conductivity than 0.00, 0.05 and 0.50 which all have similar magnitudes of conductivity. From Fig: 5.17C and D the x range 0.00 - 0.20 show a similar trend to the 80 ℃ annealed samples on both cycles.

Fig: 5.18A shows the conductivity Arrhenius plot of x = 0.00, - 0.10 and - 0.20 on a heating cycle. Initially on heating, the conductivity of x = 0.00 is about half an order of magnitude higher than - 0.10 and - 0.20. This decreases at about 85 ℃ after which conductivity rises with temperature again and all have similar values.

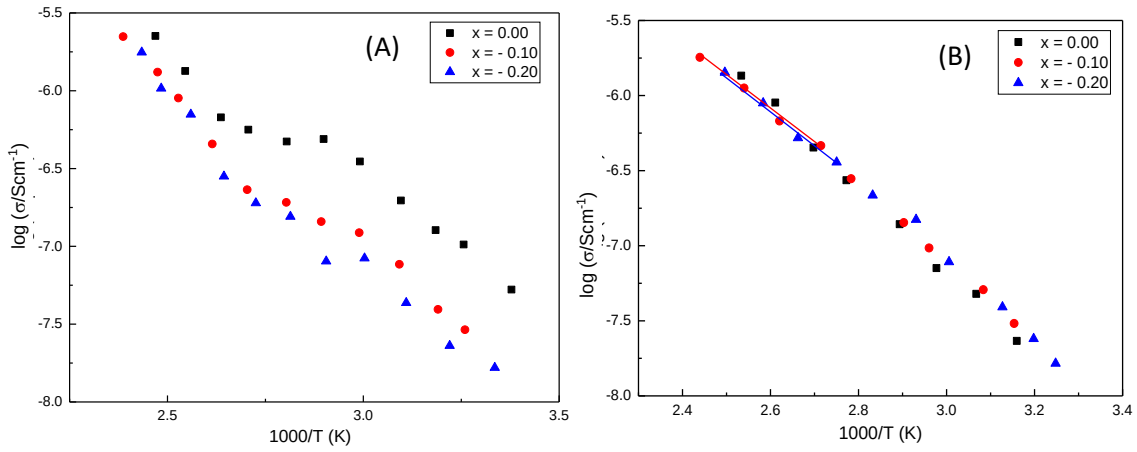

Figure 5.18. Arrhenius conductivity plot response on the heating cycle for the organic deficient x series. (B) Conductivity Arrhenius plot response on the cooling cycle for the organic deficient x series

Fig: 5.18B shows the Arrhenius plot for the same samples but on the cooling cycle. This shows there does not seem to be any variation in the conductivity as x is altered to make the starting composition MAI deficient (or PbI_2 rich).

Table 5.7 and Fig: 5.19 show how the activation energy for bulk conductivity varies across the x series in the higher temperature range, indicated by the best fit lines in Fig: 5.17 and 5.18. When errors are taken into account there is little variation in E_a between x = -0.20 to 0.50, with the possible exception of x = 0.50, indicating a higher E_a.

Table 5.7. The activation energy for bulk conduction at the high temperature region for the x series calculated from Fig: 5.17-5.18.

Sample	80 ˚C	120 ˚C
X = - 0.20	0.48 (±0.01)	
X = - 0.10	0.46 (±0.01)	
X = 0.00	0.60 (±0.02)	0.34 (±0.01)
X = 0.05	0.44 (±0.01)	0.43 (±0.03)
X = 0.07	0.51 (±0.02)	
X = 0.10	0.49 (±0.06)	0.48 (±0.08)
X = 0.20	0.51 (±0.07)	0.56 (±0.02)
X = 0.50	0.85 (±0.03)	

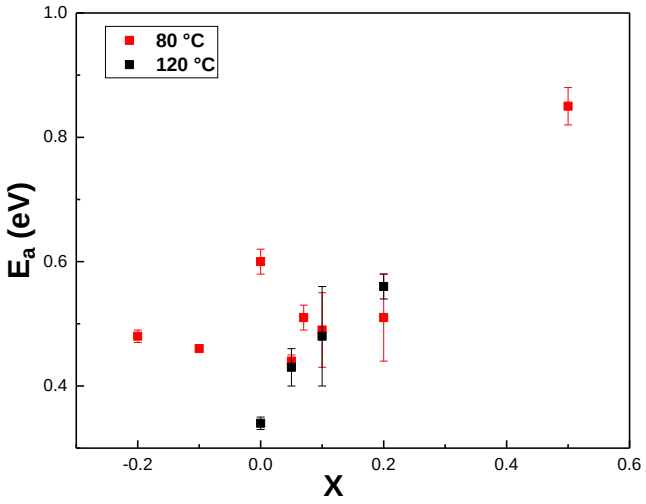

Figure 5.19. Activation energy for conduction along the x series from x = -0.20 to 0.50 at the high temperature region from Fig: 5.17B and D and 5.18B.

5.7. Equivalent circuit fitting of impedance spectroscopy data

5.7.1. x-series annealed at 80 ˚C

The circuits used previously in Figs: 4.15A & B were used to extract data for this x series, on both cycles. The capacitance and real admittance spectroscopic plots show the fits for both of these circuits.

Fig: 5.20A-C shows fitting data for x = 0.00. Fig: 5.20 A shows the Y' spectroscopic plot on the 1st heating cycle. The RQC circuit does not fit the data well, whereas the RQC-RC circuit shows a better fit. During the cooling cycle, Fig: 5.20B shows a similar result,

albeit with the RQC fit improving slightly at high frequency. The second heating cycle (Fig: 5.20C) again shows a better fit with RQC-RC, especially at high frequency. Therefore, once the material has gone through the first heating cycle, RQC-RC is still the best fit on the second heating cycle.

Fig 5.20D-F show the heating and cooling cycle for x = 0.05, respectively. The heating cycle fit (plot D) of RQC-RC is better than RQC in the lower frequency region, whereas in the higher frequency region the capacitance for both RQC and RQC-RC fit well with the experimental data. The cooling data (plot E) show that both circuits give a better fit. Fig: 5.20F shows the Y' spectroscopic plot, where the RQC circuit fits well only for the low frequency data, whereas RQC-RC fits better throughout the frequency range.

Fig: 5.20G and H show the fitting for x = 0.07, both cycles show a better fit with the RQC-RC circuit, however even at high frequency the simulations from this circuit diverges from the experimental data. This is more notable on the cooling cycle because it is more resistive (all the data shift to lower frequency and therefore more of the high frequency response is observed).

Fig: 5.20: I, J and K for x = 0.10, L, M and N for x = 0.20 and O and P for x = 0.50 show the comparison between RQC and RQC-RC circuits for each sample, respectively. RQC-RC fits better across the frequency range. The RQC circuit tends to have higher errors at lower frequencies when looking at the C' plot and at higher frequency for the Y' plot. Their cooling data maintain a good fit for the RQC-RC circuit. The fit for the RQC circuit is improved at the lower frequency region on the cooling cycle.

Fig: 5.20Q and R shows fitting an RQC and RQC-RC circuit to x = - 0.20 data during a heating and cooling cycle, respectively. The heating data shows that the capacitance of RQC-RC and RQC are similar in the higher frequency region but deviate slightly from the experimental data at lower frequency where RQC has a slightly higher capacitance. During the cooling cycle this trend has increased, whereas at higher frequency the experimental data still fits well to both circuits.

Although the RQC-RC fit is clearly better for x = 0.00 - 0.20 for x = -0.20 and 0.50 it gets harder to distinguish, even from Fig: 5.20O, the mid frequency range for x = 0.50 appears slightly off from the RQC circuit. For x = -0.20 the fit gets harder to separate out.

When both circuits are compared (throughout the x series) on both the heating and cooling cycles in Fig: 5.20 they show a better fit with the RQC-RC circuit. This is especially the case for the lower frequency region in the C' plot, and the higher frequency region of the

Y' plot. This indicates there are at least two possible elements present in the impedance data of the samples, and if the data are only hand fitted these cannot be deconvoluted.

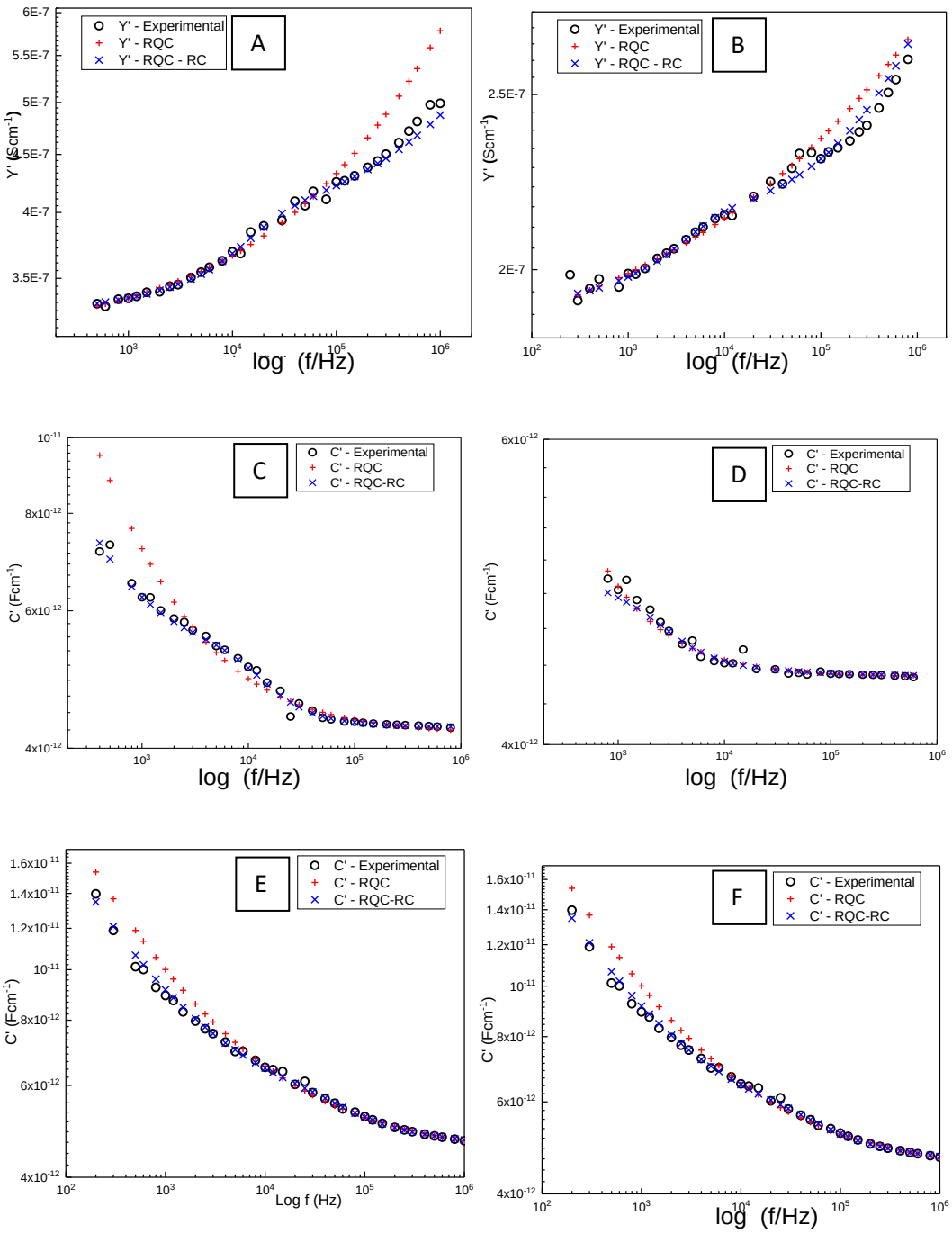

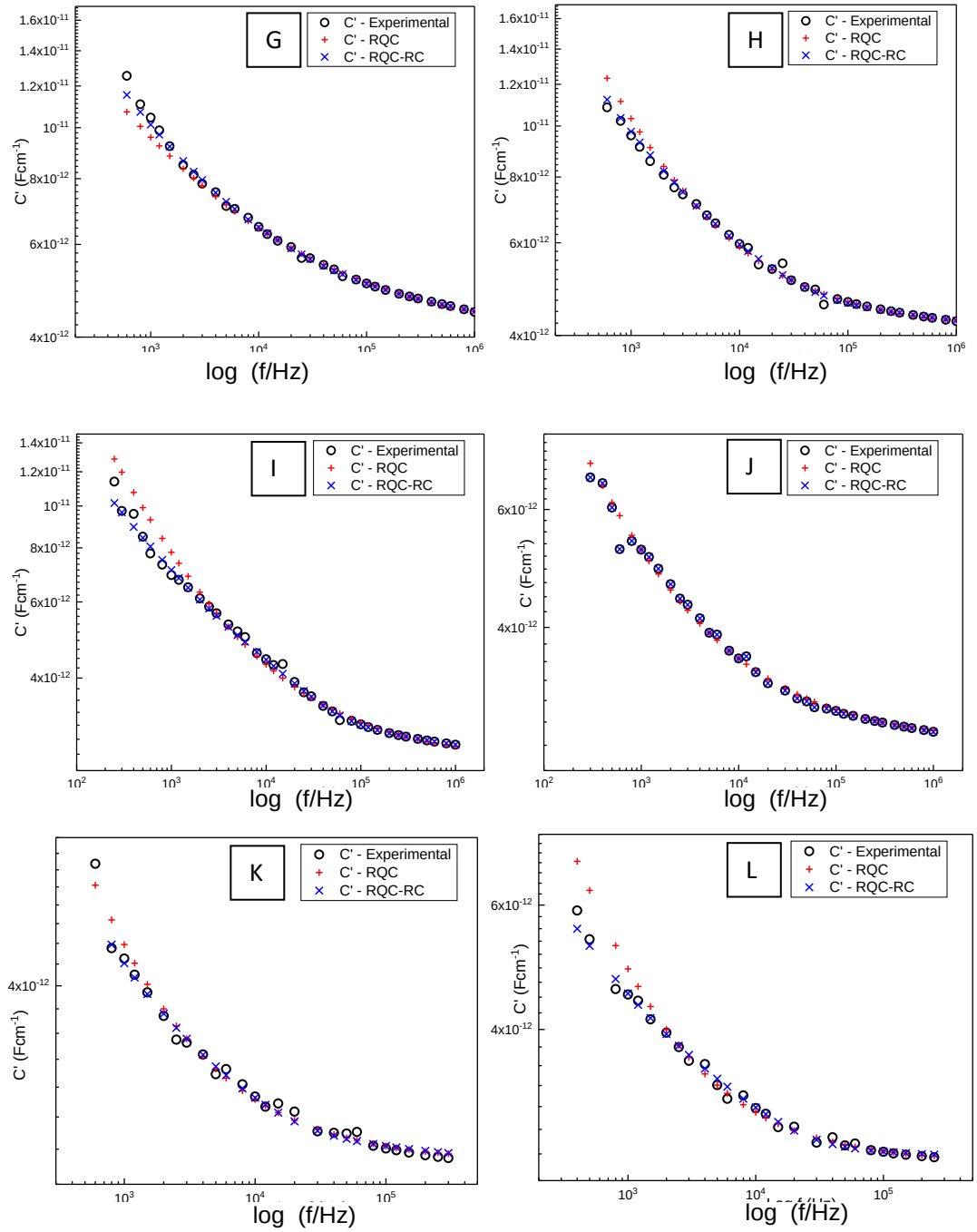

Figure 5.20. (A) x=0.00 at 84 ˚C during heating and (B) 86 ˚C during cooling (1st batch 1st time), (C) x=0.05 at 76 ˚C during heating, (D) 77 ˚ C during cooling. (E) x=0.10 at 76 ˚C during heating, (F) 77 ˚C during cooling, (G) x=0.20 at 95 ˚C during heating and (H) 93 ˚C during cooling. (I) x=0.50 at 89 ˚C during heating and (J) 87 ˚C during cooling. Capacitance vs frequency plots for x = - 0.20 during heating (K), and during cooling (L)

5.7.2. Ball-milled samples at 120 ˚C

IS was also performed on samples annealed at 120 ˚C. There was no significant change in their XRD data from that obtained from the 80 ˚C annealed samples. However, the samples are clearly sensitive to many different environmental conditions, especially temperature. As the electrical properties are sensitive to temperature, IS was performed on the 120 ˚C annealed samples to observe any differences in their electrical response(s).

Equivalent circuit fitting was then performed on the IS data of these samples, Fig 5.21A and B shows Y' spectroscopic plots during heating and cooling for x = 0.00. The RQC-RC circuit for these samples fit better during the heating and cooling cycles. Fig: 5.21C and D for x = 0.05 and E and F for x = 0.10, show that for all frequency ranges the experimental data fit better with the RQC-RC circuit than RQC, on both cycles. This is especially the case in the higher frequency region, where the circuit with one element is not able to produce a satisfactory fit. However, the two-element circuit fit has some divergence at very high frequency values from the experimental data. Therefore, when the material is annealed at higher temperature, the electrical response still shows that at least two different elements are required for equivalent circuit fitting.

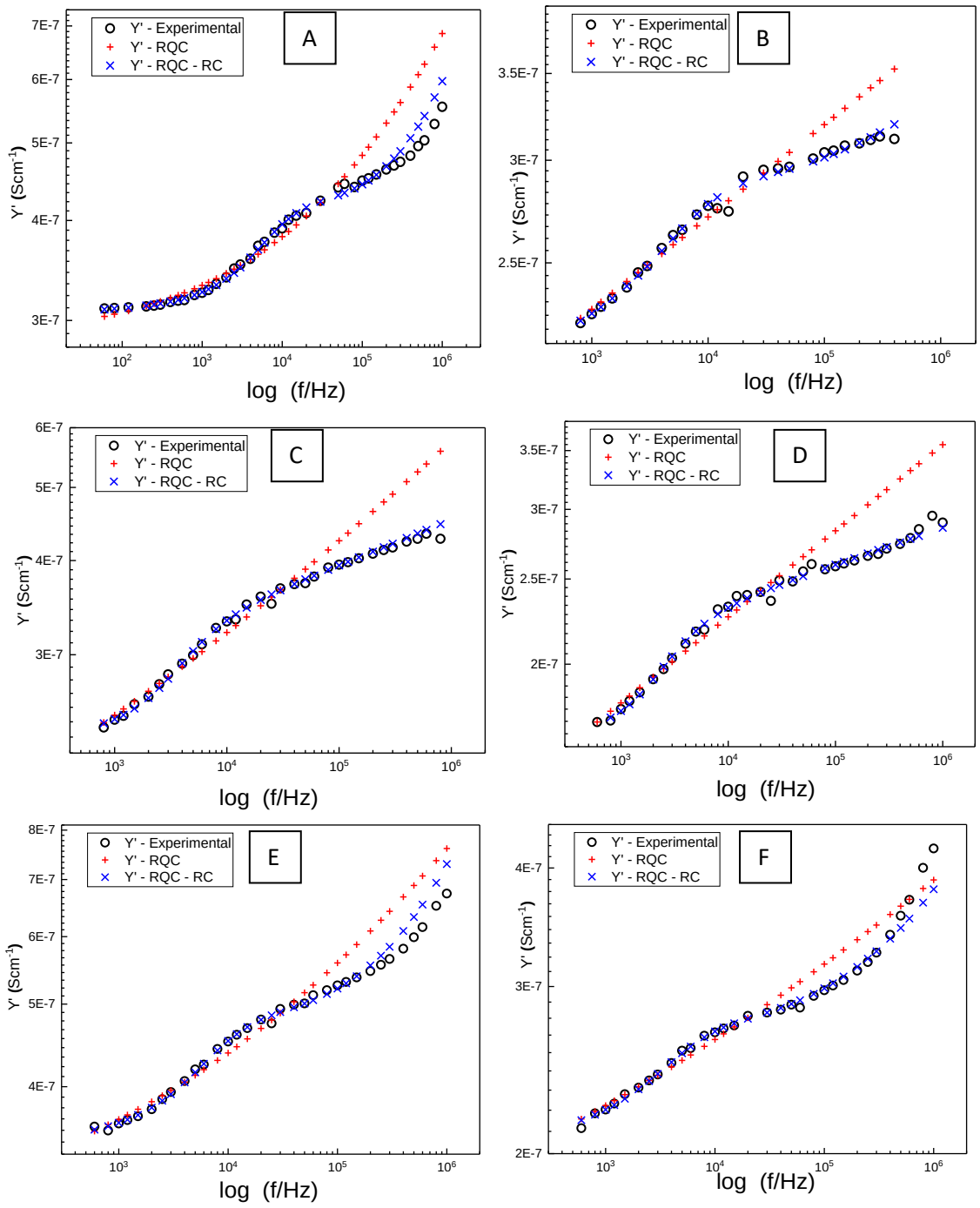

Figure 5.21. Y' spectroscopic plots for x = 0.00 during heating (A), during cooling (B). x = 0.05 during heating (C) and during cooling (D). x = 0.010, during heating (E) and during cooling (F).

The R1, C1 and R2, C2 values from the circuit fitting of the 80 ˚C samples are plotted for the x series and their variation with temperature shown in terms of conductivity (1/R) and C' vs. 1000/T and T, respectively. Fig: 5.22A shows the conductivity values from R1, for x = -0.20 to 0.20. The general trend in conductivity shows that as x increases from -0.20 to 0.10, so does the conductivity, however for x = 0.20 its lower than 0.10. This was also seen from the hand fitting data, where x = 0.50 was the most resistive/least conductive sample.

For x = -0.20 and 0.00 the conductivity decreases after ~ 60 ˚C, for x = 0.05, and 0.07 this occurs slightly higher at ~70 ˚C. In contrast, x = 0.10 shows only a change in activation energy after ~ 70 ˚C, and for x = 0.20 it shows linear behaviour. This drop followed by an increase in conductivity is more pronounced when x is lower. For x = -0.20 to 0.07 the temperature range between 60 - 85 ˚C shows a region where conductivity is more or less constant.

On the cooling cycle from Fig: 5.22B, the conductivity for x = -0.20 to 0.07, more or less stays the same with a change in slope seen below 85 ˚C. For x = 0.10 and 0.20, the conductivity is still an order of magnitude higher than the other samples. Only at a lower temperature of ~ 50 ˚C is there a change in the slope observed for these samples.

Fig: 5.22C and D show how C1 changes with temperature during the heating and cooling cycle, respectively. During the heating cycle C1 increases as x increases from -0.20 to 0.07, for these samples there is a rise in C1 observed after 85-90 ˚C.

C1 for x = 0.10 is initially similar to 0.07, however with increasing temperature it decreases, with a peak at around ~ 40 ˚C. For x = 0.20, C1 mostly stays constant with a slight decrease after ~ 40 ˚C. For these samples however C1 at higher temperatures remains constant. On the cooling cycle there does not seem to be any significant trend except that as temperature decreases there is a slight increase in the capacitance value.

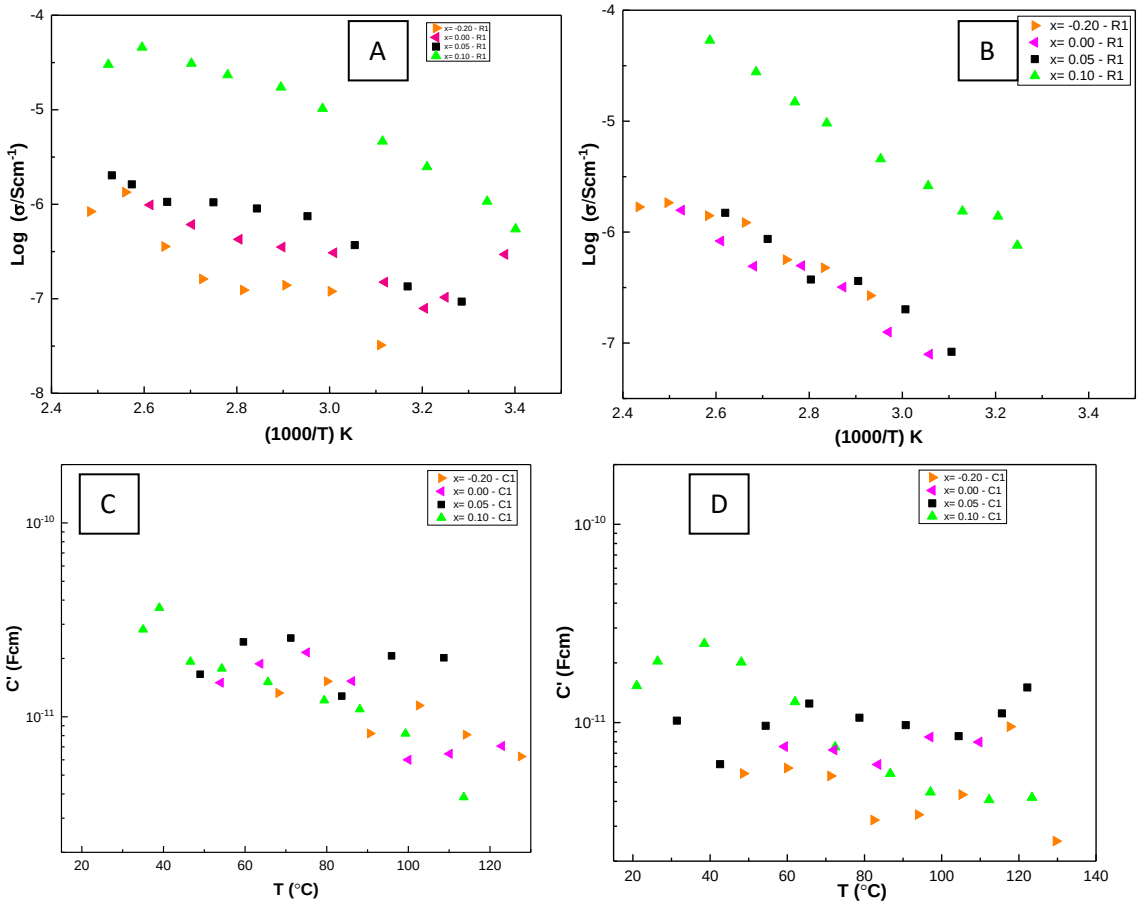

Figure 5.22. R and C values against temperature along the x-series. Conductivity Arrhenius plot on heating (A) and cooling (B) from R1 values. C1 on heating (C) and cooling (D).

Fig: 5.22A shows the heating cycle for 1/R2 conductivity across the x series. The lowest conductivity is for x = - 0.20, whereas for x = 0.00 to 0.07 the conductivities are more or less the same. x = 0.10 and 0.20 both have the highest conductivities. On the cooling cycle, Fig: 5.23B shows that for x = -0.20 to 0.07, the 1/R2 conductivity values are the same, with x = 0.10 and 0.20, having similar values and with a conductivity of an order of magnitude higher.

C2 on heating from Fig: 5.23C, shows that across x, C2 remains similar except for x = 0.20 which has the highest capacitance value, with a peak at ~50 ˚C after which there is a decrease with temperature. On the cooling cycle, Fig: 5.23D shows a clearer trend, as x increases from x = -0.20 to 0.20, C2 also increases. This trend is clearer at temperatures below 90 ˚C, since there is tendency for C' to rise with temperature after 90 ˚C, as seen for x = 0.00.

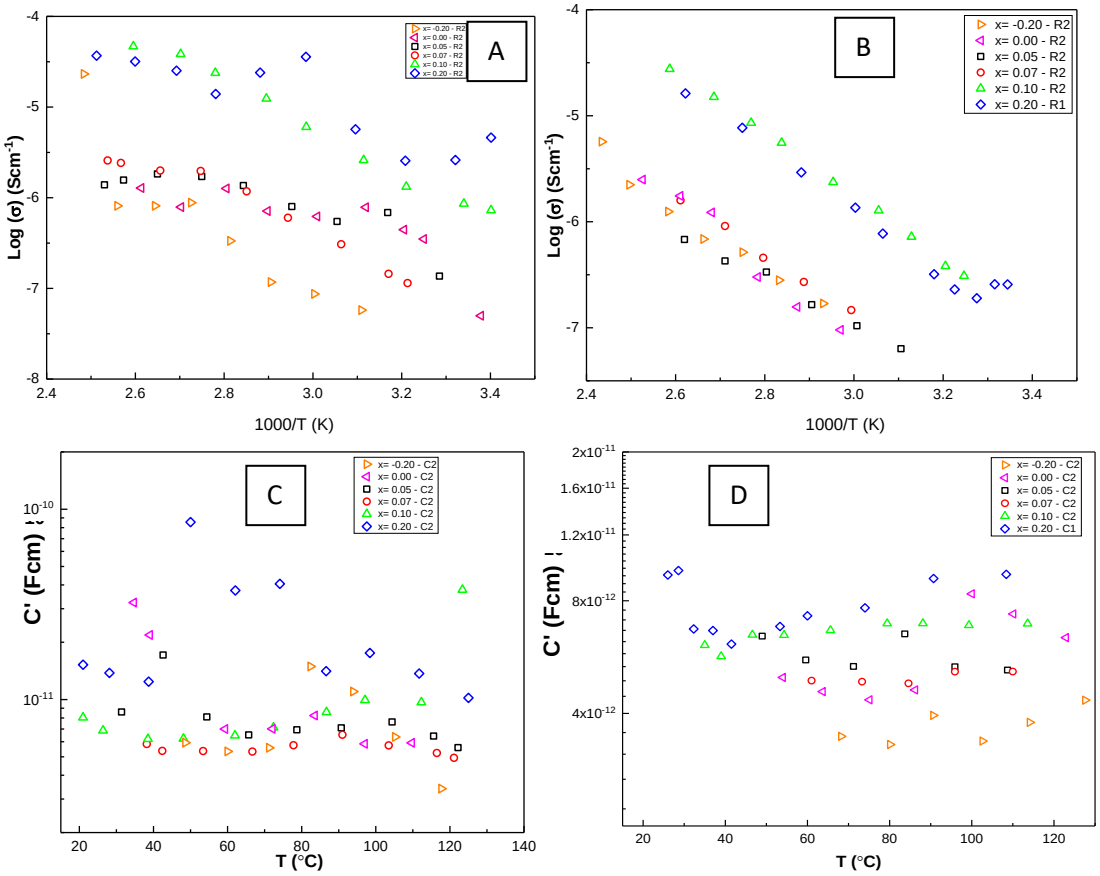

Figure 5.23. R and C values against temperature along the x-series. Conductivity Arrhenius plot on heating (A) and cooling (B) from R2 values. C2 on heating (C) and cooling (D).

Fig: 5.24 shows the comparison in 1/R1and 1/R2 between the 80 and 120 ˚C annealed samples on heating and cooling cycles. From plot A, except for x = 0.20, where 1/R1 is the same between 80 and 120 ˚C annealing temperatures the rest (x = 0.00 to 0.10) show that the 80 ˚C annealed samples have a higher conductivity, and the difference between the conductivity is higher along x. A similar trend is observed from 1/R2 values in plot B, although the difference in conductivity is smaller when annealed at higher temperatures. This trend remains on the cooling cycle as can be seen from plots C and D for 1/R1 and 1/R2, respectively, however, the difference in conductivities of 80 vs. 120 ˚C become even smaller.

It is noteworthy that the 80 ˚C samples are being heated to a higher temperature (~120 ˚C) than the temperature at which they were synthesised. Therefore, only the temperature region up to 80 ˚C on the heating cycle show the real trends, after which the 80 ˚C annealed samples should gradually become similar to those annealed at 120 ˚C albeit not completely due to the difference in annealing time.

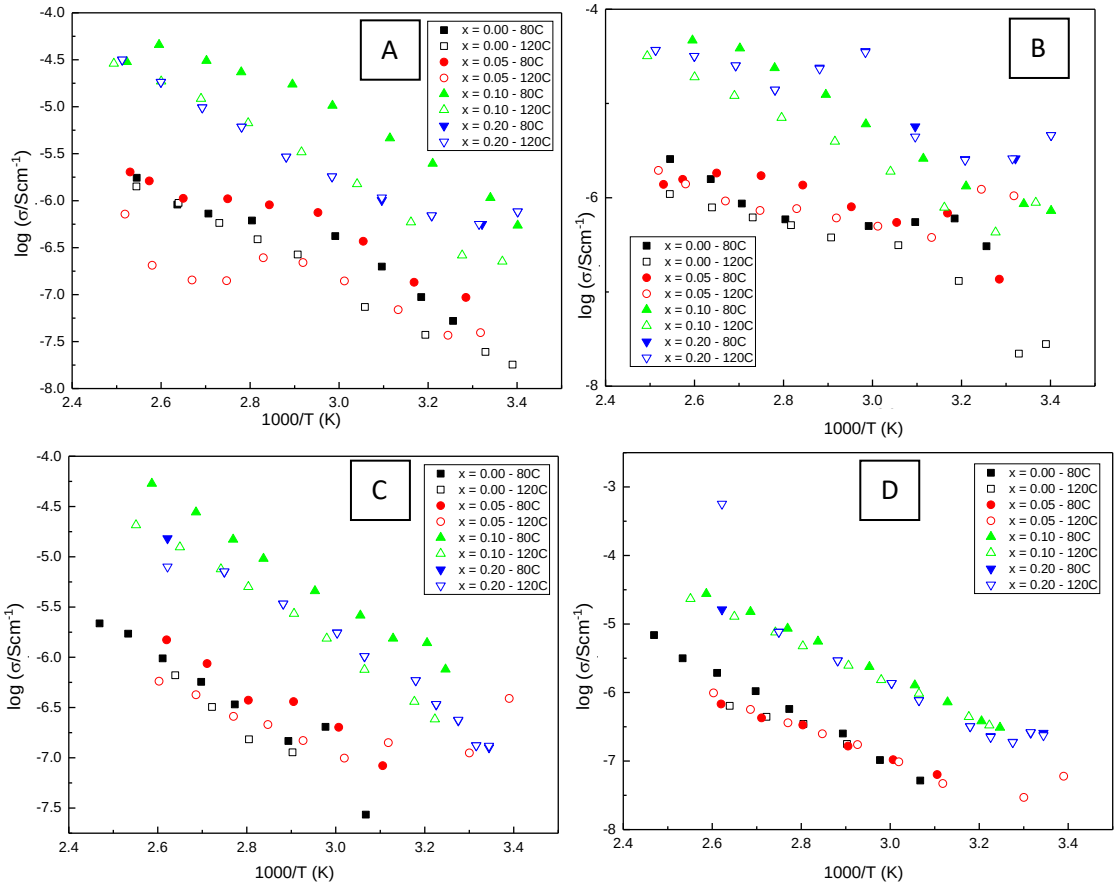

Figure 5.24. Conductivity Arrhenius plot comparing 1/R1 (filled symbols) and 1/R2 (open symbols) of x-series samples annealed at 80 ˚C and 120 ˚C. The conductivities from 1/R1 on the heating cycle (A) and 1/R2 on the heating cycle (B). Conductivities from 1/R1 on the cooling cycle (C) and 1/R2 on the cooling cycle (D).

ε_r of the samples calculated from C1 and C2 on both heating and cooling cycles do not seem to change much by increasing the annealing temperature of the powders from 80 to 120 ˚C, as shown by Fig: 5.25. The trend and magnitude for both remain similar, except for x = 0.05, 120 ˚C annealed sample where ε_r from C2 on heating (Fig: 5.25B) shows an increase after 80 ˚C. When below that temperature both ε_r values are the same, as they are also on the cooling cycle, from Fig: 5.25D.

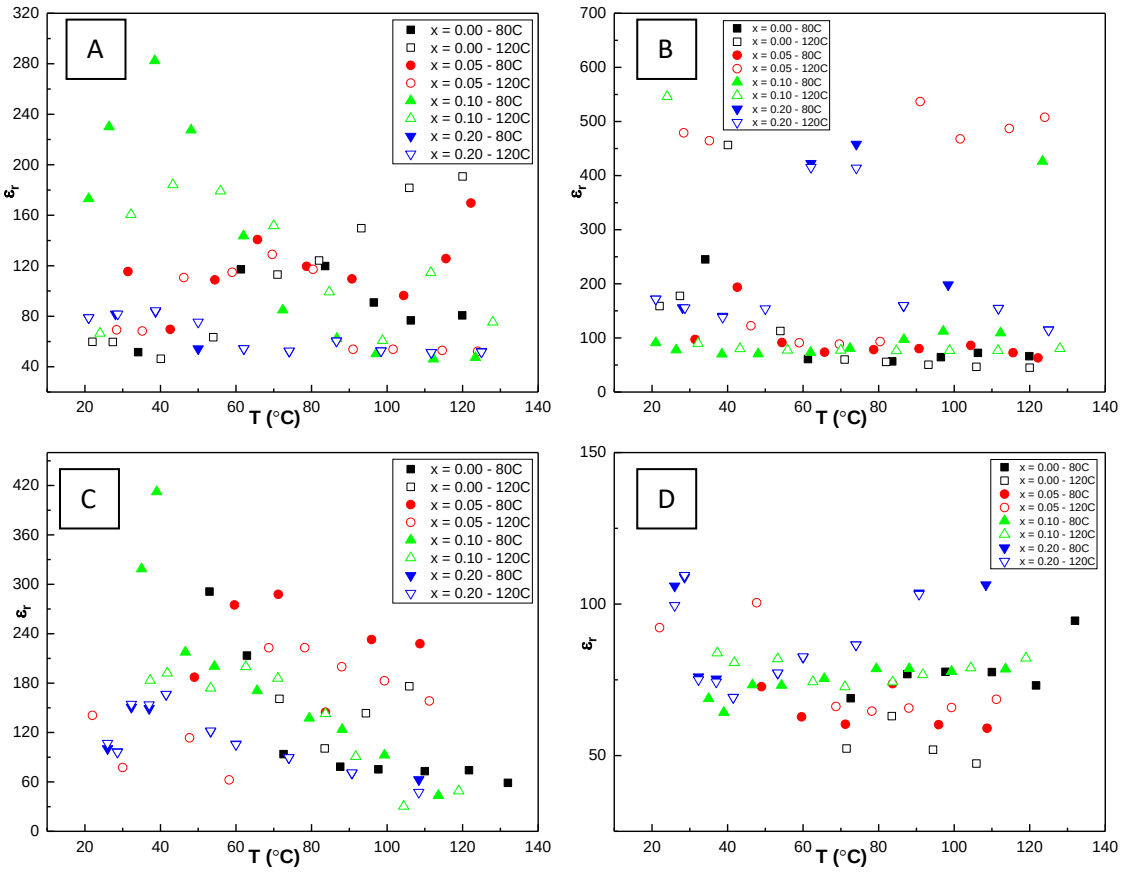

Figure 5.25. Permittivity vs. temperature plot comparing C1 (filled symbols) and C2 (open symbols) of the x-series annealed at 80 ˚C and 120 ˚C. The ε_r from C1 on the heating cycle (A) and C2 on the heating cycle (B). ε_r from C1 on the cooling cycle (C) and C2 on the cooling cycle (D).

The comparison of R and C values of the equivalent circuit (RQC-RC) to the hand fitting data shows that 1/R1 resembles the conductivity estimated from the M" peak, whereas 1/R2 is always higher on the heating cycle but decreases to resemble 1/R1 and M" values on the cooling cycle. On the second heating cycle 1/R2 has a higher magnitude compared to 1/R1. The values of 1/R1 from the RQC circuit resemble Z" values which tend to be slightly lower than M" on the heating cycle.

The trend in the capacitance from the hand fitting data shows that the M"(C') stays constant with temperature, however from the Z" (C') there seems to be a peak at ~60 ˚C. The trend in the C1 and C2 seems to be that initially C1 is higher and C2 lower, but upon increasing the temperature C1 decreases and C2 increases. Therefore, unlike the resistance elements (where at least on the heating cycle) it's easier to link 1/R1 values to the M" values and 1/R2 to the second response with a higher conductivity. The capacitive elements are more challenging to assign due to subtle variations with temperature.

Analysing the ε_r values in table 5.8 shows the LCR data closely resemble ε_r estimated from M'' and Z'' data for the 80 ˚C annealed samples, whereas for the 120 ˚C annealed samples the values from Z'' tend to be slightly higher.

Table 5.8. ε_r of x series from LCR data and ε_r values estimated from M''/Z'' peaks, from samples annealed at 80 and 120 ˚C respectively, on both cycles.

x	ε_r - LCR (65 ˚C)	ε_r - M'' / Z'' (80 ˚C)	ε_r - M'' /Z''(120 ˚C)
0	53	46/59	47/68
0.05	55	59/59	61/111
0.1	58	59/63	63/84
0.2	52	59/62	64/83

Table 5.9. ε_r of C1 and C2 from the equivalent circuit fitting of x series when annealed at 80 ˚C. ε_r shown from two different temperatures of ~65 and 120 ˚C, on both cycles.

x (Heating/Cooling)	ε_r C1 ~65 ˚C	ε_r C1 ~120 ˚C	ε_r C2 ~65 ˚C	ε_r C2 ~120 ˚C
- 0.20	60/150	108/68	60/37	38/48
0.00	115/93	80/74	60/66	65/77
0.05	120/287	170/227	73/60	63/65
0.10	143/170	47/43	80/75	110/79
0.20	54/89	51/48	458/86	114/106

Table 5.9 shows ε_r from C1 and C2 (at two different temperatures of ~65 and 120 ˚C) of the equivalent circuit applied to the 80 ˚C annealed samples. For x = -0.20 to 0.05 C1 at both temperatures and on both cycles are higher than C2, which resembles the bulk permittivity more closely although still slightly overestimating if compared to LCR and hand fitting data. The ε_r from C1 of x = 0.10 and 0.20 resemble the bulk more so than C2. The attributed bulk ε_r estimation from circuit fitting being more accurate for these samples than when x is lower, i.e. more PbI_2-rich.

The trend in n is shown for the x-series in Fig: 5.26. On the heating cycle from plot A it appears that n, for x = 0.00 to 0.07 has a similar trend where n increases with temperature with a peak at ~65 ˚C, after this n decreases but it starts to rise again on a further increasing of temperature. For x = 0.10 and 0.20, there seems to be an increase in n with temperature and after 70 ˚C, it remains constant. However, for x = 0.10 at ~70 ˚C and for x = 0.20 at ~40 ˚C, there is a rapid decrease in n with a small error after which the trend is maintained.

On the cooling cycle n stays constant, except at temperatures close to room temperature where it starts to decrease. The error in n is higher during cooling than on the heating cycle for all of the x series and the absolute error is also larger at lower temperatures.

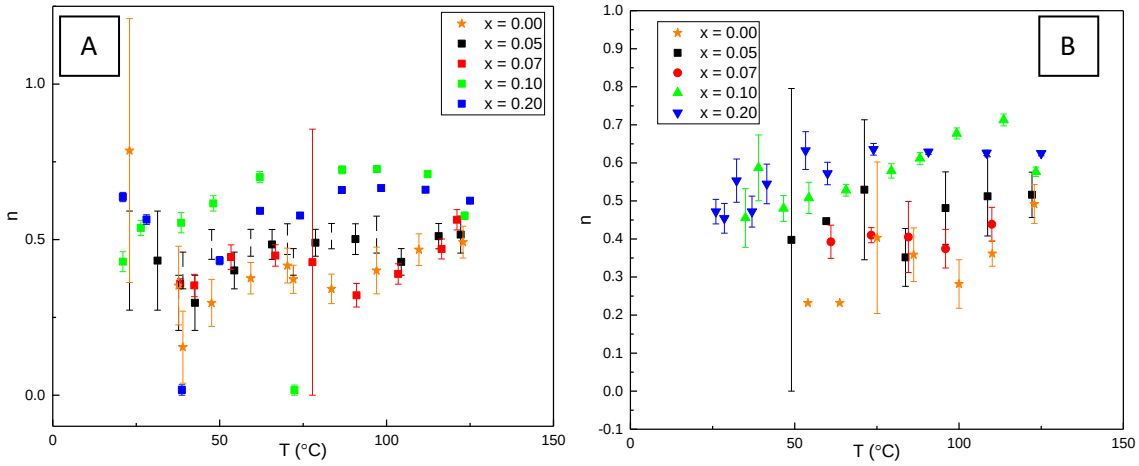

Figure 5.26. Variation of n with temperature for the x series on heating (A) and cooling (B) cycles. All data for 80 ˚C annealed samples.

5.8. Discussion of XRD/SEM

The mechanism of the ball milling reaction of MALI perovskite is similar to the one discussed in the beginning of the solid-state chapter. The only difference is the milling media and the use of ethanol. This milling process provides higher energy, better mixing due to the powders being submerged in a solvent and little to no loss of material [1]. Any material stuck to the milling media or inside the bottle is washed with extra ethanol.

The RT phase assemblage diagram for the ball milling route is shown in Fig: 5.1, for compositions from x = -0.90 to 0.90. The left-hand side (x <0.00) of the phase diagram was explored. This is where excess PbI_2 is added and the amount of organic precursor is reduced. The main difference observed is that using ball milling, (once the ethanol is evaporated at 80 ˚C and only the powder left), there does not seem to be any change in the XRD patterns of the material assemblage until above a temperature of 140 ˚C. This change was due to the start of the decomposition of the organic cation and the lack of any change below 140 ^{o}C implies samples have achieved equilibrium. A rotating mill where milling media is used to break down powders rather than using hand grinding is more efficient. This is because it is a higher energy process than hand grinding, with the additional factor of mixing for a longer duration which generally reduces agglomeration. As shown from the solid-state processing, not much energy is needed to form some MALI. The solvent also acts as a lubricant and aids better mixing. One parameter that could be explored was the ball milling time. This can be seen from Fig: 5.2 and 5.3, where a sample was milled for 1 and 6 hours, respectively. Even milling for a short time produced the same XRD pattern but there was a slight reduction in PbI_2 peak intensities in XRD data after 6 hours of milling. Therefore, just observing the

effects of milling time and temperature there is little effect on the phase assemblage after evaporation of the ethanol at 80 ̊C prior to decomposition at elevated temperatures.

The reduction of almost all MAI content, shown by x = -0.90 still produces MALI based on the low intensity peaks in XRD data. This left hand side of the phase diagram also matches with that from literature produced from thin films [2]. Similar to solid state synthesis, x = 0.00 can't be prepared as a phase-pure material. Using ball milling, an excess amount of MAI is added to produce a phase-pure MALI sample based on XRD data. The ball milling synthesis produces both x = 0.05 and 0.07 as a mixture of MALI and PbI_2 based on XRD data. A single-phase sample based on XRD analysis only emerges at higher values of x = 0.10 and 0.20. In contrast, solid state produces phase pure material at x = 0.05 and 0.10 whereas at x = 0.20 crystalline MAI was present in the XRD data. In contrast, crystallised MAI appears at x = 0.50 for ball milled samples. Therefore, the phase assemblage trend as a function of x is 'shifted' slightly to the right-hand side on ball milling compared to the solid-state method. The reason for this could either be due to the slightly higher temperatures reached in the ball milling process or due to the ethanol solvent. The best explanation is that MAI can partially dissolve in ethanol [3]. This prohibits full reaction between all reactants, since now some MAI is dissolved into solution. The MAI (at least small amounts of it, due to its low dissolution kinetics) could be lost when all the milling media and the milling bottle itself are washed with extra ethanol so as to collect all the milled material. When the ethanol is evaporated at 80 ̊C, it could evaporate with the ethanol itself. It could also be that the MAI that dissolves in ethanol does not react with the PbI_2 to form MALI; therefore, excess MAI is needed compared to the solid-state synthesis.

In thin film fabrication, ethanol is not generally used whereas organic solvents like dimethylformamide (DMF) and dimethylsulfoxide (DMSO) or even Gamma-Butyrolactone (GBL) are used [4]. This is because of the film quality produced by these polar aprotic solvents whereas polar protic solvents like ethanol have sluggish dissolution kinetics [3]. However, when using ball milling, a solvent like ethanol has to be used due to safety reasons as more dangerous and hazardous solvents like DMF are generally used in a glove box. Furthermore, ball milling uses a substantively larger amount of solvent especially at the end of the milling process in order to wash the milling media for any residue of the milled products left behind. Another important factor is also if these polar aprotic solvents are used there wouldn't be any need for milling since the precursors easily dissolve, because they have faster dissolution kinetics than ethanol so the reaction does not require any mechanosynthesis. Despite slow dissolution kinetics, Liu et al [1] indicate that ethanol can

enter the lattice of these crystals via hydrogen bonding with the organic ion or in coordination with the lead ions, but the interaction is not strong enough that it will actually dissociate MALI [1]. They designate this to the fact that when MALI crystals are exposed to ethanol they don't dissolve but turned into a yellow precipitate after ultrasonic treatment, and the colour change implied that ethanol can enter the lattice via hydrogen bonding. Ethanol itself can also absorb moisture from the atmosphere, and since the experiments weren't carried out in a glove box there wasn't any need to dry the ethanol beforehand because at some stage of the process the ethanol and the mixture would both be exposed to ambient conditions.

Observing the x-series XRD patterns and their changes with temperature, the PbI_2-rich samples ($x<0$) have the same phases present. Even above 140 ˚C, which is where the organic cation starts to decompose. Whereas, excess MAI samples ($x > 0$) show new XRD peaks and therefore phases emerging. Either unidentified peaks are observed or LDP and PbI_2 emerge again due to the decomposition of the organic cation.

Investigating the pellet surfaces using low voltage SEM of samples with excess MAI show similar results to the solid-state synthesis. However, the trends become clearer as well as the confidence in allocating the different phases due to changes in the fractions of the different contrasting regions. From Fig: 5.9 it becomes more obvious that the dark and light regions on the surface belong to a MAI-rich phase and PbI_2, respectively. This is attributed to better mixing and less agglomeration of the reagents in the ball milling route.

5.8.1. Discussion of the electrical data

5.8.1.1. LCR

The LCR results in Fig: 5.10 showing the ε_r and tan δ plots for the x series synthesised via ball milling reveal $x = 0.00$ and 0.05 to show a gradual decrease in ε_r with temperature. Although from the tan δ plots even these show a discrepancy between heating and cooling data when heated above 80 ˚C. This hysteresis doesn't occur at the MALI phase transformation temperature but at a higher temperature and may again be due to loss of water.

$x \geq 0.10$ show an increase in ε_r with temperature and a discrepancy between the heating and cooling responses. Especially during the temperature range of 50-90 ˚C. In the ball milled samples it becomes more challenging to determine the exact temperature where either a phase change or the loss of water occurs. If the ability to observe these phenomena is related the higher conductivity due to increased presence of MAI-rich regions, then the better mixing processing conditions and reduced agglomeration associated with ball milling may reduce this effect, therefore making these phenomena harder to observe. It could be that the

better, more energetic milling process changes the ratio of β and α' MALI ratio. However, both the ball milled and solid-state compositions show that it is the addition of excess MAI that has more effect on the electrical data. In contrast, x= 0.00 and 0.05 that contain excess PbI_2 show a more stable dielectric response, where ε_r decreases with temperature and there is less hysteresis between heating and cooling cycles.

5.8.1.2. Impedance and circuit fitting

The ball milled samples showed no differences in their XRD patterns as they were heated from upwards of 80 ̊C until decomposition. Based on results from the previous chapter and also comparing to the SEM results in this chapter it is clear that XRD is not a sensitive technique to elucidate minor changes in composition and/or phase assemblage. In contrast, the electrical response can change dramatically especially with the addition of a small excess of MAI and this can change with temperature even if the XRD results remain similar. Therefore, the ball milled samples were examined using IS when the x-series powders were annealed at 80 and 120 ̊C, respectively. Their results are shown in Fig: 5.12 to 5.14. The trends for both across the x series remain similar, i.e. as more MAI is added, the total sample resistance initially decreases, with the smallest resistances being for x = 0.10 and 0.20. When further MAI is added, for example x = 0.50 (so when MAI can be observed in XRD as its crystallised form) the total sample resistance is the highest.

IS measurements at similar temperature and for the same composition show the materials at 120 ̊C have slightly higher total resistance values when extracted from Z^* plots. The ε_r values are higher on heating than on cooling, similar to the LCR results; however, the heating cycle results for the same composition and batch can vary. This is attributed to up-take of moisture which is then lost upon heating. To compare actual material properties it is therefore best to analyse data only from the cooling cycle.

The ball milling results show a single Debye peak, with little difference between the M" and Z" f_{max} values. This would generally indicate the material is electrically homogenous. However, analysing the ε_r values on both cycles show that they don't seem very homogenous. ε_r extracted from the M" data resembles the MALI bulk property as shown in tables 5.3 and 5.5. However, comparing the difference between the heating and cooling data, ε_r values across the x-series from both the M" and Z" plots it can be observed that the differences are larger in the Z" plots. The bulk ε_r values from M" plots stay relatively constant compared to that extracted from the Z" plots. The ε_r values extracted from the Z" peaks, especially at higher x values, can be as high as ~70-111. This is not in the range of MALI where ε_r is

typically in the range of ~45-50. Although even these are slightly higher when compared to the literature which shows a range of ~35-45 [5]–[7]. This could be the influence of a secondary response that is albeit hard to detect, most probably because the time constants are similar to that of the bulk. And as was discussed in chapter 4, related to a mixture of different types of MALI being present.

The Arrhenius plot for the x series in Fig: 5.17 shows the conductivity temperature relationship for both 80 and 120 ̊C annealed pellets. They have similar trends and also similar values on the cooling cycle. The Arrhenius plots also show behaviour that could be attributed to either the loss of water on heating and the up-take of it on cooling. As shown in Fig: 5.16 the same composition from different batches can have significantly different conductivities. On the heating cycle, due to having different levels of moisture in a given sample, one sample has a much higher conductivity. Their conductivities decrease above 85 ̊C and then subsequently on the cooling cycle the conductivity is the same as other batches of the same composition. Evidence for picking up moisture from the atmosphere seems to be evident from the last room temperature measurement on the cooling cycle where the conductivity increases again, and therefore a linear conductivity Arrhenius relationship over the complete cooling cycle is not obtained.

The major result is that a slight increase in nominal MAI content above the ideal stoichiometry, i.e. when x = 0.10 and 0.20, produces an increase in the conductivity of more than 1 order of magnitude. As this is maintained on the cooling cycle it is a genuine sample-related phenomenon, rather than an artefact due to proton conduction or residual solvent present in the material.

This suggests that when there is PbI_2 present as a secondary phase the preferred current pathway is via MALI perovskite phase. Comparing the impedance response of MAI deficient samples to x = 0.00 (Fig: 5.15) showed f_{max} stays the same and the total resistance also does not change significantly (only a slight increase for x = -0.20). However, the addition of excess PbI_2 decreases ε_r, (with a value of ~45 for x = 0.00 & -0.10, and ~35 for x = -0.20) and this is probably due to the low dielectric constant of PbI_2. When a pellet of PbI_2 was pressed and measured it showed a value of ~11 compared to a literature value of ~7 [8]. The decrease in ε_r is due to the increased volume fraction of the lower permittivity PbI_2 present in x < 0 samples. In the conductivity behaviour of these PbI_2-rich samples, from Fig: 5.18 it shows no change on the cooling cycle. This gives further proof along with the LCR results that it is the addition of a small amount of MAI that has a dramatic effect on the electrical properties of the samples, since too much MAI also makes it too resistive so the

current also avoids the crystallised MAI. As is the case for when x = 0.50, the conductivity decreases to similar levels as x = 0.00.

Fig: 5.27 shows some impedance data of these precursor phases. The room temperature data for MAI shows that it is a rather conductive material considering its M'' f_{max} is $1.2x10^5$ Hz whereas the response for the PbI_2 shows a suitably clear response in the frequency domain at much higher temperatures of about 156 ˚C. A sample of nominally stoichiometric MALI at room temperature has an f_{max} of $1.5x10^4$ Hz.

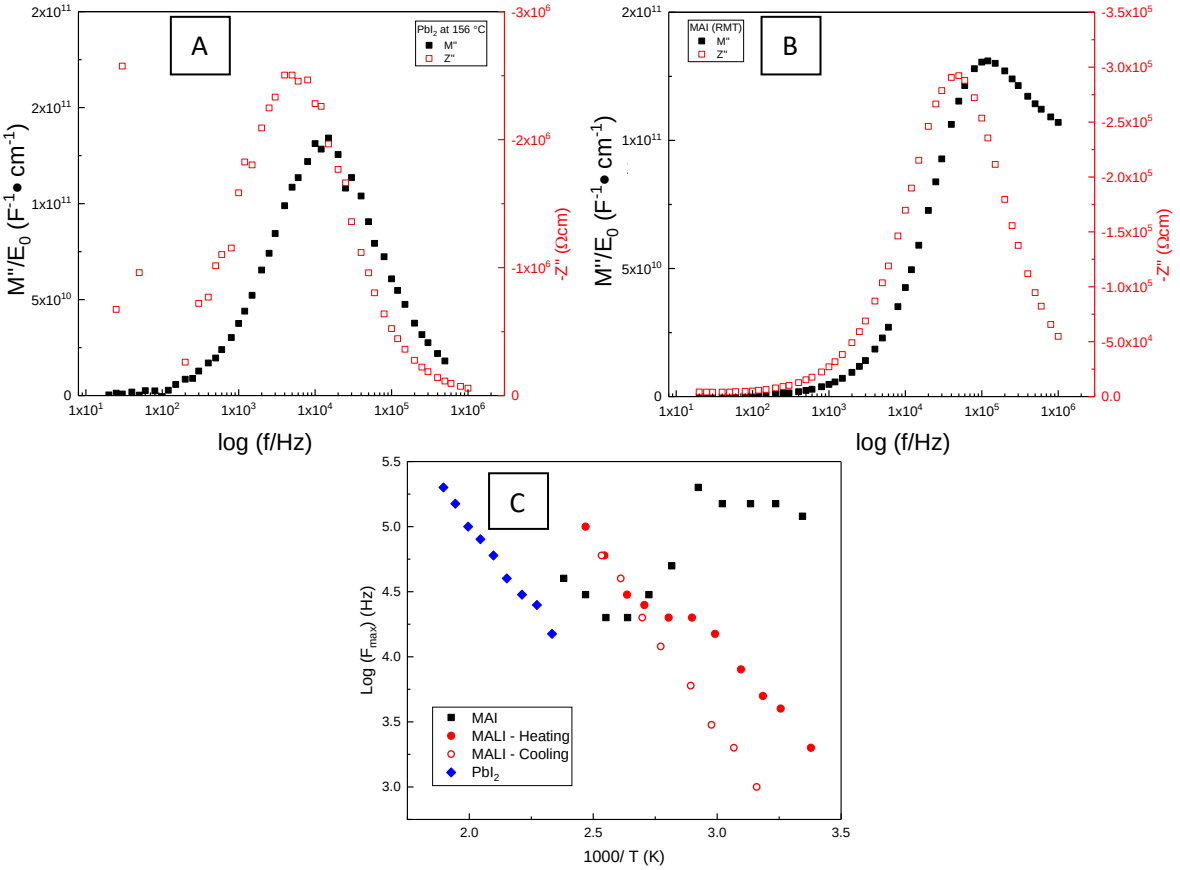

Figure 5.27. Plot (A) an M''/Z'' spectroscopic plot for a PbI_2 pellet at 156 ˚C. Plot (B) an M''/Z'' spectroscopic plot for a MAI pellet at room temperature. Plot (C) shows the log f_{max} vs. 1000/Temperature relationships for PbI_2, MAI and x = 0.00 MALI pellets. The values are calculated from the M'' peak.

From Fig: 5.27C, the log(f_{max}) vs. inverse temperature plots (for the M'' data) are shown for MALI, PbI_2 and MAI. In all cases, the M'' peak is taken to be representative of the bulk response of each material. f_{max} is a geometry independent parameter that is intrinsic to the conductivity and permittivity values (and their temperature dependencies) of each material. Given that the permittivity of the phases is not strongly temperature dependent, the exponential temperature dependence of f_{max} in Fig: 5.27C is dominated by the conductivity of the material. The f_{max} trend for MAI shows similar heating behaviour to MALI, where after heating above 70 ˚C there is a decrease in the f_{max}, which indicates a decrease in conductivity;

however, in the initial stage of heating the f_{max} (and therefore conductivity) of MAI is significantly higher than MALI. This high f_{max} and subsequent drop at ~ 70 ^{o}C is most likely due to water loss due to desorption of water molecules associated with the MA ions in MAI. Further heating increases f_{max} and after 150 ̊C, the M" plot moves outside the measurable frequency range. After this decrease in f_{max} both in MAI and MALI, MALI seems to have slightly higher f_{max} values. The permittivity of MAI is measured to be around ~40, higher than PbI_2 and closer to that of MALI. Therefore, the increase in conductivity of MAI-rich MALI samples corroborates with the higher conductive precursor of MAI; however, this doesn't necessarily mean that it is residual MAI itself that increases the conductivity of the x series. This is because at very high x values such as x = 0.50 (where crystalline MAI is present as a secondary phase), the conductivity is similar to x = 0.00, indicating a decrease in conductivity compared to x = 0.10. These results implicate that although MAI itself has a high conductivity and a similar behaviour on the heating cycle it is not the additional MAI itself that seems to be causing the higher conductivity. This is because it would have then appeared that as x increases so does the conductivity; however, when x = 0.50 the conductivity is closer to x = 0.00 rather than x = 0.10 when the M'' bulk response from MALI has the highest magnitude. What this does indicate is that the enhanced conductivity on the first heating cycle of x-series MALI samples is associated with water absorption due to molecular interactions between the A-site MA ion and water in the MALI.

The discrepancy between the M" and Z" extracted permittivity values probably indicates two different elements with similar time constants so that IS does not enable clear identification of it through hand fitting alone. Therefore, circuit fitting was implemented to compare single and two element circuits. The M" peak could easily be attributed to the bulk MALI ε_r, the values from the Z" spectra were slightly higher. The two circuits RQC and RQC-RC were then fitted to the data and from Fig: 5.20 and 5.21 it is quite clear that RQC-RC has a better fit. Although this on its own does not necessarily mean that there are two elements present, because the use of more elements usually allows better fitting to the data. However, with a much better fit with RQC-RC it is reasonable to assume that there is a second element present in these ball milled materials. This is most significantly seen from the SEM data, as there is always the MAI-rich phase present in the organic-rich compositions. But this is hard to distinguish in some samples, especially at higher x values. This is not only because the time constants are already probably too similar too each other, but the better processing conditions under ball milling makes it harder for the differences to be distinguished. As discussed before it is the small increase in excess MAI that increases the

conductivity. Going to either of the extreme ends of the phase diagram, it seems clear that it is not excess crystallised precursors (PbI_2 or MAI) that causes this phenomenon. It is therefore proposed (as discussed in chapter 4) that samples prepared by ball milling can also contain β MALI and SPS MALI (α'), especially for those with x> 0.

The organic-inorganic hybrid perovskite materials tend to be both physically and chemically unstable under conditions of heat, light, humidity and internal or external biases. These are related to their crystal structure and molecular or atomic stability [9].The main source of instability in MALI is its organic cation making it possible for many intrinsic defects to form due to their low formation energy [9]. The defect formation can be affected by the fragmentation of the organic cation which can occur during operating conditions or thin film (or bulk) fabrication. Not only can these fragmented groups (e.g.: CH_2, CH_4, NH_4,CH_3NH_2 etc) then interact with the halide or Pb but also the dissociation of hydrogen from the MA^+ can undergo secondary reactions with surrounding species and molecules [9]. How much these effects can be seen in bulk powders is not yet established, however they could possibly contribute especially in MAI-rich samples.

5.8.1.3. Self-doping and conduction mechanisms

MALI perovskite represents an electrochemically active system with mobile hydrogen cations and iodine anions. This was observed when MALI thin films were investigated under electric fields. MALI has been shown to be a mixed conductor with significant levels of ionic conductivity, and shown to have increased photovoltaic performance in the presence of protons in the form of moisture [10]. This self-doping mechanism, (where the precursor ratio is altered in order to change the defects) under illumination has been seen to give rise to the strong photoconductivy of MALI thin films and an increase in their dielectric constant in the order of 1000, although this is in the low frequency region, rather than the high frequency region where bulk material values are obtained [10]. Even under illumination, thin films showed the formation of negatively charge hydrogen vacancies and positively charge iodine vacancies leading to p- and n-type materials, respectively. The migration of these ions under an electric field seems to be responsible for hysteresis of the current voltage characteristics of the photovoltaic cells.

From computational defect studies under I-rich/Pb-poor conditions acceptor Pb-vacancy defects V_{pb} have a low formation energy. Higher formation energies were calculated for donor defects and this makes the Fermi level move nearer to the Valence Band Maximum, VBM, and therefore produces p-type conductivity. The opposite conditions where it is I-

poor/Pb-rich and the donor defects MA_i (interstitial) and MA_I (anti-site) have lower formation energies whereas those for the acceptor defects (V_{Pb}, MA_{Pb}, and I_i) increase and shift the Fermi energy level closer to the conduction band minimum, CBM, resulting in n-type conductivity. Altering the chemical conditions can change the conductivity and may result in the donor MA and dominant acceptor V_{Pb} defects having comparable formation energies [11].

MALI has many low energy donor and acceptor intrinsic defects so can form compensated charge neutral clusters. Three types of these vacancy clusters or Schottky defects have been investigated. These are MALI itself, MAI and PbI_2. Removal of all of them from the perovskite lattice requires low energy and therefore their concentration is high, therefore they are energetically favourable to be removed from the lattice. The high concentration of Schottky defects makes 0.4% of the lattice sites unoccupied by any ions. The dominant defects are then p-type V_{Pb} and n-type MA_i. These low formation energy defects create shallow bands, while deeper levels have higher formation energies. These properties are due to the strong Pb lone pair s orbital and I p orbital antibonding coupling of MALI [12].

The self-doping or unintentional doping is related to intrinsic defects. During MALI synthesis the relative abundance of either precursors may result in Schottky defects such as PbI_2 or MAI vacancies [13]. Therefore, MALI can be self-doped by defect engineering by changing the precursor ratio. Stoichiometric MALI was reported to be an n doped material with high electron concentration. It was also reported that a slightly higher amount of MAI was needed to achieve phase purity, with the ratio diverging from a stoichiometric value of 0.50 to 0.52 [14]. Making the composition more MAI rich reduced the electron concentration, and converted it into a p-type material. Whereas, increasing the PbI_2 content increased the electron concentration and made it an n-type material. However, it is in the p-type materials that the carrier mobility is much higher. A similar effect is seen in thermal annealing of these thin films. Starting out with a p-type material and heating above 150 ̊C where it then becomes thermally unstable. The material then turned into an n-type with high electron concentration and significantly reduced mobility [14], all by decomposing the MALI thin film.

This change in the stoichiometry changes the Fermi energy level and therefore changes the type of conductivity present in the material without affecting the band gap, as shown in Fig: 5.28A. The MAI-rich materials are p-type while the PbI_2-rich materials are n-type [15] since changing the stoichiometry affects the point defects in MALI. The p-type material is observed to have a higher conductivity, and under Hall effect measurements these p-type materials have lower carrier concentration than the n-type material but much higher Hall mobility [14]. A stoichiometric ratio has an electron concentration of 2.8×10^{17} cm^{-3},

where reducing the ratio to get a p-type material has an electron concentration of 4 x 10^{16} cm^{-3} and increasing the ratio for a n-type material produces an electron concentration of 3.5 x 10^{18} cm^{-3}. These results are summarised in Fig: 5.28B, where MALI is MAI-rich the perovskites possess a lot of Pb and I vacancies due to the deficiency of PbI_2. And it is most likely that Pb vacancies also play a critical role in contributing to the p-type conductivity [14]. It could be that the small increase in MAI while decreasing the carrier concentration increases the mobility much more therefore leading to a higher conductivity.

The work in this thesis shows that the variation in the electrical properties based on variable MAI/PbI_2 precursor ratios (x values) may also be related to the development of composite microstructures. For $-0.20 \leq x \leq 0.05$ the β-form of MALI (tetragonal) dominates the electrical properties whereas there is compositional range of $x \sim 0.10$ to 0.20 where the β- and α' phases of MALI can coexist and as discussed in chapter 4 and this can give rise to much higher conductivity. However, for x = 0.50 when the excess MAI is crystallised as a secondary phase, the samples revert to more insulating behaviour.

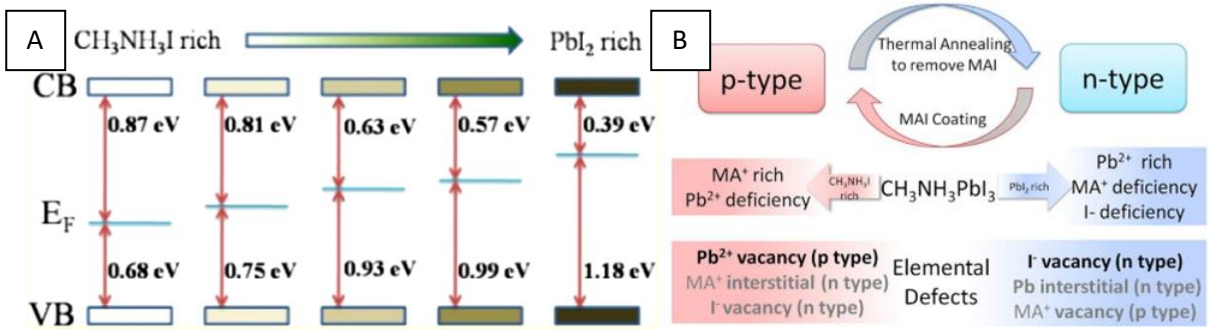

Figure 5.28. (A) shows the variation in the Fermi energy level by changing precursor ratio in the MALI system and (B) shows its effects on changing the material into either P or a N type semiconductor and its possible defect mechanism. Figure reproduced from [14].

The activation energies, E_a shown in table: 5.7 for the x series, from x = -0.20 to 0.20 are in the region of 0.44 - 0.60 eV, with only x = 0.50 having $E_a \sim$ 0.85 eV. This does not follow the trend in Fig: 5.28A. For x = 0.50 the closest value should be 0.68 eV and for x = -0.20 the closest value should be 0.99 eV, which don't correlate with these results. However, the E_a's calculated in this work from the impedance data are only in the higher temperature range of above 70 ̊C. Their data range is shown in Fig: 5.17 and 5.18; however, the data in Fig: 5.28A were measured at ambient conditions on thin films using scanning tunnelling spectroscopy. These values can't then be used to pinpoint if the composition is either n- or p-type. Also the observation that the increased conductivity of the p-type materials is due to higher mobility makes less sense because it is the n-type material which has a large increase in carrier concentration when Hall measurements of the thin film are carried out.

In conclusion, there is a significant increase in conductivity with a small increase of MAI in the MALI system. The electrical results on the heating cycle are affected by the possible presence of moisture, which not only gives significantly higher conductivity for all samples including the stoichiometric and PbI_2-rich ones, but also for differing batches of the same nominal composition. Therefore, it is the cooling cycle that shows a clear difference based on the intrinsic properties of the compositions rather than artefacts due to moisture or solvents. However even on the cooling cycle, there is evidence of picking up moisture from the atmosphere at lower temperatures. This is because there is a significant amount of time in-between different temperature measurements in IS.

The possibility of the higher conductivity being related to the material switching from an n- to a p-type by increasing the organic content remains unclear. Most significantly because it is the n-type that has higher carrier concentrations, and although the p-type has increased mobility due to it lower carrier concentration, it does not seem feasible to attribute the more than 1 order of magnitude higher conductivity to it. The experiment on MAI itself reveals that it has high conductivity at room temperature but this is most likely due to water being present, which is removed upon heating and results in a less conductive response but still higher than MALI itself. The subsequent higher conductivity of $x = 0.10$ than 0.50 indicates the increase in conductivity is most probably intrinsic to the composition of MALI because the composite samples that have crystallised MAI present have lower conductivity. Furthermore, the enhanced conductivity on the first heating cycle is most probably associated with proton conduction due to adsorbed water molecules bonding with the A-site MA ions within MALI.

References

[1] Q. Liu *et al.*, 'A mixed solvent for rapid fabrication of large-area methylammonium lead iodide layers by one-step coating at room temperature', *J. Mater. Chem. A*, vol. 7, no. 31, pp. 18275–18284, 2019.

[2] Z. Song, S. C. Watthage, A. B. Phillips, B. L. Tompkins, R. J. Ellingson, and M. J. Heben, 'Impact of Processing Temperature and Composition on the Formation of methylammonium Lead Iodide Perovskites', *Chem. Mater.*, vol. 27, no. 13, pp. 4612–4619, 2015.

[3] B. J. Kim *et al.*, 'Selective dissolution of halide perovskites as a step towards recycling solar cells', *Nat. Commun.*, vol. 7, no. May, pp. 1–9, 2016.

[4] S. Thankaraj salammal, V. Panneerselvam, K. K. Chinnakutti, P. Manidurai, and K. Parasuraman, 'Highly crystalline methylammonium lead iodide films: Phase transition from tetragonal to cubic structure by thermal annealing', *J. Vac. Sci. Technol. A*, vol. 39, no. 2, p. 022801, 2021.

[5] M. N. F. Hoque *et al.*, 'Polarization and Dielectric Study of methylammonium Lead Iodide Thin Film to Reveal its Nonferroelectric Nature under Solar Cell Operating Conditions', *ACS Energy Lett.*, vol. 1, no. 1, pp. 142–149, Jul. 2016.

[6] I. Anusca *et al.*, 'Dielectric Response : Answer to Many Questions in the methylammonium Lead Halide Solar Cell Absorbers', Advanced Energy Materials., vol. 7, no. 19, pp. 1614-6832, 2017.

[7] T. Y. Yang, G. Gregori, N. Pellet, M. Gretzel, and J. Maier, 'The Significance of Ion Conduction in a Hybrid Organic-Inorganic Lead-Iodide-Based Perovskite Photosensitizer', *Angew. Chemie - Int. Ed.*, vol. 54, no. 27, pp. 7905–7910, 2015.

[8] D. P. Yadav, H. N. Acharya, and K. V. Rao, 'Effect of quenching and X-ray irradiation on the dielectric properties of PbI_2 single crystals', *Phys. Status Solidi*, vol. 64, no. 1, pp. 413–417, 1981.

[9] B. wook Park and S. Il Seok, 'Intrinsic Instability of Inorganic–Organic Hybrid Halide Perovskite Materials', *Adv. Mater.*, vol. 31, no. 20, pp. 1–17, 2019.

[10] L. A. Frolova, N. N. Dremova, and P. A. Troshin, 'The chemical origin of the p-type and n-type doping effects in the hybrid methylammonium–lead iodide ($MAPbI_3$) perovskite solar cells', *Chem. Commun.*, vol. 51, pp. 14917–14920, 2015.

[11] W.-J. Yin, T. Shi, and Y. Yan, 'Unusual defect physics in $CH_3NH_3PbI_3$ perovskite solar cell absorber', *Appl. Phys. Lett.*, vol. 104, no. 6, pp. 63903, Feb. 2014.

[12] D. Han, C. Dai, and S. Chen, 'Calculation studies on point defects in perovskite solar cells', *J. Semicond.*, vol. 38, no. 1, pp. 1674-4926, 2017.

[13] J. Kim, S. Lee, J. H. Lee, and K. Hong, 'The Role of Intrinsic Defects in methylammonium Lead Iodide', J. phys. chem. lett., vol. 17, no. 5, pp. 1312-7, 2014.

[14] Q. Wang *et al.*, 'Qualifying composition dependent p and n self-doping in $CH_3NH_3PbI_3$', *Appl. Phys. Lett.*, vol.105, no.16,pp.163508, 2014

[15] G. Paul, S. Chatterjee, H. Bhunia, and A. J. Pal, 'Self-Doping in Hybrid Halide Perovskites via Precursor Stoichiometry: To Probe the Type of Conductivity through Scanning Tunneling Spectroscopy', *J. Phys. Chem. C*, vol. 122, pp. 20194–20199, 2018.

6. Organic Solvent synthesis

6.1. Executive Summary of Chapter 6.

In this chapter two different solvents were examined in the synthesis of x = 0.00 MALI, DMF and DMSO. The DMF solvent took less time to evaporate and produced a cleaner sample (by XRD analysis), whereas the DMSO required a long time to evaporate, with PbI_2 still being present in the final product. DMF was therefore used throughout the rest of the experiments to synthesise the x series. Some DMF remains attached to MALI after the solvent is evaporated at 80 ˚C. This produces a DMF-MALI complex(es) and all samples needed to be heated to at least 100 ˚C to decompose the complexes and remove any residual DMF.

The structural and morphological data from XRD and SEM combined showed the only sample to be clean is x = 0.00 at 120 ˚C. This is also the only stoichiometric sample that is clean from all the different synthesis methods used in this project. Unlike the ball milled samples in chapter 5 the DMF samples are more sensitive to temperature, since they have been mixed on the atomic level and heated only to evaporate the solvent. They had not been exposed to mechanical shearing and deformation as is present in solid state and ball mill processing. The phase assemblages become consistent after annealing at 120 ˚C, whereas above 140 ˚C decomposition starts. As with the previous synthesis methods, clean XRD patterns does not imply samples are single phase. For example, x = 0.05 and 0.10 show clean XRD patterns however SEM reveals the presence of MAI-rich dark regions. Heating these samples at higher temperature results in a reduction of these MAI-rich regions due to decomposition and an increasing amount of PbI_2 regions is observed.

The lack of exposure to mechano-synthesis combined with mixing on an atomic level means that there is better mixing of these samples. This may be why the DMF samples are the only ones that show any evidence for formation of a solid solution. Based on XRD analysis there is an increase in cell volume from x = 0.00 to 0.10.

The LCR results show more similarity to the solid state (chapter 4) route than ball milling (chapter 5). This might be linked to lower mechanical deformation in the solid state and DMF routes compared to ball milling. The similarity is that the DMF samples also display large hysteresis between the initial heating and cooling cycle and peaks are observed at 60 and 90 ˚C on the initial heating cycle. These are attributed to the phase change and loss

of moisture, respectively. These peaks tend to become less attenuated with cycling, which again shows that they are related to the presence of moisture in the samples. The trend in permittivity and tan δ along the x series is similar to previous synthesis methods where PbI_2 rich samples have low loss and permittivity and higher x samples have higher loss and permittivity at increased temperature. This is related to the higher MAI-content because once the samples are decomposed at 180 ̊C the dielectric loss and permittivity are both low.

IS results also display hysteresis behaviour however in the DMF samples at 80 ̊C, the higher conductivity during the initial heating cycle is not only due to moisture but also DMF due to the DMF-MALI complexes. Annealing powders over 100 ̊C removes these conductive complexes and any subsequent hysteresis is due to moisture alone. Conductivity based on cooling cycle data shows the same trend to that observed in the solid state and ball milled samples, where samples with intermediate x-values (just above x = 0.00) have the highest conductivity; however, the conductivity for these DMF samples are considerably higher. Equivalent circuit fitting showed the electrical microstructure was better fitted to the dual R-C-CPE and RC circuit compared to a single R-C-CPE circuit.

The samples were measured by IS when a dc bias (up to 4 V) was applied and this produced some interesting results. First, f_{max} of the M'' Debye peak associated with the MALI response altered, i.e. it moved to a higher frequency, indicating increased conductivity. The change in f_{max} occurred at a faster rate when a higher voltage was applied. Removing the bias moved f_{max} closer to the original value but was never fully reversible. The bulk response of MALI was clearly altered by a modest dc electric field. XRD analysis on these pellets after the dc bias had been applied and removed, showed extra unidentified peaks along with some colouration of the electrodes. Polishing the electrodes removes these peaks from the XRD patterns, with a similar effect observed when the samples are heated (as opposed to polished). These results suggest electromigration of constituent ions in MALI to the electrode surfaces in response to a dc bias. This strongly supports that ionic conduction (via, $CH_3NH_3^+$ and/or I^-) can readily occur in MALI and confirms that this material is best described as a mixed ionic-electronic semiconductor.

6.2 XRD

Compositions of $CH_3NH_3Pb_{(1-x)}I_{(3-2x)}$ with $0.00 \leq x \leq 0.50$ and $(CH_3NH_3)_{(1+x)}PbI_{(3+x)}$ with $-0.90 \leq x \leq 0.00$ were synthesised using dimethylformamide (DMF) solvent. x = 0.00

was also synthesised under different conditions such as at lower pressure and altering the solvent to dimethylsulfoxide (DMSO), to establish any changes in the structural or electrical properties associated with a different solvent.

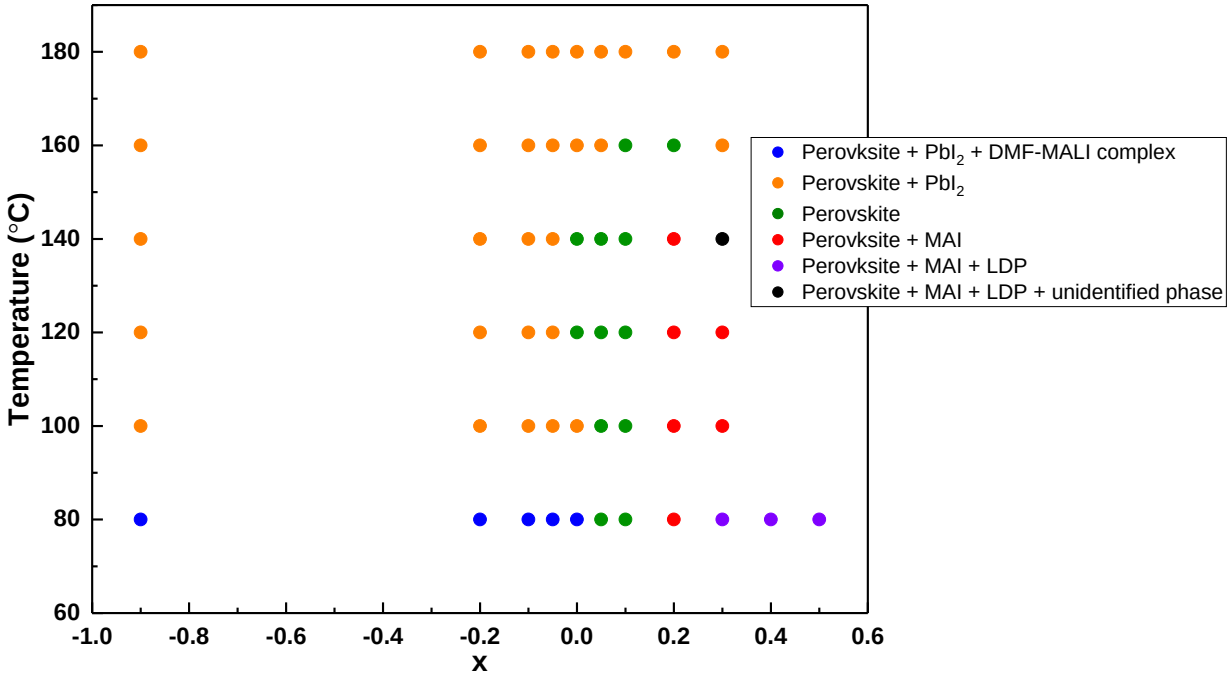

Figure 6.1. Phase assemblage diagram for compositions prepared using DMF solvent based on $(CH_3NH_3)_{(1+x)}PbI_{(3+x)}$.

The compositions synthesised using DMF solvent where x was altered to make MALI more PbI_2-rich by reducing MAI, or making it more organic-rich by reducing the PbI_2 quantity is shown in the room temperature phase assemblage diagram in Fig: 6.1. Starting with the PbI_2-rich composition of x = -0.90, the phases present after 80 ˚C are MALI, PbI_2 and a form of the perovskite MALI phase in which DMF remains and has not fully evaporated. Annealing the composition at 100 ˚C removes these DMF-MALI complexes with only PbI_2 and MALI remaining. These phases remain present upon heating up to 180 ˚C. The same trend is observed across x up to x = -0.05.

x = 0.00 after 80 ˚C shows similar phases present as the previous PbI_2-rich compositions at 80 and 100 ˚C. After 120 ˚C however, phase-pure MALI perovskite is formed. Annealing at 160 ˚C and higher shows the PbI_2 phase emerges in addition to the perovskite phase. MAI-rich compositions from x = 0.05 - 0.50, show x = 0.05 and 0.10 behave similarly. After 80 ˚C phase-pure MALI XRD patterns are observed and after higher annealing temperatures the samples remain phase-pure. x = 0.05 remains phase-pure after annealing up to 140 ˚C, like x = 0.00, whereas x = 0.10 remains phase-pure after annealing up to 160 ˚C

(probably due to containing more MAI). The results alter slightly when compositions are significantly reduced in their PbI_2 content. At x = 0.20 the perovskite and the precursor MAI phase are present after 80 ˚C and they remain until 140 ˚C. After 160 ˚C the XRD data show a phase-pure MALI pattern and after 180 ˚C, PbI_2 emerges as a secondary phase.

Increasing x to the range 0.30 - 0.50, a peak in the XRD data associated with LDP appears alongside the perovskite and MAI phases after annealing at 80 ˚C. When x = 0.30 is annealed at higher temperature the peak associated with the LDP phase disappears and only the MAI precursor and the perovskite phase are present. After 140 ˚C the peak associated with the LDP phase emerges alongside lower angle peaks that don't correspond to MAI, LDP or the DMF-MALI complex based on existing literature, therefore they remain unidentified. Annealing beyond this temperature shows only the perovskite and PbI_2 phases to be present.

In summary, synthesising MALI by the DMF route and varying the composition between the precursor end members shows that after annealing at 80 ˚C from x = -0.90 to 0.00 peaks associated with the DMF-MALI complex are seen in the XRD pattern. These disappear after annealing at 100 ˚C and are not observed again. As expected, compositions which are PbI_2-rich (x = -0.90 to -0.05) have the perovskite and PbI_2 phases present throughout different annealing temperatures. x = 0.00 becomes phase-pure only after annealing at 120 ˚C and remains so until 140 ˚C. After this, decomposition of the organic cation starts to occur, thereby after annealing at 160 ˚C and higher PbI_2 emerges. This decomposition and subsequent changes in the XRD data are observed for x = 0.05 - 0.30 after annealing at 140 ˚C. For x = 0.20, a phase-pure perovskite is produced on annealing at 160 ˚C not due to completion of reaction but presumably to decomposition of the excess MAI. The LDP peak appears only for x = 0.30 and remains so with increasing x but only when annealed at 80 ˚C. No peaks attributed to the DMF-MALI complex are seen when x is higher than 0.00. When the starting compositions are too organic-rich, as is the case for x = 0.30, and the annealing temperature is sufficiently high for decomposition to occur, then other unidentified phases are formed.

6.2.1 MALI - polymorphs for x = 0.00

As phase-pure 3D MALI has three polymorphic phases, x = 0.00 MALI (powder annealed at 120 ˚C) was placed in a Stoe (Mo) PSD XRD machine to collect low and high temperature XRD data, shown in Fig: 6.2. At room temperature it has a tetragonal structure, whereas at a low temperature of around -123 ˚C, it has an orthorhombic structure whereas at ~ 67 ˚C it has a cubic structure. The easiest way to observe this is to concentrate on the peak at

$2\theta = 23.4^{\circ}$, with 1/d value 0.26 $Å^{-1}$, corresponding to the peak (211). This is seen as a split peak in the orthorhombic phase, a single peak in the tetragonal phase and disappears in the cubic phase. Another main peak of the tetragonal phase appears at 1/d = 0.31 $Å^{-1}$, in the orthorhombic phase this splitting is clear, whereas in the cubic phase it appears as a single peak.

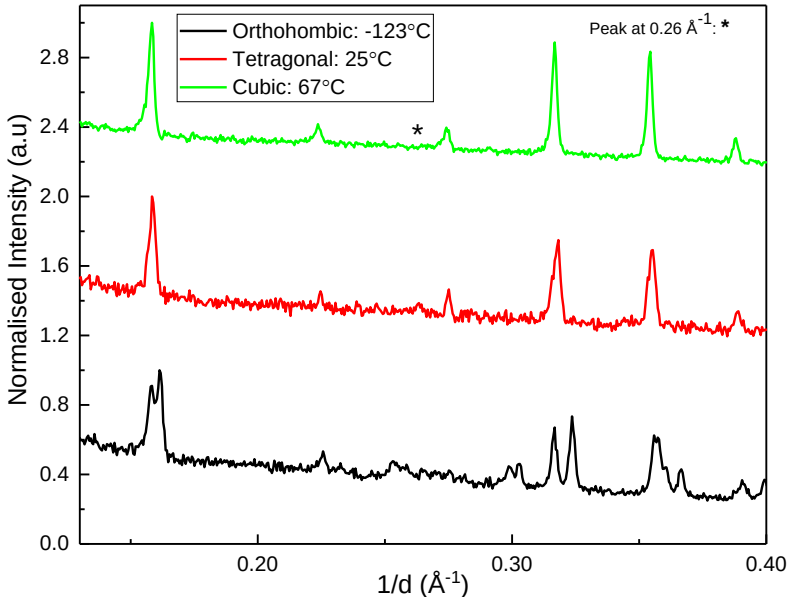

Figure 6.2. High-, room- and low-temperature X-ray diffraction patterns for x = 0.00 annealed at 120 °C. The orthorhombic polymorph was observed at -123 °C, the tetragonal polymorph was observed at room temperature and the cubic polymorph was observed at 67 °C.

6.2.2. MALI synthesised in ambient conditions

The XRD results show that x = 0.00 was synthesised to be phase-pure MALI when heated to a minimum of 115 °C. This is shown in Fig: 6.3, where after heating at 115 °C phase-pure MALI was formed, whereas at 80 °C there were extra peaks attributed to a DMF-MALI complex (6.5,7.9 and 9.5 degrees), PbI_2, and MAI (9.8 degrees). The material remains phase-pure when annealed at higher temperatures, up to 170 °C. Annealing at this temperature showed the appearance of PbI_2, as shown by the reflection at 12.7 degrees. Further annealing at 190 °C the peaks associated with PbI_2 seems to have increased and another PbI_2 peak appears at 25.9 degrees.

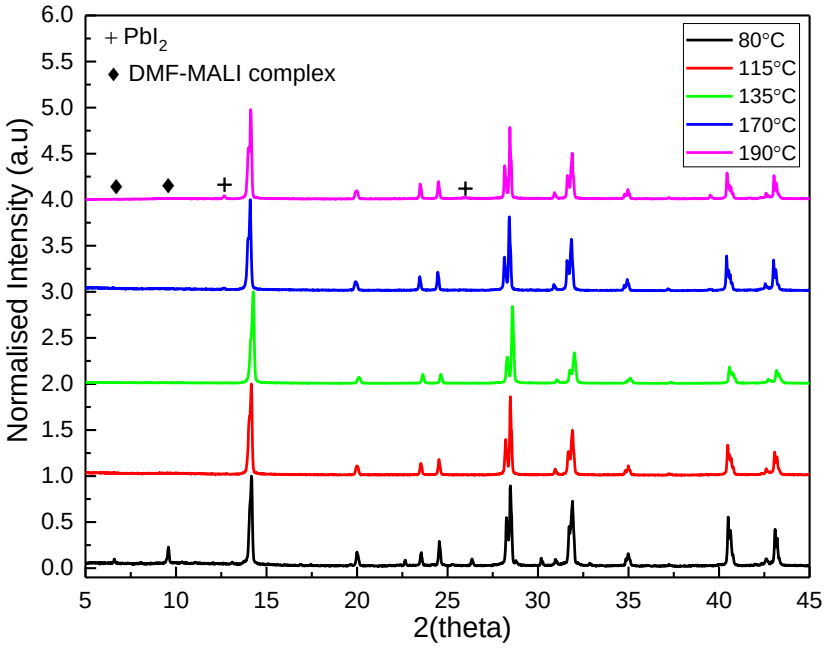

Figure 6.3. X-ray diffraction patterns for x = 0.00 MALI synthesised using DMF and oven dried at atmospheric pressure at 80 ˚C. Subsequently powders annealed further at higher temperatures.

6.2.3. MALI synthesised at low pressure

x = 0.00 was annealed at different temperatures while being under vacuum. The results from Fig: 6.4 show that after 80 ˚C MALI will still not form a single-phase even under low pressure with the DMF-MALI complex still being present. It does form pure-phase MALI at a lower temperature of 95 ˚C rather than 115 ˚C (when it's in ambient conditions of pressure). When x = 0.00 is heated under vacuum the characteristic PbI_2 peak starts to appear after annealing at 150 ˚C.

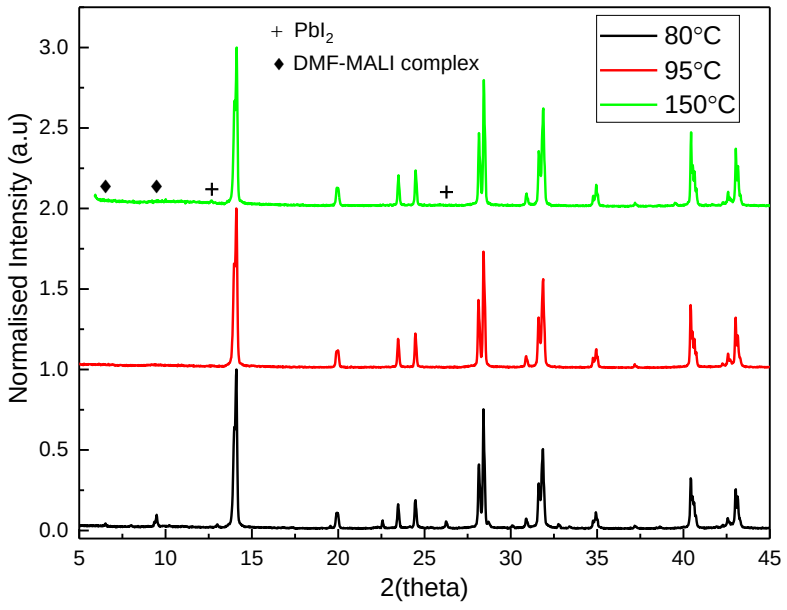

Figure 6.4. X-ray diffraction pattern of x = 0.00 MALI, synthesised using DMF under vacuum and then further annealed at higher temperature still under vacuum conditions.

6.3. MALI synthesised using DMSO solvent

Fig: 6.5 shows x = 0.00 synthesised using DMSO rather than DMF as the solvent. A major difference is that unlike DMF which seems to evaporate after 48 hours DMSO evaporates after around 168 hours when being heated at 80 ˚C. Also, when comparing XRD patterns at 80 ˚C for x = 0.00 synthesised using DMF and DMSO, it can be observed that the DMSO sample contains many unidentified precursor peaks. Even when the powders are annealed at a temperature as high as 130 or 150 ˚C with DMSO, phase-pure MALI can't be obtained. This is in contrast to DMF. Unlike x = 0.00 prepared using DMF, which becomes phase pure at 115 ˚C, x = 0.00 made using DMSO still has PbI_2 present when the powder is annealed at 130 ˚C.

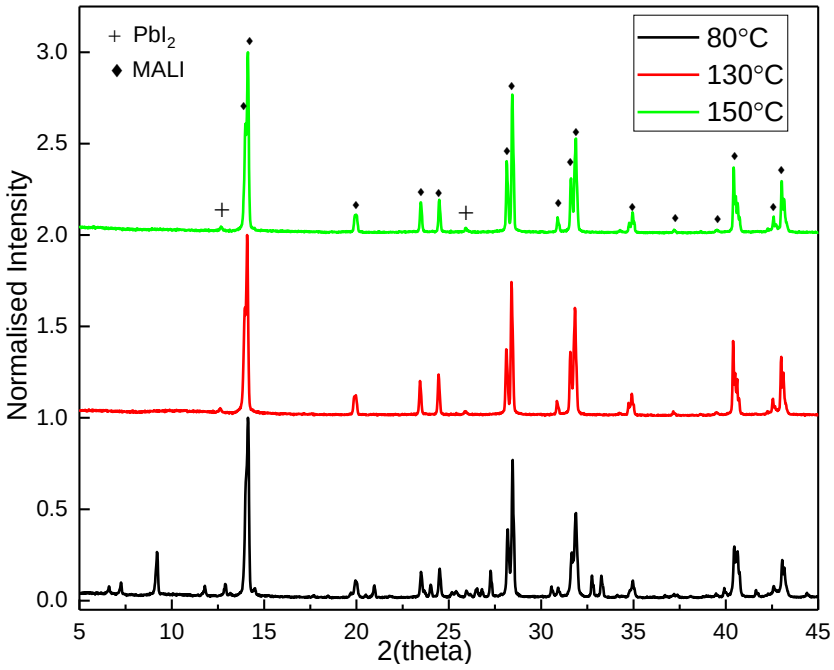

Figure 6.5. X-ray diffraction pattern of x = 0.00 MALI synthesised using DMSO solvent and then heated at 80, 130 and 150 ˚C.

MALI can therefore be synthesised using DMF solvent and then annealed at a minimum of 115 ˚C, since at lower temperature a DMF-MALI complex is formed. This temperature can be lowered to 95 ˚C if samples are annealed at lower pressure. If the solvent is altered to DMSO then phase-pure MALI can't be formed.

6.4. XRD of compositions across the x-series

Fig: 6.6 shows XRD patterns of the x series synthesised at 80 ˚C. The trend along x (aside from altering the phases present already mentioned in Fig: 6.1) from -0.90 - 0.50

shows that only very significant reductions in MAI content (x = -0.90) produces very low intensity peaks for the perovskite phase. The only compositions which appear phase-pure at this temperature are x = 0.05 and 0.10. The LDP phase starts to appear at x ≥ 0.30. The peaks due to the DMF-MALI complex appear only at 80 ˚C and only for x = -0.90 to 0.00.

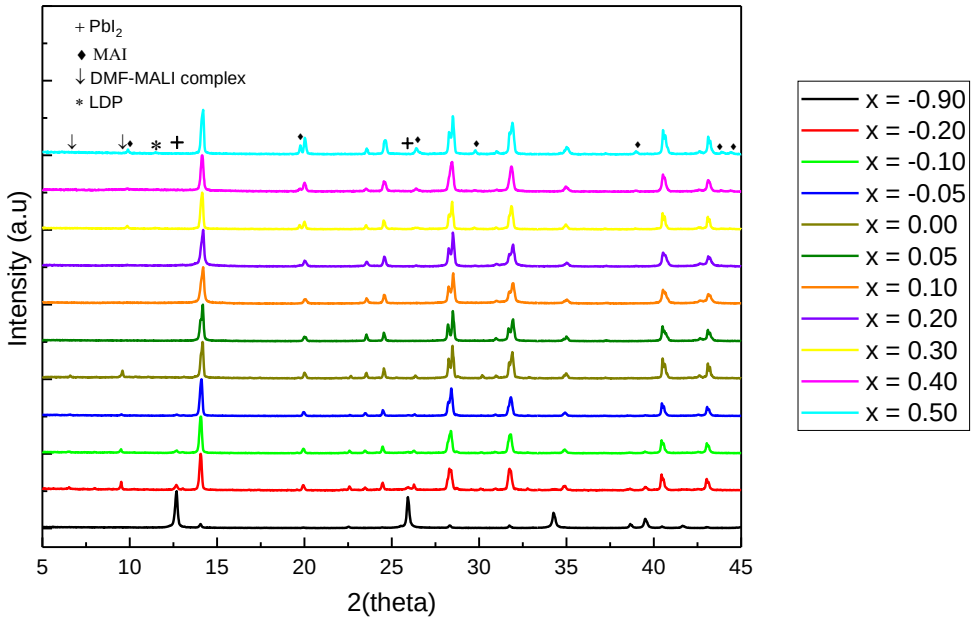

Figure 6.6. XRD patterns of the x series from x = -0.90 to 0.50, synthesised using DMF and annealed at 80 ˚C.

6.4.1. Lattice parameters

The lattice parameters and cell volume of MALI for the x series annealed at different temperatures are shown in Fig: 6.7.

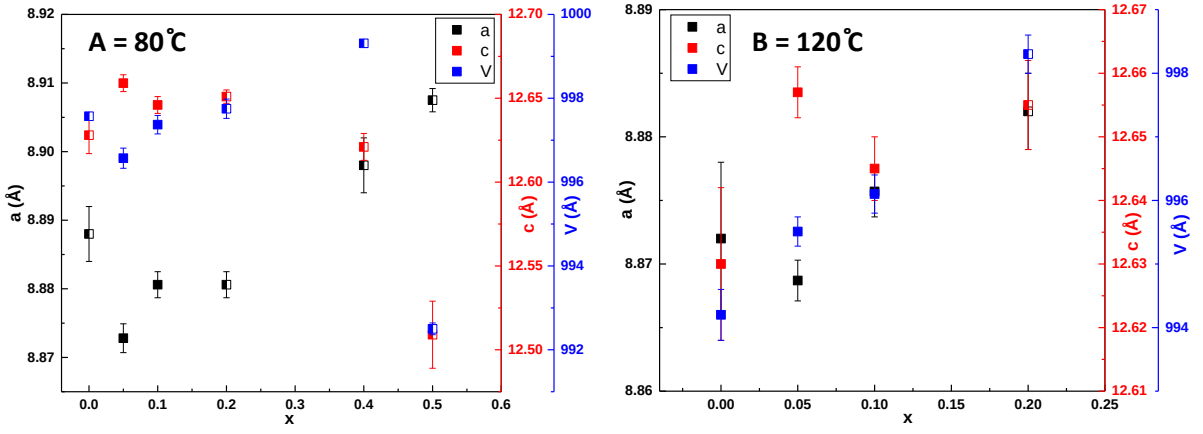

Figure 6.7. Lattice parameters for the x-series showing lengths a, c and volume, V. (A) Values for samples annealed at 80 ˚C, and (B) 120 ˚C. Filled data points represent values for phase-pure perovskite samples from XRD, whereas half-filled data points represent multi-phase samples.

When the samples are annealed at 80 ˚C (plot A) only x = 0.05 and 0.10 are phase-pure. c seems to stay constant unless x is higher than 0.20, whereas a and V after x = 0.00 appear to

increase with x. When samples are annealed at 120 ̊C (plot B), 0.00 - 0.10 are phase-pure, and the clearest trend seems to be that V increases with x. When the samples are annealed at 120 ̊C, there could be a limited solid solution between 0.00-0.10

6.5. SEM

Low voltage SEM was carried out and Fig 6.8 shows images of the x series from -0.20 to -0.50 when annealed at 80 ̊C. As x is varied from PbI_2-rich to MAI-rich samples, light regions attributed to PbI_2, alongside the grey MALI perovskite regions are observed. x = 0.00 is shown to contain some of the dark MAI-rich phase. As x is increased, the dark organic-rich regions increase in the area covered, this becomes prominent after x = 0.10. The powders were then annealed at 120 ̊C. They still show the presence of MAI-rich dark regions for x = 0.00 - 0.30, even though XRD data for x = 0.00 - 0.10 suggest they are phase-pure. Heating samples from 80 to 120 ̊C is insufficient in detecting if there is a decrease in the fraction of the darker regions. Powders from the x series were then annealed at 180 ̊C, there is almost no dark organic-rich regions for x = 0.05, 0.10 and 0.20. For x > 0.30, there is still some present, although very little when compared to samples annealed at 120 ̊C. At this temperature the corresponding XRD data also show peaks attributed only to PbI_2 and MALI.

Alternatively, if the light regions attributed to PbI_2 are considered there are none present in MAI-rich samples, as x is decreased from x = 0.50. There are some indications of its presence in x = 0.00 (which is also seen in the XRD data) and as x decreases from 0.00 to -0.20 these light regions also increase.

Comparing the SEM images to the corresponding XRD data for this x series suggests it is not possible to obtain any phase-pure samples. This is clearly shown by the 120 ̊C annealed powders, where x = 0.00 - 0.10 appear phase-pure by XRD, however their SEM images display the presence of two-colour contrast regions.

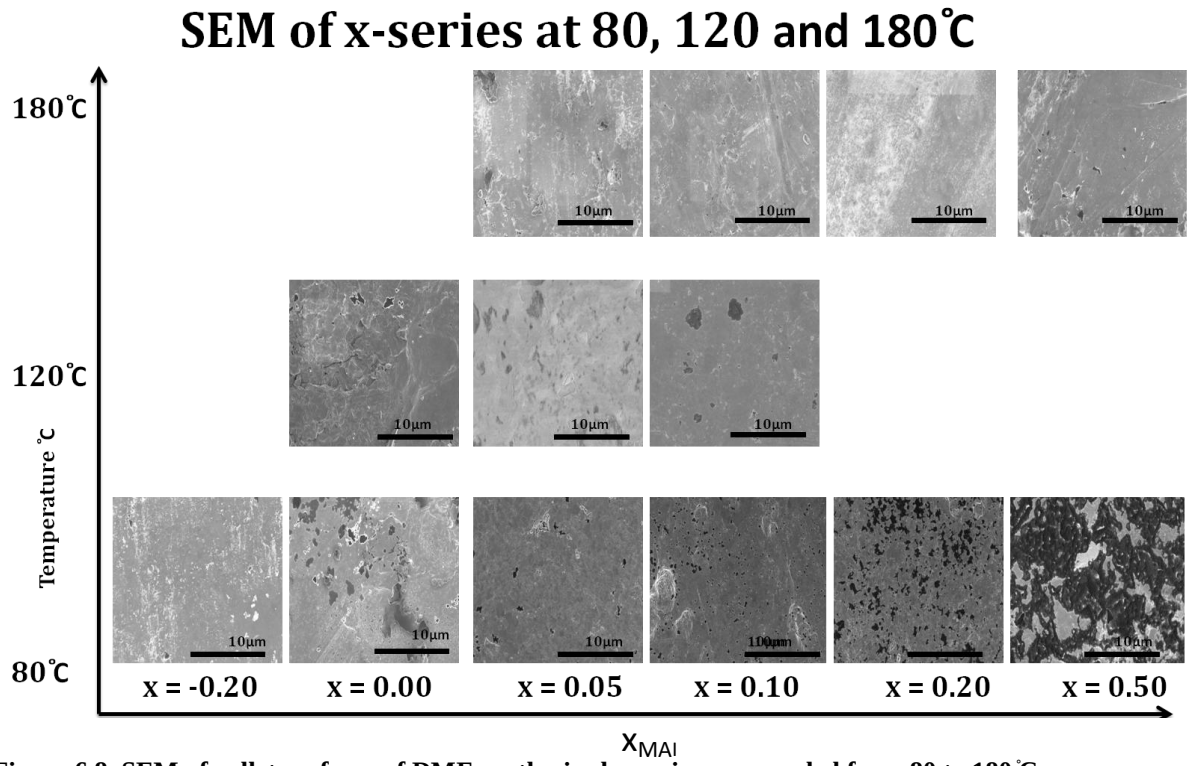

Figure 6.8. SEM of pellet surfaces of DMF synthesised x-series as annealed from 80 to 180 ℃.

6.6. LCR of the x-series

The samples annealed at 80 ℃ were cycled through LCR to measure permittivity and dielectric loss as a function of temperature, Figure 6.9 show the 80 ℃ annealed powders, as x increased from 0.00 to 0.10, room temperature ε_r remains similar for these samples. Increasing x further to 0.20 and up to 0.50 shows a reduction in ε_r. For x = -0.05 to - 0.90, there is also a trend of decreasing ε_r. These PbI_2-rich samples show a constant ε_r value with no changes or peaks across the temperature cycle. However, as compositions become more organic-rich there is a rise in ε_r with increasing temperature. At high x values (eg, x = 0.30) ε_r shows peaks at ~60 and ~100 ℃. This sharp increase in ε_r becomes less pronounced if the LCR cycle is repeated on the same organic-rich samples, as observed for x = 0.10 and 0.30.

Fig: 6.9C,D and F shows the tan δ behaviour of the x-series when annealed at 80, 120 and 180 ℃. For samples annealed at 80 ℃, from Fig: 6.9C, as x increases from -0.90 to 0.50 the loss increases more sharply with temperature, whereas on the cooling cycle the loss is lower when compared to a similar temperature on the heating cycle. Therefore, there is a divergence between the two cycles as was observed in the ε_r data at higher temperatures. This difference in loss between the heating and cooling cycles is larger with increasing x. Fig: 6.9D shows tan δ data for the x series when the samples are annealed at 120 ℃ and they show a similar trend to the 80 ℃ annealed samples. There seems to be two distinct regions which emerge more clearly with increasing x. First there is a peak at ~60 ℃, with another one at ~85

˚C, most clearly seen for x = 0.50. The peaks observed in ε_r vs. T for samples that are PbI_2 deficient are also observed in the tan δ data. After these peaks at 60 and ~90 ˚C (most clear for x = 0.50), the loss increases with temperature. On cooling these peaks are not observed and tan δ value are smaller, returning to their initial value at room temperature. The second cycle shows these effects are harder to observe.

The permittivity and tan δ of samples annealed at 180 ˚C are shown in Fig: 6.9F and 10C, respectively. From Fig: 6.9E the permittivity decreases with temperature for all x series with no signs of other phenomena occurring during the heating cycle. The initial starting permittivity values also tend to be similar than when they are annealed at 80 ˚C. Fig: 6.9C shows tan δ increases with temperature, however compared to the samples annealed at 80 and 120 ˚C, the temperature at which this rise starts to occur is higher and the final value of losses are also smaller. The other phenomena observed with the 80 ˚C samples, for example the peaks at temperatures of ~60 and ~90 ˚C are not observed in samples annealed at 180 ˚C.

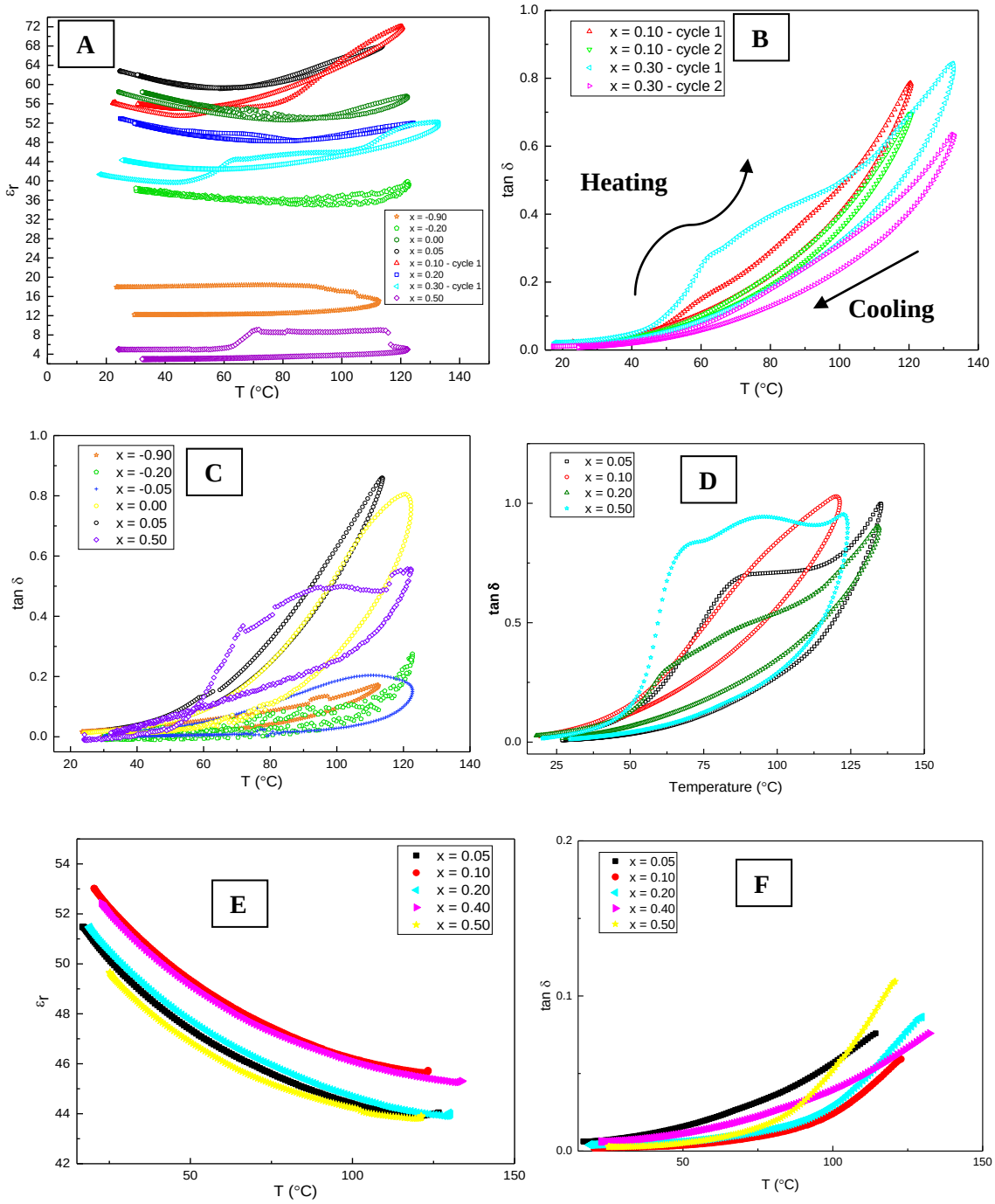

Figure 6.9. ε_r versus temperature for the x series synthesised using DMF. (A) Samples annealed at 80 ℃ (B) elucidating the 1st and 2nd cycles of x = 0.10 and 0.20 when annealed at 80 ℃. Tan δ vs. temperature of the x series for samples synthesised using DMF and annealed at (C) 80 ℃ and (D) 120 ℃ . (E) shows versus temperature sample annealed at 180 ℃. and (F) shows the tan δ for 180 ℃ annealed samples.

The LCR data shows that PbI_2 deficient samples annealed at 80 and 120 ℃ show peaks in both the permittivity and tan δ and both increase with temperature. These trends disappear when samples are annealed at 180 ℃, with the permittivity decreasing with increasing temperature. The MAI deficient samples annealed at 80 ℃ show a response where the permittivity decreases with temperature without any peaks. The permittivity of x = 0.00 -

0.10 remains similar and increasing x further or decreasing below 0 shows a decrease in permittivity. The density of the pellets remained similar to previous synthesis methods, with all the pellets being over 90% dense.

6.7. Impedance Spectroscopy (IS)

IS was carried out on samples along the x-series for powders annealed at different temperatures to observe any trend(s) across x and with different annealing temperatures. From Fig: 6.1 it can seen that samples synthesised via the DMF route shows changes in their XRD patterns when annealed between 80 - 180 ̊C. x = 0.00 was also tested under different atmospheres to see if varying the PO_2 influences the electrical behaviour.

Fig 6.10 shows the impedance response of x = 0.00 annealed at 80 ̊C on a heating and cooling cycle whereas Fig: 6.11 shows the IS response of pressed powders annealed at higher temperatures. The sample annealed at 80 ̊C is a DMF-MALI complex and its IS response shows two responses on heating and one on cooling, with Z'', M'' f_{max} values changing on thermal cycling. When x= 0.00 is XRD phase-pure MALI after annealing at 115 ̊C and when annealed at higher temperatures until decomposition occurs at ~200 ̊C there is a singular Z'' and M'' IS response. Fig 6.12 shows the IS response of a sample under different atmosphere conditions. An increased resistance is seen as PO_2 is decreased, where an extra response is observed at higher PO_2. Fig: 6.13 shows the IS response across the x series, as x increases from 0.00 - 0.20 resistance decreases. Further increases in x show a larger and increased resistance. When x is decreased from -0.05 to -0.90 resistance increases for these PbI_2-rich samples. The organic-rich samples show an increased resistance as the powders are annealed from 80 to 120 and finally to 180 ̊C.

6.7.1. Response of x = 0.00 at different annealing temperatures

The impedance data of x = 0.00 annealed at 80 ̊C (which from the XRD contains the DMF-MALI complex and PbI_2 phases) is shown in Fig: 6.10, where plot A shows the M", Z" spectroscopic plot on heating and plot B shows the cooling data at a similar temperature, once it has been heated to a maximum temperature of 140 ̊C. The heating data shows a large M" peak at a frequency of 150 kHz, and two separate responses in the Z" plot. $Z"_1$ peak occurring at a higher frequency of 60 kHz, whereas $Z"_2$ has a peak at 2.5 kHz. The resistance, R and ε_r values estimated from these peaks show that M" corresponds to an ε_r of 73, with a R of 0.16 MΩcm. $Z"_1$ has a ε_r of 90 and R of 0.33 MΩcm. The $Z"_2$ peak has a R of 0.58 MΩcm and ε_r ~ 1240 ($C' = 1.1x10^{-10}$ Fcm^{-1}). Plot B shows a single M" and Z" response, with f_{max} occurring at

6 and 3 kHz, respectively. The corresponding R and ε_r values are 3.9 MΩcm and 76 from the M" peak, and 5.4 MΩcm and 111 from the Z" peak, respectively.

Based on the heating data the M" and $Z"_1$ ε_r can be attributed to the bulk MALI response, whereas $Z"_2$ with a large ε_r value is due to a second element, which is more resistive than the bulk MALI. This second element is harder to distinguish on the cooling cycle (due to there being only a single Z" peak), however since the ε_r from this peak is 111, it must still have some contribution in the electrical response because the bulk MALI permittivity is lower and matches the M" peak. The cooling response is also more resistive, with both peak responses moving to a lower frequency.

Since the sample is initially an DMF-MALI complex the heating process during impedance measurement changes the phase assemblage of the sample with more of the MALI response appearing on the cooling cycle.

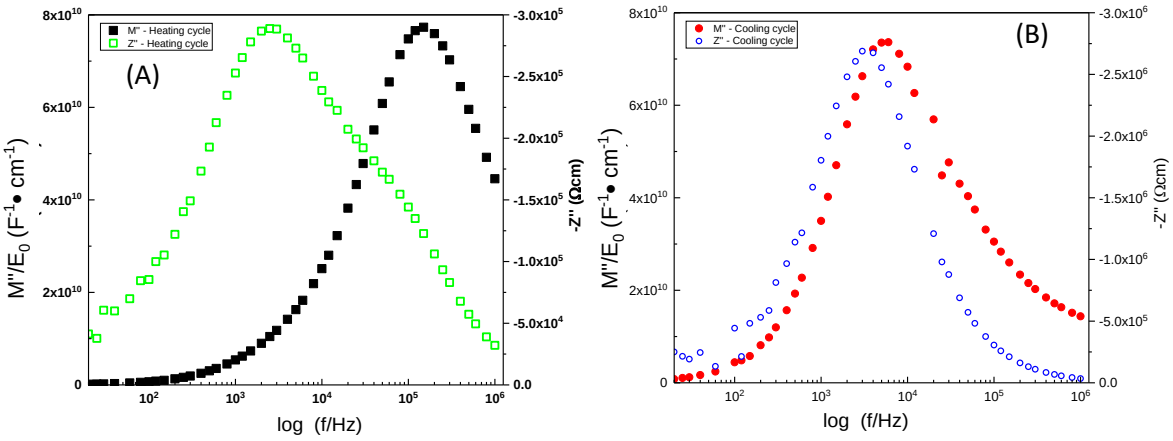

Figure 6.10. Combined M'', Z'' spectroscopic plot at ~70 ̊C (A) on heating and (B) cooling for x = 0.00 for powders annealed at 80 ̊C.

Fig: 6.11 shows the impedance response on a cooling cycle, comparing x = 0.00 powders annealed at different temperatures. Plot A shows M" spectra and the powders annealed at 80 ̊C show a singular broad M" response at an f_{max} of 6 kHz, with corresponding R and ε_r values of 3.9 MΩcm and ~ 76, respectively. The powders annealed at 115, 150, and 200 ̊C have an M" peak with similar time constant occurring at lower frequency than for the 80 ^{o}C annealed sample. They have an f_{max} at ~2.5 kHz, and the M'' peak is less broad. Estimating R and ε_r values for powders annealed at higher temperatures show that the resistance increases to ~12 MΩcm and ε_r decreases to ~64 for 115 ̊C annealed powders and then to ~ 59 for 150 and 200 ̊C annealed samples. Plot B shows the corresponding Z^* plots, indicating that the total resistance of the samples annealed at 80 ̊C is smaller (6.4 MΩcm) than the powders annealed at 115,150 and 200̊C (~16 MΩcm), which all show a similar

magnitude in the total resistance. These results show that when x = 0.00 is annealed at 80 ℃ its electrical behaviour is not stable and changes during the heating process, initially having two distinct responses that then converge and/or the contribution of the second response being much reduced. However, once an XRD phase-pure MALI sample is synthesised at 115 ℃ or partially decomposed at 200 ℃, the overall electrical behaviour remains similar.

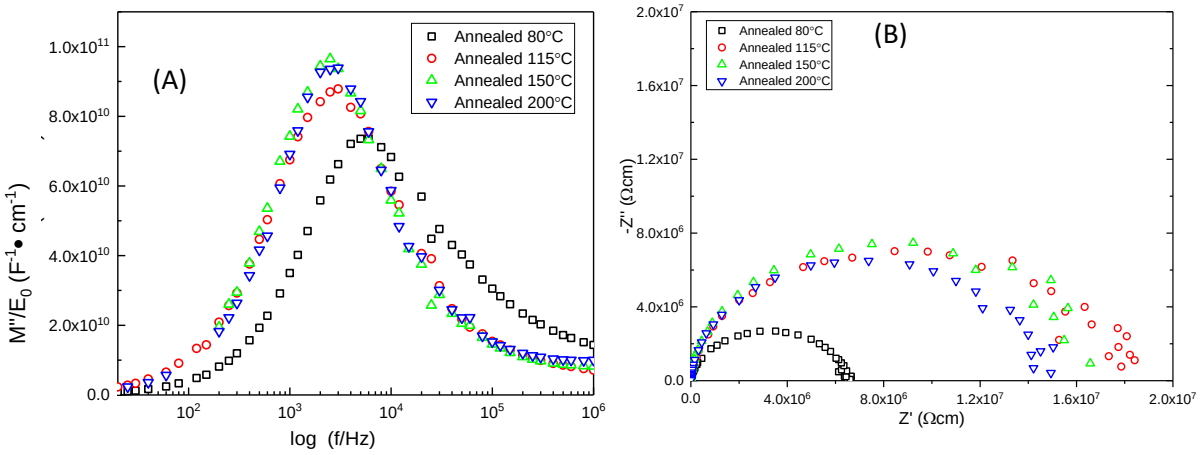

Figure 6.11. (A) M'' spectroscopic plots for x = 0.00 samples annealed at different temperatures. (B) Corresponding Z^* response. Data collected at ~70 ℃.

6.7.2. Response of x = 0.00 in different atmospheres

x = 0.00 annealed at 120 ℃ was analysed using IS under varying PO_2. This was varied by changing gas under which impedance measurement conducted. The pellet was exposed to oxygen, nitrogen and Argon gas under the same flow rate by looking at the rate of the bubbles. Fig: 6.12A shows Z^* plots of x = 0.00 under ambient air, and high PO_2.

The results for an air atmosphere show two responses, an initial semi-circular arc with a total resistance of 0.22 MΩcm and a second depressed spike. At high PO_2, there are now three responses, there is the semi-circular arc with the same total resistance as measured in air attributed to the bulk. A secondary response due to the exposure of higher oxygen content, and finally a third response which is a spike that must be related to ionic diffusion at the electrode. The difference between the cooling cycle and heating cycle at higher PO_2 does not change the bulk or the secondary response.

A new set of pellets were then used to conduct atmosphere impedance measurements, however this time rather than the flowing gas being passed through silica beads to absorb moisture, the flowing gas was passed through a beaker of water to create moist conditions. The results showed little variation to the dry gas conditions; however, the same trends were seen again as previously shown. Figure 6.12B shows the conductivity under oxygen is higher and under nitrogen and argon it is similar. The Z^* plot under high PO_2 has three different

responses, as discussed before. The results under N_2 and Ar show two distinct responses, the first semi-circular arc attributed to the bulk and a low frequency spike related to ionic diffusion. The bulk resistance decreases under the higher PO_2 of flowing O_2 with a value of about 0.43 MΩcm with the bulk resistance under N_2 and argon being ~2.5 and ~2.3 MΩcm, respectively.

Plot 6.13C shows the M", Z" plot response when the sample was exposed to higher PO_2, estimating the R and C' values from the single M" and the three responses in the Z" peaks are tabulated in table 6.1. The M" and $Z"_1$ peak occur at the same frequency and have similar R values. They can be attributed to the bulk with C of 5 $x10^{-12}$ Fcm^{-1}, corresponding to an ε_r of ~ 56. $Z"_2$ occurs at a lower frequency, has a much smaller R than the bulk, with C of 7.6 $x10^{-8}$ Fcm^{-1}, while $Z"_3$ attributed to the spike associated with ionic conduction occurs at low frequencies, with C of 2 $x10^{-5}$ Fcm^{-1}.

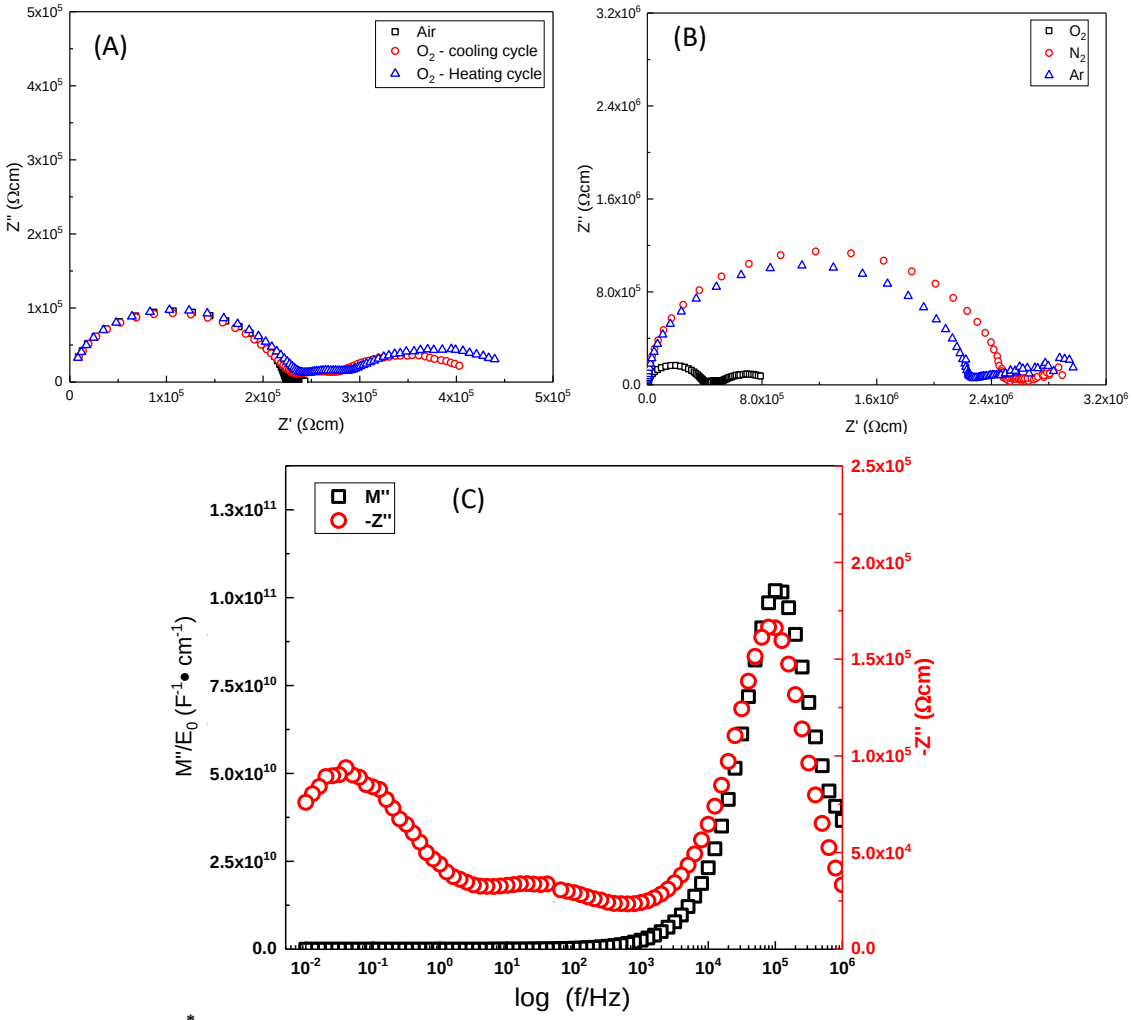

Figure 6.12. (A) Z^* plot for a sample measured under air and flowing O_2 during heating and cooling cycles. (B) Z^* for a sample measured in flowing O_2, N_2 and Ar. (C) M'', Z'' spectroscopic plot for x = 0.00 measured in flowing O_2 when annealed at 120℃. Data collected at ~135℃.

Table 6.1. Estimated R and C' values from plot (C) and their f_{max} values.

	f_{max} (Hz)	R (MΩcm)	C (Fcm^{-1})
M''	$1x10^5$	0.33	$5\ x10^{-12}$
Z''_1	$1x10^5$	0.33	$5\ x10^{-12}$
Z''_2	32	0.07	$7.6\ x10^{-8}$
Z''_3	0.04	0.2	$2\ x10^{-5}$

6.8. Impedance response across the x-series

Powders annealed at 80 ˚C were pressed into pellets, gold electrode were deposited on these pellets and their impedance response measured. x = 0.00 however shows data from the 120 ˚C annealed powder sample because at 80 ˚C it is a DMF-MALI complex and from Fig: 6.10 it shows the samples response changes during the impedance measurements. This is so that the other samples are compared to a phase-pure response of stoichiometric MALI, that does not alter during measurements.

Fig: 6.13A and B show the Z^* response along the x series from -0.90 to 0.50, whereas Fig: 6.13 C-F, shows M", Z" spectroscopic plots for -0.20, 0.00, 0.05 and 0.50, respectively. From Fig: 6.13A, as x increases from -0.90 to 0.00, the total resistance decreases, as x is increased further, (seen from Fig: 6.13B and inset) the lowest resistance is for x = 0.05, after which the total R starts to increase again. From Fig: 6.13C-F, at x = -0.20 the separation between M" and Z" f_{max} gets larger than for x = 0.00 and 0.05. With further increases in x to 0.50, the time constants again separate out. The estimated R and C values from Z^* and M", Z" plots are shown in table 6.2.

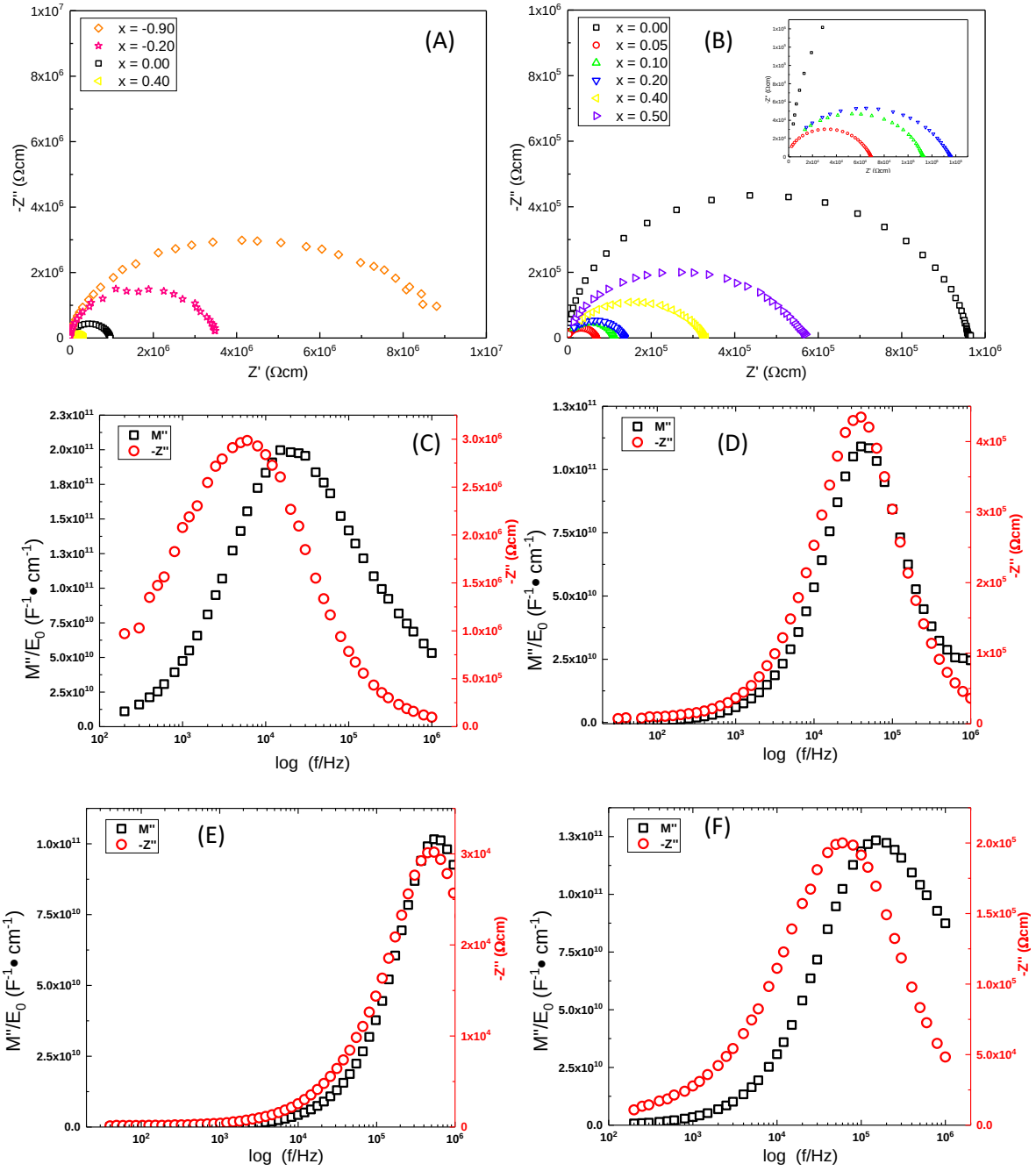

Figure 6.13. (A) Comparing Z^* plots for x = -0.90 and -0.20 to 0.00. (B) Z^* as x is increased. M'', Z'' spectroscopic plot of (C) x = -0.20, (D) x = 0.00, (E) x = 0.05 and (F) x = 0.50. Data collected at ~110℃.

From Fig: 6.13A and B, all the responses look like a single depressed arc, and their corresponding M", Z" peaks appear broad when x is either small (x = -0.20) or large (0.50), however they all still show a single peak. From the Z^* plots the total resistance of all the x-series can be estimated. Table 6.2 shows x = -0.90 has the highest total resistance with a value of 8.80 MΩcm and this decreases across x with the smallest R being for x = 0.05 with a value of 0.07 MΩcm. R for x = 0.10 and 0.20 remains close to x = 0.05 with values of 0.11 and 0.14 MΩcm, respectively. However, increasing x beyond x = 0.05 increases the total resistance, with values of x = 0.40 and 0.50 being 0.33 and 0.57 MΩcm, respectively. The

comparison of the M" and Z" peaks across x from table 6.2 shows that when decreasing x below 0.00, the f_{max} of the two peaks separate out, the same is observed when x is increased in the other direction (x = 0.50). In contrast, for x = 0.00 and 0.05 they occur at the same frequency. This also produces a difference in ε_r values. At lower x = -0.20, ε_r from M" is ~ 29 (and ~50 from Z") and lower than for x = 0.00 and 0.05, where its ~52 and ~55, respectively from both peaks. At higher x of 0.50, ε_r from M" is ~46 whereas from Z" it is ~75. R values at either end of the x series also show higher values from Z" compared to that obtained from M" spectra. The results indicate that when x is at either extreme the difference in time constants between M" and Z" is more pronounced therefore they are becoming more electrically heterogeneous. The bulk ε_r behaviour from M" is similar to that seen from the LCR, where PbI_2-rich samples have lower ε_r values, and the same is seen if it is too MAI-rich. Furthermore, slightly MAI-rich samples (i.e. x =0.05) tend to show an increase in conductivity.

Table 6.2. R and ε_r values estimated from Z^* plots (Fig: 6.13A and B) and M'', Z'' peaks from (Fig: 6.13C-F), alongside their $f_{max,}$ for x = -0.9 - 0.50 for powders are annealed at 80℃.

x		f_{max} (kHz)	R (MΩcm)	ε_r
-0.90	Z^*		8.80	
-0.20	M''	20	3.15	29
	Z''	6	6.00	50
	Z^*		3.5	
0.00	M''	39	0.87	52
	Z''	39	0.87	52
	Z^*		0.97	
0.05	M''	541	0.06	55
	Z''	541	0.06	55
	Z^*		0.07	
0.10	Z^*		0.11	
0.20	Z^*		0.14	
0.40	Z^*		0.33	
0.50	M''	150	0.26	46
	Z''	60	0.40	75
	Z^*		0.57	

6.8.1. Response of x-series at different annealing temperatures

As the x-series is annealed at higher temperatures, the general trend shows the total resistance increases on annealing from 80 to 180 ˚C, as shown by Fig: 6.14. The response from Z^* is shown for x = 0.20 for three different annealing temperatures of 80, 120 and 180 ^oC with the total R being ~ 1.9, 2.9 and 8.8 MΩcm, respectively.

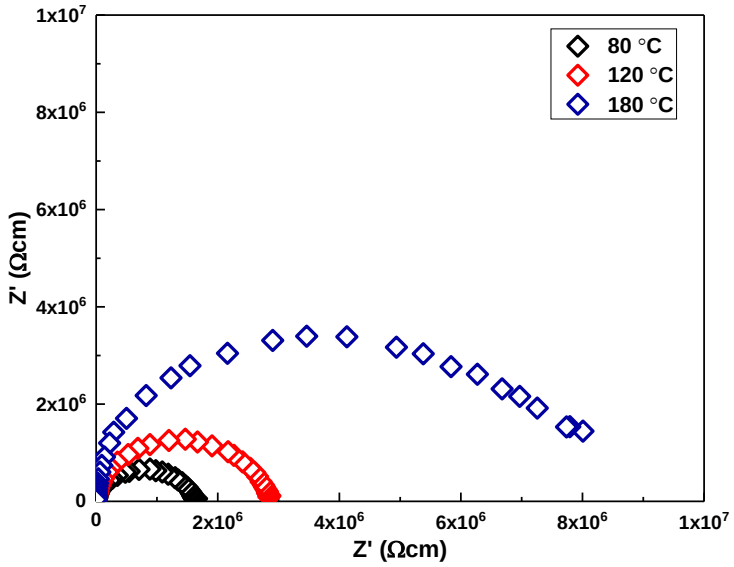

Figure 6.14. Z^* plot for x = 0.20 annealed at 80, 120 and 180 ˚C. Data collected at ~70 ˚C on the cooling cycle.

6.9. Arrhenius plots - Hand fitting of the M'' peak

The Arrhenius plot in Fig: 6.15A shows that for powder annealed at 80 ˚C, x = 0.00 has very high conductivity on the heating cycle, almost two orders of magnitude higher than when the powders are annealed at 150 ˚C. Upon heating (the 80 ˚C annealed sample) the conductivity shows an almost linear relationship, however there is a decrease in the conductivity at ~130 ˚C (1000/T = 2.5). On the cooling cycle the conductivity is lower and changes more rapidly with temperature when compared to the heating cycle. Comparing this to powders annealed at 150 ˚C, there is again higher conductivity in the initial heating stage but this drops at around 64 ˚C after which it increases with temperature in a linear fashion. This is reciprocated on the cooling cycle. There is a greater discrepancy between the heating and cooling conductivities for samples annealed at 80 ˚C compared to 150 ˚C.

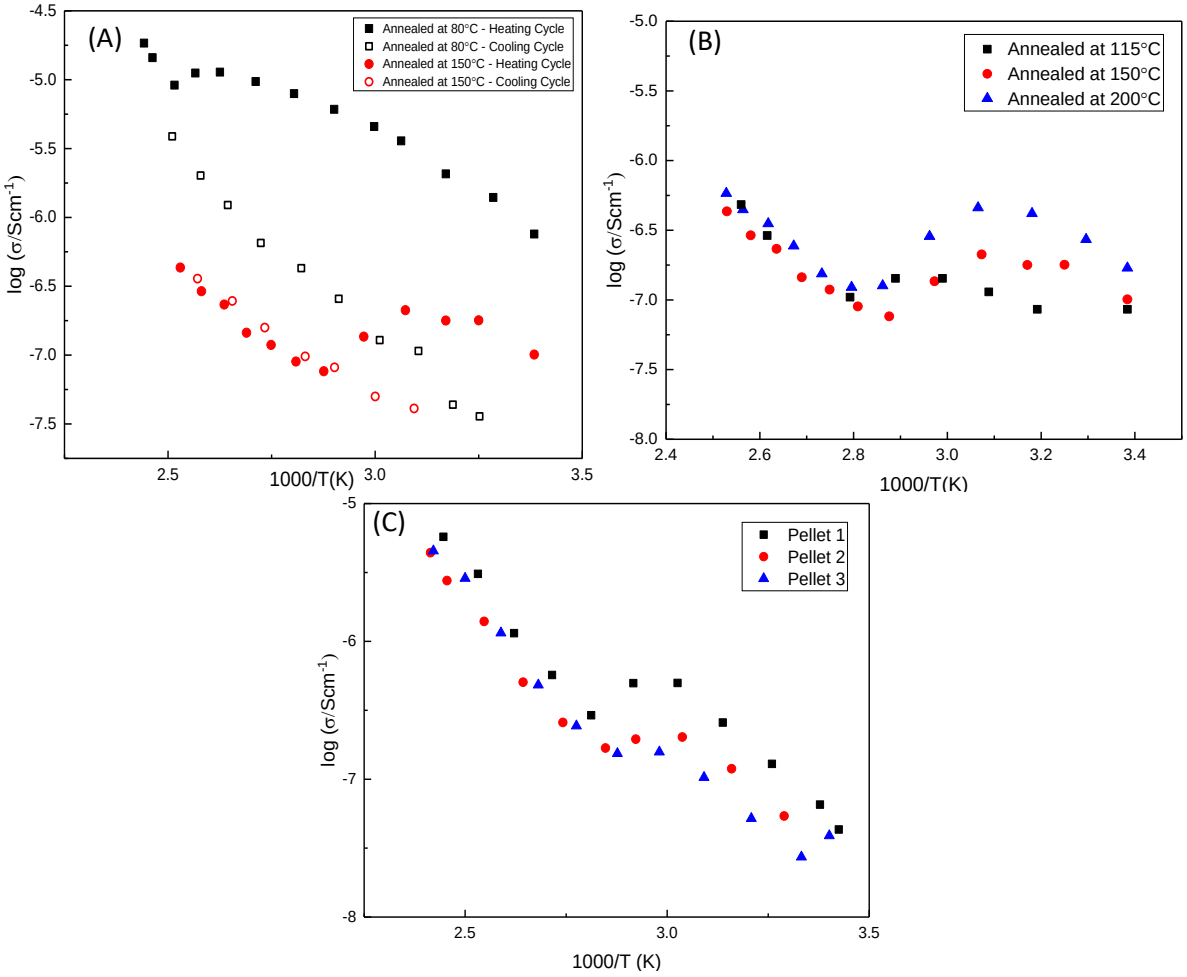

Figure 6.15. (A) Conductivity Arrhenius plots for x = 0.00 annealed at different temperatures of 80 and 150 ℃, showing both the heating and cooling cycle. (B) Conductivity Arrhenius plots on the heating cycle for x = 0.00 for powders annealed at 115, 150 and 200 ℃. (C) Conductivity Arrhenius plots for three x = 0.00 samples from the same batch. All data values calculated from M'' spectra.

x = 0.00 powders were annealed at other temperatures and their impedance response measured. They all showed the same trend. Fig: 6.15B shows only the heating data. The conductivity at the initial heating stage seems to be higher for all the powders annealed at varying temperatures. The drop in conductivity starts to occur at a similar temperature of ~ 65 ℃ for powders annealed at 150 and 200 ℃, however, it occurs at ~ 84 ℃ for powders annealed at 115 ℃. After this the conductivity seems to be similar for all of them and behaves in a linear trend.

Fig: 6.15C shows data for three pellets from the same batch of x = 0.00 annealed at 115 ℃, on which IS was performed. Comparing their conductivity shows there is inconsistency in the magnitude of the conductivity during the initial heating stage in the temperature range of 23 – 70 ℃, although their gradient is similar. Heating higher than 70 ℃ decreases the conductivity of the samples. The magnitude of the conductivities thereafter is comparable.

Since MALI is readily affected by its environment and from other studies its known that the solar cell efficiencies are affected by atmosphere and humidity. Experiments were therefore performed to see how the samples behaved when exposed to differences in atmosphere and humidity.

Three separate pellets were prepared where each exposed to a different atmosphere (i.e. Oxygen, Nitrogen and Argon, respectively) and their impedance responses measured. Initially the pellets were heated under ambient conditions and their response measured. Upon reaching the maximum heating temperature, the pellets were then exposed to one of the three aforementioned gases. The impedance was then measured upon cooling and on heating while under different atmosphere.

Fig: 6.16 shows the Arrhenius plot for x = 0.00 under differing atmosphere. Fig: 6.16A shows that at a higher PO_2 the conductivity is higher. The same trend is seen from Fig: 6.16B where the gas is passed through water to make it a wet rather than a dry atmosphere as shown in Fig: 6.16A. The conductivity under higher PO_2 also rises at a higher rate compared to N_2 or Ar at higher temperatures.

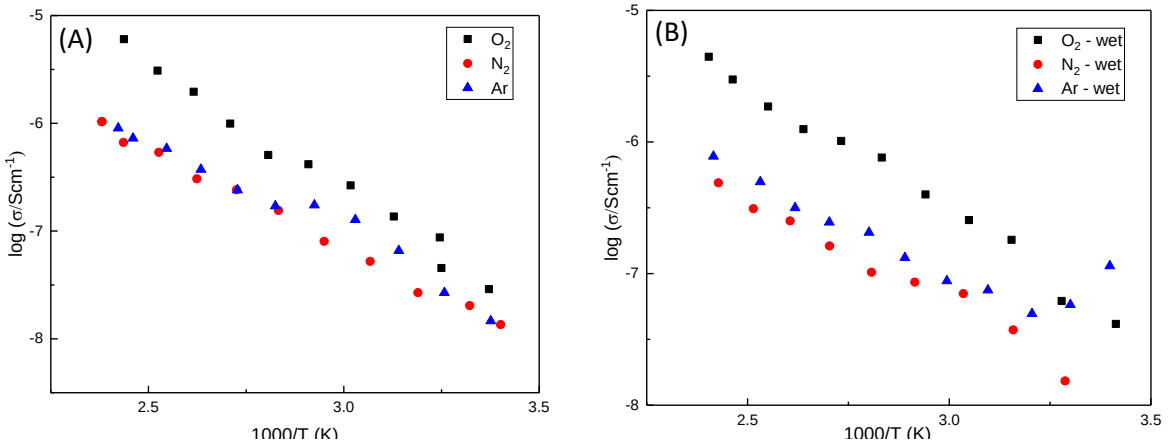

Figure 6.16. Conductivity values for x = 0.00 annealed at 120° C. (A) Conductivity Arrhenius plot under different dry atmosphere. Plot (B) shows the conductivity Arrhenius behaviour under different wet atmosphere. All data obtained from M'' spectra.

Fig: 6.17 shows the Arrhenius plot of the x-series, where plot A is the heating cycle and plot B is the cooling cycle. The heating cycle data show that the conductivity changes at different temperatures as samples are heated. For example, x = -0.20 starts off with a very high conductivity such that the M" peak is outside the available frequency range. When heated above 60 ˚C its conductivity starts to drop until 95 ˚C, where from then on it rises with heating. Therefore, due to these changes it becomes hard to establish a trend in conductivity with x, except it is quite clear that the PbI_2-rich samples have a lower conductivity than x = 0.00, whereas the organic-rich samples have higher conductivity.

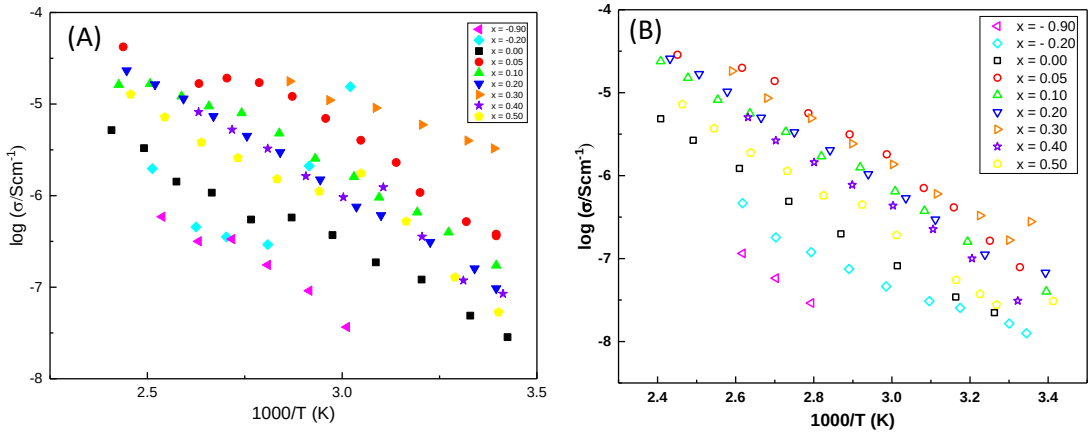

Figure 6.17. Conductivity Arrhenius plots for the x-series on (A) heating and (B) cooling for samples annealed at 80℃, except x = 0.00 where powders were annealed at 120 ℃. All data obtained from M'' spectra.

The Arrhenius plot (Fig: 6.17B) shows the cooling cycle conductivity remains more linear, therefore the trend across x can be more readily observed. As x increases from -0.90 to 0.05 the conductivity increases, with the conductivity for x = 0.05 remaining an order of magnitude higher even on the cooling cycle. Increasing x further appears to decrease the conductivity, most easily seen for when x = 0.50, which is only slightly higher than x = 0.00.

6.9.1. x-series annealed at 180 ℃

Samples annealed at 180 ℃ were characterised by IS. Fig: 6.18 shows the Arrhenius conductivity plot on the cooling cycle (data obtained from M'' spectra). The conductivities are similar at least at low temperatures. At higher temperature, slight differences exist, where 0.00 and 0.05 are similar with 0.10 being slightly higher and 0.20 the highest.

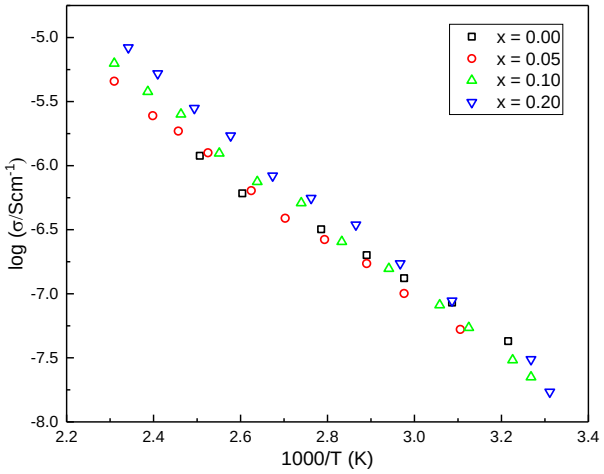

Figure 6.18. Conductivity Arrhenius plots on the cooling cycle for x-series powders annealed at 180 ℃. All data obtained from M'' spectra.

The impedance results show that x = 0.00 from powders annealed at 80 ̊C (not phase pure from XRD) has very high conductivity on the heating cycle, this then decreases rapidly on the cooling cycle. The impedance response contains two elements, the bulk MALI response, albeit with a slightly higher permittivity and a second more resistive response with a permittivity of ~ 1240. Annealing these powders at 120 ̊C produces a singular response however the initial high conductivity on the heating cycle still persists. This phenomenon remains even if powders are heated treated beyond the decomposition temperature and as high as 200 ̊C. Annealing x = 0.00 powders at higher temperatures decreases their permittivity. It is also observed from the Arrhenius plots that the same batch can produce differences in the conductivity during the initial heating cycle, however as the drop starts to occur after 60 ̊C, at higher temperature and on the cooling cycle conductivity values remain similar for all batches.

The IS response was observed under different gases for x = 0.00, high PO_2 produces an extra response with an associated permittivity of around $8.6x10^6$. Higher PO_2 also enhances the conductivity and measuring at lower frequency shows a Warburg type-spike in all three atmospheres, showing that it is a mixed conductor.

Comparing phase pure MALI along the x series shows that the PbI_2 rich compositions have slightly lower conductivity whereas increasing x to make it more organic rich increases the conductivity. If x is increased by too much, conductivity decreases again. At low and high x values the f_{max} between the M" and Z" peaks diverge. As the powders across the x-series are annealed from 80 to 180 ̊C their total resistance increases, so at 180 ̊C when all compositions have PbI_2 present as a secondary phase their conductivity is similar.

6.10. Equivalent circuit fitting

The circuit fitting followed a similar procedure as explained in the previous chapters and showed similar results and for conciseness is not included.

6.11. DC Bias

Powders of x series from 0.00 - 0.20 were synthesised via ball milling and DMF solution processing. Their pellets were subjected to a DC bias and the impedance response measured versus time when subjected to the bias. When carrying out DC bias measurements, the initial room temperature measurement at 0 V is recorded and then 0.5 V applied. The impedance response was then measured with time, after which the bias is removed and the

impedance response measured during the relaxation period. After a certain period of time when either the sample had relaxed back to the initial state or remained constant the bias was then increased further on the same sample to 1 V and the same procedure was carried out for 2 and 4 V.

6.11.1. XRD of samples after DC bias

The pellets subjected to the bias were analysed using XRD to observe if the application of a DC voltage resulted in any structural changes in the samples. The pellets were gold (Au) coated to perform the DC bias experiments, the Au peaks are identified to separate them from those associated with the sample.

Fig: 6.19 shows XRD of x = 0.05 powders synthesised by DMF and of a pellet after DC bias, where the voltage was increased from 0 V to a maximum of 4 V. XRD peaks appear after applying the bias which remain unidentified, alongside the gold electrode peaks as labelled in Fig: 6.19A. Also shown is an XRD pattern when the surface of the pellet had been polished with sandpaper showing the peaks that appeared due to the bias are removed. On closer inspection of the data, a very weak intensity peak at around 28.8° degrees may remain after the polishing of the pellet surface, Fig: 6.19B. The XRD on both sides of the pellet showed the emergence of the same peaks.

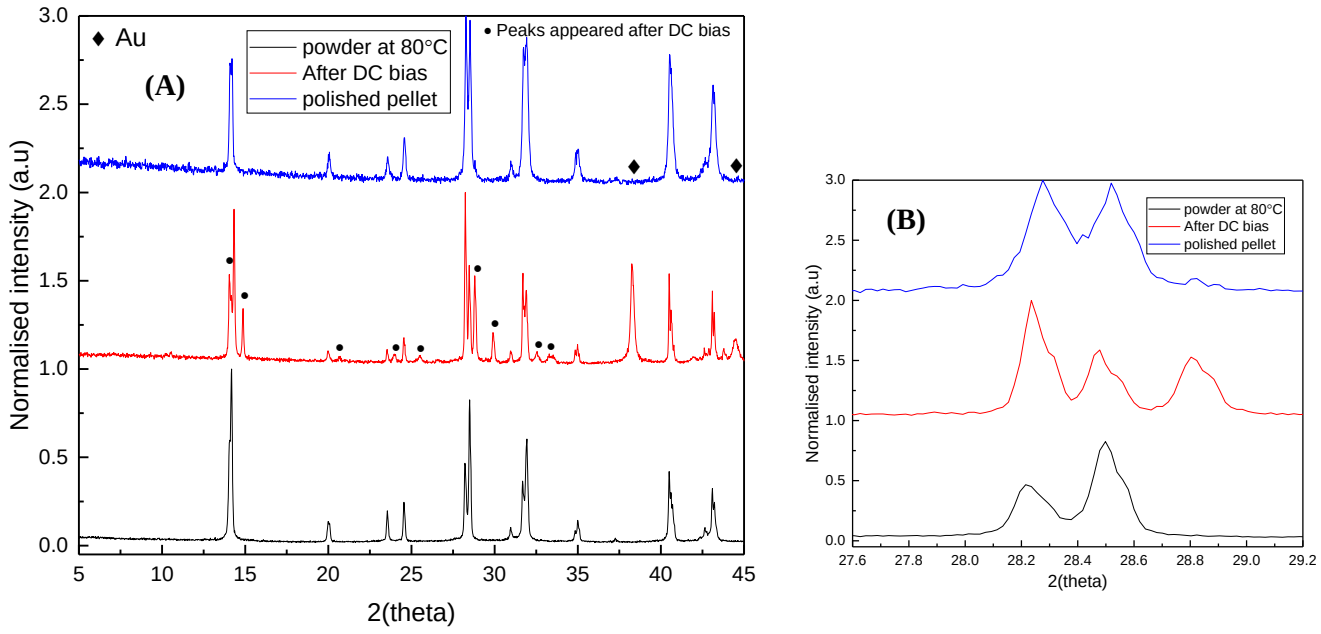

Figure 6.19. XRD patterns for x = 0.05 synthesised via DMF before and after application of DC bias and then after being polished. (A) Before and after DC bias on the pellet. (B) Expanded view of selected main peaks for MALI. A maximum of 4 V was applied.

Fig: 6.20A and B show the comparison between samples synthesised by DMF and ball milling (BM) after they have been subjected DC bias, with a max of 4 V. The results from the

DC bias showed the XRD patterns on the surface of a sample generally changes. This can be clearly seen by comparing the other samples to x = 0.05 (BM) which doesn't seem to change much or at all from the MALI pattern. All ball milled and DMF samples except for x = 0.05 (BM) and 0.10 (DMF) showed additional peaks in their XRD data after the application of a DC bias. The changes in the XRD patterns are similar with their main peaks being split and extra peaks at 15.05 and 28.8 degrees with others appearing at low angles.

From Fig: 6.20B, the easiest differences are seen in the main perovskite peaks at ~14 and ~28 where there is some peak splitting occurring but also new peaks close to the main peaks as mentioned before at 15.05 and 28.8 degrees. The extra peaks are not due to gold or any combination of interaction (alloying) between gold and elements in MALI, like lead or iodine. The effect is large enough to be measured by XRD but occurs at the surface, since polishing the pellets either completely removes the extra peaks or severely diminishes them. However, the fact that even after polishing off the electrodes and some surface of the pellet, there are still signs of the extra peak at 28.8 (from Fig: 6.19B) shows this effect occurs from the surface to a substantial depth. Heating samples to 80 ̊C also removes the peaks produced due to the applied bias. Since the compositions tested were synthesised via both ball milling and DMF it gives more precedent to an actual effect of the material rather an artefact associated with the processing conditions.

As to why x = 0.05 (BM) and 0.10 (DMF) do not show any changes in their XRD patterns could indicate some individual sample influence. However, their geometries were similar across all samples therefore it can't be an effect of the applied electric field. Also, from Fig: 6.22 the samples generally had similar time (in number of hours) in which a voltage was applied across them. x = 0.05 (BM) sample however is different to the rest in that it is not clean from its XRD pattern and contains PbI_2.

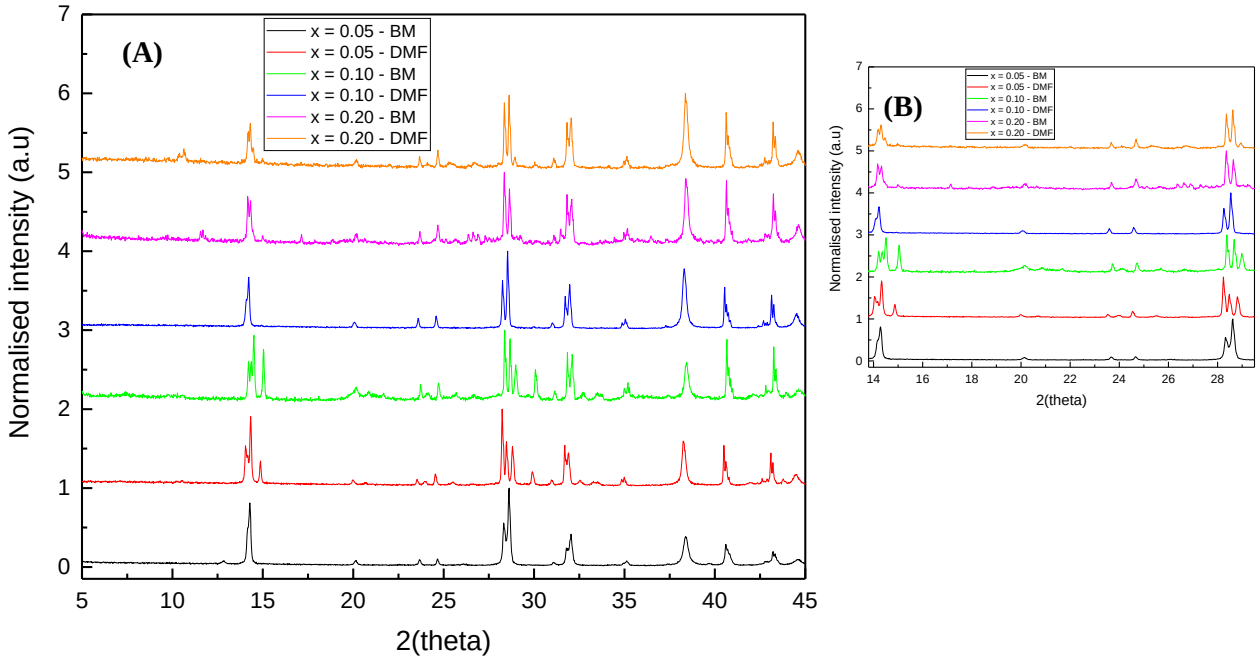

Figure 6.20. (A) X-ray diffraction patterns of x = 0.05 - 0.20 pellets for both ball milled and DMF synthesized powders after application of a DC bias, a maximum of 4 V was applied. (B) Expanded view between 13-29 degrees, to show the main peak.

6.11.2. Impedance results

Fig: 6.21 shows impedance data for x = 0.05 synthesised via DMF and table 6.3 shows the estimated R and ε_r values during applied bias. Plot A shows a single M" peak with a f_{max} of 15 kHz and when 2 V is applied it increases slightly to 18 kHz, with a drop in the M" peak height. When 4 V is applied the M" peak height decreases further and f_{max} increases to 66 kHz. The permittivity calculated from the M" peak increases from 66 to 121 on going from 0 to 4 V. When the bias is removed, measuring after 24 hours, f_{max} decreases to 55 kHz. The M" height increases with a corresponding ε_r of 80. The high frequency ε_r from plot B stays similar with a value of 62. Once again however the C' value at lower frequency is affected much more with values of C' being in the region of 10^{-9} Fcm^{-1}.

Plot C shows the total resistance at 0 V being 2.5 MΩcm and it decreases as the voltage is increased. At 4 V the single arc become two separate responses, seen from the inset. Having a total resistance of 0.4 MΩcm, the first arc has a corresponding resistance of 0.18 MΩcm and the second arc has a resistance 0.22 MΩcm, with capacitance values of $1.1x10^{-11}$ and $1.1x10^{-9}$ Fcm^{-1}, respectively. Once the bias is off and the sample allowed to relax, the total resistance increases to a value of ~ 0.85 MΩcm, with a low frequency spike being present. Plot D shows that as the voltage is applied the conductivity of the sample increases by almost an order of a magnitude at 4 V. After the bias is removed and a

measurement taken after 24 hours, the total conductivity still remains higher than the initial measurement at 0 V.

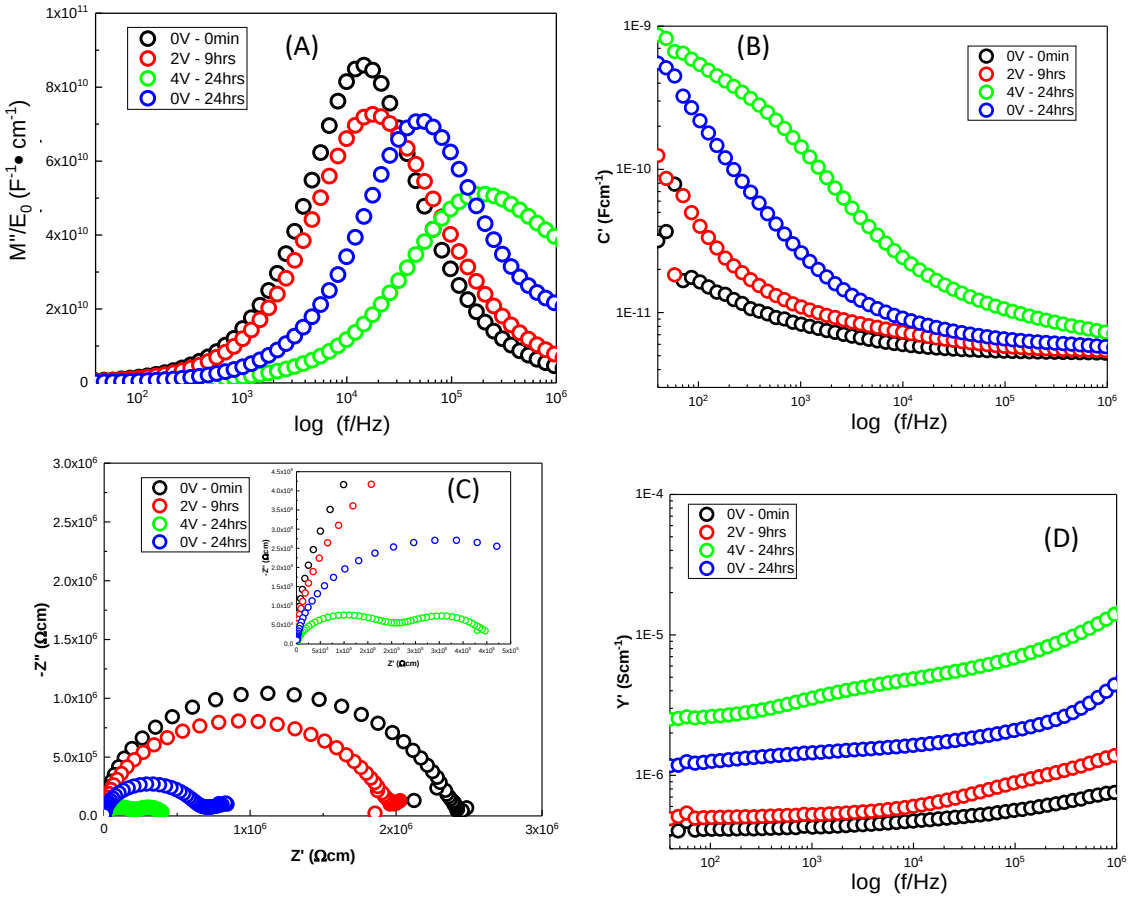

Figure 6.21. x = 0.05 synthesised via DMF. (A) M'' spectra, (B) C' spectra, (C) Z^* plots and (D) Y' spectra after a maximum of 4V being applied during the DC bias and then 0 V when the bias was removed.

Table 6.3. Estimated R and ε_r values from M'' and Z'' peaks for x = 0.05 synthesised via DMF, alongside their f_{max} values.

Applied Bias/Duration		Frequency (kHz)	R (MΩcm)	ε_r
0V-0MIN	M''	15	1.9	66
	Z''	12	2.1	72
2V-9HRS	M''	18	1.3	78
	Z''	12	1.1	138
4V-24HRS	M''	66	0.22	121
	Z''	32	1.4	391
0V-24HRS	M''	55	0.41	80
	Z''	38	0.54	88

6.11.3. Variation in f_{max} with applied bias

f_{max} from the M" spectra was plotted at each voltage versus time held in hours. This gives a broader picture of how the sample response alters at room temperature when the voltage is varied and along the time domain. It does not show the results when the voltage is removed, only the variation during the period when the voltage is applied. Data for x = 0.05 synthesised using DMF are shown in Fig: 6.22. f_{max} increases with applied voltage in the range up to 2V; however, during the application of 4 V it initially drops to a value lower than when 0.5 V was applied but then increases dramatically to a value that is an order of magnitude higher.

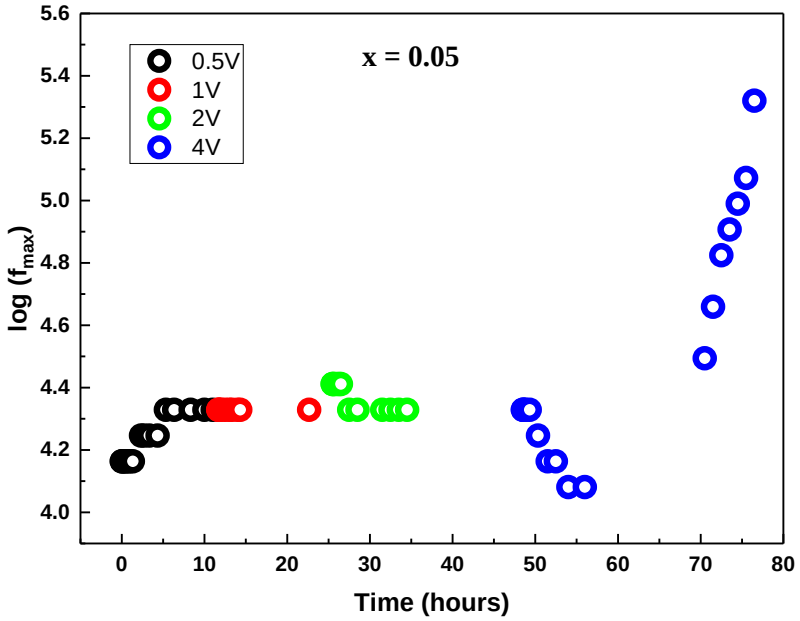

Figure 6.22. Variation of f_{max} for the M'' peak as a DC bias is applied (with the highest voltage being 4 V) with time (in hours) for x =0.05 prepared using DMF.

DC bias results from other samples are provided in appendix.

6.12. Discussion

6.12.1. Discussion of XRD/SEM

A similar assemblage diagram for MALI was made by using DMF solvent using a 1 step method, where the precursor powders were dissolved in the solvent and the mixture heated to evaporate the solvent, leaving the powders of the product. The DMF samples heat-treated at 80 ℃ show the perovskite phase along with PbI_2 and other additional XRD peaks corresponding to a DMF- MALI complex. However, after being annealed at a higher temperature of 100 ℃ these DMF complexes disappeared. The DMF-complexes only appear in the PbI_2-rich samples. This could be explained by looking at the pathway of how the

perovskite is formed by the reaction of precursors whilst using a solvent, either DMF or DMSO. This process (shown in Fig: 6.23) is facilitated by a reversible solvent participation of a polymeric plumbate acting as an important intermediate [1]. It is reversible because as DMF or DMSO solvent is used to synthesis the MALI perovskite, once the perovskite is formed if it is then exposed to these solvents again they act as a base to remove the acidic MAI from the crystal structure of the perovskite. When using DMF as a solvent the process is as follows, PbI_2 (PI, as labelled in the diagram) and MAI are mixed in DMF and heated which produces the intermediate, dinuclear plumbate (i.e. PbI_3^-) that is isolated as a crystalline fibre $(MA^+)_2(PbI_3^-)_2.(DMF_2)$, which then loses the DMF to give MALI perovskite [1]. This occurs in two steps, the 2D lead iodide sheets give a polymer strip of $(PbI_2)_2$ and when MAI coats this strip, it creates ligand exchange to give $(MA^+)_2(PbI_3^-)_2.(DMF)_2$. When heated to 100 ˚C it loses the DMF and produces a perovskite. The DMSO mechanism is similar to that for DMF with the exception that it produces a more complex plumbate fibre, $[(MA^+)_2.(PbI_3^-)_2.PbI_2].(DMSO)_2$. This needs additional MAI to produce the perovskite, making the process slightly more complicated [1].

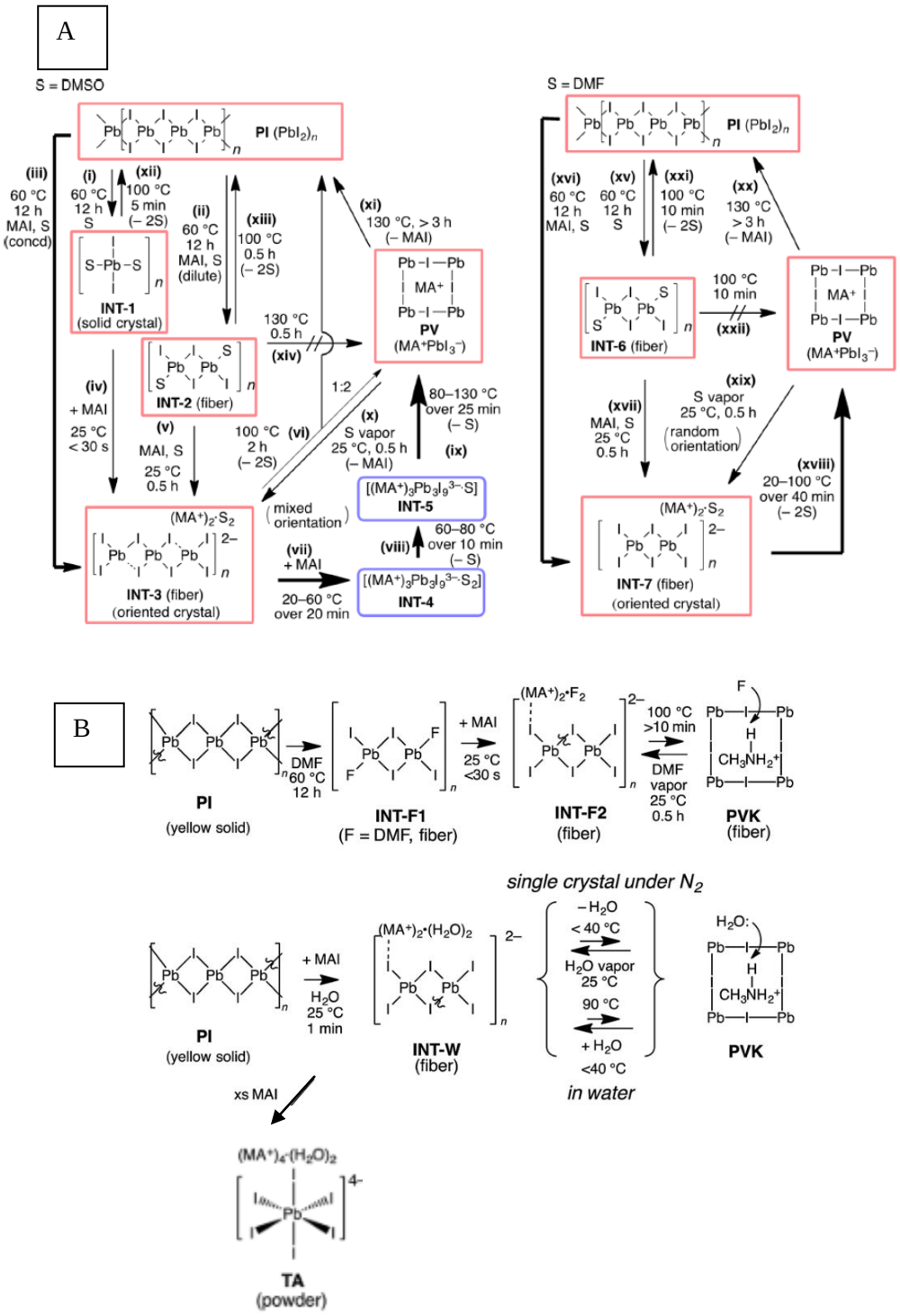

Figure 6.23. (A) Reaction mechanism for how MALI perovskite is formed from the two precursors PbI_2 and MAI using DMF and DMSO solvents with the intermediate steps being determined by which solvent being used. Figure reproduced from [1] (B) Reaction mechanism showing the role of DMF solvent to synthesise MALI compared to when water is used as a solvent. Figure reproduced from [2].

Therefore, if the materials are not heated at sufficient temperature so that the solvent can't leave the plumbate fibre structure, it will remain in the material and a phase pure perovskite sample will not be formed. As these are attached to the lead iodide dimer, when there is an excess of PbI_2 they are easily observed by XRD. It is also the case that instead of DMF or

DMSO, water can be used and when present in the solvent it can act as a catalyst [2]. As shown in Fig: 6.23B, the water acts in the same way in that it is attached to the MAI, which is then bonded to the lead iodide dimer, and once the water is heated, the crystallised perovskite remains. Although this mechanism is when water is used instead of an organic solvent if moisture is present either in MAI or in the DMF/DMSO it can follow the same mechanism [2].

At higher x values the XRD patterns remained similar, where there is a narrow region where compositions appear phase pure by XRD. For the DMF synthesis they occurred at x = 0.05 and 0.10. At higher x values than these the LDP phase and crystallised MAI appear. The LDP is removed after heating above 80 ˚C.

The DMF samples were affected by temperature even prior to decomposition. Firstly, both the LDP and DMF complex phases were removed by 100 ˚C but also x = 0.00 generated a phase-pure XRD pattern when heated at 120 ˚C. MALI decomposition appears to occur again over 140 ˚C. This can be observed in Fig: 6.3 where after 135 ˚C PbI_2 starts appearing in the XRD data. The phase-pure XRD data for x = 0.00 can also be attained at lower temperature if the DMF and powder mixture are heated under lower pressure, as seen in Fig: 6.4. XRD data show the MALI synthesised to exhibit all three polymorphic forms based on a tetragonal to cubic polymorphic transformation when heated above room temperature and from the tetragonal to an orthorhombic form when cooled below room temperature, Fig: 6.2. The solvent used can also be changed, however, using DMSO MALI could not be synthesised into a phase-pure material since it always contained PbI_2. Another difference was the time taken to evaporate DMSO at 80 ˚C. Ethanol took about 12-16 hours, DMF took about 48 hours, however, DMSO took 168 hours for the solvent to fully evaporate. The solvents take different crystallographic conversion pathways, since using DMSO requires an extra MAI molecule and in the final conversion loses two DMSO molecules, whereas in the DMF mechanism it just loses one of these molecules [1]. Also the hydrogen bond acceptor strength is lowest for water and highest for DMSO amongst the three possible solvents present during this synthesis method [2].

6.12.2. SEM

The SEM results corroborate with the explanation that the light regions can be attributed to PbI_2 and the MAI-rich region can be attributed to the dark regions on the surface images. This is not only clear in the solid state and ball milling samples but also in the DMF samples along the x series from -0.90 - 0.50, where the PbI_2-rich samples exhibit light regions

whereas x = 0.00 has a small number of black regions which is probably why it appeared as being phase-pure in XRD unlike solid state and ball milled samples where it was mostly light regions as the second phase. As the amount of MAI increased the area fraction of darker regions increased. At higher temperature the area of darker regions decreased, whereas after annealing at 180 ̊C, when the excess organic material decomposed, they showed light PbI_2 regions alongside the perovskite phase which correlates with the XRD data. The confirmation of this trend was further observed by secondary electron hyperspectral imaging. This is where energy spectra (shown in Fig: 6.24) from MAI-rich, PbI_2-rich and stoichiometric MALI, from the SEM images were collected and compared to the differing regions of contrast present in the images themselves. This could elucidate the presence individual MAI or PbI_2 phases in the samples and also as to whether or not individual MALI grains were stoichiometric or non-stoichiometric [3]. How Kumar et al differentiated between these different contrast regions was discussed in more depth in the literature review chapter, in the processing condition and degradation section.

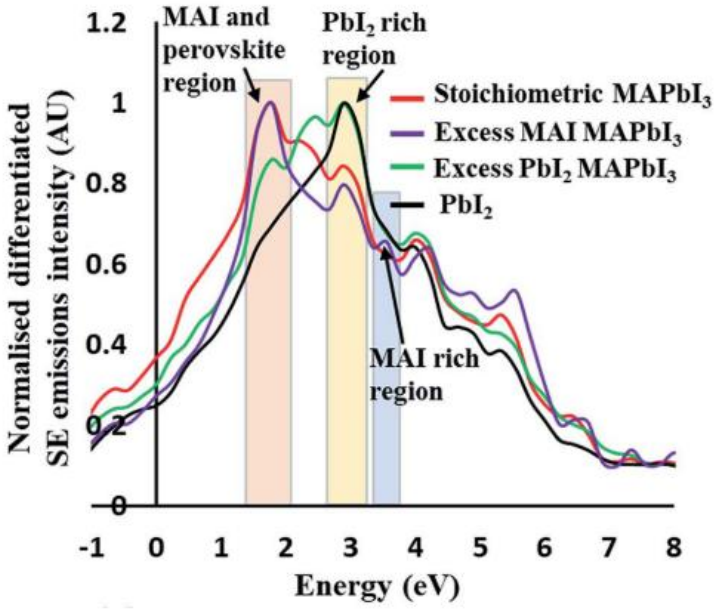

Figure 6.24. Secondary electron hyper spectral imaging's energy spectra collected for four different samples, where there is the base stoichiometric MALI, MAI-rich and PbI_2-rich MALI along with the energy spectra for PbI_2. [3]

6.12.3. LCR

The general trend in the ε_r vs. temperature relationship along the x series is that PbI_2-rich samples have dielectric behaviour where ε_r decreases with temperature and as they are made more MAI-rich there comes the usual behaviour observed previously in both the ball milled and solid-state samples, where it rises with temperature. The room temperature ε_r at

the start of the heating cycle and at the end of the cooling cycle are the same, therefore it seems like addition of excess PbI_2 and too much MAI (when x = 0.50) decreases the room temperature ε_r of the samples. Near x = 0, the room temperature permittivity is ~60, Fig: 6.25.

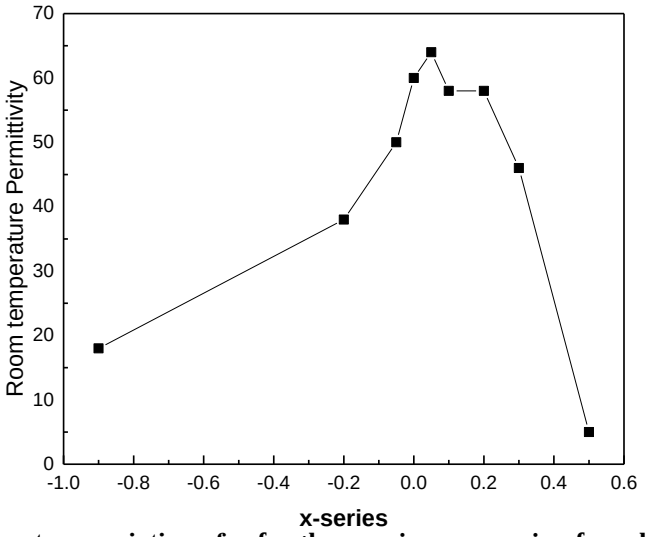

Figure 6.25. Room temperature variation of ε_r for the x series as on going from being PbI_2-rich (x< 0) to being MAI-rich (x>0). Permittivity at frequency of 1MHz.

The reason for the lower ε_r with excess PbI_2 is probably because PbI_2 has a lower value (ε_r = ~11) and as more is added it lowers the overall permittivity of the sample. However, the room temperature ε_r of MAI was measured to be ~ 40, therefore the addition of excess MAI lowering the overall permittivity may require another explanation.

For the powders annealed at 80 ˚C, tan δ and ε_r for the MAI-rich samples show a similar trend as previously discussed. When a second cycle is measured there is still a rise in ε_r but the hysteresis between the heating and cooling cycle data is smaller. When the samples are annealed at 120 ˚C, a similar trend is seen, i.e. the MAI-rich samples show peaks on the 1st heating cycle at ~60 and in the ~85-90 ˚C range. Finally, when the samples are annealed at 180 ˚C, such that any excess organic and the organic cation in the MALI itself is partially decomposed, PbI_2 is evident in the XRD data and the LCR behaviour is akin to PbI_2-rich samples. The general dielectric behaviour being ε_r decreasing with increasing temperature.

The peaks in both permittivity and tan δ are seen on the first heating cycle. As these are only seen in the MAI-rich compositions, it could be that the extra MAI allows the absorption of water from the atmosphere more readily. The PbI_2-rich samples annealed at 80 ˚C have DMF-complexes present in them, however their LCR data show no unusual behaviour during the heating cycle to indicate that it doesn't have any significant effect on the LCR data.

6.12.4. Impedance Spectroscopy

6.12.4.1. Results for x = 0.00

One of the main differences observed in the DMF prepared samples is that after annealing at 80 ℃ MALI-DMF complexes were observed in the XRD data. Therefore, looking at the x = 0.00 when synthesised at this temperature using IS could elucidate what effect it has on the electrical data of samples. Fig: 6.10 and 6.11 show that the higher f_{max} during heating compared to the cooling cycle in M'' spectra for x = 0.00 shows a drop in conductivity on cooling for this component and there is also another component with a much lower f_{max} in the Z" spectra that is evident on the initial heating cycle. This indicates another time constant that is not MALI's. On heating this response disappears, and the only remaining response is seen to be from the bulk MALI. On comparing to samples annealed at higher temperatures this behaviour disappears for powders annealed above 80 ℃, which also relates to the disappearance of MALI-DMF complexes.

The DMF complexes give a false high conductivity to the samples, at least on the initial heating cycle and this then drops significantly back to the conductivity of phase pure MALI samples as observed in Arrhenius plot shown in Fig: 6.15, where based on the cooling cycle data the longer it spends at higher temperature the more significant the drop in conductivity. After the MALI material is made phase-pure or via partial decomposition (from Fig: 6.15B) they all show a change in conductivity at around 70 ℃, which is probably due to the phase change and/or water present in the sample. This is because looking at the MAI data, from Fig: 5.32C (chapter 5 Fig: 32C), MAI's f_{max} also indicates a change in this temperature region. However, the LCR data indicates two peaks at 60 and 90 ℃, of which the first one is indicative of the tetragonal to cubic phase transition. The MAI however does not have a known phase transition and since it has the ability to absorb moisture it is most likely to be associated with water.

The heating cycle results are shown in Fig: 6.15 B and C and show the same material in the same batch. Three separate pellets were pressed from this batch and show slightly different conductivity values during this initial heating stage. Therefore, along with the phase change which results in a change in conductivity, the differing values are due to the amount of moisture in the material. Varying levels of moisture contained in the sample will give different conductivity values on the heating cycle for samples from the same batch. In contrast, the cooling cycle results all have the same conductivity, due to the loss of moisture on the heating cycle.

The flowing gas experiments measured to lower frequency show (from Fig: 6.12) that MALI is a mixed conductor due to the spike observed at low frequency in the Z* pots. Under higher PO_2 the conductivity increases, Fig: 6.16. Since the variation is in partial pressure of oxygen, and MALI is based on a halide anion rather than an oxide anion, the usual interpretation of whether to allocate this PO_2 dependence to p- or n-type conductivity remains uncertain. However, it has been shown that under exposure to oxygen and light, superoxides can form which can then degrade MALI. From computational techniques it seems that the iodide vacancies might be the defect source where the photoinduced superoxides are located [4]. It is believed that the superoxide O_2^- de-protonates the MA^+ leading to the degradation of MALI into PbI_2, CH_3NH_2, H_2O, and iodine, as shown in Fig: 2.24. Where oxygen is incorporated into the lattice and upon exposure to light, electrons and holes are produced since the energy of the photon is higher than the band gap, this can then induce the formation of O_2^-, which will lead to the degradation.

6.12.4.2. x- series when annealed at different Temperatures

The impedance results across the x-series (shown in Fig: 6.13) again show a similar trend where the small increase in MAI in the initial composition makes the total resistance much smaller compared to x = 0.00 and the PbI_2 rich samples. If the MAI content is increased too much, where its crystallised form is shown in the XRD data as is the case for x = 0.50 then the resistance is larger compared to x = 0.05 - 0.20. The M"/Z" plots show that only when too much PbI_2 or MAI is added then the MALI systems show signs of electrical heterogeneity because for x = 0.00 and 0.05 the M'' and Z'' peaks occur at similar f_{max}.

From Fig: 6.14 it is seen that as the materials are annealed at a higher temperature their total resistance increases, with the highest resistance being for those annealed at 180 ℃ where there is evidence of partial decomposition of MALI. For samples annealed at 80 ℃ however it is only the PbI_2-rich samples that have the DMF complexes which influences their initial conductivity. Therefore, it appears that although the LCR results did not show any signs of the DMF-complexes affecting the permittivity data, the impedance data clearly shows the initial conductivity being very high for samples x = 0.00 and -0.20, when annealed at 80 ℃ because at this temperature the DMF has not been removed from the lattice.

This can all be seen from the Arrhenius plots in Fig: 6.17A and B. When the powders are annealed at 80 ℃, x = 0.00 and x = -0.20 both have very high conductivity on the heating cycle. However, once the conductivity has decreased when samples are heated at 60 ℃ during the IS measurements there is a large drop in conductivity. On the cooling cycle both of their

conductivities are similar, in fact x = -0.20 is slightly lower probably due to excess PbI_2. On the heating cycle, samples will undergo evaporation of the DMF complexes, a polymorphic phase change and loss of possible moisture (which gives a much larger conductivity value). This means the heating data are complex due to multiple factors but that the cooling cycle data are more representative of the samples after the DMF has been evaporated and the level of uptake of moisture is limited to near room temperature.

The addition of excess PbI_2 decreases the conductivity of the material with x = -0.90 showing the lowest conductivity on the cooling cycle. This is also seen when all samples are annealed at 180 ˚C (from Fig: 6.18) and the excess organic decomposed resulting in similar conductivity values. As PbI_2 is present, the current has to travel through more tortuous pathways to avoid the resistive PbI_2 phase.

6.12.4.3. x- series DC bias experiment

The DC bias results for both DMF and ball milled samples were investigated (not all shown for the sake of brevity) with x = 0.05 DMF results being presented in Figures: 6.19-6.22. The results generally indicated that applying a small voltage (maximum 4 V) produces very large effects not only in the electrical data but the structural data of the material, and since the thickness of the pellet tends to be about 1 mm this makes the maximum field in the region of 0.004 V/m. Extra unidentified peaks are seen in both ball milled and DMF samples generally at the same 2θ angles. f_{max} of the M" peak changes which indicates a bulk change. This effect is not fully reversible because once the bias is switched off, the f_{max} reverts closer to original value of pre-bias but not exactly to the same value.

It does appear that when results from both ball milled and DMF samples are taken into account that the changes in f_{max} (which are moving to a higher frequency range) occur more readily when the voltage is higher and when the composition is at a higher x value. Therefore, there is the implication that excess MAI causes the electrical response to alter at a faster rate, especially at higher voltages, which should not be surprising because the electrical force is larger. It is also easier to decompose organic species compared to inorganic species with increasing bias.

In the literature electrical fields applied to thin film solar cells causes both electronic and ionic movement, albeit at different temperatures. There is also some degradation of thin films which occurs at higher electrical fields, with a limit in some papers set to 0.8 V. As most thin film are about 400 nm, this corresponds to a field of ~2 V/μm. However, all this ion movement becomes more complicated in thin film solar cells. Not only due to the different

arrangement of the cells but also what is present in the different layers. The changes seen in the bulk data of MALI in this work can be hard to link with the thin film work with confidence.

The changes in the MALI due to the applied DC bias shows the material is not very stable because only a small voltage can dramatically change its structural integrity and electrical properties. The altered electrical data not only occurs at lower frequencies (which can be related to an electrode layer or surface layer) but to the M" peak which is associated with the bulk response.

The additional XRD peaks are unidentified, they neither belong to the precursor nor to the Au electrode or any material that has lead-gold or iodine-gold in them. As they occur in both the ball milled and DMF samples its unlikely to be due to any solvent that is present. Both the grinding of the pellet surface and heating of the pellet removes these peaks and the XRD is returned back to the tetragonal MALI phase. The most plausible suggestion is that applying the bias to these MAI-rich samples possibly moves some ions to the pellet-electrode surface. There could also be a possible change in the orientation of the organic cations. What can be said with some certainty is that excess MAI brings about more dramatic changes to the structural and electrical data of the sample under applied bias. The changes in the XRD that appeared due to the DC bias, appeared on both sides of the pellets.

The upper electric field applied across the pellets was ~ 0.004 V/m and at room temperature MA^+ ions in MALI films can readily move under an applied electrical field as small as 0.3 V/μm [5],[6]. Therefore, very small voltages can induce this effect. When a voltage is applied to solar cells in the literature it is mostly to investigate degradation and the mechanisms responsible for it and also to observe effects such as hysteresis. As the solar cell has to be implemented in a circuit there would be at least some effect from the electric field when in usage.

The electric field studies on cells showed that the forward bias to the cells during operation is probably similar to applying a DC bias to the bulk pellet [5]. Although the effects are probably quicker and larger in thin films due to the surface to volume ratio. It is also important to note that in thin films, the perovskite layer being photoactive it is much more sensitive to the presence of light compared to bulk powders. Therefore, such studies are conducted under dark. The effects of voltage are also more pronounced on thin films, as the voltage was increased the perovskite film showed some degradation, similar to the one observed to the light induced degradation [5]. This can be observed by the film turning from black to transparent. In the bulk powder pellets some colouring was observed on the electrode

layer so structural and morphological differences occurred. This was seen via XRD and when the pellets were heated the XRD peaks disappeared and the pattern reverted back to the original MALI pattern. This reversion might also be related to removing of the surface layer due to heating.

The degradation and colouring and extra peaks in the XRD which appeared in both thin films and bulk powder, both in this work and the literature is most likely related to the phenomena that occurs when the electric field that is applied influences the migration of the ions in the perovskite material. It was seen in thin films that applying an electric field is similar to the photoelectric effect due to self-doping effects that occur in the perovskite [7]. As there is an applied field, the perovskite can become non stoichiometric due to the internal migration of the ions. These effects were observed in cells via switchable photovoltaic effects by either forward or reverse bias [6],[7],[8]. This showed that the dominant mechanism was the motion and accumulation of ions inducing a doping effect. These can change the perovskite to have p-type doping behaviour while the n-type doping occurs with the positively charged iodine vacancies. The vacancies with the lowest formation energies move to the Au electrode during poling. In this way the MA^+ concentration is higher near the cathode and the MA^+ is depleted from the centre and the anode. This electromigration of MA^+ can be directly observed in thin films [9]. The MA^+ has rotational dynamics in the inorganic framework and has weak ionic bonding in the perovskite lattice, so little energy is needed in order to cause it to migrate. Compared to charge carrier conduction, electromigration of MA^+ dominates the conductivity only at relatively high temperatures (40-90 ℃) because of its large activation energy. The transition occurs around room temperature where the ionic conduction only contributes slightly to the total conduction. The high ionic conductivity imposes another challenge for the use of MALI materials in solar cell applications because of the higher solar panel temperatures observed in operating conditions.

In both this work and the literature increased C' at low frequency was observed, albeit in different physical forms. It indicates that amount of charged ions affect the dielectric properties of this perovskite. Increased C' is due to increasing ion density in the space charge region of the electrical junction going from the bulk to the contact layer [6],[7],[8],[9]. This behaviour (MA^+ moving along the material) seems to be more easily induced when the samples are MAI-rich, as in it either occurs quicker (less time) or the f_{max} changes much more rapidly at similar voltage levels. However, once the changes start to occur, they tend to be similar in nature (i.e. material becomes more conductive and similar peaks occur across the x

series and synthesis techniques). This can indicate that if these MAI-rich compositions are implemented in solar cells they could degrade faster, even if they have higher conductivity.

References

[1] Y. Guo *et al.*, 'Chemical Pathways Connecting Lead(II) Iodide and Perovskite via Polymeric Plumbate(II) Fiber', *J. Am. Chem. Soc.*, vol. 137, no. 50, pp. 15907–15914, 2015.

[2] K. Shoyama, W. Sato, Y. Guo, and E. Nakamura, 'Effects of water on the forward and backward conversions of lead (II) iodide to methylammonium lead perovskite *J. Mater. Chem. A*, Vol. 5, no. 45. 23815–23821, 2017.

[3] V. Kumar *et al.*, 'Stoichiometry-dependent local instability in $MAPbI_3$ perovskite materials and devices', *J. Mater. Chem. A*, vol. 6, no. 46, pp. 23578–23586, 2018.

[4] N. Aristidou *et al.*, 'Fast oxygen diffusion and iodide defects mediate oxygen-induced degradation of perovskite solar cells', *Nat. Commun.*, vol. 8, no.1, , pp. 2041-1723, 2017.

[5] S. Bae *et al.*, 'Electric-Field-Induced Degradation of methylammonium Lead Iodide Perovskite Solar Cells', *J. Phys. Chem. Lett.*, vol. 7, no. 16, pp. 3091–3096, Aug. 2016.

[6] Z. Xiao *et al.*, 'Giant switchable photovoltaic effect in organometal trihalide perovskite devices', *Nat. Mater.*, vol. 14, no. 2, pp. 193–198, 2015.

[7] Y. Yuan *et al.*, 'Electric-Field-Driven Reversible Conversion Between methylammonium Lead Triiodide Perovskites and Lead Iodide at Elevated Temperatures', *Adv. Energy Mater.*, vol. 6, no. 2, pp. 1501803, Jan. 2016.

[8] Q. Wang *et al.*, 'Scaling behavior of moisture-induced grain degradation in polycrystalline hybrid perovskite thin films', *Energy Environ. Sci.*, vol. 10, no. 2, pp. 516–522, 2017.

[9] T. Leijtens *et al.*, 'Mapping Electric Field-Induced Switchable Poling and Structural Degradation in Hybrid Lead Halide Perovskite Thin Films', *Adv. Energy Mater.*, vol. 5, no. 20, pp. 1500962, Oct. 2015.

7. General Discussion

The initial aim of this project was to investigate MALI material in bulk rather than in thin film form to understand the intrinsic nature of the material rather than all the other factors (i.e. interfaces and other materials) that come into study once thin film solar cell devices are prepared. The initial synthesis method investigated was the general way MALI is synthesised as commonly reported in the literature, i.e. mixing the precursor powders of PbI_2 and MAI using DMF as a solvent. The investigation of these materials, both structurally and electrically left further questions. This resulted in investigating MALI through three different synthesis methods. These were solid state, ball milling and solvent-based methods. Their various conditions were altered along with the starting stoichiometries to assess how they influenced the phase assemblage and electrical properties.

Table 7.1 shows the samples going from PbI_2-rich to MAI-rich starting compositions, the way they were processed and their structural and electrical data summaries. When taken together both XRD/SEM show that it doesn't matter how they are processed it is very hard to synthesis a phase pure material. It was seen repeatedly that clean XRD patterns showed two or three phases in the corresponding SEM images. However, since some samples such as x = 0.00 synthesised using DMF show clean XRD patterns, it means that the quantity of second phase(s) present can be small. This was observed from SEM images, which show very small regions of MAI-rich phases.

When samples were made PbI_2-rich they never showed clean XRD patterns, therefore there was never any hint of classing them as producing a solid solution. However, making samples MAI-rich showed a small region (generally in the range of x =0.00 - 0.20) depending on the processing condition, that showed clean XRD patterns. Measuring their lattice parameters showed that for solid state and ball milled samples the errors were large enough in order for no trend to be concluded with any confidence. However, with the DMF samples going from x = 0.00 to 0.10 did show an increasing volume, as shown in Chapter 6, Fig: 6.7B suggesting that a level of non-stoichiometry in MALI can be obtained.

Although the XRD/SEM showed the physical microstructure to always contain at least two phases the electrical microstructures could be different. In order to investigate this electrical circuit fitting was carried out on the impedance data. The circuit fitting was carried out for both RQC and RQC-RC circuits. The RQC-RC circuit always showed a better fit, this was more often because the results and the fit for an RQC circuit diverged for the lower frequency data. Based on the magnitude of the capacitance, the higher frequency data resembled the behaviour expected from MALI whereas the lower frequency data showed the

response of a secondary element. The source of this secondary response was discussed in the relevant chapter discussions.

Looking at the electrical data overall the main issue seems to be the hysteresis between the heating and cooling data. The electrical data are also only affected dramatically when there is an excess of MAI rather than PbI_2. However excess PbI_2 can also affect the electrical properties depending on the processing conditions. When DMF solvent is used and the materials are annealed at 80 ̊C (to evaporate the DMF) there are still DMF-complexes in the samples. This can produce very high conductivity on the heating cycle. As seen from Chapter 6, Fig: 6.18A for x = - 0.20 too much PbI_2 can also cause the permittivity to reduce and also the conductivity of the sample, however that is when x goes into region of - 0.90, where it is mostly lead iodide with very little MALI being present.

Due to the amount of time spent between IS measurements the hysteresis behaviour in the data can be hard to observe in some samples and they can appear to have a more stable electrical response than reality. This can be more easily observed from the tan δ behaviour, where samples such as x = -0.20 or 0.00 synthesised using ball milling, which appear to have a stable electrical response (i.e. not showing unusual behaviour with temperature) actually show some rise in loss at higher temperatures. Since this can't be due to PbI_2 it could be due to some MAI-rich grains, as the reactions don't always produce stoichiometric grains throughout the microstructure. This is why in IS and permittivity data this was not able to be observed but was in the tan δ data, as shown later in this chapter (see Fig: 7.5D-F).

MAI-rich samples have a more complicated electrical response. Their electrical hysteresis is larger since they are probably more prone to absorption of water from the atmosphere. The moisture must be absorbed post annealing since during processing, whatever moisture is absorbed must be evaporated during annealing of powders at different temperatures. Leaving samples exposed to air near room temperature can regain the moisture which was lost during annealing (as seen from Fig: 7.4E in this chapter). The moisture present is responsible for the higher conductivity on the heating cycle. It is also what elucidates the tetragonal to cubic transition temperature in the LCR data. This has not been observed electrically before. It was also seen that a small increase in the amount of MAI can cause the conductivity of the sample to increase by an order of magnitude. This increase is an intrinsic property of the material since it remains stable on multiple cycles, even when the moisture is evaporated, which can also give increased extrinsic conductivity. This is probably due to the change in defects and possibly the change in the type(s) of MALI (between SPS and tetragonal phase), or either it being n- or p-type by varying x, as discussed previously.

Table 7.1.Table shows x from -0.20 to 0.30 synthesised by different routes and their structural and electrical results summaries

X	Processing	XRD/SEM	ε_r	ε_r and Tan δ	EQC	I.S conductivity (H/C)
-0.20 PbI_2 -rich	Ball Milling	XRD: PbI_2 + MALI SEM: PbI_2 + MALI	~60	Little difference between heating and cooling cycle	RQC-RC	Lowest conductivity. Hysteresis always present, but less significant than higher x samples.
	DMF solvent	XRD at 80℃.: PbI_2 + MALI + DMF complexes XRD at 120℃: PbI_2 + MALI SEM at 120℃: perovskite + PbI_2.	~ 40	Similar to the ball milled sample. No signs of peaks or hysteresis.	RQC-RC	Conductivity high for 80℃ samples due to DMF complexes. But at 120℃, lower than x = 0.00.
0.00 Stoichiometric	Solid state	XRD at 120℃: MALI + PbI_2 SEM: organic -rich region, PbI_2 and perovskite.	~63	Not much hysteresis, but somewhat of a rise at higher temperature.	RQC-RC	All synthesis procedures solid state , BM and DMF produce similar conductivity values. Hysteresis also present between heating and cooling cycles.
	Ball Milling	XRD at 80℃: MALI + PbI_2 SEM: MALI + PbI_2	~63	Similar to x = -0.20, no peaks or hysteresis.	RQC-RC	
	DMF solvent	XRD at 80℃: MALI + PbI_2 + DMF complexes. Which are removed at 100℃. XRD at 120℃: MALI SEM: MALI + organic rich regions.	~60	Similar trend to solid state	RQC-RC	
0.05 MAI-rich	Solid state	XRD: MALI, SEM: MALI + organic rich phase.	~60	Peaks at 60 and 90℃. With rising value with temperature. significant hysteresis between heating and cooling cycles.	RQC-RC	Highest conductivity, with heating cycle having a larger value. So hysteresis present.
	Ball Milling	XRD: MALI + PbI_2 SEM: MALI + PbI_2	~63	No signs of a peak, but rising values with temperature.	RQC-RC	Similar to x = 0.00, i.e. lower than x = 0.05 synthesised by S.S and DMF.
	DMF solvent	Similar to solid state	~63	Similar to BM sample	RQC-RC	Highest conductivity, hysteresis present
0.30 Excess MAI	Solid state	XRD: MALI + MAI + PbI_2 + LDP SEM: MALI + organic rich phase	~38	Peaks at 60 and 90℃, hysteresis also present.	RQC-RC	Conductivity lower than x = 0.05. Hysteresis always present.
	Ball Milling	XRD: MALI + LDP SEM: MALI + organic rich phase	~52	Rising value with temperature.	RQC-RC	Conductivity lower than x = 0.05. Hysteresis always present.
	DMF solvent	MALI + MAI + LDP SEM: MALI + organic rich phase	~45	Peaks at 6 and 90℃. With Rising value with temperature. Hysteresis also present.	RQC-RC	Conductivity lower than x = 0.05. Hysteresis always present.

7.1. XRD and SEM

The advantage of solid state synthesis is avoiding the use solvents and therefore avoiding heating to modest temperatures to evaporate them. A step by step change in the reaction between the precursors PbI_2 and MAI can be observed based on XRD patterns. This approach can start from room temperature and then at elevated temperatures until the formation of MALI or when thermodynamic equilibrium has been reached. Since this is the only method from which room temperature reaction data are obtained, it shows in Fig 7.1A that grinding the precursors together produces some MALI, LDP (based on XRD peaks between 11.3-11.7 $^{\circ}$ [1]) alongside the precursor phases. These phases occur for all compositions, along the x series. The presence of the perovskite peaks show that MALI has low formation energy and is easily synthesised, as stated in the general literature and shown in Fig: 7.1D [2].

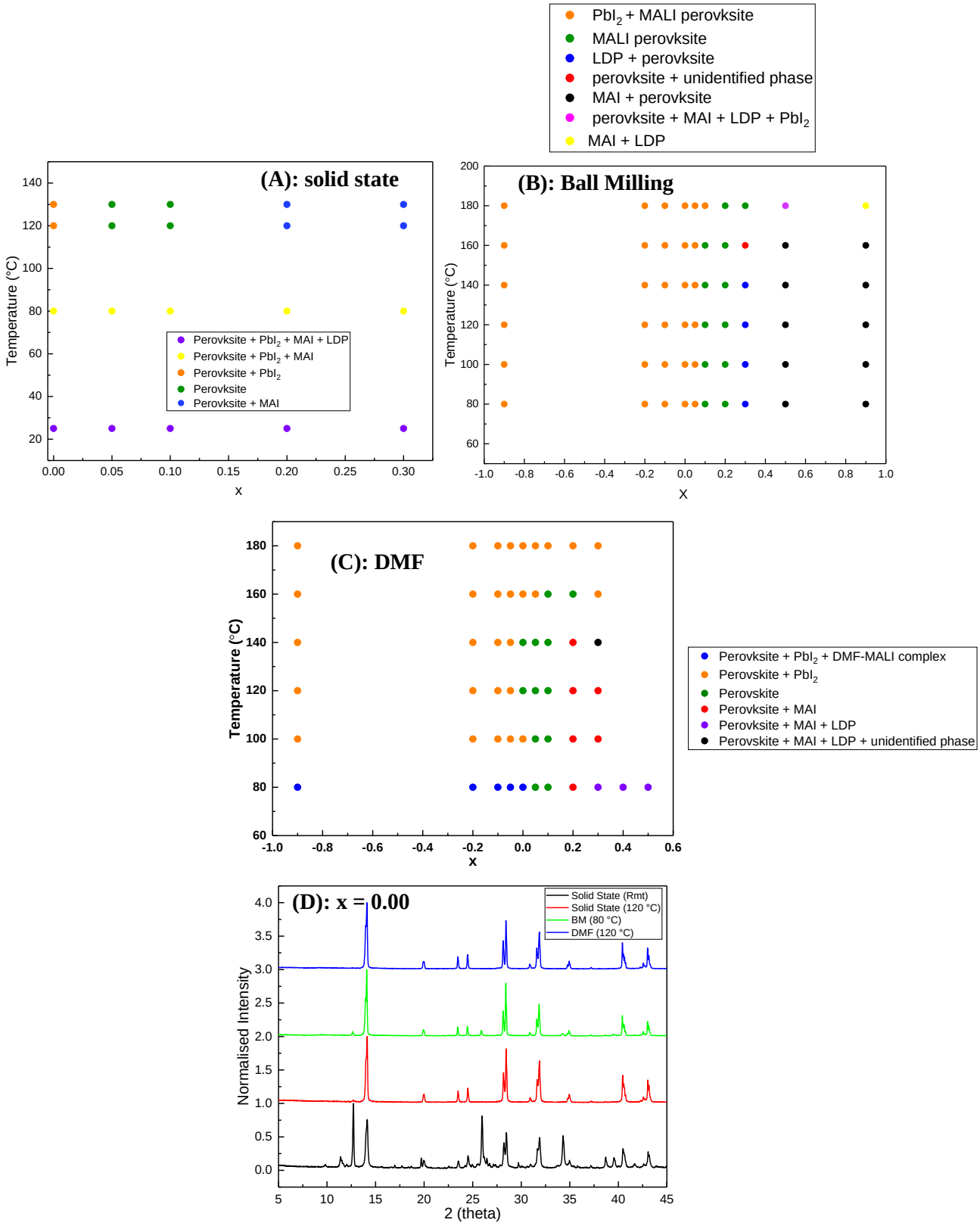

Figure 7.1. Phase assemblage diagrams constructed from solid state (A), ball milling (B) and DMF solvent (C) routes. (D) shows the XRD for x = 0.00 synthesised using different routes.

Annealing solid state samples at higher temperatures of 80 ̊C allows a direct comparison with the other synthesis procedures, i.e. ball milling (Fig: 7.1B) and DMF solvent methods (Fig:

7.1C). This is because both of these methods required different solvents, ethanol in the ball milling case and DMF in the solvent synthesis case. This requires them to be heated at a minimum of 80 ˚C to remove the solvents to obtain bulk powders. Solid state synthesis showed only the presence of the perovskite phase, along with the precursors phases. Therefore, the LDP phases disappeared. Fig: 7.1D shows that only the DMF route produces a clean XRD for x = 0.00, while the other two contain PbI_2.

The ball milled and DMF solvent samples show a larger variation in the phases present along x. More so when they are MAI-rich. The ball milled samples at x = 0.00 shows the perovskite phase alongside PbI_2. Increasing the MAI content results in phase pure XRD patterns being produced at x = 0.10 and 0.20, and further increases in x show peaks for LDP and then crystallised MAI.

This indicates that for DMF and solid state samples, heating the powders at 80 ˚C does not put enough energy in the system to complete the reaction or reach thermodynamic equilibrium. However, ball milling the materials does provide enough energy initially or at least more than the other two methods. This is shown by the unchanging nature of the XRD or the phases present unless heated over the decomposition temperature, which is generally observed to be > 140 ˚C. The DMF solvent compositions at 80 ˚C shows a MALI DMF-complex, whereas ball milled samples show the perovskite and PbI_2 phases. The powders which contain the DMF-complexes appear as dry powders but when XRD analysis was conducted there is some DMF molecules attached to MALI. After being heated to 100 ˚C these DMF molecules evaporate and the results are similar to ball milled materials.

At higher x values, DMF solvent synthesis produces clean XRD patterns. These are seen at x = 0.05 and 0.10. More MAI is therefore required in ball milled synthesis compared to the other two methods to produce similar XRD patterns, because x = 0.05 for this method still has PbI_2. The DMF synthesis also shows the presence of crystallised MAI early, i.e. at x = 0.20, whereas for the ball milled synthesis, it is for when x > 0.3. The shifting to the right hand side in the ball milled phase assemblage diagram is attributed to partial loss of MAI being dissolved in ethanol. PbI_2 is stable until much higher temperatures than the organic cation in MAI and MALI. There is also no evidence or reports of PbI_2 interacting with ethanol. The fact that x = 0.05 and 0.07 both produce PbI_2 peaks in XRD patterns when synthesising via ball milling implies the composition is not MAI-rich and that could be due only to loss of MAI. The DMF samples also show the presence of LDP but it is removed on annealing.

Since both ball milled and DMF samples require less energy via heating to produce a complete reaction, comparison to solid state at 80 ˚C is not possible, since for the solid state route thermodynamic equilibrium occurs at 120 ˚C. This shows x = 0.00 can't be made phase pure. From Fig: 7.1 solid state results indicate that good quality samples only occur after heating to 120 ˚C and for x = 0.05 and 0.10. x = 0.00 always contains PbI_2, reflecting that MAI is lost during the long reaction times and the repeated heating and grinding of the powders so as to encourage reaction equilibrium. The ball milling method is not very reliable to obtain high quality samples, since the same batch can give different results especially when x is close to 0.00. The DMF synthesis produces x = 0.00 as phase pure at 120 ˚C by XRD unlike the other two for whom both x = 0.00 contain PbI_2, both at 80 and 120 ˚C. Aside from that difference, the solid state and DMF routes show similar trends along the x series in their phase assemblage diagram, where both have x = 0.05 and 0.10 appearing as being clean based on XRD and containing crystallised MAI at x = 0.20.

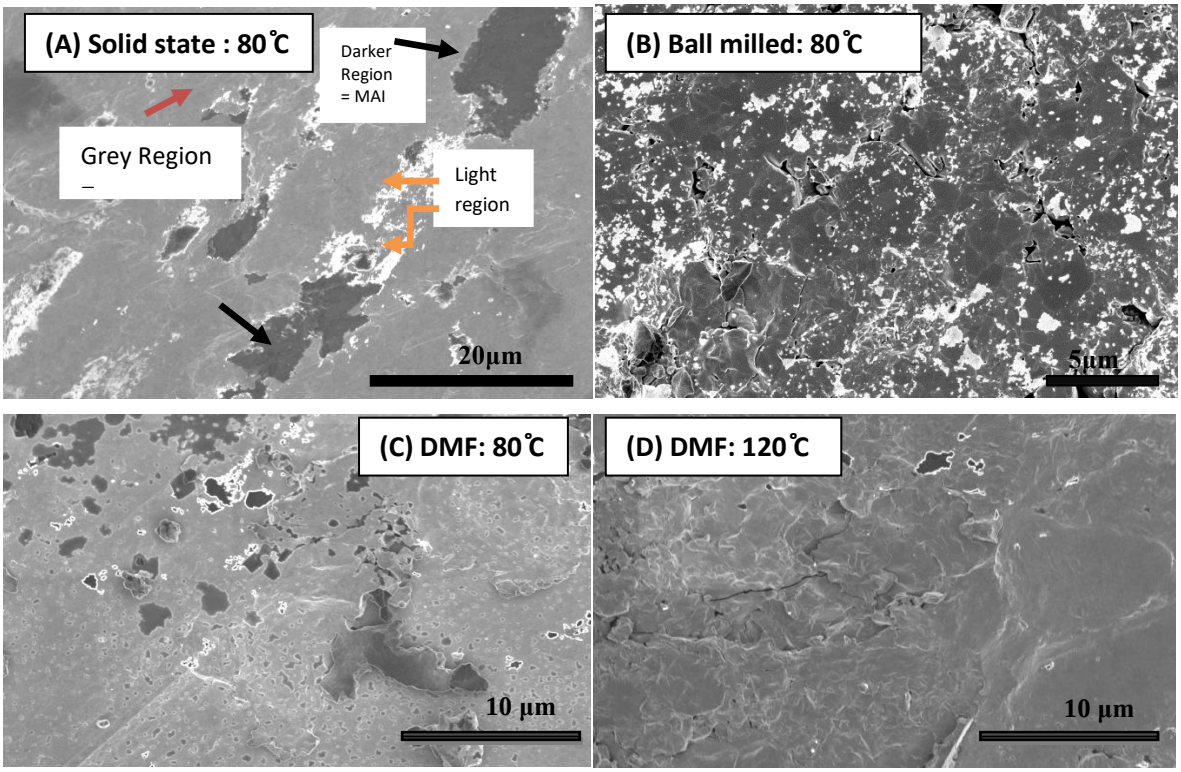

Figure 7.2. SEM images of x=0.00 MALI synthesised using the solid-state method at 80 ˚C (A), ball milled method at 80 ˚C (B) and DMF solvent method at 80 ˚C (C) and 120 ˚C (D).

The XRD technique was observed not to be sensitive enough to determine whether a sample was phase pure, especially in the narrow compositional range between x = 0.00 - 0.20. Therefore, along with SEHI and low voltage SEM it was determined that MAI-rich areas

could be observed as dark contrast regions and PbI_2-rich regions observed as bright light regions. The MALI perovskite being observed as the grey background region.

Fig: 7.2 shows x = 0.00 synthesised using all the various methods. The images show good agreement with the XRD results. For example, a solid state sample has the perovskite material but also the presence of both precursors. A ball milled sample contains a significant amount of PbI_2 and a DMF sample after heating at 120 ̊C looks the cleanest, which is also a phase-pure MALI sample based on XRD data. Based on a combination of these XRD and SEM results, it does appear that DMF is the best route to obtain high quality samples for x = 0.00, when heated at 120 ̊C. This is not only from the high quality XRD data, but also by producing the cleanest SEM images, where minimal light or dark regions being present. This shows the low sensitivity of the XRD results for assessing phase purity of MALI based samples and that this technique should not be used in isolation when attempting to do so. For example, from the phase assemblage diagram in Fig: 7.1 x = 0.10 shows a high quality XRD for all three different synthesis methods but alongside the SEM it indicates that either there is some non-stoichiometry in MALI or low sensitivity of XRD to the organic-rich secondary phase. In chapter 6, Fig: 6.7, there is some indication of slight volume expansion, but from the SEM in Chapter 6, Fig: 6.8 there is evidence of increasing darker regions, associated with organic rich phases. This shows that concentrating on results from one technique alone should be avoided when trying to assess if a sample is high quality or not, or which synthesis method to use for producing the highest quality samples.

There are also limits to the SEM data in analysing sample quality and also to distinguish between β and α' MALI, if present. The low voltage SEM is able to show differences in phases that are present but is not able to show any real differences in the microstructure. Considering that there are fundamental differences between the solid state, ball milling and DMF solution processing routes to produce the powders, it would be anticipated to see some real differences in the particle sizes of the powders from the various routes. However, this was not able to be elucidated.

It is interesting to compare the combined phase assemblage picture from the XRD and SEM results, from the solid state, ball milling and solvent methods for bulk powders to that obtained based on thin films. These thin films were formed by the basic 1 step method. The thin films however did have a constant supply of MAI gas as a control otherwise evaporation of MAI is very easy in the thin films [1]. It can first be seen that below 60 ̊C the β MALI (which is the *I4/mcm* tetragonal phase) [1] is formed and above that temperature it's the α MALI (a *P4mm* tetragonal phase, which they state is similar to the *Pm-3m* cubic phase) [1].

This is the first major difference between the literature and this work. Firstly at 80 ℃ (where in this work, was the lowest temperature at which MALI was heated) none of the synthesis methods produced phase-pure MALI of any polymorph. In the solid state, it had the perovskite with the precursors, via ball milling it had PbI_2 present and via the DMF method it had PbI_2 and MALI-DMF complex(es).

Going to the left hand side of the diagram, both ball milled and DMF synthesis methods showed MALI and PbI_2 above 100 ℃. Below this temperature there were MALI-DMF complexes via the DMF route which does not appear in the phase diagram below. This is probably due to it being in thin film form in which DMF can evaporate easier, especially since other solvents are used for this specific purposes like chlorobenzene. At lower x values where it is made very PbI_2-rich they only observe PbI_2 even though there must be a small amount of MAI added. This should mean that via the thin film solvent method all of the MAI probably evaporates and its loss is easy. In the ball milling and DMF synthesis from this work, even at very high PbI_2 contents, such as when x = -0.90, there is some MALI formed alongside a large quantity of unreacted PbI_2.

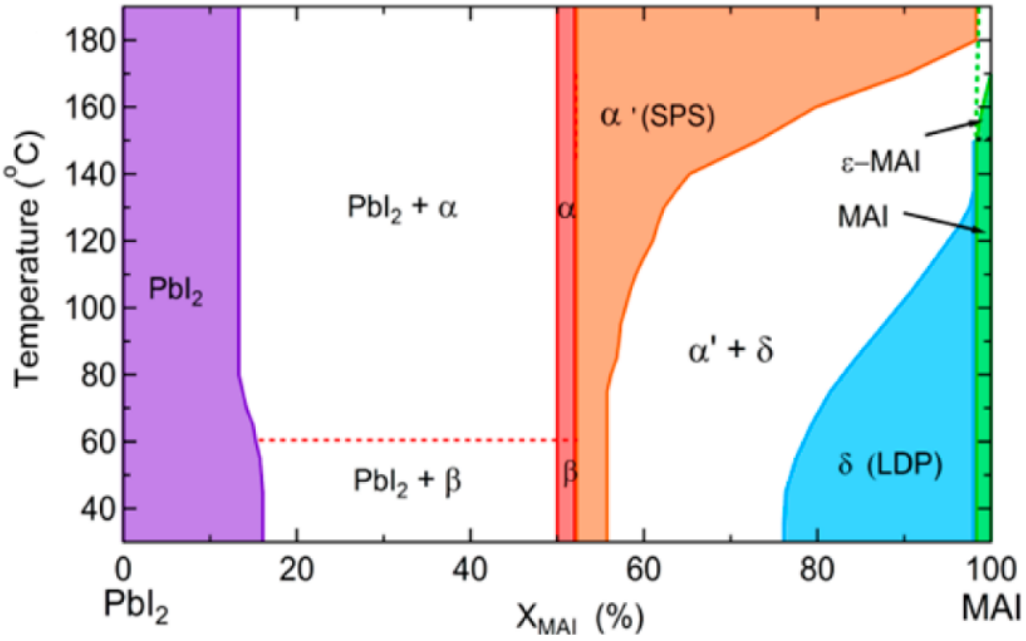

Figure 7.3. Thin film solution phase diagram from literature. Figure reproduced form [1].

When compositions are MAI-rich, the thin films also show a small range (at lower temperatures) that are phase pure but are attributed to an α' phase, consisting of stacked perovskite sheets (SPS). These are present as 3D perovskites but are hard to distinguish since the crystal structure of highly ordered and stacked perovskites are not distinguished, due to

the same long-range periodicity of the 3D perovskite framework [1]. They are MAI-rich as based on energy dispersive x-ray spectroscopy [1]. Low dimensional perovskites (δ phase) were observed by XRD at low angles, at 2θ = 11.3-11.7 ° and become more dominant at higher MAI content. If these (SPS) phases are more MAI rich they could be the same phase observed in the low voltage SEM results in this work (appearing as dark regions). However, one major incongruity is that these phases are present at higher temperatures and at higher x values. In fact even more so above temperatures of 140 ℃ (as seen from Fig: 7.3). At these temperatures, there should be a reduction of the organic content due to decomposition. This effect was seen in the bulk powders, therefore in thin films this effect should probably be predicted to be even more dominant. However, this is not reported from the thin film work. The diagram in Fig: 7.3 in fact shows the thin film of MALI being stable at temperatures as high as 180 ℃.

At higher values of x in all synthesis procedures it was observed that crystallised MAI is formed, which is not observed at all in the thin films unless the composition is 100% MAI. Whereas in this region of MAI-rich compositions (75-99%) from Fig: 7.3, what is observed using thin films are the LDP phases. When heated above 110 ℃ this turns into a region containing MALI + LDP. However, from the bulk powder results (Fig: 7.1), it shows MALI with crystallised MAI, with the MAI peak intensities increasing with x. Above 140 ℃, the organics start decomposing, this either results in LDP phases reappearing, or unidentified peaks probably due to decomposition. After the excess organic is decomposed all that appears is PbI_2 and MALI. The thin film phase diagram constructed for a DMF solvent process showed a much larger difference. As described earlier this could be due to a variety of factors, such as surface-volume ratio, thickness of film, reaction time, other organic solvents used in order to produce a clean MALI film without the DMF solvent present and the volatility of MAI.

Analysing the different synthesis methods it is suitable to state that the end product is greatly dependent on the amount of energy and level of mixing initially input into the system. This is a bigger factor when a mechanosynthesis method is applied, i.e. where precursor powders react through solid state reaction (e.g. chapter 4 and 5) rather than when the precursors mix together at an atomic level by using organic solvents (e.g. chapter 6). This gives the DMF route a more controlled synthesis method especially if microstructural effects are taken into consideration. This could be a reason why the XRD and SEM results tend to be more sensitive when x is varied and also across the temperature ranges at which they are annealed. This can also affect the electrical response, especially at higher x, where the excess

MAI might be more difficult to dissolve in the microstructure. This could be why the enhanced conductivity for DMF x = 0.30 might be linked to the better/more controlled synthesis method of DMF compared to solid state. It may also be because the SPS phases are more likely to occur in solid state and especially in the mortar and pestle method where the energy input from grinding is low. Maybe the better and more energetic milling process gives more MALI (β) than SPS (α') and/or the α' is better dispersed.

In conclusion, the XRD and SEM data of the different processing procedures of MALI bulk powders produce mostly similar results with only small variations. Where it does make a difference is that depending on the processes, the starting MAI:PbI_2 ratio can slightly alter the phase assemblage diagram. This is attributed to the different mechanisms involved in the solid state and ball milling synthesis, where mechanosynthesis is implemented. Compared to when an organic solvent is used, where mixing of the precursors occurs on a molecular level. This initial difference in the synthesis method then leads to varying of other important parameters like the temperature at which the material is annealed to reach equilibrium.

The changing of such parameters causes variation in the composition due to MALI being a very sensitive material. Especially with temperature, where the results can be altered to a large extent. The compositions were also varied, first in order to produce a phase pure MALI material from XRD and when further techniques like low voltage SEM revealed that this was complicated due to various phases being present depending on the initial conditions. This showed that although XRD can show an apparent clean composition, the SEM generally always shows some MAI-rich phase being present. The lattice parameters showed that for solid state and ball milling the large errors range and the small window in which clean XRD patterns were produced could not show any evidence of solid solutions. However, for the DMF solution synthesis there was an increase in volume within the error, which could indicate a small solid solution being present.

Compositional variation was then investigated to see the emergence of different phases within the MALI system and how these might affect the other electrical properties. The decomposition of MALI is also a very important factor, this was seen to be largely dependent on the temperature at which the material is heated to rather than the synthesis method. It was seen that over 140 ̊C problems with decomposition could start to emerge due to the organic cation being the most easily affected. This could lead to various other phases emerging in the XRD patterns. This is because for MAI-rich compositions decomposition of MAI changes the stoichiometry and sometimes even an apparent phase pure material is formed as seen in Fig: 7.1C, for x = 0.20 annealed at 160 ̊C.

The solid state processing route was able to remove the effects of solvent and also allow the gradual change in the XRD to be observed from room temperature to higher temperatures. However, hand grinding is a low energy process and unable to complete the reaction at room temperature. This makes it harder to control the reaction and the final microstructure. The solid state and ball milling reaction mechanisms are more similar since they both depend on the solid state diffusion of the organic cation into PbI_2. The PbI_2 also breaks due to its deformation by mechanical force, which is where the organic cation can channel itself into. It could also be done the other way round where the PbI_2 diffuses into the deformed MAI [3]. As it is the deformation of the precursors that play an important role, it can be seen that the ball milling process introduces more energy and therefore deformation at a faster rate than is present in solid state, hand grinding route. This is why the solid state route requires multi-step heating and grinding stages to achieve equilibrium.

The ball milling process uses an electrical mill rather than hand grinding and it also uses ethanol as a solvent and these factors make the mixing of the precursors more energy intensive and efficient compared to hand grinding. As a consequence, the phase assemblage, once formed (seen after the evaporation of ethanol at 80 ˚C) doesn't change until decomposition starts. As the decomposition is dependent on the organic group, the different processing conditions altered in this work did not have any effect on the stability of MALI, since they all showed decomposition above 140 ˚C. The ball milling method did use ethanol as a solvent and this could possibly dissolve some of the excess MAI, which is why the phase diagram for MALI formation is compositionally shifted when compared to the solid state and DMF routes.

The DMF solvent method has a different mechanism, as stated earlier. This process is also more sensitive to temperature, like the solid state process because both initially use lower energy. This is because initially both of the precursors are dissolved in the organic solvent. It is also the only synthesis route which produced a phase pure sample at x = 0.00. The DMF solvent synthesis (like the solid state process) produces similar phases along x (albeit at different temperatures) for when a small amount of excess MAI is added, i.e. for x = 0.05 and 0.10. In contrast, for the ball milled process both x = 0.05 and 0.07 have PbI_2 present, probably due to MAI loss in ethanol.

7.2. LCR

As was observed from both the XRD/phase assemblage data and the SEM images one of the main parameters that effects these organic based perovskites is temperature. This is

because there is a small range mainly between 80-140 ̊C, where depending on the synthesis method the phases present can change readily but also due to when the organic cation decomposition can also start, especially when annealing time is also considered. There are however also other effects that can occur due to the heating of the samples. There is a phase change of MALI from tetragonal to cubic that occurs in the temperature range of 45-60 ̊C. There is also a change in the amount of the dark organic-rich phase as it is annealed as seen from the SEM data. Fig: 7.4 A-C shows the tan δ of DMF samples x = 0.00, 0.05 and 0.30, respectively when they were annealed at 80,120 and 180 ̊C. The ball milled samples didn't change in their XRD once ethanol was evaporated at 80 ̊C and the solid state synthesised samples still had significant amounts of precursors at 80 ̊C and didn't reach reaction equilibrium until 120 ̊C. Therefore, the best samples to study electrically using different annealing temperatures were the DMF samples. For these samples, from the summary table 7.1 and Fig: 7.1C it was seen that as x goes from PbI_2-rich to MAI-rich the amount of dark regions in the sample increases even if the XRD is clean. Furthermore, higher quality XRD patterns are produced along with cleaner SEM images at 120 ̊C, whereas at 180 ̊C the samples become decomposed and now have PbI_2.

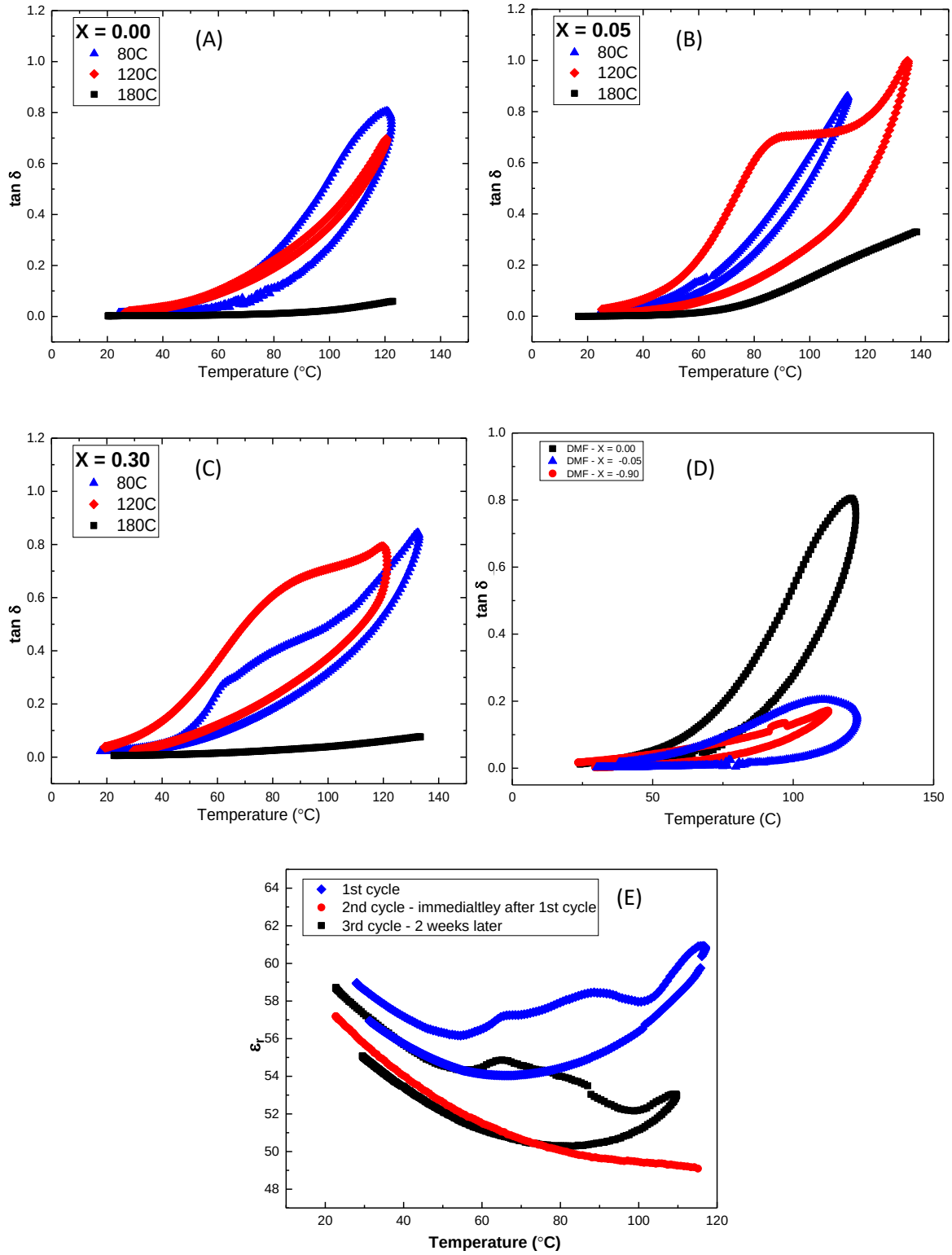

Figure 7.4. Plots (A) shows the LCR data for DMF sample x = 0.00 annealed at three different temperatures. (B) shows the LCR data for DMF sample x = 0.05 annealed at three different temperatures. Plots (C) shows the LCR data for DMF sample x = 0.30 annealed at three different temperatures. Plot (D) shows DMF synthesised PbI_2-rich samples at 80 ˚C. Plot (E) shows the ε_r profile for x = 0.10 synthesis from solid state at three different time intervals.

The tan δ results for x = 0.00 corroborates with the XRD/SEM results in that those synthesised using DMF at 120 ˚C show the stoichiometric sample is of the highest quality.

This is because not only is it clean from the XRD and has negligible dark areas in SEM, its loss is also smaller than x = 0.05 and 0.30. There is also little difference between the heating and cooling cycle of this sample. This hysteresis tends to increase with x. This is also backed up by the 180 ˚C sample data. Once they are partially decomposed and only MALI and PbI_2 are present their losses are significantly lower. The PbI_2-rich samples having larger amount of lead content and less MAI, have significantly lower loss, as seen from Fig: 7.4D. Although there are still signs of hysteresis (common for MALI samples) because not only are they very susceptible to water intake, which they lose on the heating cycle (meaning that conduction on heating is higher than on cooling, therefore losses are also higher on heating) but the PbI_2-rich samples, having a higher lead content are attached to DMF complexes which will also make the material more leaky.

Water being present in MALI, either taken up during the processing or from atmosphere over time is known to be both beneficial and a problem. Beneficial because it can act as a catalyst [4] but also lead to eventual degradation of MALI and therefore a decrease in the solar cell efficiency. Water present in bulk powders can also lead to artefacts in the electrical data. Fig: 7.4E shows LCR data for a solid state sample, x = 0.10 as was discussed in chapter 4, Fig: 4.11G. The difference between the 2nd and 3rd cycles is attributed to uptake of moisture after 2 weeks which results in the elucidation of the peaks at ~60 and 90 ˚C. These data sets show that excess MAI plays a larger factor in how leaky a sample is rather than the annealing temperature. This is because both 80 and 120 ˚C annealed samples produced more or less similar results. But the results dramatically changed when either the PbI_2 content was increased, and therefore decreasing MAI in the sample or by decreasing the MAI content through decomposition by heating to 180 ˚C. The DMF complexes might play a part in the hysteresis behaviour but they can't be a major factor because at 120 ˚C (at which point they are removed) samples also have high losses.

LCR data for the x series (annealed at 80 ˚C) synthesised by the three different routes are overlaid in Fig: 7.5. The main detail elucidated by the ε_r data (Fig: 7.5A-C) is that samples that are PbI_2-rich or have PbI_2 present in their XRD patterns, such as x = 0.00 show a decrease in their permittivity response with increasing temperature. This occurs for both solid state and ball milled MALI. The difference between their heating and cooling cycle data is either negligible or very small. MAI-rich MALI samples however show peaks that occur at ~60 ˚C, and also a rise in ε_r value with increasing temperature. As it is clear from Fig: 7.5C, these are more clearly elucidated in some than others (say comparing for when x = 0.30).

The tan δ data (Fig: 7.5D-F) show that materials with high conductivity, (such as for Solid state and DMF when x = 0.05), their loss or leakiness is also comparatively high. Therefore, this shows that for a given sample x, once a small excess of MAI is added to increase the conductivity of the composition, the different materials processes have similar dielectric and loss values. What does however seem to be of an important difference is that the DMF samples tend to show a more pronounced difference between the heating and cooling cycle.

The elucidation of peaks is due to moisture being present, which increases with MAI due to more organic content present, so more prominent at higher x. The moisture is taken over time from the atmosphere as shown by Fig: 7.4E. This might be why the peaks are observed more readily at higher x values and in DMF samples. Because in BM due to ethanol and milling, loss of MAI is easier, as is also the case in solid state due to constant heating and grinding. For x = -0.90 permittivity is constant with no variation with increasing temperature and also low tan δ values which means that it still might pick up some water. The hysteresis on heating and cooling could be related to indicate uptake of water. The DMF samples are generally more conductive so have higher tan δ values and are more leaky.

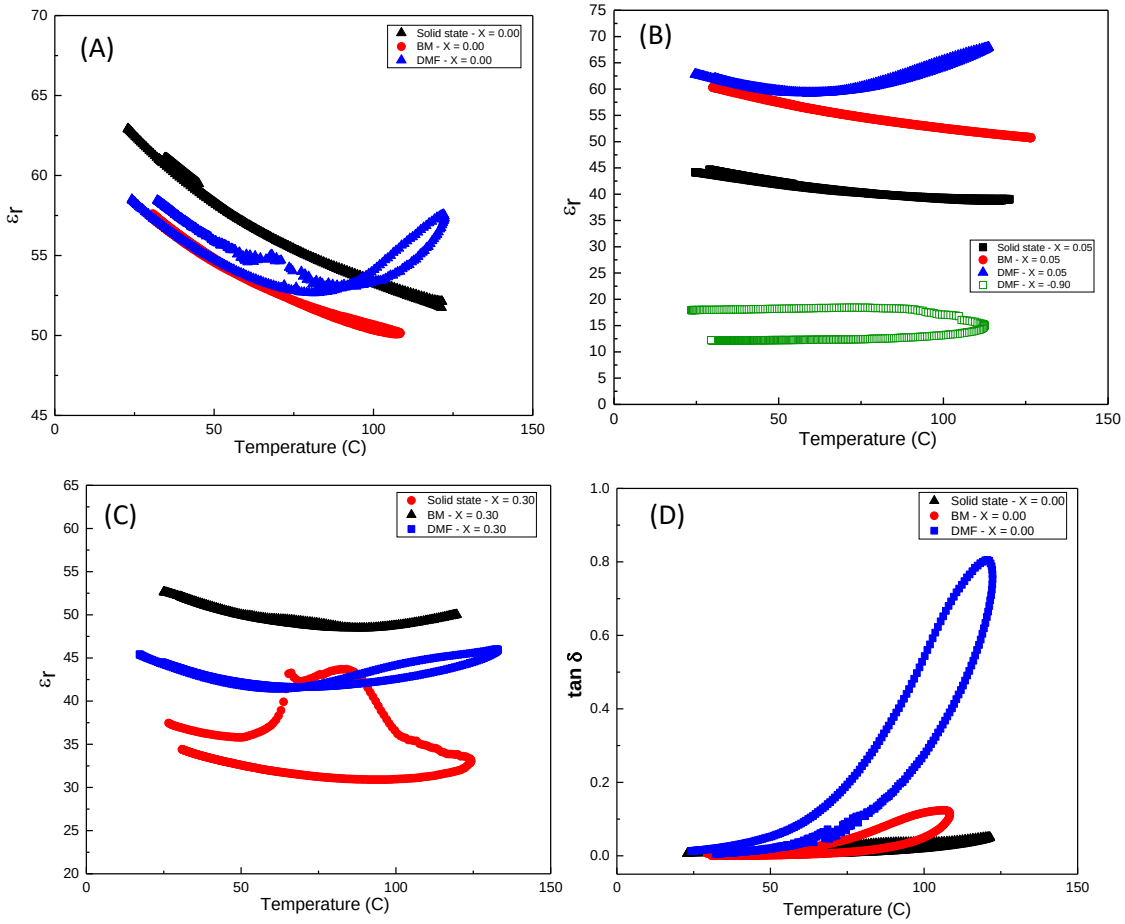
(A)
Solid state - X = 0.00
BM - X = 0.00
DMF - X = 0.00
εr
Temperature (C)
(B)
Solid state - X = 0.05
BM - X = 0.05
DMF - X = 0.05
DMF - X = -0.90
εr
Temperature (C)
(C)
Solid state - X = 0.30
BM - X = 0.30
DMF - X = 0.30
εr
Temperature (C)
(D)
Solid state - X = 0.00
BM - X = 0.00
DMF - X = 0.00
tan δ
Temperature (C)

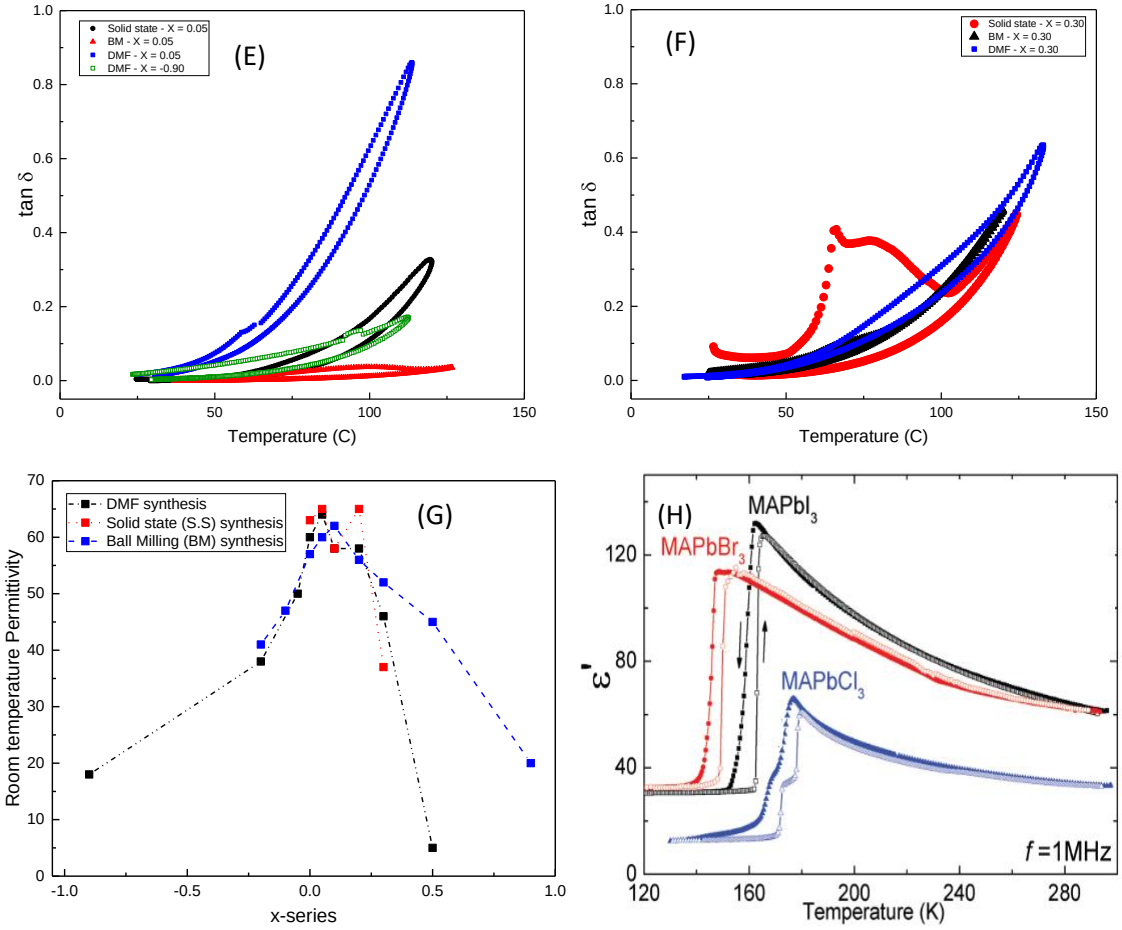

Figure 7.5. Permittivity vs temperature plot synthesised via the three synthesis methods solid state , BM and DMF are shown in Plot (A) for x = 0.00. Plot(B) for x = 0.05, and Plot (C) for x = 0.30. Tan δ Vs temperature plot synthesised for the three synthesis methods are shown in Plot (D) for x = 0.00. Plot(E) for x = 0.05, and Plot (F) for x = 0.30. Plot (G) shows the room temperature ε_r of the x series synthesised using solid state (Red), ball milling (Blue) and DMF (Black) methods. Plot (H)[5] **shows the low temperature phase transitions for MALI and other organic-halide perovskites from the literature.**

It can also be observed from the LCR data that the PbI_2-rich MALI samples not only have lower permittivity but also lower loss, meaning they are less leaky and conductive than the organic rich samples. The MAI-rich MALI also decrease in their permittivity value, if too much MAI is added (as seen from Fig: 7.5G). This is when it starts to appear as crystallised MAI based on XRD data. Since the permittivity of the PbI_2 is low it makes sense that the permittivity of MALI in the x series decreases when PbI_2 content of the pellets is increased. With MAI however it has a permittivity of ~ 40, therefore the large decrease in x = 0.50 and 0.90 when they are made from DMF and ball milling respectively, makes it harder to explain this result. It could either be that MAI being measured on its own in the form of a pellet and MAI being present as an extra phase within the mostly perovskite phase has different dielectric responses due to factors such as density or how its agglomerated in the pellet

microstructure. Especially during the MALI synthesis, when it is also dissolved either in a solvent like DMF or when partially dissolved in ethanol or mechanically sheared during ball milling and then subsequently annealed. From their SEM data (chapter 6: Fig: 6.8) no difference is seen except for a higher surface area of the darker regions. The crystallised MAI in higher x values such as x = 0.50 has the same contrast as the darker region in x = 0.05. This lack of any difference between the contrast region of these two samples shows that the dark regions can't be associated with α' MALI which the secondary electron spectra show is associated with MAI-rich regions. If α' MALI does in these samples it must be part of the grey MALI perovskite regions that are attributed to the tetragonal MALI, β.

MALI exhibits an orthorhombic to tetragonal phase transition at -111 ̊C [5] and this is consistent with the orthorhombic structural polymorph observed from chapter 6 Fig: 6.2, which was measured at -123 ̊C. The dielectric studies from the literature were able to identify the orthorhombic to tetragonal phase transition but no signs of a permittivity change associated with the tetragonal to cubic transition [6]. These studies indicate that this phase transition should occur at ~57 ̊C [5],[6]. When a phase transition occurs either into an antipolar/polar state then the dielectric permittivity should show an anomaly, however its absence in the data could mean that this transition does not have polar character [5], [6]. The peaks that are seen in the x series in this work could be observed due to the fact that there is moisture present and also the excess MAI which is a conductive material on heating elucidates this more easily, because the phase change alters the behaviour of the water molecules present and therefore the phase change is then able to be observed in the electrical data.

The dielectric response is also dependent on the frequency and in this frequency range of 20 Hz - 1MHz, the ionic transport should dominant [5], [6]. The rise in permittivity is related to a conduction mechanism. This is clearly seen in the tan δ data and is most likely due to ionic conduction and since this was seen more extremely in the MAI-rich MALI it shows that a small region, generally between x = 0.05 - 0.20 has a large effect on MALI conductivity. Although this seems not to be due to MAI itself because ε_r and tan δ for samples of x > 0.30 tend to be decreasing and sometimes lower than x = 0.00. Anusca et al [5] state that for MALI the base value for dielectric constant should be around 30 but from measurements it is close to 62, which is a similar value to this work as seen from Fig: 7.5H. They attribute this higher value due to polycrystallinity of thin films, size effects, and or effect of mechanical stresses. However, since this work measures bulk powders then it would

seem to rule out these explanations and could be due to an intrinsic nature of MALI itself. However, it also may be variable if there are different levels of α' present

7.3. Impedance Spectroscopy

The impedance results are summarised in the form of f_{max} vs. temperature and capacitance (which is extracted from the M" peak, corresponding to the bulk value of the MALI composition) vs. Temperature in Figures 7.6 and 7.7, respectively.

The electrical results of the precursors were measured to see if they have any effect on the overall response of the MALI samples, and are shown in Fig: 7.6A. PbI_2 is very resistive compared to MALI and MAI. It becomes conductive only at much higher temperatures and generally in the range where the organic cation of the MALI would start to decompose. MAI initially has a high conductivity (Fig: 7.6A) but upon heating it decreases and then starts to increase again. This shows a similar pattern to that for MALI on the heating cycle. At these higher temperatures MALI has a higher conductivity than MAI, whether it is synthesised by solid state, ball milling or DMF solvent. The higher conductivity of MAI on heating shows that it is most likely related to water. However, it does not follow that the more MAI being present in MALI system, the higher conductivity. Otherwise, x = 0.50 would have the highest conductivity, which is not the case. The previous LCR data where the effects of moisture were discussed, and how they get pronounced with higher x can then be related to this. Since Fig: 7.6A shows that MAI on its own also seems to readily absorbs moisture.

Comparing the f_{max} of each composition synthesized via these three different routes (seen in Fig: 7.6B-H) shows that for x = 0.00 on the cooling cycle the results are similar. When the samples are clean based on XRD but still MAI-rich (so when x is in region 0.05-0.20) it has an enhanced conductivity compared to x = 0.00, or for x = 0.05 BM sample. This is when the x = 0.05 ball milled sample had PbI_2 as stated in the summary table 7.1 and Fig:7.1. Whereas for the solid state and DMF samples which had clean XRD patterns but a small excess of MAI, resulted in a much higher conductivity. For x = 0.10 when all samples were clean from XRD, all had a similar conductivity on the cooling cycle. When x values are further increased (x > 0.20), i.e. when crystallised MAI shows up in the XRD the conductivity starts to decrease. It therefore means that aside from the heating cycle which is strongly influenced by the amount of moisture present or DMF solvent present, the method of synthesis produces similar conductivities as long as a similar phase assemblage is formed.

The DMF samples (for x > 0.20) have a higher magnitude than the other two processes, as seen from Fig: 7.6E. This could be most likely related to the microstructure

because in DMF, the MAI precursor dissolves and then reacts with the PbI_2. The excess MAI which also dissolves and then once the solvent is evaporated it recrystallises and possibly percolates along the microstructure of the pellet differently compared with a mechanosynthesis approach. In this way, the DMF route ensures that MAI loss and distribution is different to that in the BM and solid state synthesis.

The f_{max} (or the time constant) of a material at a certain temperature should remain the same unless affected by artefacts. If the f_{max} values appear similar, it correlates with the materials having similar conductivity and permittivity values. This is even when they are synthesised by different methods, because the product of their conductivity and permittivity values match. The x = 0.00 result from Fig: 7.6B, show that a solid state sample is more conductive and has a different time constant than the DMF and ball milled samples. This indicates that the processing conditions in solid state produces a different type of MALI compared to ball milling and DMF. This is probably due to a different stoichiometry which results from the processing conditions. From inspection of the IS results from Fig: 4.10 and 4.13A it can be observed that the solid state sample shows two responses. It also appears less electrically homogenous than the ball milled samples (Fig: 5.12). which shows a more singular response. This is most likely due to incomplete mixing using the mortar and pestle method, compared to ball milling and solution mixing. It is also why a higher temperature and multiple grinding steps were needed in the solid state synthesis process to get better quality samples. However, it still did not produce a completely homogenous electrical response as was seen from the impedance results, especially when compared to the ball milling and DMF IS results. This is more clearly displayed due to the two responses present in the solid state sample. Making the RQC-RC circuit fit much clearer than compared to when ball milled samples were fitted, where the difference between RQC-RC and RQC circuit was less clear. This means the second element is more enhanced in the solid state samples, and as it is clear from the SEM data there always seems to be at least two phases present. As has been mentioned previously, especially in the Chapter 4 discussion, the possible presence of the stacked perovskite sheets, α' could be a reason but it could also be due to excess MAI present in the sample, because as observed from Fig: 7.6A, the MAI behaviour closely resembled that of MALI itself.

For x = 0.05 - 0.30 the time constants of these samples for all three synthesis procedures are similar to each other when their XRD patterns are also similar, which is why x = 0.05 for BM has a lower conductivity, since it has PbI_2 present. This means that the different methods of synthesis produce similar behaving materials in terms of their intrinsic

properties. For x > 0.20, the DMF samples then produce a different response compared to the solid state and ball milled ones. They are more conductive and have different time constants. Once again this might be due to less MAI loss and possible retention along the grain boundaries in the DMF synthesis.

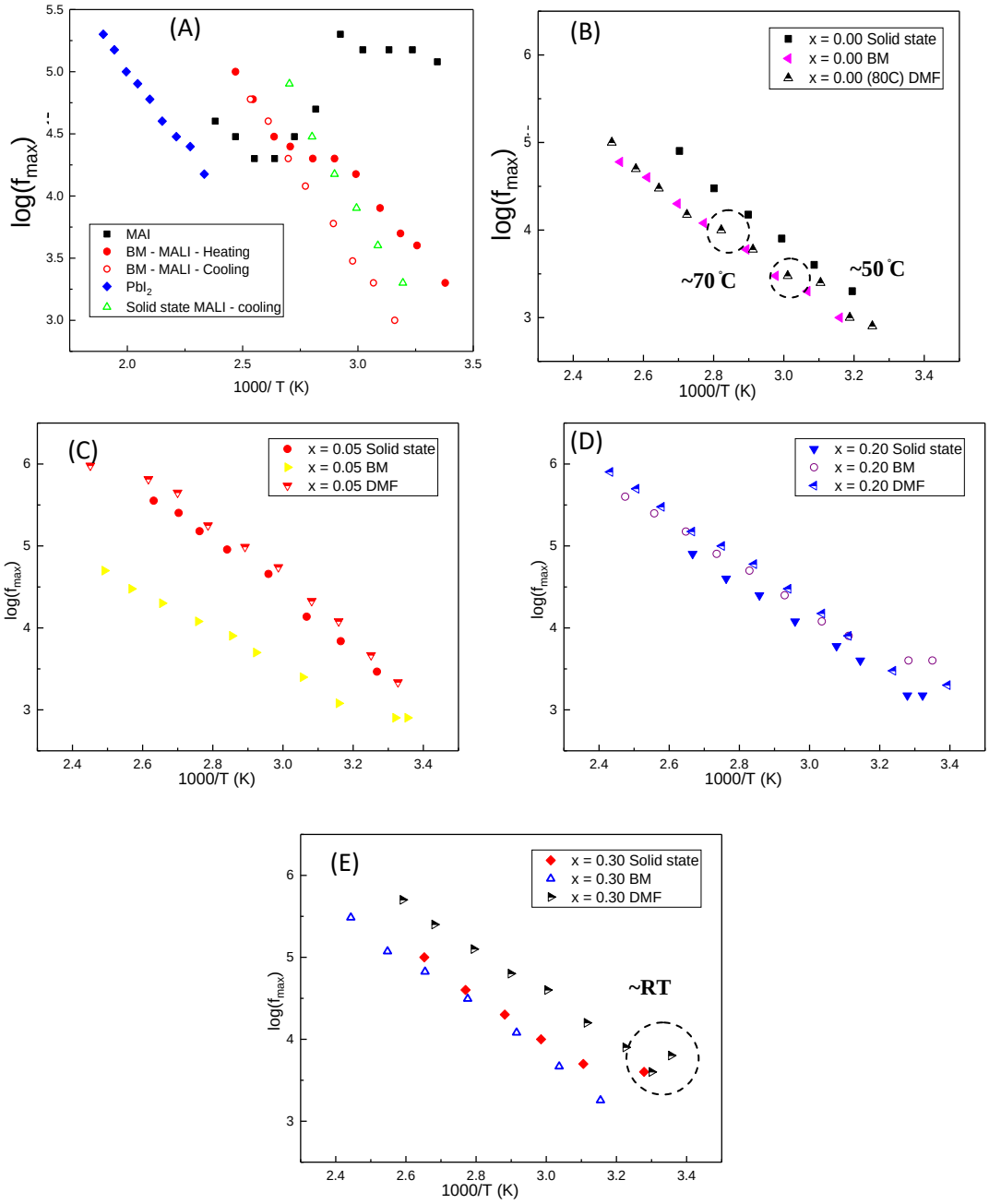

Figure 7.6. f_{max} vs. inverse temperature plot synthesised via all three different processes, solid state labelled as (solid state), ball milling as (BM) and DMF solvent as (DMF). Plot (A) shows the precursors and MALI. Plot (B) x = 0.00 on the cooling cycle. Plots (C) x = 0.05 on cooling, respectively. Plot (D) for x = 0.20 on the cooling cycle. Plot (E) for x = 0.30 on the cooling cycle.

The easy nature in which MALI is decomposed especially at higher temperature then puts a barrier to explore the lower frequency region, since the decomposition itself will affect

the results. The equivalent circuit fitting (from Fig 4.18) of the solid state materials showed that even samples like x = 0.10 and 0.20 which appear to have a single response have two components present in them. And because their time constants are so similar they become hard to separate out, reaching the resolution limits of the IS technique. When low frequency impedance data were collected for the DMF sample, it did show a second response, however this was due a Warburg type response that is associated with ionic diffusion at the electrode and this supports the existence of ionic conduction of iodide ions, meaning that MALI is a mixed conductor. In contrast, the second response in the solid state material could be due to a secondary phase or grain boundary. The DMF sample for x = 0.00 also showed two responses (Fig: 6.10A) on the Z" plots, however this was for the 80 ˚C annealed sample, which contains the MALI-DMF-complex phase and not just MALI perovskite on its own. Not producing phase pure MALI means the electrical response is also not going to be homogenous.

The MAI-rich samples show that a small amount of excess MAI can dramatically affect the electrical results. The solid state synthesis results could then suggest that controlling the stoichiometry can be difficult because insufficient energy can be put in the system with mortar and pestle alone and due to the limited temperature at which it can be heated. It can then produce regions where there is excess PbI_2, excess MAI and also stoichiometric grains across the microstructure, and possibly grains with both β and α' types of MALI. The ball milled materials tend to produce materials whose XRD patterns do not change with temperature. This is in the sense that once a specific stoichiometry is synthesised, and ethanol is evaporated at 80 ˚C their XRD data does not change with annealing to higher temperature. It also doesn't differ greatly on how much MAI-rich dark regions there are along their surface images from SEM data. Also the ball milling process takes more time in the mixing stage between precursors. This is 6 hours, whereas for the solid state process, each grinding session might be between 30 to 40 min and there were a maximum of four sessions, coming to a total of 2.5 hours. In contrast, the DMF synthesis was given 30 min of mixing of precursors on a hot plate at 60 ˚C to fully dissolve in the DMF.

The ball milled impedance results (Fig: 5.13 & 5.14) also showed that compared to the solid state process it produced much more homogenous responses in the electrical data. When circuit fitting was conducted on the data (Fig: 5.20 and 5.21), the series two element parallel circuit produced a better fit than the single circuit however, it was less obvious than the fitting results for the solid state samples. The DMF results for the PbI_2-rich samples at 80 ˚C have these DMF- complexes which give a very high conductivity on the heating cycle and

once the materials are heated above 100 ̊C, which is the temperature at which they evaporate their response seems closer to what would be expected, which is having a lower conductivity. This was seen in two different ways, one was seeing in-situ results of 80 ̊C samples on heating and cooling (Fig:6.10), where the initial conductivity is very high in the case of x = -0.20 outside the 1MHz frequency range whereas on cooling there was a dramatic drop in conductivity. Secondly, for 115 ̊C annealed samples (Fig: 6.11) (where the DMF-complexes have been removed) that showed low conductivity even on a heating cycle.

The better the processing conditions the less difference there is between the time constants of the two elements. It is then easy to separate out and fit the two elements for the solid state processing. Whereas for ball milled and DMF samples the fitting between the RQC and RQC-RC gets harder to distinguish.

The f_{max} plot for different samples synthesised by different processes is seen to change at certain temperatures, these are labelled on the plots. The most common change in the gradient of the plots occurs after 70 ̊C and at room temperature during the cooling cycle. The most likely explanation for these is that at 70 ̊C there is a cubic to tetragonal change and at room temperature, the samples are presumably picking up moisture again. From the capacitance plots (Fig: 7.7B and C) similar small changes are seen in the temperature region of ~40-60 ̊C. The LCR results when overlaid on top of the permittivity data from impedance (when capacitance values from the M" peak is extracted) are in agreement with each other, as seen from Fig: 4.13 from equivalent solid state and DMF samples, Fig: 7.4C.

The hysteresis in the electric results of MALI thin film solar cells is seen frequently and has been connected to ferroelectric phenomena, ionic migration or exposure to humidity. The exposure to humidity has been seen to result in the formation of $CH_3NH_3PbI_3.H_2O$ or $[CH_3NH_3]_4PbI_6.2H_2O$. These have been seen to be reversible [7]. Water absorbs rapidly (in thin films where it has been studied, the time scales have been shown to be in the scale of seconds) into the perovskite structure [8]. Even low humidity (10%) has been shown to absorb water into the MALI thin films. Masconi et al [9] showed that when water is encapsulated into MALI it does not change its crystal structure and its band gap is also seen to be similar. Just as water is seen to infiltrate into MALI so can oxygen, MALI's photocurrent for thin films were measured under ambient environment and they were larger than under dry air or moist N_2. It can be that water and oxygen adsorption can affect the electronic conductivity via doping or trap state filling. Or it could increase the ionic conductivity [8].

Fig: 7.7 shows the capacitance vs. temperature trends for each specific composition synthesised by the three different processes. The DMF samples being slightly more conductive are also observed by the fact that the DMF samples also show higher capacitance values than the solid state and ball milled ones. The capacitance behaviour also shows there is some temperature dependence even on the cooling cycle at similar temperature as seen from the LCR and impedance data. From literature Ansuman et al [7] showed that the temperature dependence can change how the perovskite can become hydrated and dehydrated. The hydrated perovskite was studied by in situ x-ray diffraction. MALI showed a tetragonal to cubic phase change at 60 ˚C [7]. The dihydrated perovskite $[CH_3NH_3]_4PbI_6.2H_2O$ goes through a phase change by releasing the water that is in the structure. When cooled back to below this temperature it picks up water again. These results were easier to observe from the XRD of thin films. The same reason why when too much MAI is added in thin films the perovskite peaks almost disappear, and only MAI is seen, as observed from the thin film phase diagram. While in bulk MALI these effects are less transparent due to the effective sample size which can have a large effect on XRD measurements.

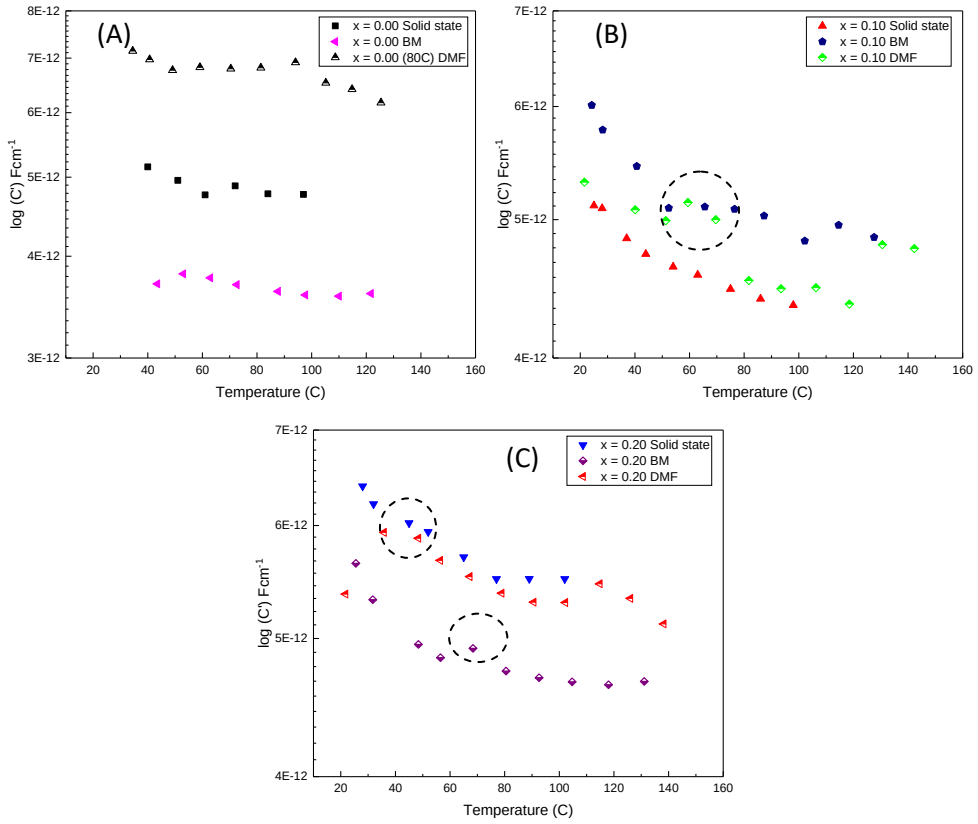

Figure 7.7. Capacitance vs. temperature profile for x = 0.00 - 0.20 for the three different processes on the cooling cycle. Capacitance was extracted from the M'' peak, which represents the bulk.

Infrared results of thin films also showed that the O-H group, which is related to the water appears in MALI and after 60 ℃ it disappears but then reappears when cooled down below that temperature [7]. Therefore, the results seen in LCR and impedance due to water being present is found to be a necessary condition of this temperature dependent phase change of the perovskite system. In thin films when MALI is exposed to more humid environments and therefore picks up water, it turns into a brown colour. This was also observed in the DMF sample synthesis because the surface layer formed the black perovskite but the bottom was still unreacted yellow powder. This had to be mixed and during the mixing of this powder where it had to be exposed to air, some of the surface turned brown. When heated again in the oven at 80 ℃, it turned black.

The higher conductivity when it is MAI-rich most likely seems to do with the defect chemistry, or the different types of phases present MAI-rich regions, of MALI which has both β and α' types. The mobile ions are shown to be iodide ions with iodine vacancies shown to represent the mechanistic centres under equilibrium conditions. Pb^{2+} and MA^{+} ions do not significantly contribute to the long range transport [10]. The electronic contribution to the mixed conductivity stems from electron holes as holes can be attributed to iodine orbital's local variation in the iodine stoichiometry and the transport may be fast. Aliovalent doping of Na instead of Pb (which resembles lead deficient MALI) enhances the concentration of iodine vacancies and electron holes results in a large and significant increase in the ionic and electronic conductivity (>1 order of magnitude) compared to undoped MALI [10]. Other techniques like SIMS showed an absence of long range MA^{+} diffusion [10]. Yang et al [11] carried out impedance on MALI from room temperature to 70 ℃, they carried it out under Ar gas on pellets of MALI. They found a conductivity value of $1.2x10^{-8}$ Scm^{-1} at 30 ℃ [11], which has a value similar to this work for x = 0.00 samples on cooling. Therefore, they did not see this high conductivity on the heating cycle. Furthermore, it does not seem to be of relevance to perform measurements under Ar, because in this work even under Ar or N_2 dried gas the initial heating cycle showed the enhanced conductivity behaviour. Implying that it depends on how samples are stored prior to conducting electrical measurements in any atmosphere.

MALI is therefore sensitive to many variables. These include the material synthesis process and the history of the sample and depending on whether it is in thin film or bulk form. The characterisation time and length scale of the measurement being conducted are also

important factors. There can be large differences in the average overall behaviour and local behaviour within MALI.

Taking all the results together showed that it is very difficult to produce a completely phase pure MALI material when both XRD and low voltage SEM results are taken in conjunction. This remains true even if the stoichiometry of MALI is altered or even different processing methods are implemented. This was also further seen by carrying out equivalent circuit fitting of the impedance data of the different compositions along the x series and differing processing methods. Where comparing RQC and RQC-RC circuits for solid state, ball milling and solvent produced samples showed better fit with the two series element circuit. This was easiest to observe for the solid state samples because hand grinding means the processing conditions are harder to control giving a less homogenous microstructure.

The different processing methods do produce extrinsic differences such as DMF complexes or shifting of the phase assemblage diagram when ball milling; however, once the material stoichiometry is controlled, the same composition have the same intrinsic electronic response on cooling. On the initial heating cycle, however there are large differences due to the extrinsic effects of moisture being present and sometimes due to excess solvent. However, their presence can be helpful to pinpoint the MALI tetragonal to cubic transition temperature.

The variation in the stoichiometry of MALI, when it is made MAI-rich can cause the intrinsic conductivity of the sample to increase. Since the conductivity of samples such as x = 0.05 and 0.10 is higher even on cooling compared to PbI_2-rich samples or x = 0.00. This however has an upper limit and occurs only in addition of a small amount of excess MAI. The amount of MAI that induces this phenomena is dependent on the processing method and how this might relate to self-doping or a switch between p- and n-type MALI remains unresolved.

References

[1] Z. Song, S. C. Watthage, A. B. Phillips, B. L. Tompkins, R. J. Ellingson, and M. J. Heben, 'Impact of Processing Temperature and Composition on the Formation of methylammonium Lead Iodide Perovskites', *Chem. Mater.*, vol. 27, no. 13, pp. 4612–4619, 2015.

[2] C. C. Stoumpos, C. D. Malliakas, and M. G. Kanatzidis, 'Semiconducting tin and lead iodide perovskites with organic cations: Phase transitions, high mobilities, and near-infrared photoluminescent properties', *Inorg. Chem.*, vol. 52, no.15, pp. 9019-9038,2013.

[3] V. Panneerselvam, S. T. Salammal, K. K. Chinnakutti, and P. Manidurai, 'Vibrational modes , chemical states and thermal stability of mechanochemically synthesized methylammonium lead iodide', *Mater. Lett.*, vol. 241, pp. 140–143, 2019.

[4] K. Shoyama, W. Sato, Y. Guo, and E. Nakamura, 'Effects of water on the forward and backward conversions of lead (II) iodide to methylammonium lead perovskite', sp - 482, vl - 10, Is -1, pp. 23815–23821, 2017.

[5] I. Anusca *et al.*, 'Dielectric Response : Answer to Many Questions in the methylammonium Lead Halide Solar Cell Absorbers', vol.7, no. 19, pp. 1–12, 2017

[6] N. Onoda-Yamamuro, T. Matsuo, and H. Suga, 'Dielectric study of $CH_3NH_3PbX_3$ (X = Cl, Br, I)', *J. Phys. Chem. Solids*, vol. 53, no. 7, pp. 935–939, 1992.

[7] A. Halder, D. Choudhury, S. Ghosh, A. S. Subbiah, and S. K. Sarkar, 'Exploring Thermochromic Behavior of Hydrated Hybrid Perovskites', *J. Phys. Chem*, vol.6, no.16, pp. 3180–3184, 2015.

[8] C. Müller *et al.*, 'Water Infiltration in methylammonium Lead Iodide Perovskite: Fast and Inconspicuous', *Chem. Mater.*, vol. 27, no. 22, pp. 7835–7841, 2015.

[9] E. Mosconi, J. M. Azpiroz, and F. De Angelis, 'Ab Initio Molecular Dynamics Simulations of Methylammonium Lead Iodide Perovskite Degradation by Water', *Chem. Mater*, vol.27,no.13,pp.4885-4892 2015.

[10] A. Senocrate *et al.*, 'The Nature of Ion Conduction in methylammonium Lead Iodide : A Multimethod Approach', Angew. chem. int., vol. 55, no. 27, pp. 7755-7759, 2017 [11] T. Y. Yang, G. Gregori, N. Pellet, M. Gratzel, and J. Maier, 'The Significance of Ion Conduction in a Hybrid Organic-Inorganic Lead-Iodide-Based Perovskite Photosensitizer', *Angew. Chemie - Int. Ed.*, vol. 54, no. 27, pp. 7905–7910, 2015.

8. Conclusions and Future work

8.1. Conclusions

The work was conducted to establish the structure-property relationships of bulk MALI powder materials by altering the processing conditions and also by changing the stoichiometry of the parent material. This was done by altering the precursor ratios of PbI_2 and MAI and the reaction temperature. The results showed that processing MALI can be challenging. The main reason for this is associated with organic cation present in the perovskite structure and as organics are more susceptible to change (i.e. moisture attack and decomposition) along the temperature domain it affects the structure-composition-property relationships.

The different processing conditions made it possible to narrow down which parameters were affecting the material properties. In the solid state method it made the removal of the solvents that are common during synthesis and made it possible to see how the phase assemblage altered along the temperature domain from room temperature. In contrast, solvent-based processes needed annealing of the products at 80 ˚C to evaporate the solvent. The reaction mechanisms of the different processes showed that MALI is relatively easily formed but phase purity is harder to attain. This was most easily seen in the results for x = 0.00 for the different processing methods and also at different reaction temperatures. This caused their electronic, structural and microscopic data to vary significantly.

XRD is not sensitive enough to elucidate if a material is phase pure because from the SEM data it was observed that there were local regions of dark MAI-rich or light PbI_2-rich regions depending on the processing conditions that were not detected by XRD. The MALI perovskite regions appeared as grey, which accounted for most of the surface. However, the thin film work from literature might suggest that adding MAI and moving away from the stoichiometric MALI might change the type of MALI present. And rather there being a tetragonal β MALI there might also be the presence of stacked perovskite sheets (SPS, α') MALI. However, these can't be distinguished from the β phase in XRD or in the SEM contrast. However, it might still be responsible for some of the variations observed in the electrical responses presented in this thesis.

The different processing methods and conditions examined in this work showed that the highest quality sample was produced via the DMF method for x = 0.00 when it has been heated to 120 ˚C. Because not only in x = 0.00, but throughout the x series, in the solid state there are some MAI-rich phases that could not be eliminated by temperature because any

higher annealing temperature would initiate decomposition of the organic ions in MALI. For the ball milling method there are regions of PbI_2 in the microstructure probably because using ethanol and milling for 6hrs leads to some loss of MAI. The DMF method also needs samples to be heated at 120 ̊C, because at lower temperatures it is either an incomplete reaction or also the presence of other phases like DMF-complexes.

The electrical results revealed that even a small addition of excess MAI in MALI influenced the electrical properties in a dramatic way. This was not only due to the changing of the stoichiometry but also because MALI can pick up water very easily. It can pick up water not only during processing but also when stored in lower humidity jars. The moisture present in a sample before electrical characterisation in the form of LCR or IS measurements showed that there is a tetragonal to cubic transition at around 60 ̊C. MALI was shown to be a mixed conductor, with the ionic contribution presumably associated with iodine ions. The excess MAI also increased the conductivity of MALI by (up to) an order of magnitude depending on the processing conditions. This was shown to be a material property rather than due to the moisture present, because of the reproducibility on repeated heating and cooling cycles, i.e. conductivity remained high on the cooling cycle after the initial loss of moisture during the heating cycle. The IS technique revealed the samples to be electrically heterogeneous; however, the two responses present often have similar time constants and were often difficult to separate. Although the difference was sufficient to be resolved using circuit fitting with a two-element circuit RQC-RC fitting the data better than a single RQC circuit. This however is also more easily observed depending on the processing conditions. This result also corroborates with the SEM results, since they generally show at least two different phases in the physical microstructure.

8.2. Future work

The results and conclusions from this work show that more work needs to be done to understand the composition-property relationships of MALI and to further investigate the influence of environmental factors on their stability and electrical properties. One of the first thing that could be carried out is to perform Thermal Gravimetric Analysis with Mass-Spectrometry (TGA-MS) [1] on the stoichiometric MALI and along the x series of powders from the different processing methods. This could reveal the different products that might be given off along the temperature range and at more specific and accurate temperatures. This would also help with what temperature range to use during the electrical experiments. This may reveal the level of moisture present depending on the stoichiometry and sample history.

As moisture has a significant influence on the electrical properties of MALI, some glove box work to create a more controlled environment for sample preparation would be useful to establish this relationship. Along with carrying out low-voltage SEM, there could be more work done using the SEHI technique [2]. This should reveal the precise phase(s) associated with the dark-regions. i.e. is it just MAI on its own, or MAI-rich grains of MALI or some form of core-shell structure. Related TEM work [3] has been carried out on thin film samples to elucidate this level of detail and would also be useful to perform on the samples prepared in this thesis.

Other doping elements could be investigated to reveal more about the ionic conduction, for example using bromine rather than iodine can be used to reveal how much iodine plays a part in conduction. Changing the A-site ion from an organic into an inorganic (eg Cs^{+}) to see the effects of conductivity and how much this influences the moisture sensitivity. A very interesting experiment would be to make solar cells out of the samples processed by the different synthesis methods and along the x series. This would be interesting not only to see if good quality efficient cells can be made out of these samples but more interestingly to relate the whole process together, from the initial processing conditions to the different techniques used to the final cell product and especially to see the role IS might play in assessing the solar cell quality and the photovoltaic material used.

References

[1] C. C. Stoumpos, C. D. Malliakas, and M. G. Kanatzidis, 'Organic Tin and Lead Iodide Perovskites with Organic Cations : Unique Semiconductors , with Phase Transitions and Near-infrared Photoluminescent Properties', *Inorg. Chem.*, vol. 52, no. 15, pp. 9019–9038, 2013.

[2] V. Kumar *et al.*, 'Stoichiometry-dependent local instability in MAPbI3 perovskite materials and devices', *J. Mater. Chem. A*, vol. 6, no. 46, pp. 23578–23586, 2018.

[3] A. Alberti, C. Spinella, C. Bongiorno, E. Smecca, I. Deretzis, and A. La Magna, 'degradation', *Nat. Commun.*, vol.10, Article number. 2196, 2019.

Appendix : DC - Bias

Powders of x series from 0.00 - 0.20 were synthesised via ball milling and DMF solution processing. Their pellets were subjected to a DC bias and the impedance response measured versus time when subjected to the bias. When carrying out DC bias measurements, the initial room temperature measurement at 0 V is recorded and then 0.5 V applied. The impedance response was then measured with time, after which the bias is removed and the impedance response measured during the relaxation period. After a certain period of time when either the sample had relaxed back to the initial state or remained constant the bias was then increased further on the same sample to 1 V, and the same procedure was carried out for 2 and 4 V.

XRD of samples after DC bias

The pellets subjected to the bias were analysed using x-ray diffraction (XRD) to observe if the application of a DC voltage resulted in any structural and/or compositional changes in the samples. The pellets were gold (Au) coated to perform the DC bias experiments, the Au peaks are identified to separate them out from those associated with the sample.

Plots A and B in Figure A1 show x = 0.00 and 0.05 (synthesised via ball milling) respectively. The initial powder samples are both two phase mixtures with the perovskite MALI phase and a small amount of PbI_2 as a secondary phase. After applying the DC bias the phases are still present and the XRD patterns are unchanged. The I.S responses for both x = 0.00 and 0.05, (see Fig: A6 and A7, respectively) show some variation in electrical response with DC bias in contrast to the unchanged XRD patterns.

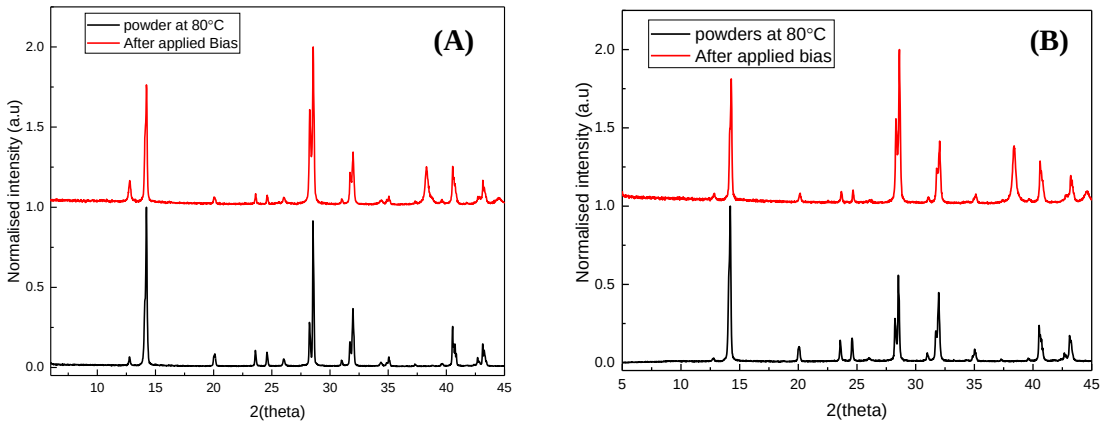

Figure A1. (A) XRD patterns of x = 0.00 synthesised via ball milling, the batch powders and the pellet after application of a DC bias. (B) XRD patterns of x = 0.05 synthesised via ball milling, the batch powders and the pellet after application of a DC bias.

XRD was carried out on an x = 0.10 pellet surface after DC bias experiments. There is a change in the XRD pattern of the sample due to extra peaks appearing (shown in Fig: A2 A). Firstly, one of the main peaks is a split peak in the tetragonal MALI with 2θ value of 14.16° associated with hkl of [110] and 14.28°. After DC bias this peak splitting seems more pronounced (seen from Fig: A2 B) with peak values of 14.20° and 14.36° and an additional peak appearing at 14.50°. A similar pattern is seen with the other main split peak from (Fig: A2 C), occurring at 28.31° associated with [004] and 28.62° associated with [220]. After the DC bias the distance between these peaks i.e. the splitting is more pronounced and the peaks occur at 28.37° and 28.67° and a further peak appears at 28.98°. Since the first Au peak appears at ~38°, the XRD data shown in Fig: A2 B and C, with expanded scales over the ranges of 13.5-15.5° and 27.5-29.5° , respectively are only due the changes occurring to the MALI phase, due to the DC bias.

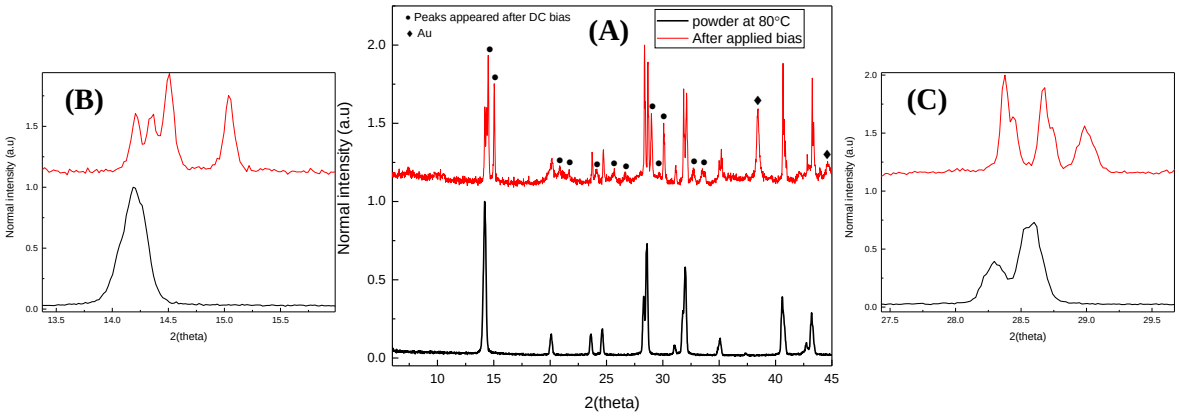

Figure A2. XRD patterns for x = 0.10 synthesised via ball milling before and after DC bias experiments. (A) before and after the DC bias on the pellet. (B) and (C) Expanded views of selected main peaks of MALI.

Fig: A3 shows the XRD pattern for powders of x = 0.20 and the pellet after DC bias. The peak splitting seen in Fig: A2 occurs in Fig: A3 but not to the same extent since the additional peaks at 14.50° and 28.37° do not occur. The general intensities of these extra peaks in Fig: A3 are lower when compared to the main MALI peaks. Although some peaks do appear in both samples, like the peak at 15.04° degrees. The region between 20-22° in Fig: A3 is quite noisy whereas peaks can be distinguished from Fig: A2. The same is seen to occur in the region of 26-27°. There are also peaks in x = 0.20 that are not seen in Fig: A2, such as the those occurring at 11.55° and 11.69°.

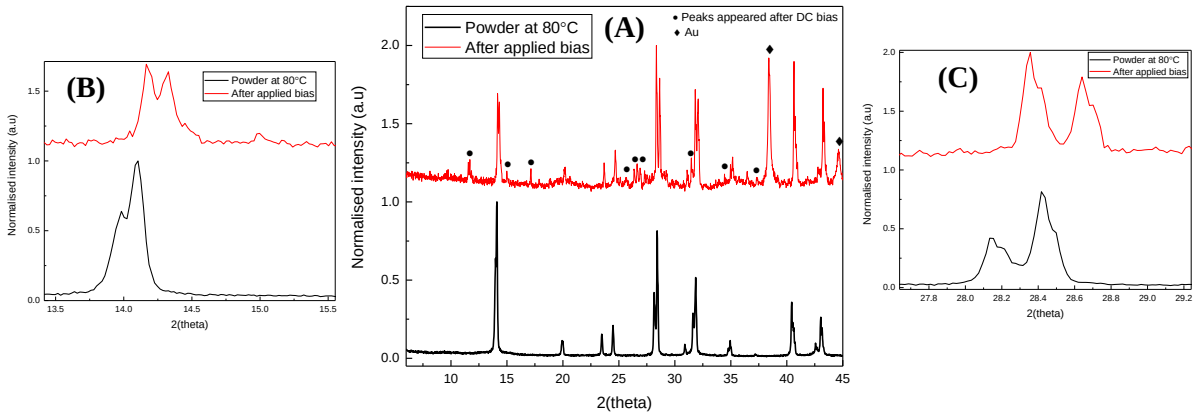

Figure A3. XRD patterns for x = 0.20 synthesised via ball milling before and after application of a DC bias. (A) Before and after the DC bias on the pellet. (B) and (C) Expanded views of selected main peaks of MALI.

Fig: A4 shows XRD of x = 0.05 powders synthesised by DMF and of a pellet after DC bias, and then subsequently from the surface of the pellet after it has been polished with sandpaper. The results show that after the DC bias the main peaks split in a similar way to that shown in Fig: A2, with the extra peaks occurring including the one at 15.04°. There is also the single peak occurring at a low angle of 11.55°. Once the pellet has been polished (so as there is no gold electrode on the surface), the extra peaks disappear including those attributed to the gold electrode, however there could be still a very weak intensity peak at around 28.8° degrees, seen from plot B.

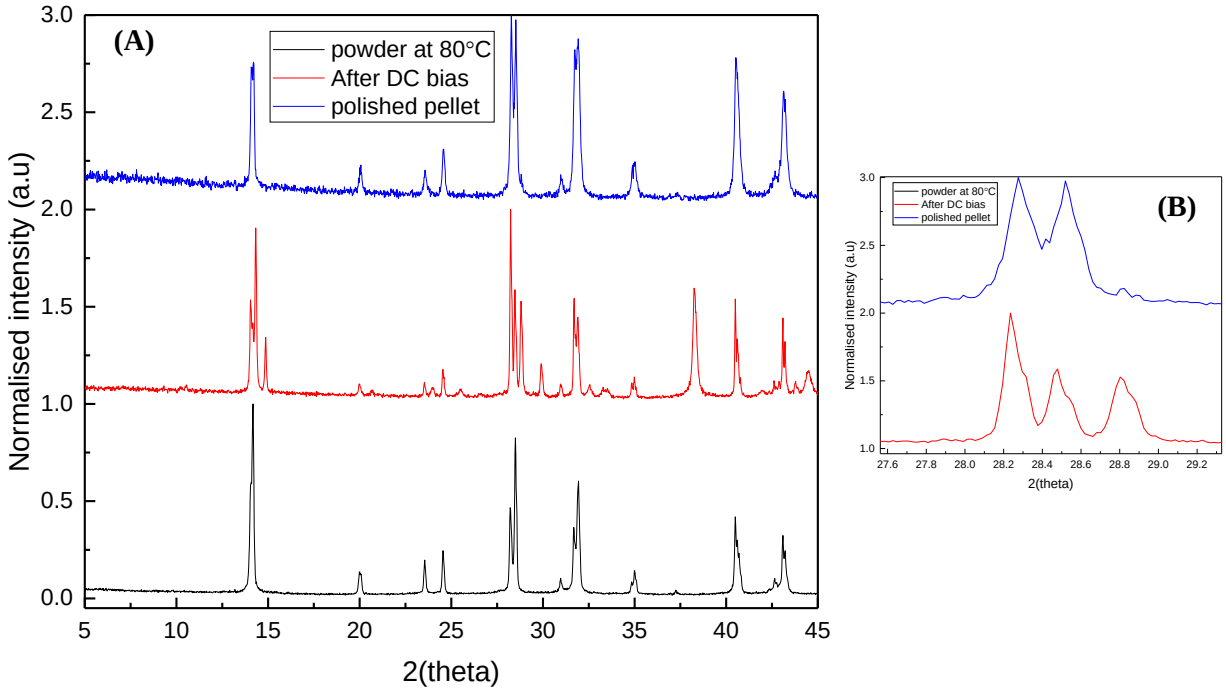

Figure A4. XRD patterns for x = 0.05 synthesised via DMF before and after application of DC bias and then after being polished. (A) Before and after DC bias on the pellet. (B) Expanded view of selected main peaks for MALI.

Figure A5. X-ray diffraction patterns of x = 0.05 - 0.20 pellets for both ball milled and DMF synthesized powders after application of a DC bias.

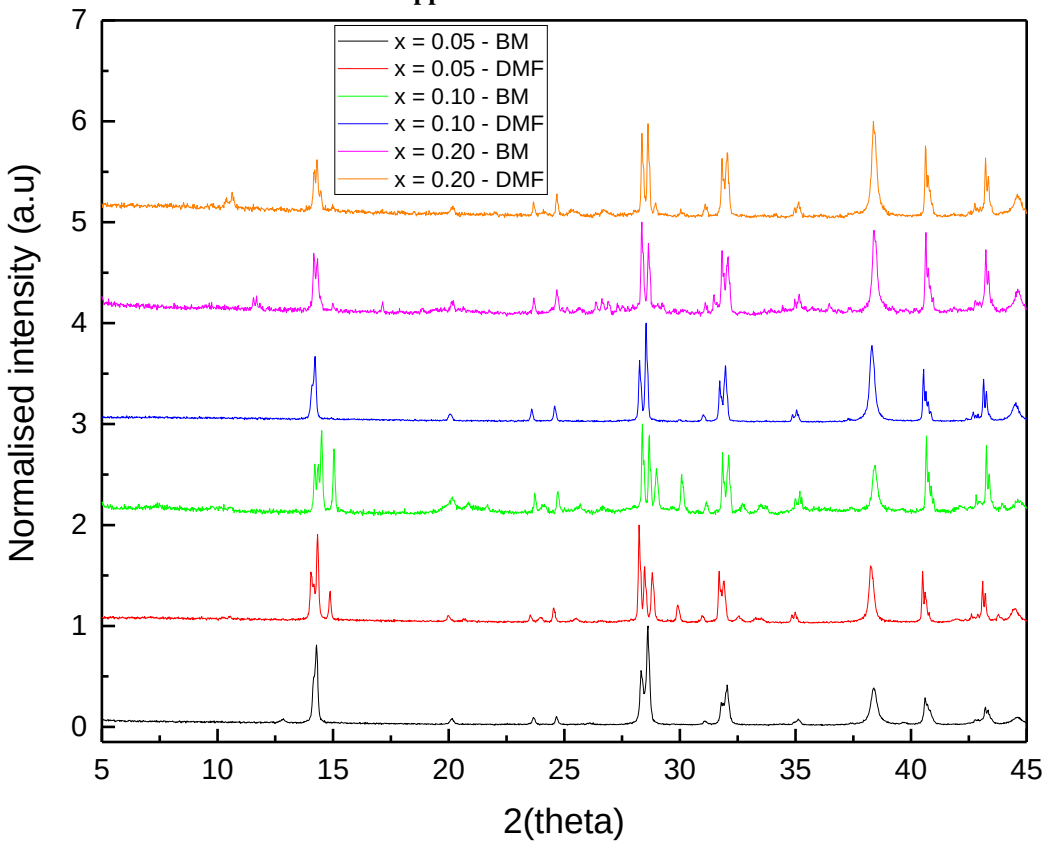

Fig: A5 shows the comparison between the samples synthesises by DMF and ball milling after they have been subjected DC bias. x = 0.05 made via ball milling and 0.10 made via DMF do not seem to show any changes in their XRD patterns. The rest, which do show some effects in their patterns demonstrate it mostly at low angle peaks, as in the case of x = 0.20, both via DMF and ball milling. The peaks appearing around the region 26-27°, the extra peak occurring at around 28.8 and 15.05 for x = 0.05 (DMF), x = 0.10 (BM), and x = 0.20 both BM and DMF.

The results from the DC bias showed that the XRD patterns on the surface of the sample changes. The extra peaks are not due to gold or any combination of interaction between gold and elements in MALI, like lead or iodine. The effect is large enough to be measured by XRD but occurs at the surface, since polishing the pellets either completely removes the extra peaks or severely diminishes it. The heating of the sample then removes the peaks produced due to applied bias. Since the compositions synthesised via both ball milling and DMF alter, it gives more precedent to an actual effect of the material rather than a processing condition.

Impedance results

Results for x = 0.00

Fig: A6 shows results using different impedance formalisms for x = 0.00 when a DC bias was applied.

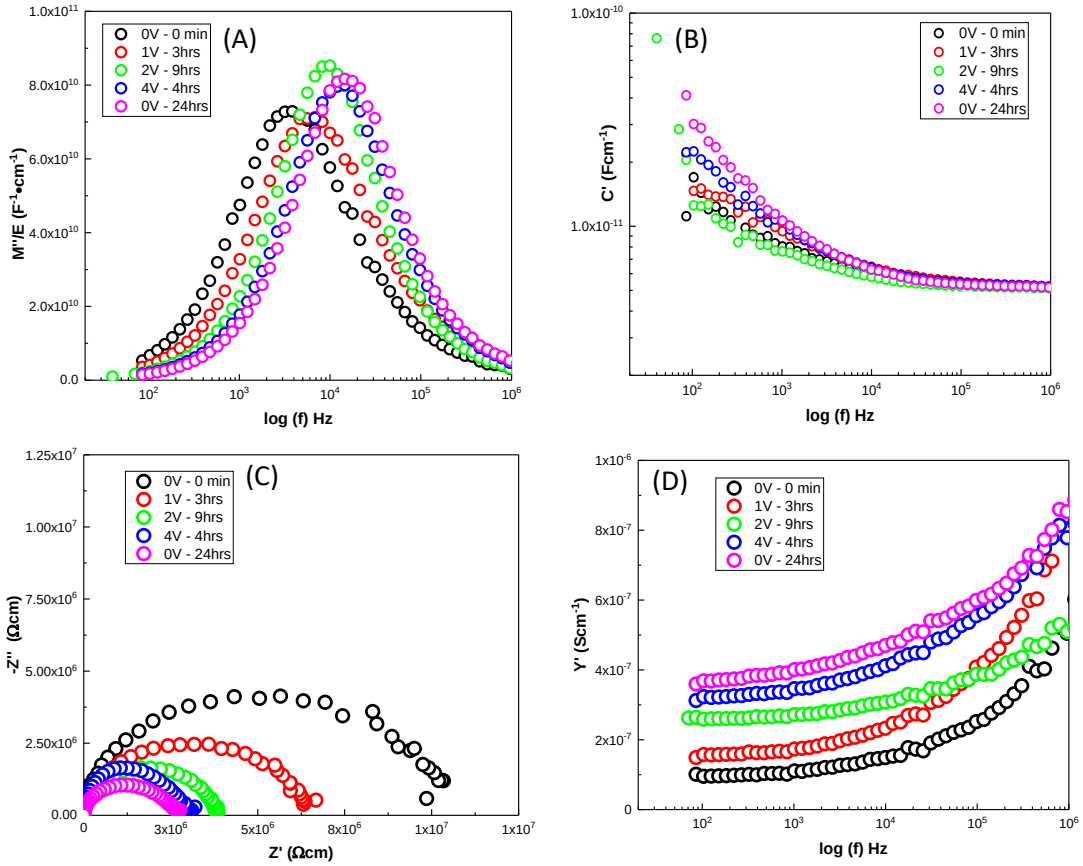

Figure A6. Room temperature impedance data for x = 0.00, synthesised via ball milling. (A) M'' spectra, (B) C' spectra, (C) Z^* plots and (D) Y' spectra.

From plot A, applying a voltage for a set amount of time shifts f_{max} of the M'' Debye peak to the right, i.e. higher frequencies. When the bias is removed, it does not relax back to the initial value. There is also a slight change in the M" height indicating a small drop in the bulk capacitance. Plot B shows that at low frequency the capacitance changes more than at high frequency.

Plot C shows the total resistance at room temperature at 0 V is 11 MΩcm. Increasing the bias decreases the overall resistance and for 4 V the value is 3 MΩcm. When the bias is removed the total resistance remains similar, however Z" decreases. Plot D shows Y' against frequency, and being the inverse of Z', shows that with the application of a bias the total conductivity of the sample increases.

The individual R and C values can be estimated from the M" and Z" spectroscopic plots and Z^* plot. These are shown in table A1. For x = 0.00 the difference between the M" and Z" f_{max} increases, as the applied voltage is increased. At 0 V, the M" f_{max} is 4 kHz, whereas the Z" f_{max} is 2 kHz, and at 4V M" f_{max} is 15 kHz and Z" f_{max} is 10 kHz. The R estimated from the M" peak is smaller than that from the Z" peak, with the total resistance

being largest from the Z* plots where the arc response is depressed, seen from Fig: A6 C. As the DC bias is increased R decreases, whether it is estimated from either of the spectroscopic peaks or from the total R from Z^* plots.

ε_r estimated from the spectroscopic peaks decreases from 78 to 66 from 0 to 2 V, and has a value of 69 when the bias is removed. ε_r from Z" data is slightly higher at 102, this also decreases when the voltage is applied. ε_r calculated from M" (generally associated with the bulk) is still slightly higher than what is normally bulk ε_r of MALI. This trend is seen for MALI from previous results, it's not a homogenous material and has different contributions from various elements, ultimately affecting it's bulk value when taken from M" spectra. This behaviour is seen to reduce once it has been heated and measured on cooling, however since DC bias results are taken at room temperature without any increase in temperature, the bulk values tend to always be higher even at higher voltages when the two contributions seem to separate out. Whereas from the Z" peak its distinctly higher than the ε_r expected for bulk.

Table A1. Estimated R and ε_r values from M'' and Z'' peaks for x = 0.00 synthesised via ball milling, alongside their f_{max} value and the total R from Z^* plots.

Applied Bias/Duration	Frequency (kHz)	R (MΩcm)	ε_r
0V-0MIN	M'' 4	6	78
	Z'' 2	8.1	102
	Z^*	11	
1V-3HRS	M'' 7	3.3	79
	Z'' 3	4.9	115
	Z^*	6.3	
2V-9HRS	M'' 10	2.7	66
	Z'' 8	3.3	66
	Z^*	3.8	
4V-3HRS	M'' 15	1.7	71
	Z'' 8	2.5	89
	Z^*	3	
0V-24HRS	M'' 15	1.8	69
	Z'' 10	2.1	86
	Z^*	2.7	

Results for x = 0.05

Fig: A7 shows Z^* plots for x = 0.05 synthesised via ball milling. There is not a great change in f_{max} with DC bias , especially at low voltages. There was a slight change when 4 V is applied with the total resistance decreasing from 6.4 to 4.3 MΩcm. When the bias is removed

the total resistance still remains at 4.3 MΩcm. Therefore, there does seem to be some irreversible alteration but not as much as observed in some other samples where the f_{max} changes by a large amount.

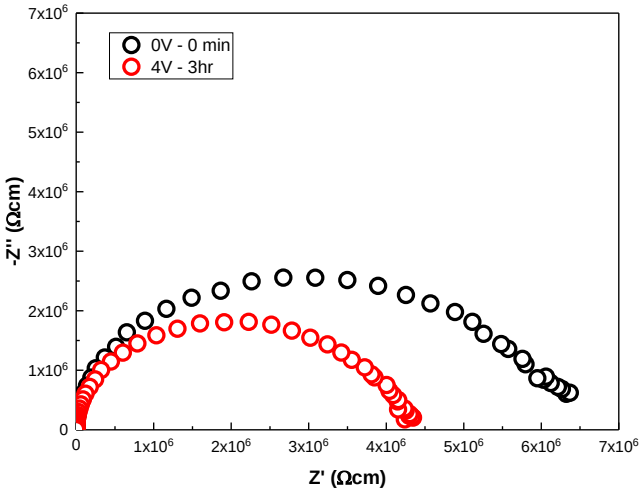

Figure A7. Z^* plots for x = 0.05 synthesised via ball milling before and after 4V DC bias for 3 hrs.

Fig: A8 shows impedance data for x = 0.05 synthesised via DMF and table A2 shows the estimated R and ε_r values, during applied bias. Plot A shows a single M" peak with a f_{max} of 15 kHz, when 2 V is applied, this increases slightly to 18 kHz, with a drop in the M" peak height. When 4 V is applied the M" peak height decreases further and f_{max} is now 66 kHz. The permittivity calculated from the M" peak increases from 66 to 121 when going from 0 to 4 V. When the bias is removed, measuring after 24 hours, the f_{max} decreases to 55 kHz. The M" height increases with a corresponding ε_r of 80. The high frequency ε_r from plot B stays similar with a value of 62. Once again however the C' value at lower frequency is affected much more, with values of C' being in the region of 10^{-9} Fcm^{-1}.

Plot C shows the total resistance at 0 V being 2.5 MΩcm and becomes more conductive as the voltage is increased. At 4 V the single arc become two separate responses, seen from the inset. Having a total resistance of 0.4 MΩcm, the first arc has a corresponding resistance of 0.18 MΩcm and the second arc has a resistance 0.22 MΩcm, with capacitance values of $1.1x10^{-11}$ and $1.1x10^{-9}$ Fcm^{-1} respectively. Once the bias is off and the sample allowed to relax, the total resistance increases again to a value of about 0.85MΩcm, with a low frequency spike being present. Plot D shows that as the voltage is applied the conductivity of the sample increases, by almost an order of a magnitude when 4V is applied.

After the bias is removed and a measurement taken after 24hours, the total conductivity still remains higher than the initial measurement at 0 V.

The x = 0.05 ball milled sample did not show dramatic changes like the x = 0.05 (DMF) sample, instead it showed a trend (seen from table A2) similar to x = 0.00, where increasing of f_{max} occurs with applied voltage, and with the time constant for each peak separating out. R calculated from the Z" peak is larger than the M" peak but for both, R decreases with increased voltage. ε_r starts off similar to x = 0.00, but increases with applied voltage, where at 4 V the M" peak gives a value 121 and the Z" peak gives a value 391. Therefore, both are much larger than the ε_r associated with bulk. The ε_r estimated from the Z" spectra remains higher than from M" spectra throughout. When the bias is removed it decreases to 80, which is still higher than the bulk.

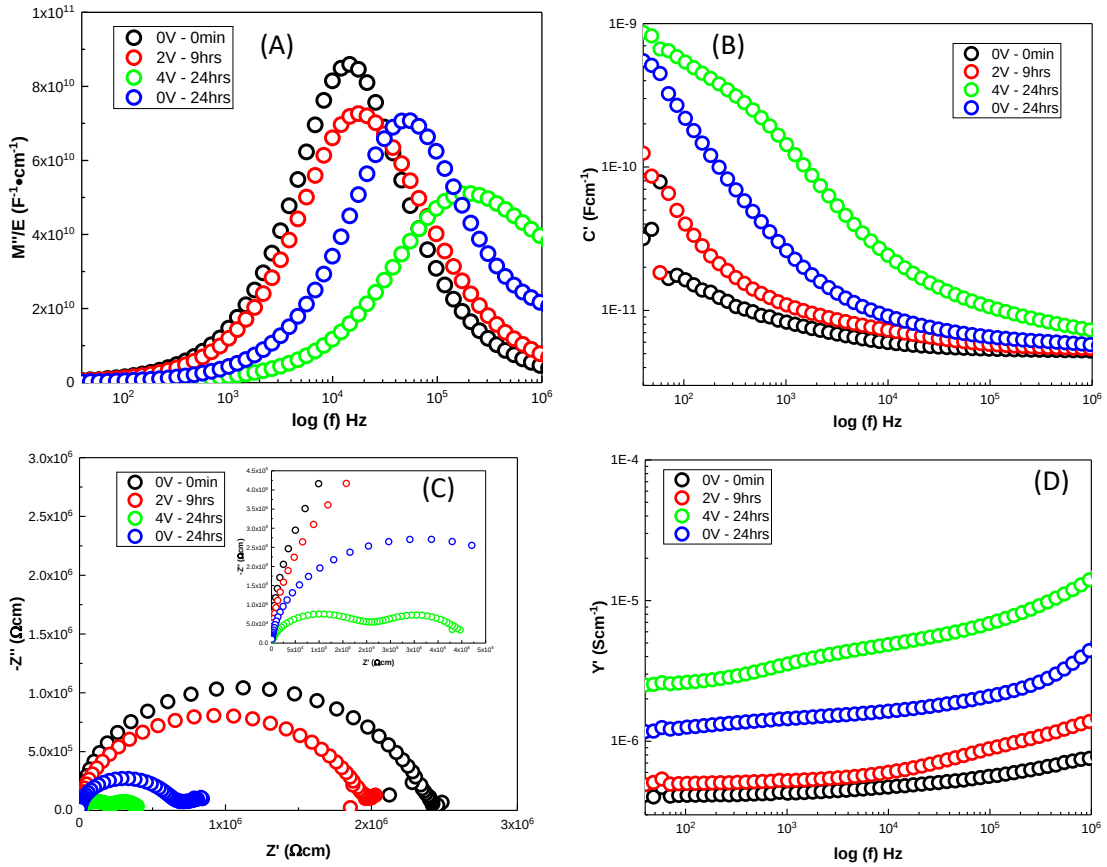

Figure A8. x = 0.05 synthesised via DMF. (A) M" spectra, (B) C' spectra, (C) Z^* plots and (D) Y' spectra.

Table A2. Estimated R and ε_r values from M'' and Z'' peaks for x = 0.05 synthesised via DMF, alongside their f_{max} values.

Applied Bias/Duration		Frequency (kHz)	R (MΩcm)	ε_r
0V-0MIN	M''	15	1.9	66
	Z''	12	2.1	72
2V-9HRS	M''	18	1.3	78
	Z''	12	1.1	138
4V-24HRS	M''	66	0.22	121
	Z''	32	1.4	391
0V-24HRS	M''	55	0.41	80
	Z''	38	0.54	88

Results for x = 0.10

Fig: A9 shows impedance data for x = 0.10 synthesised via ball milling.

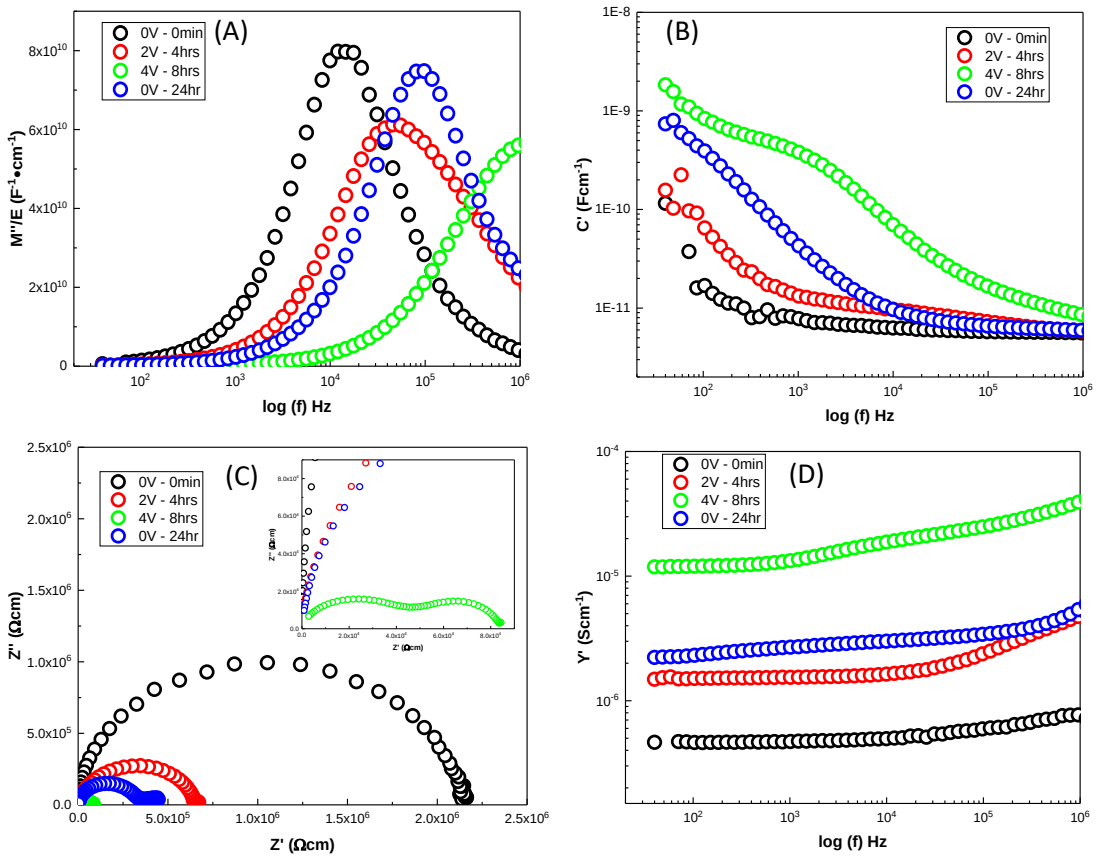

Figure A9. x = 0.10 synthesised via ball milling. (A) M'' spectra, (B) C' spectra, (C) Z^* plots and (D) Y' spectra.

The M" peaks in Fig: A9 A and their estimated R and ε_r values are given in table A3. The M'' peak has an initial f_{max} value of 15 kHz and shifts to higher frequency and then disappears off the scale with increasing bias. The response from 0 to 2 V, sees the M" peak broaden, showing a separation of two elements which is then seen more clearly at 4 V. The M" height also decreases, indicating a rise in the capacitance (ε_r increases from 71 to 93 to 100). When the bias is off and the sample is left to relax, f_{max} decreases but does not return to its original value. The M" height increases back to a similar value giving ε_r of 76. This permittivity is extracted from the M" peak.

Plot B shows that at 1 MHz, ε_r remains the same giving a value of 61. There is again a greater change of the capacitance response at lower frequencies. The response once 4V have been applied shows a low frequency response with a capacitance in the region of 10^{-9} Fcm^{-1}. When the bias is off, the capacitance in this region drops again, although at low frequency there is still a sudden rise in C'. At high frequency the response remains unchanged.

Plot C shows the total resistance decreasing from 2.1MΩcm, at 0 V to 0.7 MΩcm at 2V. At 4V it can be observed from the inset plot, the response split into two arcs, with capacitance values of ~$8.9x10^{-12}$ and ~$1.5x10^{-9}$ Fcm^{-1} respectively and with a total resistance of 84 kΩcm. When the bias is removed, the total resistance increases to about 0.46 MΩcm, with a small low frequency spike. Plot D shows that as the voltage is applied and then increased, the total conductivity increases by more than an order of a magnitude. When the bias is switched off the conductivity remains high.

Table A3. Estimated R and ε_r values from M'' and Z'' peaks for x = 0.10 synthesised via ball milling, alongside their f_{max} values.

Applied Bias/Duration		Frequency (kHz)	R (MΩcm)	ε_r
0V-0MIN	M''	15	1.6	71
	Z''	12	2	75
2V-4HRS	M''	55	0.35	93
	Z''	26	0.55	127
4V-8HRS	M''	1400	0.013	100
	Z''_1	250	0.032	224
	Z''_2	2	0.029	34000
0V-24HRS	M''	98	0.24	76
	Z''_1	67	0.3	90
	Z''_2	0.1	0.094	180000

Similar trends are seen for x = 0.10 in both BM and DMF samples as seen in the previous samples with the effect of applying and increasing voltage on the f_{max} and R values. This is also seen for x = 0.20. The effect of bias becomes more prominent in these compositions of higher x values, not only in their $f_{max,}$ but their ε_r increases to a higher degree. The ε_r from the M" spectra generally stay closer to that of the bulk. At higher voltages the Z" peak splits into two, with $Z"_1$ being more resistive and having a higher ε_r than the corresponding value estimated from M". While $Z"_2$ has the lowest resistance with ε_r being ~800-1200 for x = 0.10 DMF and x = 0.20 ball milling, while for the x = 0.10 ball milled sample ε_r is 34000. When the bias is off the ε_r from M" peak decreases back closer to the bulk value even if the overall impedance response is irreversible. Changes that are prominent are that the time constants diverge enough for the response to be able to be separately distinguishable.

Variation in f_{max} with applied bias

f_{max} from the M" spectra for each sample was plotted at each voltage versus time held in hours. This gives a broader picture of how the sample response alters at room temperature, when the voltage is varied and along the time domain. Fig: A10 shows this for ball milled synthesised x = 0.00, 0.05, 0.10 and 0.20. It does not show the results when the voltage is removed, only the variation during the period when the voltage is applied.

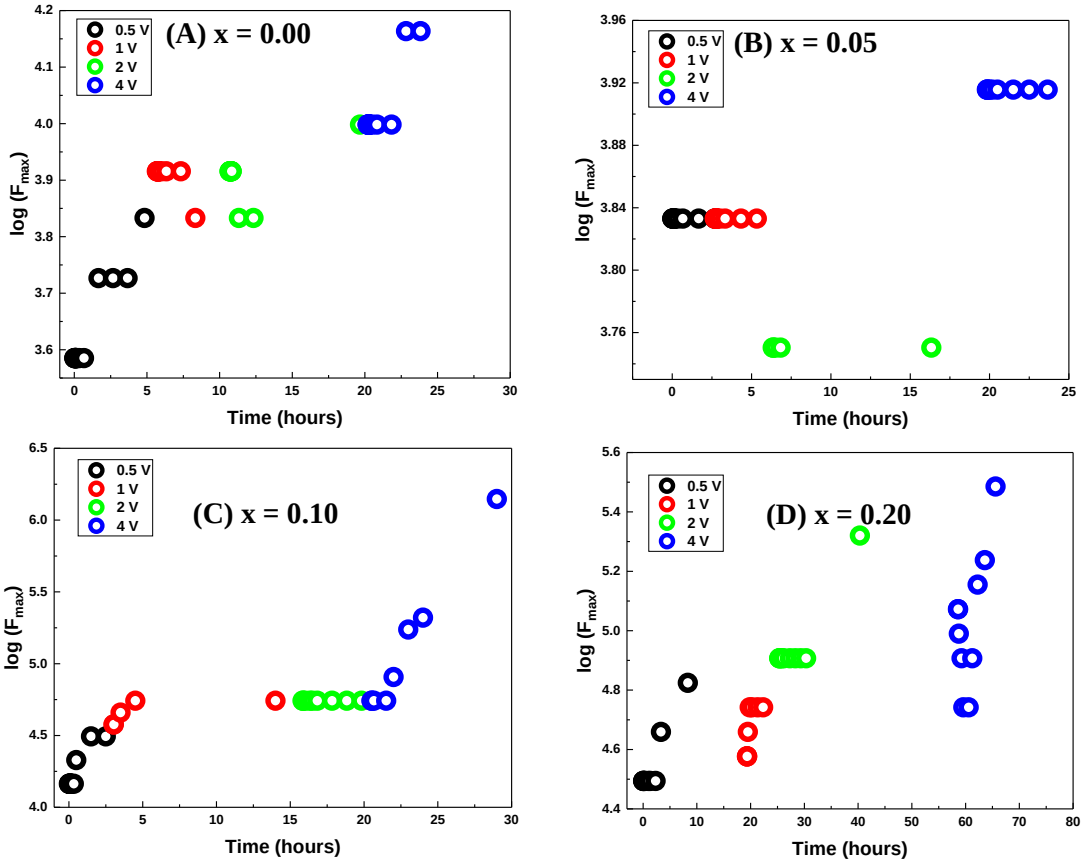

Figure A10. Variation in f_{max} for the M'' peak as a DC bias is applied (with time in hours). (A) x = 0.00, (B) x=0.05, (C) x = 0.10 and (D) x = 0.20.

Fig: A10 shows how increasing the bias from 0 to 4 V changes the f_{max} for x = 0.00 - 0.20. The results show that increasing DC bias moves the M" peak to higher frequency. f_{max} therefore increases altering the time constant. This pattern remains the same for all x series. It also appears that at higher voltages, especially at 4 V, the f_{max} increases at a faster rate, especially for higher values of x as seen from plot C and D for x = 0.10 and 0.20, respectively. When the bias is removed f_{max} decreases although it does not match the initial value.

x = 0.05, 0.10 and 0.20 synthesised using DMF were also investigated via impedance when a DC bias was applied. The results are shown in Fig: A11, the same trends that were observed in the ball milled samples are observed in the DMF samples. The f_{max} increases with applied voltage and on relaxation does not return to the initial value.

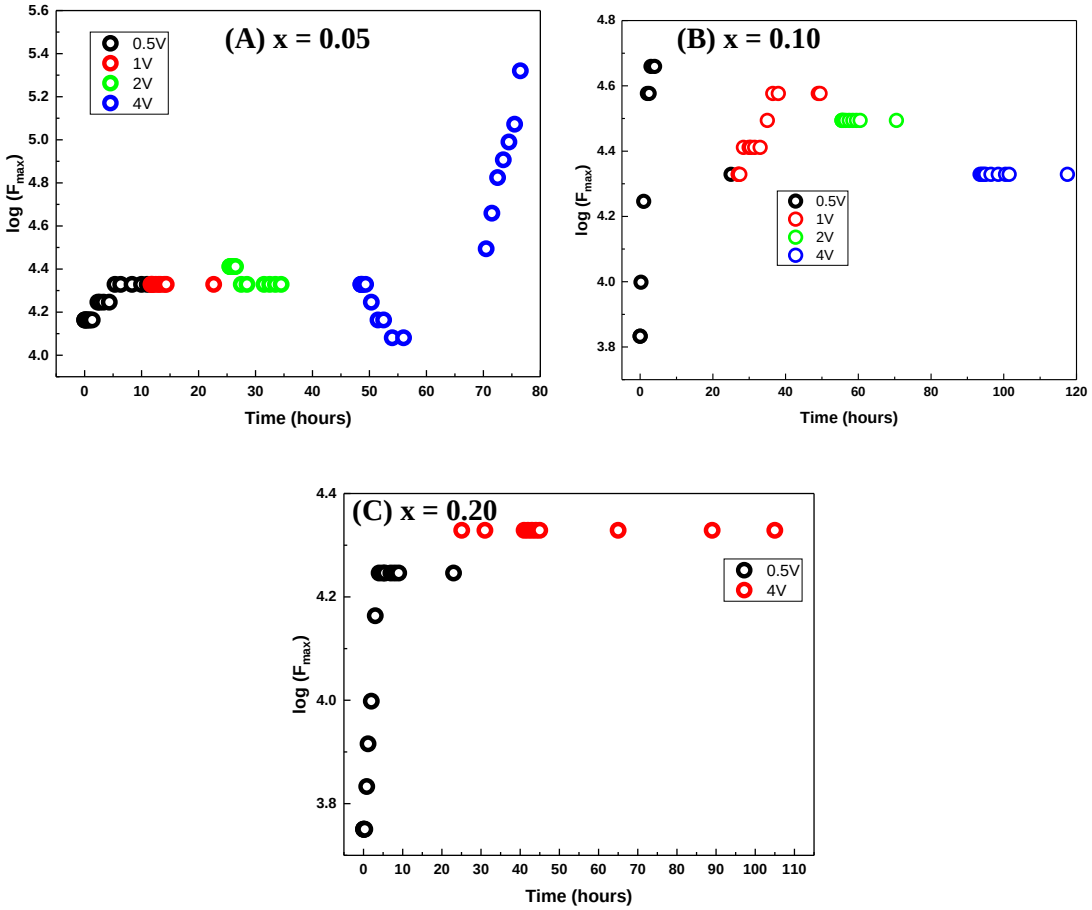

Figure A11. Variation of f_{max} for the M'' peak as a DC bias is applied with time (in hours). (A) x = 0.05, (B) x=0.10 and (C) x =0.20.